UNIVERSIDAD NACIONAL DE COLOMBIA

Universidad Zaragoza
1542

PhD Dissertation

Modelado *in vitro* de los aspectos mecánicos y bioquímicos involucrados en procesos migratorios celulares relacionados con la metástasis de cáncer colorrectal

In vitro modeling of mechanical and biochemical aspects involved in the cellular migratory processes related with colorectal cancer metastasis

Hector Alfonso Castro Abril

Advisors:

Ignacio Ochoa Garrido

Diego Alexander Garzón Alvarado

Manuel Doblaré Castellano

Doctoral programme: Doctorado en Ingeniería Biomédica (Universidad de Zaragoza)

Doctorado en Ingeniería Mecánica y Mecatrónica (Universidad Nacional de Colombia)

Tissue Microenvironment Lab

Instituto de Investigación en Ingeniería de Aragón

Laboratorio de Biomiméticos, Universidad Nacional de Colombia

University of Zaragoza, 2023

Tu ne quaesieris, scire nefas, quem mihi quem tibi
finem di dederint, Leuconoe, nec Babylonios
temptaris numeros. Ut melius, quidquid erit, pati,
seu pluris hiemes, seu tribuit Iuppiter ultimam,
quae nunc oppositis debilitat pumicibus mare
Tyrrhenum: sapias, vina liques, et spatio brevi
spem longam reseces. Dum loquimur, fugerit invida
aetas: carpe diem quam minimum credula postero.

Horace, Odes 1.11

Acknowledgements

This document is the culmination of a very long journey that started back in my homeland, Colombia. Throughout this incredible adventure, I have met amazing people who, in their own ways, have supported me during these years. It is to them that I would like to dedicate these few yet sincere words of gratitude.

First of all, I would like to thank professors Ignacio Ochoa, Manuel Doblaré, and Diego Garzón Alvarado for the oportunity to work with them and to the Republic of Colombia's Ministry of Science and the European Union's Moore4Medical project for the finantial support during these years of my PhD.

Iñaki, thank you for accepting me as a part of your team. You have opened the door to an exciting world that I didn't know I could love or even fit in. Thank you for listening to me and for giving me advice. Thank you for all the talks and the laughs. Thank you for your contagious enthusiasm, your warmth and for encouraging me to give my best. I have learned so much from you and I really hope I can continue to do so.

Manolo, thank you for your incredible support during the most crucial part of my PhD. Our dear "vomit" would not have been the same without you or your ideas. Thank you for your good sense of humor and for the swiftness of your responses. They made my life much easier, especially during this last year.

Profe Diego, without you, this dissertation would not have been possible. Without you, I would have never considered the possibility to embark in an academic career. Thank you from the bottom of my heart for your wisdom, your calmness, and for showing me the way.

I would also like to thank Dr. Jesús del Barrio, from the Instituto de Nanociencia y Materiales de Aragón, and Dr. Jónathan Heras, from the University of La Rioja, for their contributions to this thesis in the form of great collaborations. I hope we can continue working together. Thank you to Rosa and Maria José, the members of the Servicio de Microscopía de Sistemas Biológicos of the University of Zaragoza, for putting up with my incessant requests. I owe some of the best images in this dissertation to you.

To the crew of TME lab, thank you for making me feel like I was at home. Being a foreign student in a country so far from my roots is never easy, and you guys helped me relieve that burden. I am very proud of being part of this family. Roxana, thank you for helping me with the nightmare of the administrative paperwork. I may be paying off some bad karma from my previous life, but thanks to you, it was more manageable. Teodora (my dearest Serbian general), Sandra, Laura, Alodia, and Sara Abizanda. You have all been my spiritual guides. Thank you for showing me the ways of cell culture. I don't think I could have accomplished what I did here without your constant support. Thank you all for taking the time to correct my stubborn engineer self and for being there when I felt low. Thank you for the afternoons, nights, and even holidays we spent together at the lab. Teodora, I once told you that you would become a true friend of mine. Now I can say that out loud, and I am really grateful for that. Sangolán, even though we didn't start this journey at the same time, we finished it together, and I couldn't have asked for a better companion. Laura, your theater plays are great and I hope to continue watching them with you on stage. Alodia, doing "evil stuff" with you has been a bliss. Abizandis, your spontaneity and kindness really brightened up my day (although I will never forgive you for the death of my dinosaur). David, Jacobo, Marina, Clara B, Claudia, Vira, Rut, Lorena, José, Mehran, Reza, Ismael, María, Jorik, and Estíbaliz. Thank you for the good times we have spent together, especially in the "juepinchos" afternoons. Ana Rosa, thank you for your patience. I know dealing with me can be challenging at times. To Dani and Pedro, two of the three musketeers. Thank you for the great afternoons we have spent together drinking Coke and talking about life.

Thank you to my dearest friends Phoenix, Fernando, Meirin, Deixa, Oscar, and Mauri. Phoenix, you have been the shoulder I cried on so many times that I lost count. Thank you for your support. Thank you for the very interesting debates and for your aplomb in almost everything. I owe you a thousand beers. Fer, in all these years, our paths have drawn closer, but they have also taken different directions. Nevertheless, the "combo amigas" will always be there for you whenever you need it. Meirin, the high priestess of my dear **D&T** society. I will never get tired of your awesome tales. Deixa, my pure Thetis, my sensual love, my life, my personal geisha. Thank you for being part of my life. You have been my life teacher, and our pure love will never fade. Oscar, strolling through the forests of Draenor and spreading terror at the Alliance camp with you, will forever be one of my most cherished memories. Lok'tar Ogar, my friend. Mauri, you and I have faced together challenging times, but we have also shared some of the most memorable moments of my life. Even though a vast sea may separate us now, our hearts will forever remain close. Adri, since you entered my life, you have shown me nothing but unconditional and unwavering support. Thanks to you, I am a better person. So, borrowing the words of the Great Poet, I would like to say this to you: *vivamus atque amemus, rumoresque senum severiorum omnes unius aestimemus assis.*

In the end, the biggest thanks go to my family, especially to my mom. You have never stopped believing in me, so this achievement is dedicated wholeheartedly to you.

Abstract

Metastasis is one of the most lethal manifestations in cancer, accounting for up to 90% of cancer related deaths. Recently, it has been shown that the mechanics of tissues, as well as the biological response of cells to different biophysical stimuli, play an active role in the development of cancer as well as in metastasis. Since this disease is a major concern in public health, understanding the biology of metastasis and how mechanics affect this process is essential to develop new therapeutic strategies to attack and even prevent it.

The main aim of this thesis was to study the role of the mechanical environment and the nutrient availability in the evolution of Colorectal Cancer (CRC), one of the leading causes of cancer deaths worldwide. For this, we first varied different fabrication parameters of previously established protocols for generating type I collagen hydrogels. With these hydrogels, we studied the migrating behavior of CRC cell-line spheroids and found that the combined effect of the ultrastructure of the hydrogels and their mechanical stiffness generated profound distinct patterns in cell invasion.

In a parallel approach, we analyzed the response of spheroids to dynamic changes in glucose and Fetal Bovine Serum (FBS) availability in order to check whether these changes generated an adaptive response in the samples. Our results showed that the spheroids indeed had the ability to adapt to nutrient-deprived environments, especially after several cycles of nutrient-abundance and nutrient-starvation. Furthermore, in the case of the HCT-116 cell line, we observed that the spheroids expelled their necrotic core during the starvation cycles, a striking phenomenon that, to the best of our knowledge, has never been reported in literature.

Due to the notoriety of the event, we explored, in the last part of this thesis, the possible mechanisms involved in the ejection of the core. For this, we explored different cytoskeleton (CSK) blockers in the preconditioned spheroids during the starvation periods to check whether the ejection of the core was related to cell contraction. This approach allowed us to conclude that it was indeed involved in the phenomenon, since blocked spheroids did not eject their core during the mentioned period.

Keywords: Cancer, colon, spheroids, migration, invasion, collagen, hydrogels, mechanobiology, cytoskeleton, contraction.

Resumen

La metástasis es una de las manifestaciones más letales del cáncer, con un estimado de 90% de muertes relacionadas por cáncer. Recientemente, se ha demostrado que la mecánica de los tejidos y la respuesta biológica de las células ante distintos estímulos biofísicos juegan un papel activo en el desarrollo del cáncer y la metástasis. Dado que esta enfermedad es un problema de salud pública, el entendimiento de la biología de la metástasis y la forma en la que la mecánica afecta este proceso es esencial para desarrollar nuevas estrategias terapéuticas para atacarla e incluso prevenirla.

El objetivo principal de esta tesis consistió en estudiar el rol del entorno mecánico y la disponibilidad de nutrientes en la evolución del cáncer colorrectal (CRC por sus siglas en inglés), una de las principales causas de muerte por cáncer en el mundo. Para esto, se variaron diferentes parámetros de fabricación de hidrogeles de colágeno tipo I previamente descritos en literatura. Con estos hidrogeles, se estudió el comportamiento migratorio de esferoides celulares derivados de líneas celulares de CRC y se encontró que el efecto combinado de la ultraestructura de los hidrogeles y de su rigidez mecánica generaban patrones invasivos profundamente distintos.

En una aproximación paralela, se analizó la respuesta de los esferoides ante cambios dinámicos en la disponibilidad de glucosa o suero fetal bovino (FBS, por sus siglas en inglés) con el fin de estudiar la potencial respuesta adaptativa de las muestras ante dichas variaciones. Los resultados demostraron que los esferoides efectivamente tenían la habilidad de adaptarse a entornos privados de nutrientes, especialmente después de varios ciclos de abundancia e inanición. De manera adicional, se observó que, en el caso de la línea celular HCT-116, los esferoides expulsaron su núcleo necrótico durante los ciclos de deprivación, un fenómeno que, en lo que a los autores concierne, nunca ha sido reportado en literatura.

Debido a la notoriedad de este evento se exploró, en la última parte de esta tesis, los mecanismos posiblemente involucrados en la eyección del núcleo. Para esto, se exploraron diferentes bloqueadores del citoesqueleto en esferoides durante los períodos de inanición para comprobar la relación entre la expulsión y la contracción celular. Este enfoque permitió concluir que efectivamente había un vínculo, pues los esferoides tratados no eyectaron su núcleo durante los ciclos mencionados.

Palabras clave: Cáncer, colon, esferoides, migración, invasión, colágeno, hidrogeles, mecanobiología, citoesqueleto, contracción.

Contents

List of Abbreviations

2D 2-Dimensional

3D 3-Dimensional

5FU 5-Fluorouracil

Acetyl-CoA Acetyl-Coenzyme A

ADP Adenosine Diphosphate

AFM Atomic Force Microscopy

AMPK Adenosin Monophosphate-Activaded Protein Kinase

ASC Adipose Stromal Cell

ATCC American Type Culture Collection

ATP Adenosine Triphosphate

BF Bright Field

CAM Calcein AM

CMAC Cell-Matrix Adhesion Complex

CP Cyclophosphamide

CQ Cloroquine

CRC Colorectal Cancer

CSC Cancer Stem Cell

CSK Cytoskeleton

D0 Low glucose DMEM supplemented with 1% P/S and 1% L-glutamine

D10 Low glucose DMEM supplemented with 10% FBS, 1% P/S, and 1% L-glutamine

DG0 High glucose DMEM supplemented with 1% P/S and 1% L-glutamine

DG10 High glucose DMEM supplemented with 10% FBS, 1% P/S, and 1% L-glutamine

DMEM Dulbecco's Modified Eagle Medium

DMSO Dimethylsulfoxide

DNA Deoxyribonucleic Acid

DXR Doxorubicin

ECM Extracellular Matrix

EDTA Ethylenediaminetetraacetic acid

EGF Epidermal Growth Factor

EMT Epithelial-Mesenchimal Transition

ER Endpolasmic Reticulum

FBS Fetal Bovine Serum

GBM Glioblastoma Multiforme

GelMa Metacrylated Gelatin

GFP Green Fluorescent Protein

GLUT1 Glucose Transporter 1

GLUT3 Glucose Transporter 3

H&E Hematoxylin & Eosin

HA Hyaluronic Acid

HIF Hypoxia Inducible Factor

HIF-1α Hypoxia Inducible Factor 1α

HIF-2α Hypoxia Inducible Factor 2α

IF Intemediate Filaments

IGF-1 Insulin-like Growth Factor 1

IISA Instituto de Investigación Sanitaria de Aragón

INMA Instituto de Nanociencia y Materiales de Aragón

IR Irinotecan

ISC Intestinal Stem Cell

IVM Intravital Microscopy

MPLSM Multiphoton Light-scanning Microscopy

NADH Nicotinamide Adenine Dinucleotide

NaOH Sodium Hydroxide

NK Natural Killer Cell

OXPHOS Oxidative Phosphorylation

PAA Poly(Acrylic Acid)

PBS Phosphate Buffered Saline

PDA Pancreatic Ductal Adenocarcinoma

PDGF Platelet-derived Growth Factor

PDMS Polydimethylsiloxane

PFA Paraformaldehyde

PI Propidium Iodide

RI Refractive Index

ROCK Rho-associated protein Kinase

ROCK1 Rho-associated, Coiled-coil-containing protein serine/threonine Kinase 1

ROCK2 Rho-associated, Coiled-coil-containing protein serine/threonine Kinase 2

RPMI Roswell Park Memorial Institute cell medium

RT Room Temperature

SAI Servicio de Apoyo a la Investigación

SEM Scanning Electron Microscopy

SHG Second-Harmonic Generation microscopy

SNARK Sucrose Nonfermenting AMPK-Related Kinase

TCA Tricarboxylic Cycle

TEM Transmission Electron Microscopy

TME Tumor Microenvironment

TNM Tumor, Node, Metastasis Classification of Malignant Tumors

UPR Unfolded Protein Response

List of Figures

List of Tables

1. Introduction

1.1. Cancer

Cancer, the second leading cause of death worldwide, is the common name for a group of diseases characterized by the presence of abnormally dividing cells that have the ability to disseminate and invade foreign tissues inside an organism [1]. Cancer can be classified according to multiple criteria; however, one of the most common is related to the type of cell from which the tumor originated. According to this criterion, there are four major families: carcinomas, sarcomas, lymphomas, and neuroectodermal tumors [2, 3]. Carcinomas comprise cancers originated from epithelial cells, such as colorectal cancer (CRC), and constitute the most common type of human cancers. Sarcomas encompass tumors originating from cells belonging to the connective tissue, such as osteosarcoma. In turn, lymphomas cover cancers related to the lymphopoietic and hematopoietic cells, such as leukemia. Finally, the neuroectodermal family includes all tumors derived from cells of the central and peripheral nervous system, such as glioblastoma and neuroblastoma [2].

During the natural evolution of the disease, tumor cells acquire several features that allow them to surpass and even control the multiple regulatory mechanisms of an organism in order to survive and disseminate to distant parts. These features have been organized in what is called as the Hallmarks of Cancer (Figure **1-1**) [3–6]. In this PhD dissertation, the broad focus was placed into understanding how the deregularization of cellular metabolism, together with the unlocking of phenotype plasticity, could potentially alter the invasive capacity of CRC cells.

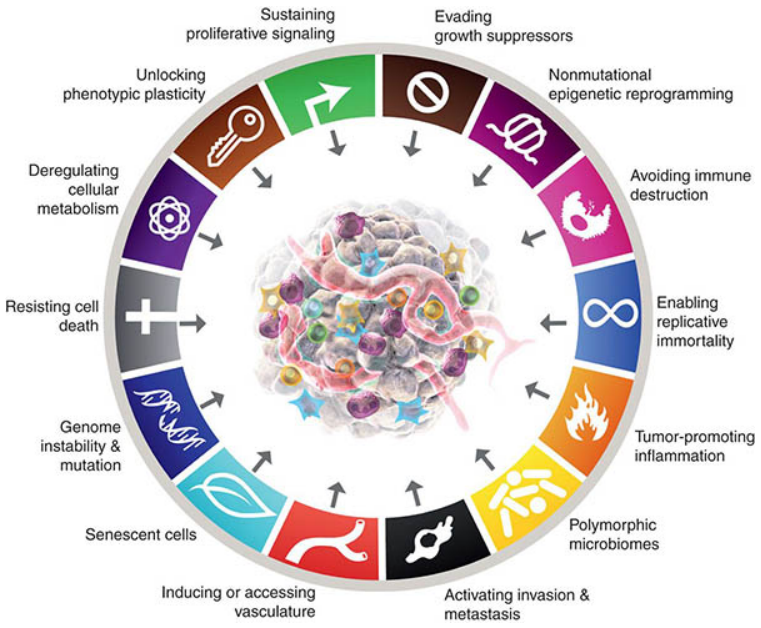

Figure 1-1: The Hallmarks of cancer. Taken from [6].

1.1.1. Colorectal cancer (CRC)

1.1.1.1. Incidence, prevalence, and mortality

CRC is the third most common type of cancer worldwide, with an estimated number of new cases in 2020 of 1.931.000 (10% of total new cancer cases), and the second leading cause of cancer deaths, with an estimated number of deaths in 2020 of 935.173 (9.4% of the total cancer deaths) [7]. Furthermore, the incidence and mortality of CRC among persons younger than 50 years has increased in recent years [8–10]. CRC initiates in the crypts of the colon (or rectum) epithelium [11]. In these zones, the elevated proliferative rates of the Intestinal Stem Cells (ISC) increase the probability to develop mutations during the replication of DNA [12, 13]. Such mutations can also be generated by other external factors, including diabetes, obesity, smoking, and elevated alcohol consumption [14–18].

1.1.1.2. Natural evolution of the disease

Following the acquisition of the mutations, transformed ISC can proliferate and form bening tumors, known as adenomatous polyps. These polyps can become malignant and invade distant organs, especially the liver.

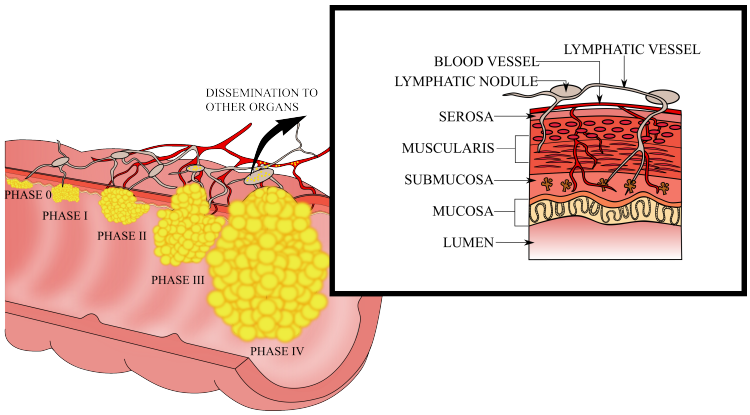

Figure 1-2: Development of CRC. Adapted from [19].

In clinics, several classifications have been proposed to group patients with similar prognosis [20]. The TNM system is nowadays the most used one. It was initially developed by Denoix [21], and is based on the size of the tumor (T), the compromise of lymph nodes (N), and the dissemination to other tissues (M). The stages under this system are also represented by Roman numerals, ranging from I to IV, to indicate the degree of development of the lesions at the histological level.

For the CRC, the classification is as follows [22, 23]:

1. Stage 0: The tumor is located in the colon or rectum mucosa layer, but has not invaded other regions.
2. Stage I: The tumor penetrated the mucosa layer and penetrated the muscularis layer of the colon/rectum.
3. Stage II: The tumor "anchors" to tissues surrounding the colon/rectum, such as the peritoneum, but it has not infiltrated in lymph nodes.
4. Stage III: The tumor has infiltrated surrounding lymph nodes, but has not spread to other zones in the body.
5. Stage IV: The tumor has metastasized.

1.1.2. Metastasis

Among the multiple features depicted in Figure **1-1**, the hallmark related to the activation of invasion and metastasis is a critical step in the evolution of the disease, as metastasis is the leading cause of cancer-related deaths [1, 24–26]. According to Weinberg et al. and López-Lázaro et al. [2, 27], metastasis is defined as the formation of one or several tumors stemming from the dissemination of tumor cells to other locations in an organism. It is an inherent characteristic of tumor cells, and is especially present in CRC and other carcinomas [5, 28, 29].

As every other hallmark, metastasis is a gradual process that initiates with the detachment of a group of cells from the main mass (either in groups or as individuals). These detached cells first invade the tissue surrounding the tumor and transform it to facilitate the communication between the tumor and the blood or lymph vessels and to promote tumor survival [2, 28, 30]. Once the cells come in contact with the blood vessels, they intravasate and travel through the blood or lymph system until they reach a specific zone. Afterwards, tumor cells extravasate and start invading the parenchima of the target tissue [2, 31]. If the cells successfully colonize the parenchima, they will form small nodules, called micrometastases, that can expand until they form clinically detectable tumors [2]. These new tumors are called metastatic tumors and, given the scarce therapeutic strategies to counter their progression, are often associated with poor prognosis and a reduced life expectancy [26].

Due to the importance of metastasis, a vast amount of research has been conducted to understand the mechanisms involved in the multiple steps that lead to its progression. As a result of this effort, several biochemical and genetic key factors in the development of metastasis [2, 5, 32], as well as biochemical signaling pathways that become altered during its evolution, have been identified [11, 33–35]. The identification of these factors and pathways have allowed researchers to develop therapeutic strategies to combat not only metastasis, but also cancer [5].

1.2. Cancer cell mechanobiology

Although metastasis is a process that has been traditionally studied from a molecular point of view [5, 11, 31–53], there is indisputably a mechanical component that also affects profoundly the dissemination of the cells. The study of this component has given birth to an emerging field called cancer cell mechanobiology. Mechanobiology is a broad field of science that focuses on the way cells can form, maintain and adapt the tissues as an active response to mechanical stimuli in their environment [54, 55]. In the context of cancer, mechanobiology focuses on studying how the physical barrier imposed by the extracellular matrix (ECM), its mechanical properties, the mechanical interaction of cells with themselves and the ECM [56], and the mechanical properties of cells [57, 58] contribute to the progression of the disease, especially in the acquisition of the invasive phenotype associated with metastasis [59].

1.2.1. Cell migration modes

Cell migration is a complex process that comprises cell morphology and the molecular cues that allow cells to migrate [60]. Cell migration modes can be roughly classified in two main categories: individual or collective [60]. Both modes of movement are related to the presence, or absence, of cell-cell unions. Thus, in the individual migration mode, cells lack these unions whereas in the collective mode, the unions are retained [60]. The migration mode chosen by the cell depends on multiple factors [60–62]. However, the adhesivity of the cells to the ECM, which depends on the architecture, composition, and mechanical properties of the matrix, and the presence of intercellular unions constitute two of the most important parameters to determine the migration mode [60, 63, 64].

1.2.2. Cell-cell and cell-matrix mechanical interactions in metastasis

1.2.2.1. Cell-cell mechanical interactions

Cell-cell interactions are responsible for the transmission of electrical, chemical or mechanical signals among cells. However, they also provide physical points of contact for other cells [65]. Adhesions are specifically related to mechanical interactivity and are supported by the presence of transmembrane proteins that, in the extracellular space, interact with the transmembrane proteins of neighboring cells, and, in the intracellular space, interact with all the major components of the cytoskeleton [66]. This gives rise to different classes of cell-cell adhesions: tight junctions, adherens junctions, and desmosomes. Tight junctions, which are commonly found in epithelial cells, such as those in the colon, act primarily as controllers of paracellular permeability by restricting difussion of molecules based on their size and charge [67]. Adherens junctions modulate cell shape, maintain tissue integrity, and helps transmitting mechanical forces among cells through the CSK [68]. Tight junctions involve the interaction of transmembrane proteins of the cadherin family, such as E-cadherin, and the intracellular catenin family members (p120-catenin, β-catenin,

and α-catenin) that connect the cadherins with the CSK of cells, especifically the actin cytoskeleton [68]. These junctions are usually lasting and stable in time, as their main function is to keep the contact between cells. Finally, desmosomes provide mechanical stability to cells subjected to high mechanical stress, such as cells in the myocardium, bladder, gastrointestinal mucosa skin, by linking intermediate filaments (IF), another major component of the CSK, to the plasma membrane of cells [69]. Figure **1-3** shows a schematic representation of these junctions in cells.

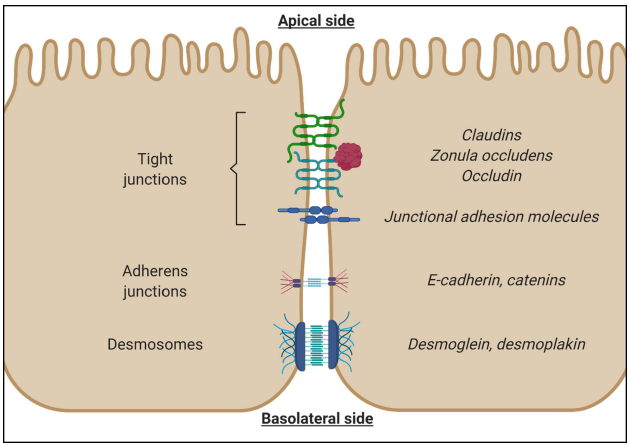

Figure 1-3: Schematic description of cell-cell adhesions. Taken from [70].

Cell-cell interactions play a key role in metastasis, as it has been demonstrated that cancer cells are able to suppress genes encoding different proteins involved in the maintenance of cell-cell adhesions, such as E-cadherin, [5, 33, 35], while upregulating the expression of genes encoding other cell-adhesion molecules, such as N-cadherin [46, 50, 71]. This shift is known as the epithelial-mesenchimal transition (EMT) and it is a major feature in epithelial cancers.

1.2.2.2. Cell-matrix mechanical interactions

Cell-matrix interactions account for the fashion cells interact with their surrounding ECM. Regarding mechanical interactions, they are mediated by specialized transmembrane receptors, called adhesion receptors, that interact with the ECM at the exterior of the cell, and with the cytoskeleton (CSK) at its interior [72]. Since the ECM is composed of several proteins (collagen, non-collagen, and proteoglycans [73]), there are also different types of adhesion receptors [74]. Adhesion receptors form cell-matrix adhesion complexes (CMACs), which are crucial to cells since they serve as sensing centers of the composition, mechanical properties, and even the geometry of the ECM [73, 75, 76]. The received signals from these receptors influence multiple processes inside the cell, such as their shape, polarity, fate, and motility [77, 78]. Thus, these complexes are continuously regulated and can be created or suppressed depending on the cell needs [74, 75]. Figure **1-4** shows a schematic representation of the different cell-matrix mechanical interactions from a contact point of view.

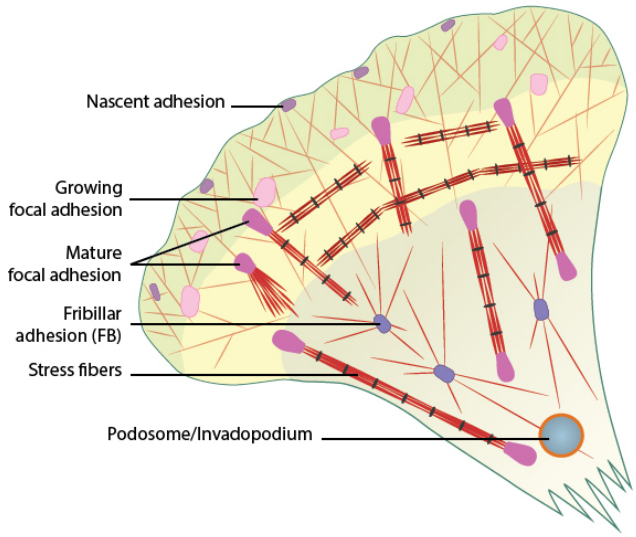

Figure 1-4: Schematic description of cell-matrix adhesions. Taken from [79].

In cancer, the interaction between cells and the ECM, and their role in cell migration have been broadly studied, mainly with the aid of 2D *in vitro* assays. For instance, Provenzano et al. visualized the mechanical interactions between the stroma and tumor epithelium to determine the influence of the ECM, its density, and composition on the formation and progression of breast cancer [80]. For this, the authors performed multiphoton light-scanning microscopy (MPLSM) and second-harmonic generation microscopy (SHG) imaging of the ECM of both healthy and pathological murine breast tissue explants. In light of these results, the authors defined three characteristic signatures of breast cancer. These signatures demonstrated that collagen fibers were denser around the tumor, and that their orientation changed on the invasive fronts and the non-invasive ones, thus concluding that fiber orientation facilitates cancer cell migration. The same authors demonstrated, several years later, that the increase in collagen density around the tumor increased tumorigenesis of breast cancer [38], probably due to the fact that collagen may stimulate cell proliferation.

The idea of collagen fibers as potential pro-cancerogenic factors was retaken by Han et al. [48]. The authors studied *in vitro* the intravasation capacity of cancer cells by changing the orientation of collagen fibers. For this, they seeded a mixture of type I collagen and matrigel inside a microfluidic device. Collagen fiber orientation at the center of the device, and at the interface with the matrigel was measured. This platform was subsequently seeded with single cancer cells and the migratory patterns of cells were tracked. With their results, the authors observed that the fibers at the interface, which had an average orientation close to 90°(with respect to the horizontal axis of the visualization field), facilitated the infiltration of cancer cells inside the matrigel.

In turn, Ritching et al. [47] studied the velocity and the persistent time of cancer cells on collagen hydrogels with fibers with varying alignment degrees. The orientation of the fibers was performed by using a uniaxial deformation device. Once deformed, the authors seeded MDA-MB-231 cells on the surface of these hydrogels and measured the aforementioned parameters. They observed that as the alignment increased, the stiffness of the hydrogels (in the direction of alignment) and the persistent time of cells increased. With their results, the authors concluded that fiber alignemt is essential to enhance cell persistent movement along a given direction and, therefore, it is a key factor to the progression of metastasis.

Ayuso et al. [81] analyzed cell migratory patterns of head-neck (OSC-19) and glioblastoma, GBM, (U-87 MG) cancer spheroids under chemotactic gradients. For this, they designed a microfluidic device in which they seeded the cells. They applied a biochemical gradient of FBS and monitored cell migration. The authors observed that, although both cell types migrated towards the positive direction of the gradient, the exhibited migratory patterns were different, as OSC-19 cells migrated collectively whereas U-87 MG cells migrated individually. These results further reinforce the notion that studying cell migration in cancer is essential to understand the diverse mechanisms used by cells to move through different matrices. Finally, Gong et al. [82] developed a protocol for generating collagen fiber bundles, which resemble the collagen observed by Provenzano et al. [80]. These bundles, which were then seeded in a microfluidic device to align fibers in the longitudinal direction of the chip, were used to demonstrate the capacity of the bundles to generate directed cell migration of MDA-MB-231 and HCT-116 cells. They were also mixed with agarose to also demonstrate that they can elicit a migratory response to better simulate in vivo observations.

1.3. Nutrients, cancer cell metabolism and growth

1.3.1. Glucose as a major component in cancer metabolsim

As every living organism, cancer cells require energy to support their needs. However, since they cannot generate it *de novo*, they need to find a source in their environment. This source comes from the food that an organism ingests and has multiple forms, including fats, proteins, and polysaccharides [83]. Cells release energy from food molecules through a series of chemical reactions (oxidation) where the electrons of a donor molecule (food) are transfered to an acceptor molecule that also stores part of the energy that is lost during the process [84]. This yields a byproduct that has lower energy content than the preceding donor molecule. At the end of the oxidation chain, the remaining carbons from the original source are released as waste in the form of carbon dioxide (CO_2) and water [83]. The transference of electrons from donor molecules to acceptors is mediated by different cellular intermediates, denominated electron carriers, that continuously accept (reduce) and give electrons (oxidate) without being consumed in the reaction [83]. There are multiple types of electron carriers accross species; however, adenosine triphosphate (ATP) and nicotinamide adenine dinucleotide (NADH) are two of the most common ones [83]. These two molecules can be used throughout the cell to sustain different functions.

After food is digested, eukaryotic cells can use three major interconnected processes to extract the energy held in the chemical bonds of food molecules: glycolysis, the Tricarboxylic Acid Cycle (TCA), and oxidative phosphorylation (OXPHOS) [83, 84]. Figure **1-5** shows a schematic representation of these processes.

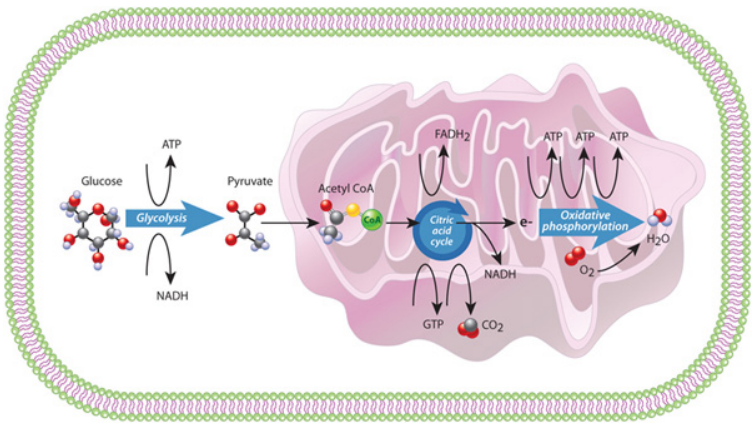

Figure 1-5: The three major metabolic pathways in eukaryotic cells. Taken from [84].

Although there are multiple sources of energy, carbohydrates and, in particular, glucose, are the major sources of energy for animal cells due to their high caloric content [83]. Once glucose enters the cytoplasm, it is converted through the glycolysis process into pyruvate [85]. Pyruvate production does not require the presence of oxygen, but it does need the presence of ATP and NADH to be produced [83, 85]. However, the fate of pyruvate depends upon whether oxygen is present. In the presence of oxygen, pyruvate can enter the mitochondrion of cells, where it serves as the input for the TCA cycle by converting into Acetyl-coenzyme A (Acetyl-CoA) [86, 87]. As the TCA cycle progresses, electrons resulting from a specific step in the cycle are transfered to a series of membrane protein complexes located in the mitochondrion to carry out the third major energetic process: the OXPHOS [87, 88]. By contrast, in absence of oxygen, pyruvate stays in the cytoplasm, where is converted into lactate, a product excreted from the cell [85]. Lactate production is crucial for cancer cells, since it has been demonstrated that the heterogeneity in nutrient and oxygen availability forces cells to reprogram their metabolic pathways to use glycolysis and lactate production as the major energy production sources, even in the presence of oxygen, in a process called the Warburg Effect [89].

1.3.2. FBS and cell growth

Similar to multicellular organisms, cells in *in vitro* cultures need multiple factors to proliferate. *In vivo*, these factors, along with nutrients, hormones, proteins, coagulants, immunoglobulins, and cells are transported in the blood [90]. Blood is therefore a mixture of native cells (erythrocytes, leukocytes, and thrombocytes), and a liquid part, called plasma, comprised by the rest of the mentioned components. When plasma is further treated to remove the coagulation factors, the resulting liquid is called serum [91]. Serum is therefore a complex mixture of components that cannot be produced synthetically in a scalable manner, mainly due to the fact that it has over 697 proteins [92], but is nonetheless essential for proper *in vitro* cell growth [93]. As such, blood serum is replaced by sera coming from other mammals. Among them, the most common is the Fetal Bovine Serum (FBS) [94]. In cancer, FBS is a standard component in cell culture media [95].

1.3.3. Nutrient preconditioning as a therapeutic target against cancer

As stated above, nutrient availability varies greatly during tumor progression, forcing cancer cells to alter their behavior in order to adapt to such changes. For instance, in glioblastoma (GBM), the lack of oxygen forces massive cell migration towards vascularized zones, giving rise to a phenomenon known as pseudopalisade [96]. In CRC, nutrient starvation has been shown to upregulate autophagy as a protective mechanism against nutrient stress [97, 98], although it can also lead to cell death [99]. Furthermore, at a systemic level, nutrient starvation has been shown to have intergenerational lasting effects via epigenetic modifications [100–102]. Epigenetics refers to modifications of gene expression via mechanisms that are not directly related to the DNA coding sequence [103, 104].

Taking into account the potential lethal effect of nutrient starvation on cancer cells, several studies have assessed the efficacy of different chemotherapeutic drugs in combination with short periods of both glucose and FBS restriction against different CRC cell lines [105–109]. These short-termed periods of starvation are known as preconditioning periods and, according to these studies, may potentitate the killing effect of the drugs.

1.4. Importance of *in vitro* models for CRC

1.4.1. Spheroid cultures as models to better recapitulate *in vivo* CRC tumor behavior

Classic *in vitro* studies in cell culture have been performed in 2D cultures [110]. In these cultures, cells grow in flat surfaces (Petri dishes, flasks or glass) as adherent monolayers to which multiple treatments can be tested with relative ease [111]. In addition, 2D cultures do not require complex configurations for maintenance and are simple to implement [110, 111]. However, despite these advantages, these cultures present two major drawbacks. In first place, 2D cultures fail to recapitulate in vivo intercellular and cell-matrix interactions of tumor masses. This results in profound differences in cell morphology, gene expression, proliferation rates, and even response to chemotherapeutic agents that limit the extrapolation of results to clinical situations [110–112]. The second major drawback is related to the uniform nutrient and oxygen availability in 2D cultures. This is crucial for cancer cells, as it has been demonstrated that both nutrient and oxygen availability is variable inside tumor masses, which critically conditions their behavior and fate [113–117].

To circumvent these issues, 3D cell cultures have emerged as a promising alternative to better recapitulate the inherent 3D architecture of tissues and tumors, wich include intercellular and cell-ECM interactions, as well as the heterogeneous nutrient and oxygen distribution in tumors [118]. Among the different type of 3D cell cultures, spheroids are one of the most commonly used models [118], mainly because they can successfully reproduce key aspects of tumors, including intercellular interactions, oxygen and nutrient gradients, drug resistance, and invasive capacity [119–121]. Figure **1-6** summarizes the main characteristics of spheroids.

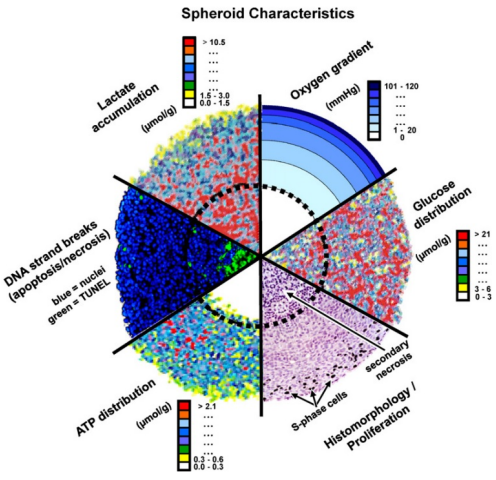

Figure 1-6: Schematic description of the main in vivo tumor characteristics reproduced in spheroids. Taken from [122].

There are various methods to form multicellular spheroids, depending on the cell type, culture condition, and experimental purpose. Some selected examples of the most common methods include: hanging drop method [123], liquid overlay [124], pellet culture [123], spinner culture [124, 125], biomaterial-aided [123, 125], microfluidic platforms [126–129], and magnetic levitation [130]. Figure **1-7** shows a graphical description of the mentioned methods to generate spheroids [118].

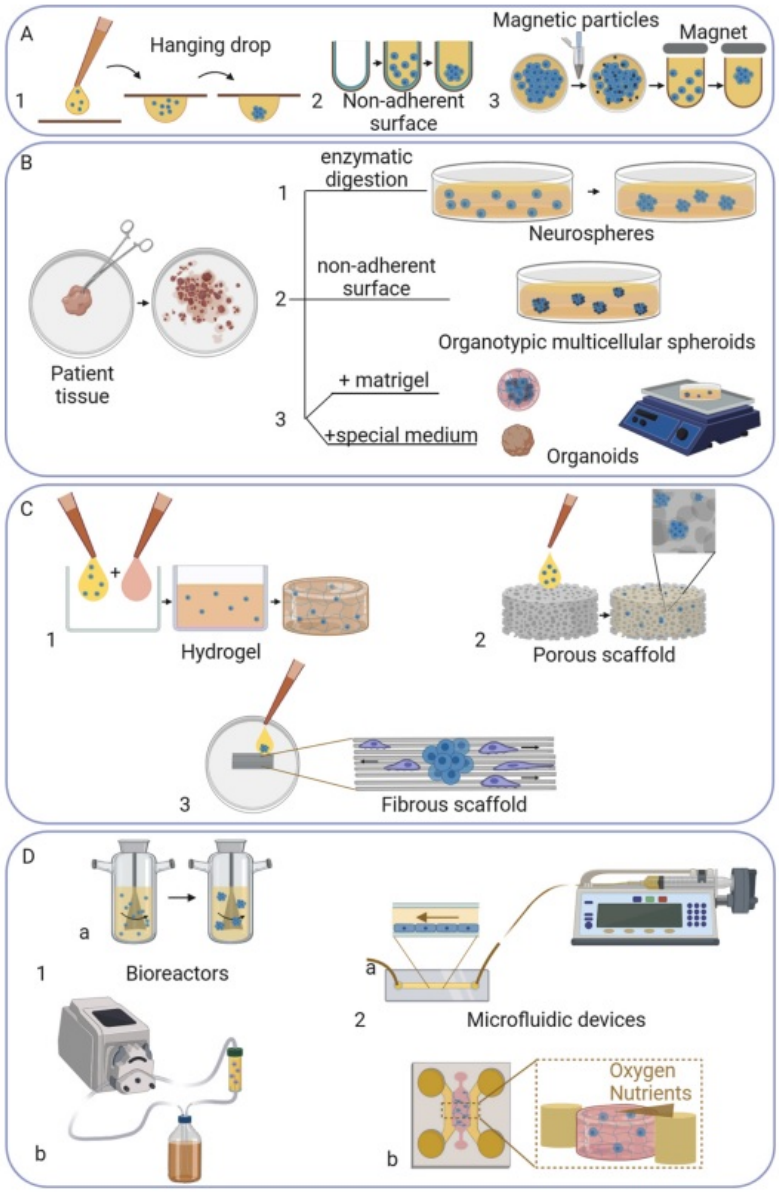

Figure 1-7: Spheroid fabrication methods. Taken from [118].

Spheroids have been widely used in CRC cancer research. For instance, Gheytanchi et al. performed morphological and molecular characterization of spheroids made of two common CRC cell lines (HT-29 and Caco-2) to evaluate the changes in the expression of stemmness genes and cancer stem cells (CSC) markers in the spheroids in comparison to adherent 2D versions made from the same lines [119]. From their analyses, the authors concluded that, compared to 2D adherent cells, spheroid cultures can enrich the stem-like features of tumor cells by up-regulating stemness genes and surface markers. In turn, Sargenti et al. performed physical characterization (weight, diameter, and mass density) of several spheroids of different CRC cell lines (HT-29, HCT-15, SW620, and DLD-1) co-cultured in presence or absence of Natural Killer (NK) cells in order to investigate: 1) whether the cell lines alone could produce spheroids with different physical properties; and 2) whether the interactions with NK cells could modify their physical properties [121]. The authors concluded that the different cell lines produced spheroids with different physical properties that, in turn, were modified by the cytotoxic effects of the immune cells. Last, Tidwell et al. demonstrated that spheroids derived from HCT-116 and SW948 exhibited increased glucose metabolism (higher glycolysis rates and enhanced activity of the pentose phosphate and glutaminolysis pathways) compared to matching 2D cultures [120].

1.4.2. Collagen hydrogels as a platform for studying CRC cell invasion and migration

Collagen hydrogels have become a valuable tool in in vitro cancer research due to their unique properties and relevance to the tumor microenvironment. They are 3D matrices made of polymerized networks of collagen molecules, especially type I collagen molecules, crosslinked by either physical or chemical procedures that have the capacity to retain high amounts of water [131]. These hydrogels can mimic the native ECM of the target tissue and offer several advantages for studying cancer cell biology. For instance, type I collagen hydrogels are biocompatible materials, with low antigenicity and low inflammatory and cytotoxic responses [132]. Thus, they are excellent materials to study cell migration, adhesion, proliferation, and even interaction with drugs while closely mimicking the physiological environment of cells [60, 61, 133–136]. They also offer the possibility to alter their mechanical and biochemical properties (stiffness, pore size, and ligand density) by adjusting their fabrication parameters to recreate specific aspects of the tumor microenvironment (TME) [137]. In addition, they can also be combined with other molecules, such as hyaluronic acid (HA) to enhance their physical properties [138]. Finally, due to their inherent properties, type I collagen hydrogels can also be used to study the interaction between cells and the ECM, providing insights in the understanding of CRC tumor progression [139].

1.5. Thesis objectives

According to the evidence presented in the previous chapter, understanding the mechanobiological response of CRC cancer cells to both physical and biochemical changes in their microenvironment is crucial to develop reliable models to simulate tumor progression into metastasis. Although cancer mechanobiology has progressed extensively in the last decades, there are still many uncertainties related to the effects of the mechanical properties of the ECM and the migratory capacity of spheroids. In addition, there are still few data relating the modulatory effects of nutrient availability on cell migration in spheroids. Furthermore, the long-term effects of nutrient availability in the biological response of CRC spheroids has also been poorly understood. Therefore, we proposed to develop 3D *in vitro* models that could serve as a basis to answer these questions.

To develop this thesis, the following objectives were formulated:

Main objective

To describe, from an experimental point of view, the effect of variations in the biochemical and mechanical microenvironment of colorectal cancer cells on their mechanobiological behavior relative to migration and invasion in the context of metastasis.

Specific objectives

The general objective of the thesis was originally divided into two specific objectives:

1. To evaluate the biological response of cancer cells to biochemical variations.
2. To evaluate the cell migration patterns under variations in the mechanical microenvironment.

These two were further reformulated and expanded in order to better reflect the work developed in this dissertation. Therefore, the new specific objectives are the following:

1. To evaluate the effect of mechanical and ultrastructural properties of the extracellular matrix (ECM) on tumor spheroid invasion.
2. To study the adaptive abilities of CRC tumor spheroids to different metabolic environments.
3. To study the mechanical response of CRC tumor spheroids to drastic changes in the metabolic environment.

2. Materials and methods

2.1. Commercial cell lines

Human colon carcinoma cell lines (HCT-116 and HT-29) were purchased from the American Type Culture Collection (ATCC). Glioblastoma cell lines (U87-MG and U-251 MG) was purchased from Sigma Aldrich (89081402). Neuroblastoma cell line (SH-SY5Y) was a kind gift from Dr. Julián Pardo, from the Instituto de Investigación Sanitaria de Aragón (IISA).

All cell lines were cultured in high glucose (4.5 g/L) Dulbecco's Modified Eagle Medium (DMEM, Lonza BE12-64F) supplemented with 10% Fetal Bovine Serum (FBS, Sigma Aldrich F7524) 2mM Ultraglutamine (Lonza, 0MB074) and 1% penicillin/streptomycin (Lonza, 17-602E). All cell lines were maintained at 37°C inside a humidified TEB-00 incubator (EBERS Medical Technology) with 5% CO_2. Subculture of the cells was performed every third day or when the culture reached around 80% confluence by using Trypsin/EDTA solution (Lonza, Be17-161E).

2.2. Fluorescent cell transfection

HCT-116 cell line was stably transduced with a green fluorescent protein (GFP)-expressing lentiviral vector, which was kindly donated by Dr. Prats, from the University Paul Sabatier in Toulouse (France). Briefly, a concentration of 5×10^4 HCT-116 cells/well were seeded in a 24-well plate and allowed to attach to the surface of the wells for 24 hours at 37°C inside a humidified atmosphere containing 5% CO_2. Afterwards, growth medium was removed and cells were washed twice with PBS. Then, Opti-MEM medium (Thermofisher, 31985062), previously supplemented with 5 μg/mL protamine sulfate (Sigma, P4505) and mixed with the lentivirus suspension (1:1 ratio), was poured into the cell-containing wells for 24 hours. Then, this transduction medium was replaced with cells' growth medium and the culture was routinely maintained for two weeks in order to assess the correct expression of the gene and also to completely remove the remaining viral particles. The culture was considered successfully transduced when more than 90% of the cells were found to be GFP-positive. This evaluation was performed by fluorescence microscopy.

2.3. Spheroid formation

3D cell aggregates (known as spheroids) were made by two commonly used techniques: hanging drop and liquid overlay. For both procedures, cells were tripsinized and manually counted using a Neubauer chamber. All the volumes reported are required for one single spheroid and can be scaled to the desired number of samples.

2.3.1. Hanging drop technique

As the name indicates, spheroids form by gravity inside a drop containing cells and growth medium. The drop is usually placed on the inner surface of the lid of a Petri dish and the dish itself is filled with either distilled water or PBS in order to prevent evaporation. Since the drops can spread along the surface of the lid, other compounds, such as methyl cellulose, can be added in order to thicken the mixture and, consequently, help to maintain the shape of the drop [140, 141]. In addition, it has been reported that methyl cellulose can also improve the circularity of the formed masses [140, 141]. The proportion of methyl cellulose added with respect to the total volume of the mixture is a variable parameter that depends on the cell line; however, it is usually around 20% of the final volume. This was the chosen value for the formation of the spheroids used in the development of this thesis.

The first essential parameter in the hanging drop technique is the number of initial cells to form the spheroids, which is also highly dependent on the cell line and the application the spheroids are meant for. In the case of this thesis, all spheroids were made with an initial number of 1000 cells.

Regarding the volume of the drops, another essential parameter, each of them was made with a final volume of 25 μL (of which 20% was methyl cellulose and the remaining 80% comprised growth medium and cell suspension).

The last essential parameter in this technique is the time required for the cells to aggregate and form the spheroids. Again, this is also highly dependent on the cell line, and it can span from 24 hours up to 96 hours. Herein, the time was set to 48 hours since it was observed that the all the spheroids of the different cell lines were formed during this period. Once formed, spheroids were passed to a 96 well plate previously treated with an anti-adherence solution, as explained in the following section.

2.3.2. Liquid overlay technique

In this technique, the spheroids were formed inside a non-adherent round-bottom 96 well plate. It is critical to ensure that the surface that comes in contact with the cells is non-adherent to prevent cell attaching. Herein, a commercial anti-adherence solution (Stemcell, 07010) was chosen due to its facility of use and its innocuous nature to cell culture. Sarstedt round-bottom 96 multiwell plates (Sarstedt, 83.3925.500) were chosen as the vessels containing cell suspension.

For the formation of the spheroids, 1000 initial cells were resuspended in 200 μL of growth medium and poured inside a previously treated 96 well plate. Thereafter, the plate was centrifuged at 1500 rpm for 10 minutes to help in the formation of the aggregates. As in the hanging drop technique, the aggregates were allowed to form for 48 hours at 37°C inside a humidified atmosphere with 5% CO_2.

2.4. Type I collagen hydrogels for spheroid migration studies

In vitro migration and invasion studies require the presence of a matrix in which cells can survive, proliferate, and migrate. Among the plethora of matrices, hydrogels made of type I collagen were chosen since this protein is ubiquitous in the colon. Furthermore, they can be easily tuned to a variety of final collagen concentrations by changing the quantities of their components. This section describes only the preparation of the hydrogels. The experiments regarding cell migration will be described in Chapter 3.

2.4.1. Hydrogel preparation

Following a previously established protocol, type I collagen hydrogels were made with the following materials:

1. Acid solubilized type I collagen extracted from rats tail tendon.
2. Sodium hydroxide (NaOH) with a concentration of 1N.
3. DMEM 5 times concentrated (DMEM 5x).
4. Sterile distilled water.
5. Growth medium.

Each component of the above list contributes to the formation and gelation of the hydrogels as well as maintaining a physiological pH (7.4) for cells to survive. Indeed, the collagen provides the raw material for the matrix. The sodium hydroxide (a base) neutralizes the collagen (an acid). In turn, the DMEM 5x supplies a high concentration of ions required to increase the ionic strength of the solution, which in turns helps the formation of the final collagen fibers present in the hydrogel. Lastly, distilled water allows to reach the desired collagen concentration present in the hydrogel, whereas the growth medium ensures cell survival.

As stated above, the final collagen content present in the hydrogels can be easily changed. For this, fixing the desired volume of the solution (V_f), the final collagen concentration in the hydrogel (C_f), and knowing the stock concentration of the collagen solution (C_0), the collagen solution volume (V_0) required is calculated as follows:

$$V_0 = \frac{V_f C_f}{C_0} \tag{2-1}$$

The volume of NaOH 1N (V_{NaOH}) is calculated at a proportion of 1:40 with respect to the collagen volume:

$$V_{NaOH} = \frac{1}{40} V_0 \tag{2-2}$$

Regarding the DMEM 5x (V_{DMEM5x}), it is calculated as follows:

$$V_{DMEM5x} = \frac{1}{5}\left(\frac{1}{2} V_f\right) \tag{2-3}$$

For the volume of distilled water (V_{dH_2O}), the following equation shows its calculation:

$$V_{dH_2O} = \frac{1}{2} V_f - V_{DMEM5x} - V_{NaOH} - V_0 \tag{2-4}$$

Last, the volume of growth medium (V_{gmed}) is calculated as:

$$V_{gmed} = \frac{1}{2} V_f \tag{2-5}$$

The mixture was prepared on ice and inside a laminar flow hood (to ensure its sterility) by adding the components in the following order:

1. Sterile distilled water.
2. DMEM 5x.
3. NaOH 1N.
4. Collagen solution.

Once these components were carefully homogenized, they were mixed with the growth medium until further homogenization. Afterwards, the hydrogel solution was ready to use in the experiments.

The specific desired final collagen concentrations employed herein were 0.8, 1.5, and 3.0 mg/mL. The collagen stock concentrations were either 3.71 mg/mL (Corning, 354236), for the 0.8 mg/mL hydrogels, or 10.57 mg/mL (Corning, 354249), for the 1.5 and 3.0 mg/mL ones. The NaOH solution was prepared by diluting the powder (Sigma, 655104) in distilled water. The DMEM 5x was also prepared by diluting the powder (Sigma, D5523) in distilled water.

2.4.2. Hydrogel polymerization

Among the hydrogel fabrication variables, polymerization temperature is one of the most important since it directly affects the kinetics of the assembly of collagen molecules and, consequently, the mechanical properties of the hydrogels. Here, two polymerization temperature schemes were tested. In the first one, the solutions were polymerized at 37°C inside a CO_2 incubator. In the second scheme, named two-stage scheme, the solutions were polymerized at room temperature (RT) for one hour before placing them at 37°C inside a CO_2 incubator. Based on the concentrations and the polymerization temperature schemes, a total of six different hydrogels were prepared.

2.4.3. Measurement of the mechanical properties of the hydrogels

Stiffness of the hydrogels defined in the last section were measured in bulk with a rheometer and locally by Atomic Force Microscopy (AFM). Both measurements were performed in an environment that reproduced as close as possible that in which cell cultures were carried out.

2.4.3.1. Rheology measurements

Bulk mechanical characterization of the six types of hydrogels was performed in collaboration with Dr. Jesús del Barrio Lasheras, from the Instituto de Nanociencia y Materiales de Aragón (INMA) at the University of Zaragoza. The characterization was performed in an oscillatory rheometer (Haake™ Mars™ 40) using parallel plates and the storage modulus, $G'(\omega)$, and loss modulus, $G''(\omega)$, were measured. Both moduli depend on the frequency of oscillation, ω. For every sample, a volume of 700 μL of the hydrogels was prepared *in situ* and loaded between the plates (which were previously cooled to 0°C). The sample was then sealed with a thin layer of low viscosity silicon oil in order to prevent evaporation and once done, the process was initialized. Due to the impossibility to reproduce the exact environmental conditions at which the hydrogels polymerize (for instance, the rate at which the temperature rises from 0°C to 37°C inside the incubator or the presence of CO_2) several assumptions regarding the heating rates were made. For the hydrogels that were polymerized directly at 37°C, temperature was raised steadily from 0°C to 37°C in 10 minutes and maintained at the latter for the remaining duration of the measurement. In samples polymerized following the two-stage scheme, temperature was also raised from 0°C to 20°C in ten minutes; then, temperature (20°C) was kept constant for one hour before raising it again to 37°C and maintaining it for the rest of the measurement. Each sample was monitored at constant shearing amplitude and frequency (0.1 Hz) for a period of 24 h to ensure sample equilibration.

All time sweeps were performed within the linear viscoelastic regime. After the equilibration period, an amplitude sweep was recorded at constant frequency at 37°C.

2.4.3.2. AFM measurements

In order to evaluate the differences in the stiffness of the surface of the tested hydrogels, Young's Modulus of gels surface was measured with an atomic force microscope (AFM) Nanowizard 3 system (JPK Instruments, Germany) mounted on an optical inverted microscope (Nikon-Eclipse). For each gel condition, small drops of 30 μL were polymerized in a Petri Dish (TPP Techno Plastic Products AG, 93040) and covered with DMEM media (DMEM, Lonza BE12-614F). The Petri Dish was placed on the PetriDishHeater (JPK Instruments, Germany) stage to maintain a constant temperature of 37°C. AFM measurements were performed in liquid with qpBioAC probes (NanoANdMore GMBH) treated with anti-adherence rinsing solution (Stemcell, 07010) to minimize gel adhesion during cantilever retraction. Tip CB3 was chosen due to the adequacy of its nominal spring constant (0.06 N/m) for samples in the Pa scale. The experimental spring constant of each used tip was determined by the Thermal Noise Method [142]. The calibrated cantilever was positioned over a gel drop and force-spectroscopy measurements were performed in the AFM contact mode at high Z-lengths (5 μm) and slow speeds (2 μm/s). At least 100 force-spectroscopy curves were acquired for each gelling condition. Force spectroscopy curves were then processed with DP Software (JPK Instruments, Germany) and fitted to a Hertz model modified for paraboloid indentors (JPK Instruments, 2008) to obtain Young's Moduli.

2.4.4. Analysis of the collagen fiber network and fibril structure in the hydrogels

Characterization of the ultrastructure of the hydrogels was carried out by Scanning Electron Microscopy (SEM) on both their surface and internal zone. For the surface characterization of the collagen fiber network, hydrogels were prepared and fixed in 2.5% glutaraldehyde for 30 minutes at RT. Then, following washing step with PBS, samples were dehydrated in ascending ethanol series up to 100% (v/v) and dried up using a critical point dryer (Leica EM CPD300). Critical point drying preserved the 3D structure of the hydrogel. Once the samples were dried, they were coated with gold/palladium nanoparticles and examined with a JEOL JSM 6360-LV microscope operated at 15 kV acceleration voltage. Images of at least two different zones whithin the sample were taken at 750, 1000, 2000, 5000, and 10000 magnifications. For the internal zone of the hydrogels, a similar protocol was followed. However, samples were first fractured after the critical point drying and then recoated with gold/palladium nanoparticles in order to visualize the interior of the hydrogels. Processing of the samples (from the dehydration to the coating) and imaging of the samples was done by the Servicio de Microscopía de Sistemas Biológicos from the Servicio de Apoyo a la Investigación (SAI) at the University of Zaragoza.

Based on the resulting images, morphological parameters of the collagen fibers (diameter) and the pores present in the structures (pore size and porosity) were measured.

2.5. Spheroid migration studies

For the purpose of analyzing the invasion and migration patterns of the spheroids, three sets of experiments were performed: 1) single spheroids seeded on top of a hydrogel (unconstrained 2D experiment); 2) single spheroids seeded on top of a hydrogel, but surrounded by another layer of hydrogel (constrained 2D experiment); and 3) fully suspended single spheroids inside a hydrogel (fully embedded). Pictures were taken every day for 3 days using a Leica DMi8 Thunder. In each of the aforementioned experiments, two main parameters were measured: the size of the spheroids and the invaded area. The spheroid size corresponded to the area of the spheroid mass. In turn, the invaded area corresponded to the migrating cells that stemmed from the spheroids. In addition to these main parameters, the percentage difference of the achieved spheroid size between the two polymerization schemes within a fixed collagen concentration $\left(\Delta_{x_i^{t,C},x_j^{t,C}}\right)$ at each timepoint was also calculated as follows:

$$\Delta_{x_i^{t,C},x_j^{t,C}} = \frac{2\left(x_i^{t,C} - x_j^{t,C}\right)}{x_i^{t,C} + x_j^{t,C}} \tag{2-6}$$

where $x_i^{t,C}$ is the mean spheroid size at time t, for the polimerization scheme i, under a fixed collagen concentration C. With these values, the resulting average of the spheroid size percentage difference for the three concentrations at every timepoint was obtained. In all these calculations, the sub-index i represents a polymerization directly at 37°C, whereas the sub-index j represents the two-stage polymerization scheme.

In a similar fashion, the percentage differences for the invaded area and the spheroid size to invaded area were also calculated. In the following sections, the experiments mentioned above will be briefly described. All experiments were performed in at least two independent replicates (10 or more samples per replicate). The following paragraphs describe briefly the experimental design of each of the mentioned experiments.

2.5.1. Single spheroids seeded on top of a hydrogel (unconstrained 2D experiment)

The aim of this experiment was to explore the migrating behavior of cells belonging to the spheroids in contact with only one layer of hydrogel. For this, a volume of 60 μL of unpolymerized hydrogel (with a fixed collagen final concentration) solution was deposited inside 96 well plate with flat bottom and left to polymerize according to the chosen polymerization scheme. Afterwards, single spheroids were suspended in growth medium and seeded on top of the polymerized hydrogels. For each well with hydrogel, a single spheroid was seeded and placed into the CO2 incubator. Figure **2-1** shows a schematic representation of the experiment.

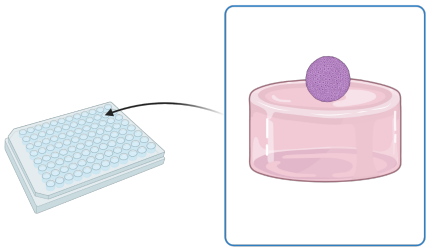

Figure 2-1: Schematic representation of the unconstrained 2D experiment. Image created with biorender (`https://biorender.com/`).

2.5.2. Single spheroids seeded on top of a hydrogel, but surrounded by another layer of hydrogel (constrained 2D experiment)

This experiment also focused on exploring the migrating behavior of cells belonging to the spheroids, but "sandwiched" between two layers of hydrogels (Figure **2-2**). To do this, a first layer of unpolymerized hydrogel solution (volume of 60 μL and fixed collagen final concentration) was deposited and polymerized inside a 96 well plate with flat bottom to polymerize according to the chosen polymerization scheme. Once this layer was polymerized, 50 μL of a mixture containing a single spheroid and collagen hydrogel solution (with the same concentration as the first layer) was deposited on top of the first layer and allowed to polymerize accordingly. Following the polymerization of this new layer of hydrogel, 100 μL of growth medium were added to maintain the culture.

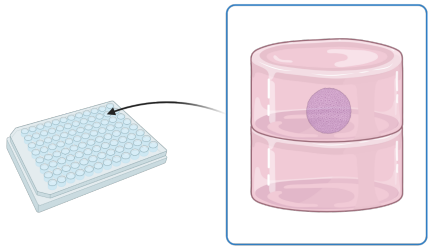

Figure 2-2: Schematic representation of the constrained 2D experiment. Image created with biorender (`https://biorender.com/`).

2.5.3. Fully suspended single spheroids inside a hydrogel (fully embedded experiment)

Finally, the goal of this experiment was, as before, explore the migrating behavior of cells belonging to the spheroids. Nevertheless, this time the spheroid was fully suspended inside the collagen matrix (see Figure **2-3** for a schematic representation of the experiment), a substantial change with respect to the other two, since in both previous cases the spheroids were on top of a previously polymerized collagen surface. To achieve the aim of this experiment, a volume of 100 μL of unpolymerized hydrogel solution was deposited inside a 96 well plate with flat bottom. Immediately following this procedure, single spheroids were seeded inside the solution. Afterwards, the plate was continuously flipped upside down during the gelation process to ensure that the spheroids did not attach to the plastic of the plates.

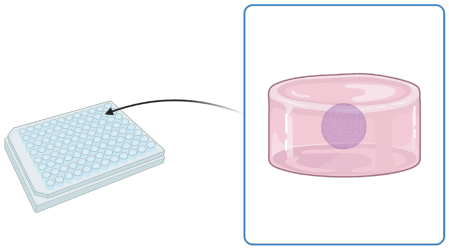

Figure 2-3: Schematic representation of the fully embedded experiment. Image created with biorender (`https://biorender.com/`).

2.6. Preconditioning experiments for analyzing the mechanobiological response of the spheroids in absence of extracellular matrix

Together with the study of the migration/invasion patterns stemming from the previously defined hydrogels and the subsequent cell-involving experiments, the analysis of the mechanobiological behavior of spheroids subjected to cyclic changes (preconditioning) in the nutrient concentration (specifically, glucose and FBS) of the media constituted the main objectives of this dissertation. In this section, a description of the experimental design of the media preconditioning is presented.

2.6.1. Experimental design

In order to analyze the biological and mechanical impact of dynamic FBS and/or glucose deprivation on CRC HCT-116 and HT-29 spheroids, cyclic changes from enriched media to a deprived counterpart were performed. Such cycles lasted 144 hours and were preceded by an initial starvation period, corresponding to the number of days a group of spheroids lasted in deprived media prior to the aforementioned cycling. For the experiment, 5 different initial starvation periods, spanning evenly from 24 to 120 hours, were tested. After completing that period, each group was passed to abundant media for 144 hours and then passed to the deprived counterpart. This process was repeated one more time, resulting in the creation of four alternating cycles of nutrient deprivation or abundance, each sharing the same duration. Media was changed every 72 hours according to each preconditioned group timeline. Furthermore, two control groups were defined: one for the enriched media and the other for the deprived media. Figure **2-4** shows a schematic representation of the experimental design.

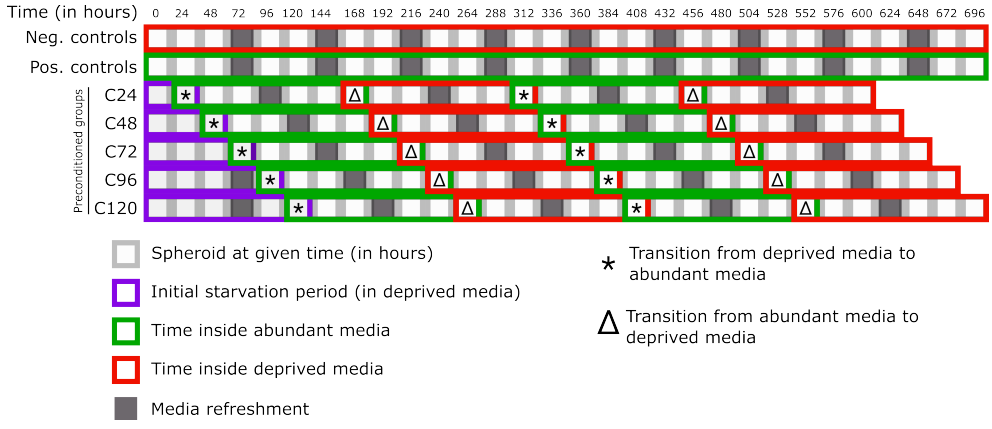

Figure 2-4: Schematic representation of the experimental design for the media preconditioning experiments. C24-C120: spheroids preconditioned for 24 hours (C24), 48 hours (C48), 72 hours (C72), 96 hours (C96), and 120 hours (C120).

2.6.1.1. Employed media

According with the previously explained design, 4 different media were defined, each containing a fixed concentration of either glucose or FBS. Table **2-1** shows the composition of the defined media, as well as their given names.

Table 2-1.: Media composition for the preconditioning experiments. All are based in Dulbecco's Modified Eagle Medium (DMEM). Values for glucose and FBS are highlighted in red.

Media name	Glucose concentration (g/L)	FBS concentration (% v/v)	P/S (% v/v)	L-glutamine (% v/v)
DG10	**4.5**	**10**	1	1
DG0	**4.5**	**0**	1	1
D10	**1.0**	**10**	1	1
D0	**1.0**	**0**	1	1

With these media, three major sets of experiments were proposed. Each of them is explained in the following list:

1. **Simulatenous changes in the concentration of glucose and FBS**: from DG10 to D0. This experiment was denominated **"best-to-worst" preconditioning experiment.**
2. **By keeping glucose constant (at 4.5 g/L)**: from DG10 to DG0. This experiment was denominated **glucose preconditioning experiment.**
3. **By keeping high concentration of FBS constant (10% v/v)**: from DG10 to D10. This experiment was denominated **FBS preconditioning experiment.**
4. **By keeping low concentration of FBS constant (10% v/v)**: from DG0 to D0.

2.6.1.2. Assessment of the role of cytoskeletal activity on the biological response of spheroids under dynamic nutrient deprivation

As will be explained in further detail in Chapter 4, the role of cytoskeleton activity on preconditioned spheroids subjected under dynamic nutrient deprivation was assessed. For this, two small molecules were used: Y-27632 and Blebbistatin.

2.6.1.2.1. Treatment with Y-27632 Y-27632 is a small molecule that inhibits ROCK1 and ROCK2, which are two downstream regulators of the RHO/ROCK signalling pathway. Briefly, this pathway is a major regulator of cell migration by controlling 1) the number of actin filaments active inside the cell and 2) increasing cell's contractility. The first part is achieved by preventing the depolymerization of the filaments, whereas the second one is accomplished by "activating" the myosin chains present in the cells (by phosphorilating the myosin light chains) or by "maintaining" the active ones.

Addition of Y-27632 was done in the "best-to-worst" experiment at:

1. The transition from the first cycle of DG10 to D0 (168^{th} hour of the experiment, see Figure **2-4**) and left for 48 hours.
2. The transition from the preconditioning period to the first cycle in DG10 (24^{th} hour of the experiment, see Figure **2-4**) and left for the entire cycle of DG10 as well as the first one of D0.

Concentrations of Y-27632 used in these experiments were 10, 25, 50, and 100 μM.

2.6.1.2.2. Treatment with Blebbistatin Blebbistatin is another small molecule capable of altering cytoskeletal activity, as Y-27632. However, its action mechanism differs from that of Y-27632. Indeed, Blebbistatin inhibits the contraction of the actin-myosin complex by binding inside the myosin head at the site where this head and the actin filament bind.

Addition of Blebbistatin was also done in the "best-to-worst" experiment at the transition between the first cycle of DG10 to D0 (168^{th} hour of the experiment, see Figure **2-4**) and left for the entire duration of the cycle in D0.

2.7. Viabiliy staining

In order to determine the viability of cell culture, calcein-AM/propidium iodide (CAM/PI) staining was used. CAM is a nonfluorescent molecule with the capacity to penetrate cell membranes. Once inside, it is converted to a fluorescent expressing molecule (excitation/emission maximum wavelengths of 488 nm/520 nm respectively) only if the cell is alive. Therefore, this compound is a marker for living cells. In turn, propidium iodide (PI) is a fluorescent stain (excitation/emisison maximum wavelengths of 493 nm/636 nm respectively) that marks nucleic acids. However, this molecule cannot pass thorugh intact cell membranes. Thus, PI can only stain nucleic acids of dead cells.

For the preparation of the stainings, stocks solutions of CAM (Life Technologies, C1430) and PI (Sigma, P4170) with respective concentrations of 1 mg/mL and 2 mg/mL, by dissolving the powders in sterile DMSO (for CAM) and distilled water (for PI). Then, the stock solutions were further diluted in 1 mL of phosphate-buffered saline (PBS, Lonza, BE17-516F) to a final concentration of 2 μg/mL for CAM and 6 μg/mL for PI. This solution was added in the dark to the spheroids and incubated for 30 minutes at RT. Afterwards, the spheroids were washed three times with PBS and immediately imaged with a fluorescent microscope. CAM/PI staining was used in all cell lines that were not transduced with the green fluorescent protein (GFP). For these cells, only PI staining was used, since the GFP itself is an indicator of viable cells.

2.8. Sample preparation for Transmission Electron Microscopy (TEM)

Spheroid samples were fixed in glutaraldehyde (2.5% v/v) for 30 minutes at RT. Afterwards, they were washed with PBS and stored at 4°C overnight. Next, they were processed with osmium tetroxide and uranyl acetate to stain, respectively, the plasma membrane and the nucleic acids of the cells. Following this step, stained samples were embedded in a plastic resin to obtain the molds for cutting. Embedded samples were then cut into semi-thin (approximately 200 nm) and ultra-thin (approximately 10 nm) samples. The former were further stained with toluidine blue and gave an overall visualization of the cell distribution inside the cells. Ultra-thin samples gave details of the ultrastructure of cells inside the spheroids.

2.9. Histological analysis

Spheroids were fixed in 4% paraformaldehyde (PFA) for 20 minutes at RT. To facilitate sectioning, they were stained with blue tissue-marking dye (Labolan, 240101K) before paraffin embedding. Sections (3 μm thick) were stained with Hematoxylin-Eosin (H&E) following standard procedures. Briefly, parafin-embedded samples were deparaffinized with heat, fixed in xylene, and rehydrated in descending series of ethanol (100, 96, 60, and 0%) before first staining them in hematoxylin. Then, samples were washed with abundant water and stained in eosin. Once finished the previous step, samples were again washed and dehydrated in ascending ethanol series (0, 60, 96, and 100%) before immersing them once more in xylene. Finally, xylene-immersed samples were dried and sealed to a glass coverslip with a universal mounting medium (DPX, PanReac AppliChem ITW Reagents, code: 255254).

2.10. Fluorescent staining of actin cytoskeleton

Spheroids were harvested at selected times and were subsequently fixed in 4% PFA for 20 minutes at RT. Following fixation, samples were permeabilized with 0.5% TritonX-100/PBS solution for 2 hours at RT in shaking conditions. Afterwards, spheroids were washed 3 times with PBS and incubated in a 1:500 phalloidin-PBS solution (Alexa Fluor 594, ThermoFisher, catalogue number: A12381) for another 3 hours. Incubation was performed in shaking protected from light. Finally, samples were washed 5 times in PBS to remove excess of the stain.

2.11. Optical clearing

Spheroid clearing was performed following the protocol by Lempereur et al. [143]. Briefly, following actin staining and washing, samples were immediately incubated in a 1:1 (v/v) solution consisting of a refractive index (RI) matching medium (50% sucrose (w/v), 20% nicotinamide (w/v), 20% triethanolamine (v/v) and 0.1% Triton X-100 (v/v)) and distiled water. Incubation was carried in agitation at 37°C for 3 hours. Following this period, samples were retrieved and incubated in undiluted RI matching solution for another 45 minutes. Samples were immediately imaged at the end of this time frame.

2.12. Imaging and analysis

With the exception of the SEM images, all were acquired using either a Nikon Eclipse Ti-E equipped with a C1 modular confocal microscope or a Leica DMi-8 (Thunder9 microscope. All analyses were performed using custom plugins or macros developed in collaboration with the University of La Rioja [144]. The codes were written for Fiji/ImageJ software (`http://fiji.sc/Fiji`). TEM images were visualized by a transmission electron microscope (JEOL JEM 1010 100kV) at 5000 magnifications. SEM images were visualized by using a scanning electron microscope JEOL JSM 6360-LV) operated at 15 kV acceleration voltage. Images of two different zones of the surface or the inner zone of the hydrogels were taken at 750 and 2000 magnifications.

2.13. Statistical analysis

Unless otherwise specified, all the experiments were repeated at least three times as independent repeats. Results were expressed as the mean $\pm$ standard deviation of the mean. Statistical analyses were performed in R (version 4.2.0) [145]. Data related to the temporal evolution of multicellular spheroids was analyzed with Linear Mixed Models [146] by using the lme function of the nlme package [147]. In these models, time was set as the independent variable and the area (either of the spheroid or the corresponding one to the invasion) was set as the dependent variable. In addition, the collagen concentration in the hydrogels and the polymerization schemes were defined as the moderator variables. Furthermore, the models included up to the quadratic terms of the time variable as well as their interactions with other variables. Lastly, random intercepts for the samples (spheroids) and random slops for time were also included in the models. The inclusion of both parameters (random slopes and random intercepts) accounts for the variability in spheroid growth as well as in their initial area and allows a better fit of the data [148]. Data related to the growth rates and percent differences was analyzed with standard t-tests or Wilcoxon tests depending on the results given by the Shapiro-Wilk normality test [149–151]. In addition, paired tests (either t- or Wilcoxon tests) were used to compare the mean growth rates obtained for two different cycles in a given preconditioned or control group [150, 152]. Unpaired tests (either t- or Wilcoxon tests) were used to compare the mean growth rates or percent differences obtained for two independent groups in a given time point [149, 152]. Results with a p-value under 0.05 were considered statistically relevant, whereas those with a p-value greater than 0.05 were considered non-significant [153].

3. The Role of Mechanical Properties and Structure of Type I Collagen Hydrogels on Colorectal Cancer Cell Migration

[0]Article accepted in **Macromolecular Bioscience** (doi: https://doi.org/10.1002/mabi.202300108).

3.1. Introduction

Metastasis is the process whereby cancer cells successfully invade and colonize a foreign tissue. It has been reported as the major cause of cancer related deaths, accounting for up to 90% of the cases [154]. In the past decades, it has been demonstrated that cell invasion and metastasis are events that do not depend exclusively on cells, but also on their interaction with the tumor microenvironment and its stromal components [155, 156]. Consequently, a plethora of either in vivo or in vitro approaches have been developed to study the migrating and invasive properties of cancer cells. In the case of the former, recently developed techniques, such as intravital microscopy (IVM), offer the possibility to visualize dynamic cell processes (such as cell invasion) in a living animal with a resolution comparable to that achieved in traditional cell cultures [157, 158]. However, this technique, as well as others that involve animal models, are expensive, hard to control, require special equipment, and carry ethical issues due to the use of animals [158, 159]. Furthermore, tissue mechanical properties can vary among species and can be difficult to measure *in vivo*. In turn, *in vitro* studies are cheaper and easier to reproduce than those *in vivo*, with the caveat that they fail to completely reproduce the complexity of a living organism. However, they provide powerful tools to comprehend the mechanobiological response of different cells to changes in the stiffness of a substrate in both physiological and pathological scenarios, which has helped to elucidate the mechanisms by which cells migrate, proliferate, or differentiate in vivo [38, 160–163]. Early *in vitro* studies on migration and invasion have been conducted in scratch wound-healing assays [164]. Yet, these platforms are limited since they fail to reproduce the three-dimensional architecture of a living tissue and have a high degree of variability in their results [165, 166]. To circumvent these issues, three-dimensional experiments have emerged in the past decades [167–178]. The Boyden assay, an early example of these three-dimensional experiments, is the benchmark technique to assess cancer cells invasion and migration [167]. However, this approach has two main limitations. First, since it relies on external membranes to separate non migrating cells from those that migrated through such membranes, pore size of the membrane is a critical factor that directly impacts on the number of migrating cells [179]. Additionally, since the membrane is made from artificial materials, the biological relevance of the migration results is limited [179, 180]. Second, it requires a chemical gradient to stimulate cell migration, which reduces the duration of the experiment due to the inherent difficulties in controlling the gradient resulting from the spatial configuration of the assay [165, 180]. Current strategies to study the invasion and migration patterns of cancer cells include the seeding of either single cells or aggregates (such as spheroids) in a hydrogel matrix, which can be made of alginate [181], matrigel [170], metacrylated gelatin (GelMa) [182], poly(ethylene-glycol) [156, 183], or solubilized type I collagen [169, 174, 175, 184, 185]. From these, solubilized type I collagen is the most common material for preparing hydrogels. There are different reasons for this. First, collagen is a natural component of the great majority of tissues in a living organism, making it an excellent biocompatible material for generating scaffolds. Second, it is preferred over matrigel or comparable basal membrane-based matrices because metastatic events occur in the stromal layers of tissues, where type I collagen predominates. Alginate lacks

the biomimetic characteristics of collagen-based hydrogels, despite the fact that it can be useful for different biomedical applications [186]. Finally, contrary to GelMa, type I collagen hydrogels do not require external crosslinkers or catalysts that can potentially alter the biological response of cells. In the case of experiments involving type I collagen hydrogels and spheroids, samples can be mixed with an unpolymerized matrix solution and then deposited on top of a previously polymerized matrix layer or can also be suspended entirely inside a matrix without any underlying bed. From these strategies, cell migration can be potentially detected in every direction, as has been demonstrated by several studies [168–171, 173–178]. Nevertheless, information regarding the mechanical and ultrastructural characterization of the hydrogels, as well as their role in the observed results, is either absent or poorly reported, since these articles mainly focus on analyzing cell response to either biochemical signals or their interaction with other cell populations (usually from the tumor stroma). This is a major issue since it has been demonstrated, both *in vivo* and *in vitro*, that the mechanical environment affects the biological behavior of individual cells [60, 61, 187, 188].

Mechanical characterization of a material can be performed using different techniques depending on its nature and the aim of the research. In the case of type I collagen hydrogels, oscillatory rheometry is one of the most commonly used approaches to describe their overall mechanical behavior due to the fact that hydrogels, as well as most soft biological tissues, exhibit viscoelastic properties [156, 189–191]. This technique applies a fixed small amplitude sinusoidal deformation (with a prefixed frequency ω) to the hydrogel over a given time. From this measurement, the complex modulus $G^*(\omega) = G' + iG''$ can be determined, where G' and G" are called the storage and loss moduli, respectively [192]. The former is related to the strain energy stored during a deformation cycle and can be interpreted as the resistance of the hydrogel to deformation. Conversely, the latter is associated with the energy dissipated during the same cycle and can be interpreted as the resistance of the hydrogel to revert to its original configuration after deformation. Surface mechanical properties of a hydrogel can be determined by atomic force microscopy (AFM) [193]. This technique allows the characterization of the stiffness (expressed, for instance, in terms of the Young's modulus) of the surface of hydrogels under liquid physiological environments with nanometric resolution [193]. This, combined with information of the fiber morphology obtained with Scanning Electron Microscopy (SEM), provides valuable data about the mechanical landscape at the surface of a hydrogel.

As explained above, mechanical interactions between cells and their microenvironment play an important role in determining cell fate, a particularly relevant event in pathological scenarios, such as cancer and metastasis. Indeed, from a mechanical point of view, metastatic cells must circumvent the different mechanical barriers imposed by foreign tissues in order to succesfully invade and colonize them. These barriers can be characterized by both the stiffness and the architecture of the network formed by thr structural proteins present in the native and host (or foreign) tissues. It was also explained that type I collagen is the main structural protein in the human body due to

its ubiquity. Therefore, *in vitro* models using this protein can be ideal to study cell migration.

In this chapter, variations in the mechanical properties of the hydrogels and in their structure are shown to modulate cell migration patterns of colorectal cancer cells. For this, three sets of experiments were designed (descriptions available in Sections 2.5.1, 2.5.2, and 2.5.3 of Chapter 2). In each of these experiments, two variables were measured. The first one, corresponded to the area of the spheroid, whereas the second variable was the area invaded by the cells. Figure **3-1** shows a schematic representation of the experimental setup as well as the measured parameters.

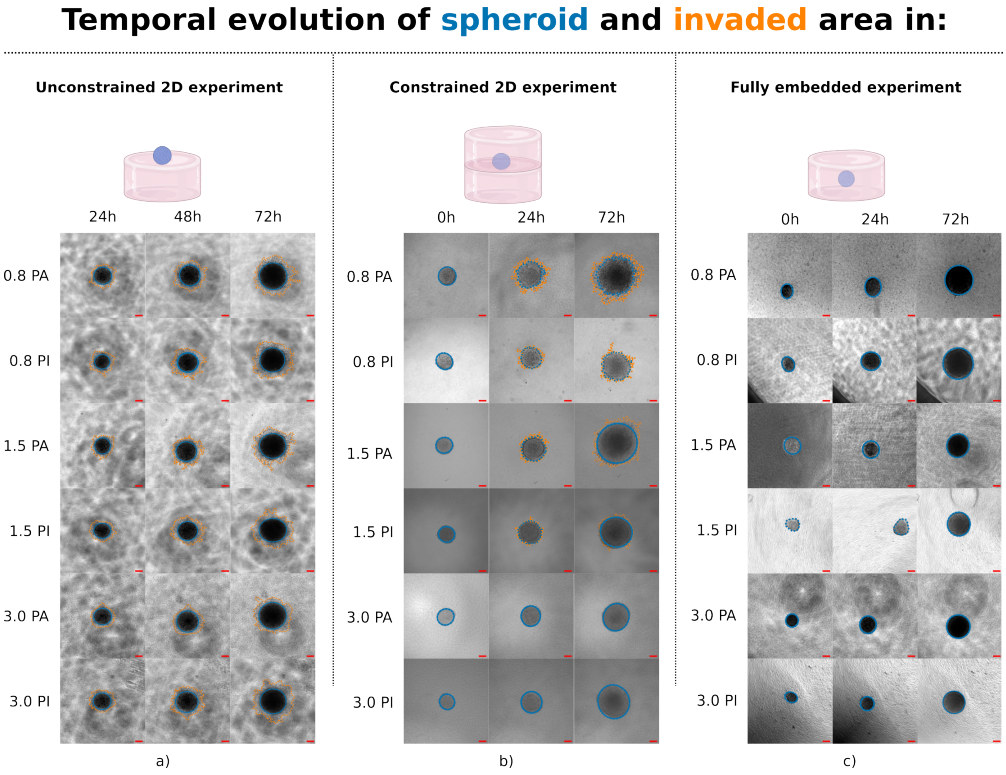

Figure 3-1: Schematic representation of the variables measured in this chapter.

3.2. Results

3.2.1. Gelation temperature increases up to two orders of magnitude the overall stiffness of a hydrogel with a fixed concentration

Figure **3-2** shows representative images of the storage ($G'(\omega)$) and loss (($G''(\omega)$)) moduli of the tested hydrogels (0.8, 1.5, and 3.0 mg/mL, columns) polymerized at 37°C and following the two-stage temperature procedure. For visualization purposes, only the first 100 minutes of the measurements are presented. Based on the Figure **3-2**, the rheological behavior can be split into three distinguishable zones; namely a liquid phase, a gelation transition, and a stable polymerized state. In the first zone, both storage and loss moduli had an erratic behavior, indicating that the solution was still in a liquid state and the viscous part of the material was predominant. During the transition period, both moduli in all hydrogels had a rapid and steep increase in their values, which highlights that the solution started to polymerize. Interestingly, the speed of the gelation increased with the collagen concentration. Lastly, in the third zone, the solution finished polymerizing and a stabilization of the inner structure of the hydrogels occurred, which reflects on the stabilization of the values of the moduli. In the samples polymerized at 37°C, the moduli stabilized right after the gelation period ended. In those polymerized following the two-stage scheme, the values had a stable plateau that started after the gelation period and ended until the temperature was elevated to 37°C. During this increase, both moduli suffered a transient and unstable increase in their values. Interestingly, once the temperature reached 37°C, their final values were very similar to those obtained prior to the temperature increase.

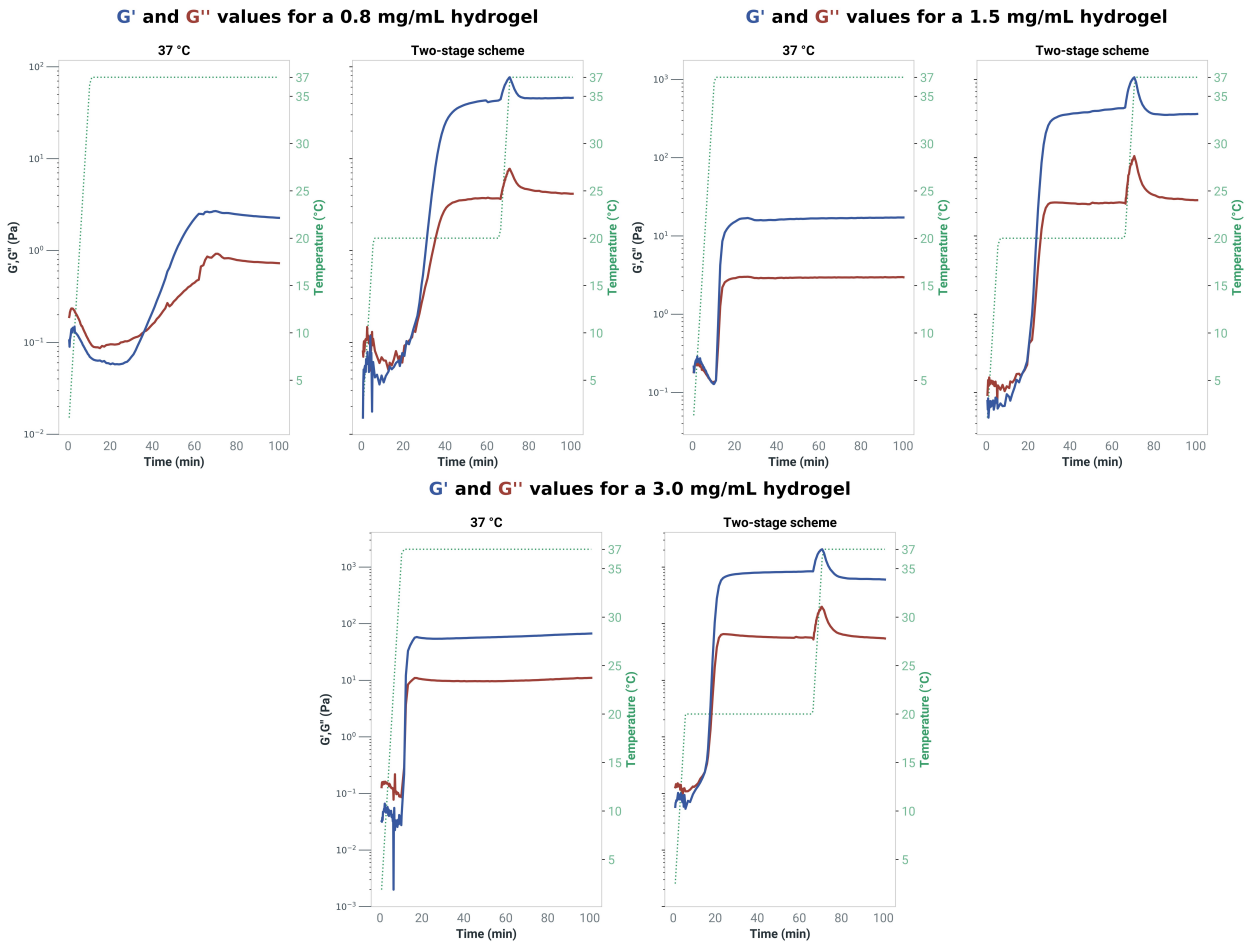

Figure 3-2: Representative examples of the rheological behavior of the six tested hydrogels (defined in section 2.4 of chapter 2). In all cases, the temperature scheme is represented by the green dotted line.

Values for the storage modulus (G') and loss modulus (G") of all hydrogels are given in Table **3-1**. When analyzing the values under a fixed polymerization scheme, we observed that the stiffness of the hydrogels increased with the collagen concentration, despite the chosen gelation protocol. When the collagen concentration was fixed, we noticed that the temperature had a marked effect on the stiffness of the hydrogels. As seen in Table **3-1**, the greatest values of both moduli were always obtained in the samples polymerized following the two-stage scheme. In addition, we observed that the storage (G'(ω)) modulus for a hydrogel with a collagen concentration of 0.8 mg/mL and polymerized following the two-stage scheme was approximately two orders of magnitude higher than the corresponding value for the same collagen concentration hydrogel polymerized at 37°C.

This trend was maintained in the rest of the tested concentrations. Nonetheless, the differences decreased as the collagen content increased. Thus, for hydrogels with a concentration of 1.5 mg/mL, the difference in magnitude was approximately seven-fold, whereas for those with a concentration of 3.0 mg/mL, the difference was approximately three-fold.

Table 3-1.: Mechanical properties of the six types of hidrogels.

		Rheological measurements of the hydrogels		**AFM measurements of the hydrogels**
Concentration (mg/mL)	**Polymerization Temperature scheme**	**Mean Storage Modulus, G' (SD), Pa**	**Mean Loss Modulus, G" (SD), Pa**	**Mean Young's Modulus (SD), Pa**
0.8	**37**	1.7 (0.5)	1.2 (0.8)	161.6 (45.5)
	Two-stage	107.5 (60.1)	9.4 (5.0)	310.1 (106.9)
1.5	**37**	26.5 (2.1)	5.5 (0.0)	916.2 (298.8)
	Two-stage	190.0 (127.3)	15.6 (6.9)	1123.0 (880.0)
3.0	**37**	103.3 (70.7)	16.7 (13.0)	1230.0 (572.1)
	Two-stage	460.0 (99.0)	44.1 (0.6)	2026.0 (765.7)

3.2.2. Surface stiffness of hydrogels is modified by the gelation temperature

Table **3-1** shows the mean Young's moduli for the different tested hydrogels. As expected, As expected, under a fixed polymerization temperature, collagen concentration significantly affected the stiffness of the hydrogels (p-value < 0.0001 for all cases). Indeed, hydrogels with low collagen concentration (0.8 mg/mL) had the lowest Young's moduli values (100 Pa for those polymerized at 37°C and 310 Pa for those polymerized following the two-stage scheme) while those with the highest collagen content (3.0 mg/mL) had the greatest values (1230 Pa for the ones polymerized at 37°C and 2026 Pa for the hydrogels polymerized following the two-stage scheme). For the hydrogels with intermediate concentration (1.5 mg/mL), Young's moduli values were in between the ones for the other concentrations (916 Pa for the polymerization at 37°C and 1123 Pa for the two-stage scheme). In addition, under a fixed collagen concentration, the surface of hydrogels polymerized following the two stage-scheme were stiffer than that of samples polymerized directly at 37°C. Nevertheless, the obtained values for the former condition had a higher variability compared to the samples polymerized at 37°C. This suggests that the surface of the hydrogels polymerized under the two-stage scheme might have a higher heterogeneity (in terms of stiffness) than that of the hydrogels polymerized at 37°C.

3.2.3. Fiber morphology changes in different zones of a hydrogel

3.2.3.1. Hydrogel surface

The upper part of Figure **3-3** shows representative images of the surface of the tested hydrogels at 750 magnifications. Qualitative evaluation of the morphology of the surface of the hydrogels revealed that collagen fiber arrangement seemed to evolve from a loosely and spider web-like layout, present in the 0.8 mg/mL hydrogels, to a more organized and tight structure, with increasing fiber bundling in hydrogels with higher content of collagen, such as that observed in the 1.5 and 3.0 mg/mL samples. This behavior repeated in both polymerization schemes (directly at 37°C or following the two-stage temperature), albeit with remarkable differences in the 3.0 mg/mL hydrogel. Indeed, fibers appeared more bundled in the two-stage temperature scheme than in the case polymerized directly at 37°C.

Results for quantitative analysis of fiber morphology for both the surface and inner zones of the hydrogels are presented in Figure **3-4**. Data for the mean fiber thickness, pore size, and porosity of the hydrogels ($\pm$ SD) for all the tested conditions measured at 750x magnifications are given as bar charts. With respect to the fiber thickness at the surface of the hydrogels (solid bars in Figure **3-4**), we observed that, in both polymerization schemes, fibers seemed to decrease their thickness in the hydrogels with low (0.8 mg/mL) to intermediate (1.5 mg/mL) concentrations, which agrees with previous observations found in the literature [194]. In addition, we found that the polymerization scheme also influences the thickness of the fibers. Indeed, hydrogels polymerized following the two-stage scheme (brown solid lines) had, in general, thicker fibers than those polymerized directly at 37°C (green solid lines). In contrast, we noted that the hydrogels exhibited similar behavior in terms of porosity regardless of the chosen polymerization scheme. This suggests that the gelation temperature does not influence these parameters at the surface of a hydrogel.

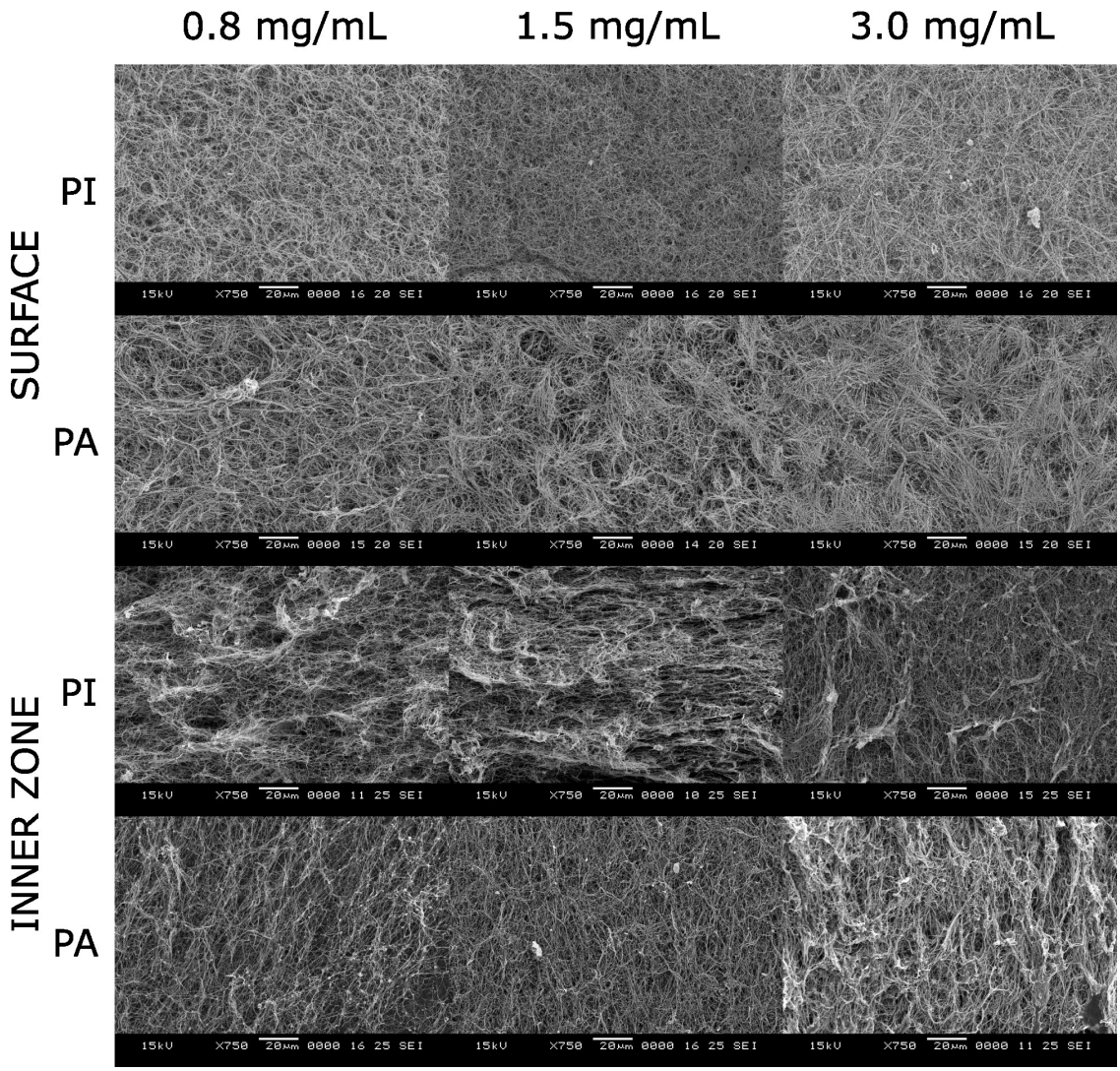

Figure 3-3: SEM images of the collagen fiber network present in the surface and inner zones of the six tested hydrogels (defined in section 2.4 of Chapter 2). PI, hydrogels polymerized at 37°C. PA, hydrogels polymerized following the two-stage scheme.

3.2.3.2. Hydrogels inner structure

Representative images of the collagen distribution in the inner zones of the hydrogels are presented at the bottom of Figure **3-3**. As seen, fiber networks seemingly did not follow the same trend as the one observed at the surface of the hydrogels when the collagen content was increased. However, in all images, fibers seemed to have a specific orientation. Regarding fiber thickness in the inner zones of the hydrogels (Figure **3-4**), we observed that, in general, inner fibers were thicker than those at the surface of the hydrogels. This trend was also enhanced by the polymerization scheme. Indeed, the inner fibers of the samples polymerized at 37°C (green striped bars in Figure **3-4**) were also thicker than those of the hydrogels polymerized following the two-stage scheme (brown striped bars in Figure **3-4**).

Figure **3-4** shows the quantitative analysis of the morphology of the collagen fibers. Results for the mean ($\pm$ SD) fiber thickness, pore size, and porosity of the hydrogels, for all the tested conditions measured at 750 magnifications, are given as bar charts. Data are grouped by the final collagen concentration. Summarizing the results in Figure **3-4**, hydrogels polymerized directly at 37°C had, in general, shorter and thinner fibers than those polymerized following the two-stage scheme. Regarding pore morphology, the latter hydrogels had larger pores, but were, in general, less porous than the ones polymerized at 37°C.

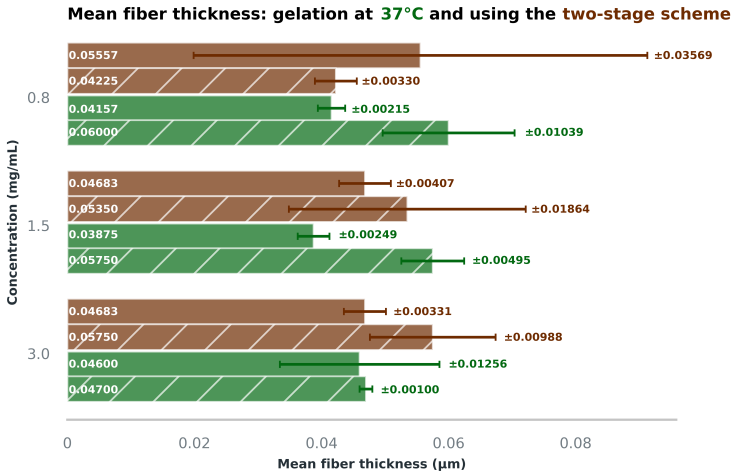

(a) Fiber thickness

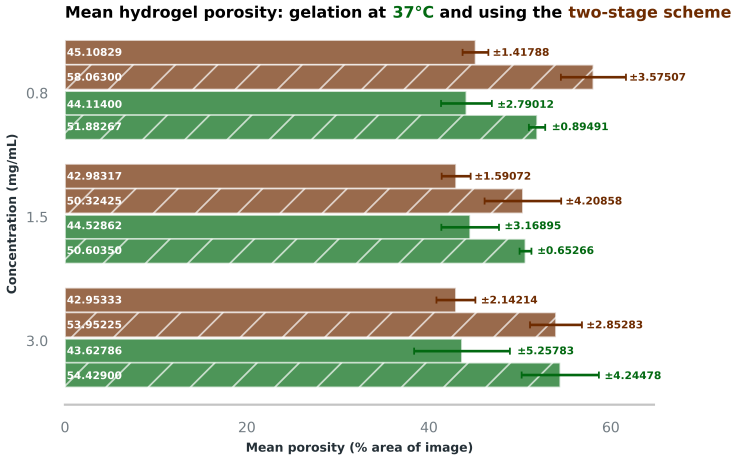

(b) Hydrogel porosity

Figure 3-4: Quantitative analysis of the morphological structure of the collagen fiber network present in the surface of the six tested hydrogels (defined in section 2.4 of Chapter 2). (a). Fiber thickness. (b). Hydrogel porosity. Plain bars: Measured parameters at the surface of the hydrogels. Striped bars: Measured parameters at the inner zones of the hydrogels.

3.2.4. HCT-116 and HT-29 migration patterns are modulated by a combination of the ultrastructure of the hydrogels and their stiffness

3.2.4.1. Single spheroids seeded on top of a hydrogel (unconstrained 2D experiment)

Figure **3-5**a (left panel) shows the migration patterns of HCT-116 spheroids placed on top of previously polymerized hydrogels and surrounded by culture medium.

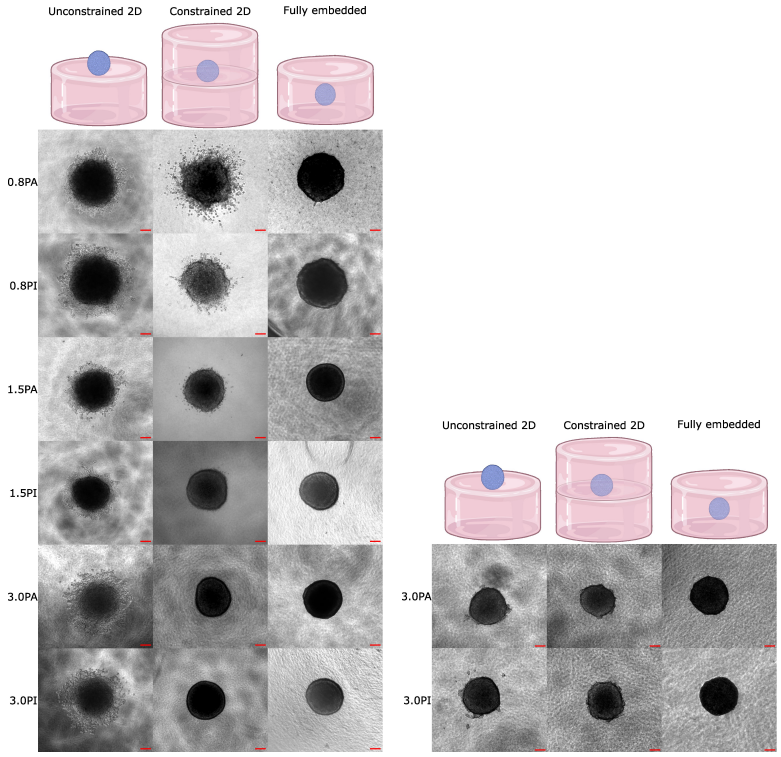

(a) HCT-116 **(b)** HT-29

Figure 3-5: Migration patterns obtained for HCT-116 and HT-29 spheroids in the Unconstrained 2D, Constrained 2D, and fully embedded experiments. The time at which the images were taken was 72 hours after the start of the experiments. The top panel depicts graphic representations of the mentioned cell-related experiments (created with biorender). Scale bar: 100 µm. PA: polymerization following the two-stage scheme. PI: polymerization at 37°C.

In this experiment, cells migrated at the surface of the hydrogel in a predominantly collective fashion (with negligible cell clusters), regardless of the final collagen concentration or polymerization scheme (Figure **3-6**). Furthermore, migration was not radially homogeneous but exhibited preferential directions, suggesting that the local distribution of the collagen fibers might promote these anisotropic migration patterns by increasing the local stiffness of the surface of the hydrogels. This was particularly evident in the cases in which the hydrogels were polymerized following the two-stage scheme.

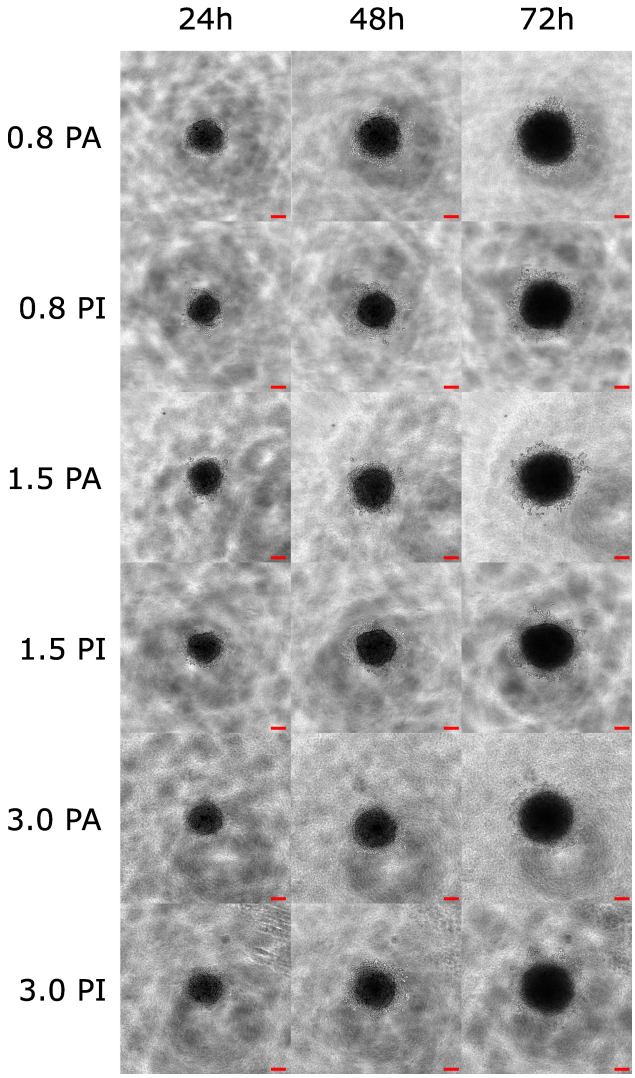

Figure 3-6: Time evolution of the migration patterns for the HCT-116 spheroids in the unconstrained 2D experiment. Scale bar: 100 µm. PA: polymerization following the two-stage scheme. PI: polymerization at 37°C.

In turn, when HT-29 cells were seeded on top of a previously polymerized layer of hydrogel (left panel of Figure **3-5**b), cell migration seemingly occurred in a combination of both collective and individual patterns. However, as in the case for HCT-116 spheroids, cells migrated in-plane and did not exhibit a radially homogeneous distribution (Figure **3-7**).

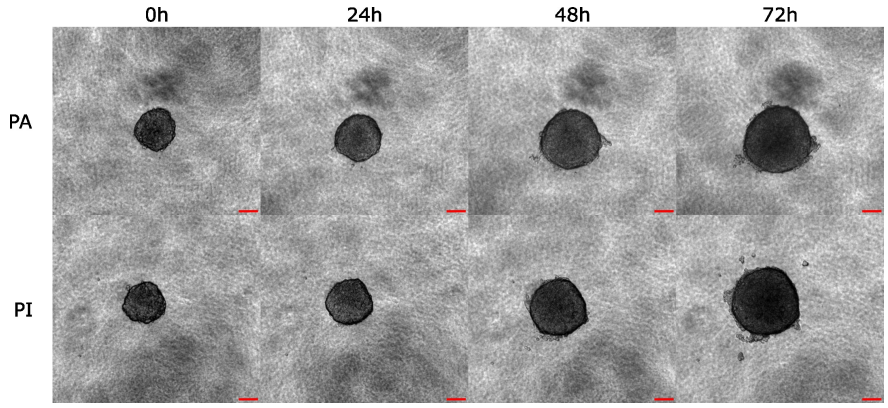

Figure 3-7: Time evolution of the migration patterns for the HT-29 spheroids in the unconstrained 2D experiment. Scale bar: 100 µm. PA: polymerization following the two-stage scheme. PI: polymerization at 37°C.

Quantitative analyses of the HCT-116 spheroid size and invaded area (schematic representations of the measurements are depicted in Figure **3-1**) of the experiment described in this section are shown in Figure **3-8** and Table **3-2**. Recalling Section 2.5, in the first two columns of Table **3-2**, we calculated the percentage differences of either the spheroid size or invaded area between the two different polymerization schemes of a given collagen concentration in every time point of the experiment. In the calculations, the reference was always the parameter (spheroid size or invaded area) in the two-stage scheme. As an illustrative example, the following equation calculates the percentage difference of the spheroid area between the two polymerization schemes for a collagen concentration of 0.8 mg/mL at 24 hours:

$$-11.6\% = \frac{Area_{PA,24h} - Area_{PI,24h}}{\frac{Area_{PA,24h} + Area_{PI,24h}}{2}} * 100 \tag{3-1}$$

where "$Area_{PA,24h}$" indicates the mean area of the spheroids polymerized following the two-stage scheme calculated at 24 hours, and "$Area_{PI,24h}$" indicates the mean area of the spheroids polymerized at 37°C calculated at 24 hours. Similar calculations were performed for the other two columns in Table **3-2**, as well as for the other results presented in this chapter. According to our results, under a fixed collagen concentration, the polymerization scheme seemed to influence the size of the spheroids in a concentration-dependent manner, particularly for the low-concentration hydrogels (Appendix Table **A-1**).

As such, for the spheroids seeded on top of hydrogels with a collagen concentration of 0.8 mg/mL, the percent differences in area were 23.9% (Table **3-2**) at the end of the experiment, followed by samples seeded on top of hydrogels of 1.5 mg/mL (4.0%, Table **3-2**) and 3.0 mg/mL (4.0%, Table **3-2**). For the other time points, we also found similar trends (Table **3-2**). In turn, within the same polymerization scheme, spheroids had similar size in all three tested concentrations (Appendix Table **A-2**). Finally, in all cases, the growth trends for both spheroid and invaded area were linear.

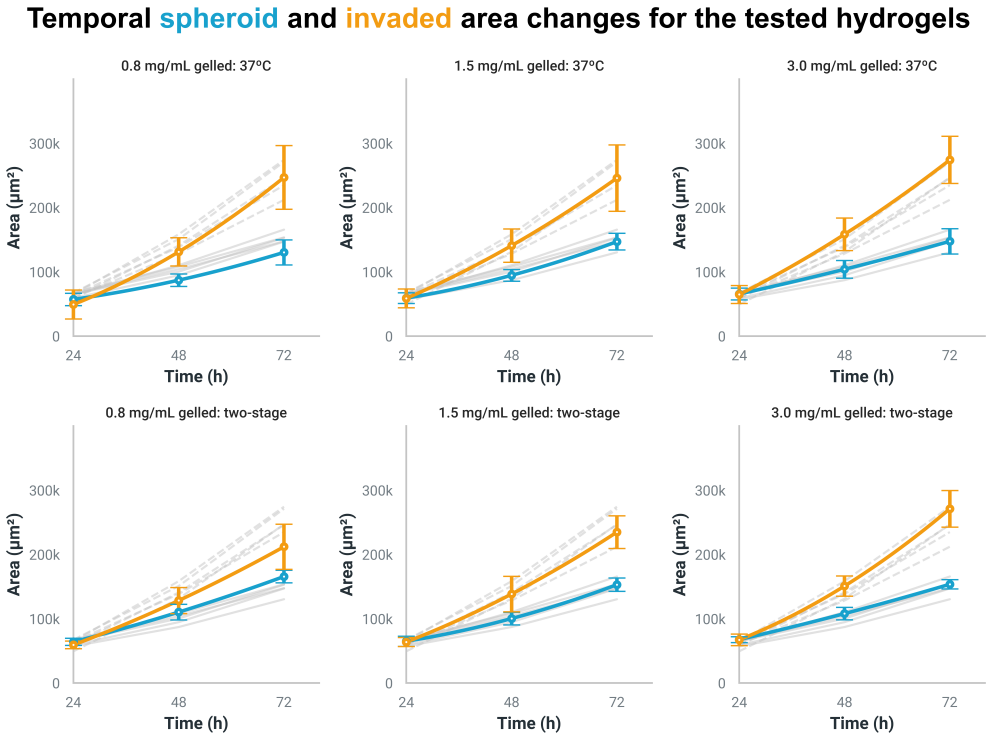

Figure 3-8: Time evolution of HCT-116 spheroid and invaded area growth of the unconstrained 2D experiment. Time scale: hours. Area scale: μm^2. Continuous lines: Spheroid areas. Dashed lines: Invaded areas. The gray color (in both solid and continuous lines) represents either the spheroid or invaded area evolution for the rest of the 5 non-highlighted experiments.

For the HT-29 spheroids, under a fixed collagen concentration of 3.0 mg/mL, the polymerization scheme did not have a significant influence on the spheroid size (Figure **3-9**). Indeed, by the end of the experiment, the percent differences in area were approximately 4.6% (Table **3-2**), agreeing with the observed trend for the HCT-116 spheroids at the same concentration. However, in contrast to the HCT-116 cell line, HT-29 spheroids seeded on top of hydrogels polymerized at 37°C were smaller than those seeded on top of hydrogels polymerized following the two-stage scheme (Appendix Table **A-5**).

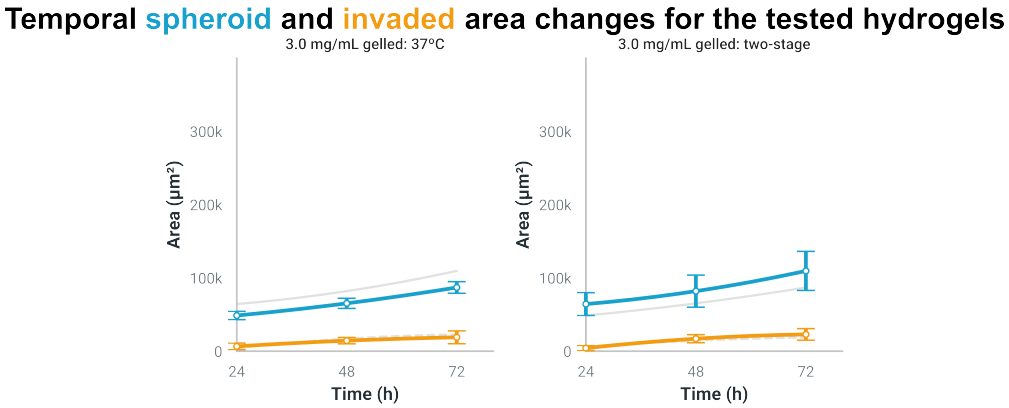

Figure 3-9: Time evolution of HT-29 spheroid and invaded area growth of the unconstrained 2D experiment. Time scale: hours. Area scale: μm^2. Continuous lines: Spheroid areas. Dashed lines: Invaded areas. The gray color (in both solid and continuous lines) represents either the spheroid or invaded area evolution for the rest of the non-highlighted experiments.

As for the invaded area, our results showed that the invaded area of HCT-116 spheroids (orange lines in Figure **3-8**) increased with the collagen concentration (Appendix Table **A-3**). When the collagen concentration was fixed, cell invasion in the hydrogels polymerized at 37°C was greater than that in the hydrogels polymerized following the two-stage scheme (Table **3-2** and Appendix Table **A-2**). This was especially true for the hydrogels with low collagen concentration, where the percent differences were up to 15.2% by the end of the experiment. For the other concentrations, the percent difference in the invaded area decreased to 4.6% for the hydrogels of 1.5 mg/mL and 1.2% for those with a concentration of 3.0 mg/mL (Table **3-2**). In the case of HT-29 spheroids (orange lines in Figure **3-9**), under a fixed collagen concentration of 3.0 mg/mL, the invaded area was greater in the hydrogels polymerized following the two-stage scheme than in their counterpart at 37°C (18.3%, Table **3-2**), which differed from the exhibited behavior of the HCT-116 spheroids seeded in the same condition. However, this increase was not statistically significant (Appendix Table **A-3**).

Table 3-2.: Percentage differences of HCT-116 and HT-29 spheroid size and invaded area between the two polymerization schemes, calculated as explained in Chapter 2. Data for the unconstrained 2D experiment. The negative sign indicates that the parameter corresponding to the polymerization at 37°C decreased with respect to the same parameter but corresponding to the two-stage scheme. In the case of spheroid to invaded area, the negative sign indicates that the invaded area was smaller than that of the spheroid.

Cell line	Time (h)	Concentration (mg/mL)	Percentage difference of spheroid area at time t (%)	Percentage difference of invaded area at time t (%)	Spheroid to invaded area percentage difference at time t (%). Polymerization: 37°C	Spheroid to invaded area percentage difference at time t (%). Polymerization: Two-stage
HCT-116	**24**	**0.8**	-11.6	-18.4	-14.7	-7.9
	48		-23.6	2.2	40.4	15.1
	72		-23.9	15.2	61.9	24.5
	24	**1.5**	-9.3	-8.1	-0.6	-1.7
	48		-5.8	1.7	39.3	32.0
	72		-4.0	4.6	50.3	42.2
	24	**3.0**	-3.0	-3.6	-1.2	-0.6
	48		-3.7	4.9	41.5	33.2
	72		-4.0	1.2	60.1	55.3
HT-29	**24**	**3.0**	-27.6	43.8	-151.7	-175.0
	48		-22.6	-16.8	-127.4	-130.8
	72		-23.0	-18.8	-128.2	-130.6

Lastly, regarding the spheroid to invaded area ratio, we observed that, despite the concentration or the polymerization scheme, the invaded area of HCT-116 spheroids was always greater than the spheroid area in all cases (Table **3-2**). This indicates that, for this particular configuration, migrating cells occupied a larger area than that of the main mass. This observation may be explained by the fact that spheroid cells are allowed to migrate freely along the surface of a hydrogel since they do not have mechanical constraints to restrict in-plane movement. In stark contrast, the invaded area by the HT-29 spheroid cells was smaller than the area of the spheroids (Table **3-2**).

3.2.4.2. Single spheroids seeded on top of a hydrogel, but surrounded by another layer of hydrogel (constrained 2D experiment)

Figure **3-5**a (central panel) shows representative examples of the migration patterns in HCT-116 spheroids "sandwiched" inside the tested hydrogels. We noticed that cells migrated from the main mass and always remained at the interface between the two hydrogel layers in a radial pattern. In addition, an individual cell migration pattern was present in hydrogels with low (0.8 mg/mL) and intermediate (1.5 mg/mL) collagen concentrations.

In both cases, individual cell clusters disseminated radially around the main tumor mass, increasing the occupied area inside the collagen matrix. This behavior started around the first day after seeding (central panel in Figure **3-1** and Figure **3-10**) and continued throughout the duration of the experiment, suggesting that in these concentrations, cells tended to migrate individually. Conversely, in hydrogels with high collagen concentrations (3.0 mg/mL), there was no cell spreading around the spheroids, leaving a well-encapsulated tumor mass throughout the duration of the experiment.

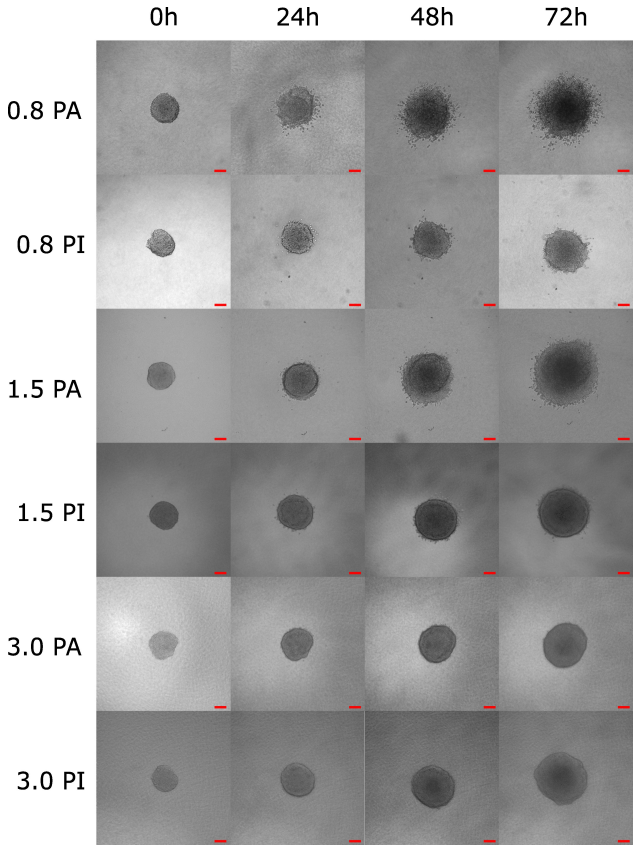

Figure 3-10: Time evolution of the migration patterns for the HCT-116 spheroids in the unconstrained 2D experiment. Scale bar: 100 µm. PA: polymerization following the two-stage scheme. PI: polymerization at 37°C.

For the HT-29 spheroids (central panel in Figure **3-5**b and Figure **3-11**), cells did not migrate in either of the polymerization schemes used. However, they did try to detach from the main mass, generating the small protrusions seen in Figure **3-11**. This behavior contrasted with the HCT-116 spheroids under the same collagen concentration (3.0 mg/mL).

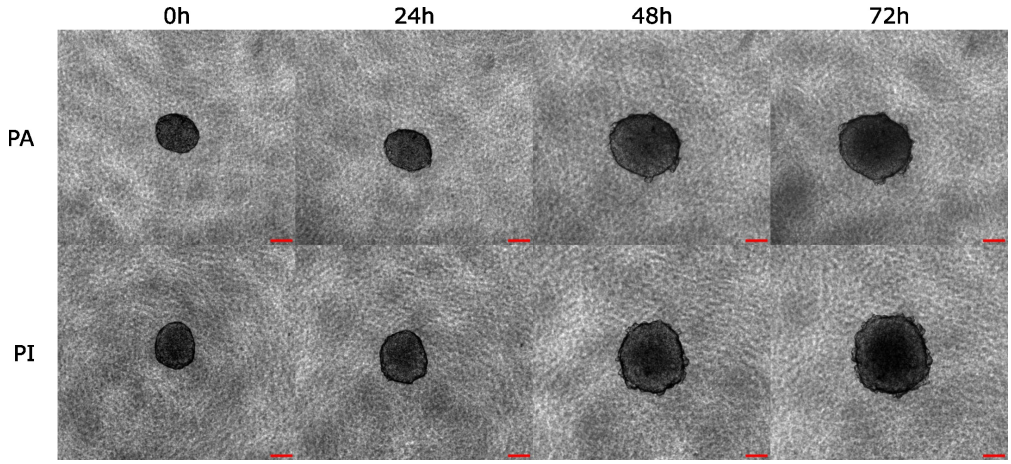

Figure 3-11: Time evolution of the migration patterns for the HT-29 spheroids in the unconstrained 2D experiment. Scale bar: 100 µm. PA: polymerization following the two-stage scheme. PI: polymerization at 37°C.

Regarding the HCT-116 mean spheroid area (blue lines in Figure **3-12**), we observed that, as in the unconstrained experiment, it was also dependent on the collagen concentration and the polymerization scheme. Indeed, in hydrogels polymerized following the two-stage scheme, spheroids decreased in area as the collagen content increased and had the opposite behavior in samples polymerized at 37°C (Table **A-4**).

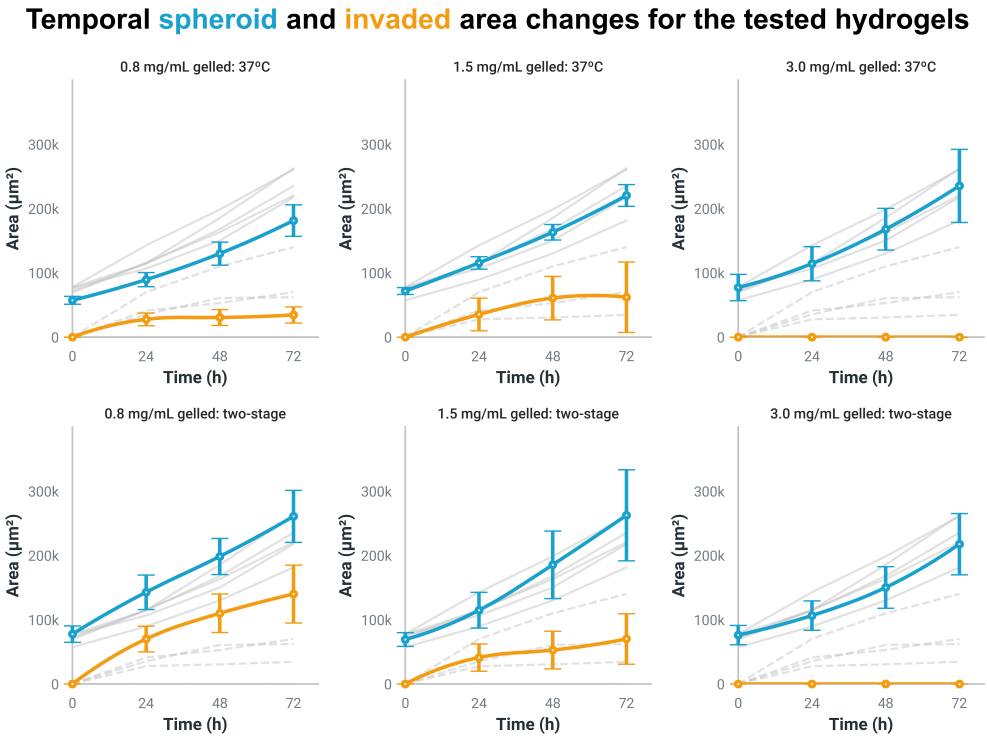

Figure 3-12: Time evolution of HCT-116 spheroid and invaded area growth for the constrained 2D experiment. Time scale: hours. Area scale: μm^2. Continuous lines: Spheroid areas. Dashed lines: Invaded areas. The gray color (in both solid and continuous lines) represents either the spheroid or invaded area evolution for the rest of the 5 non-highlighted experiments.

Instead, when the concentration was fixed and the polymerization scheme was changed, the spheroid area had variable behavior. For hydrogels with low and intermediate collagen concentrations (respectively, 0.8 and 1.5 mg/mL), spheroids "sandwiched" between layers polymerized at 37°C were smaller than the ones in between hydrogels polymerized following the two-stage scheme (see Table **3-3** and Appendix Table **A-5**). In contrast, spheroids between hydrogels of high collagen concentration (3.0 mg/mL) and polymerized at 37°C were bigger, although not statistically significant (Table **3-3** and Appendix Table **A-5**). Nevertheless, despite this heterogeneity, the differences in area decreased with the collagen concentration, as in the previously described unconstrained experiment.

Table 3-3.: Percentage differences of HCT-116 and HT-29 spheroid size and invaded area between the two polymerization schemes, calculated as explained in Chapter 2. Data for the constrained 2D experiment. The negative sign indicates that the parameter corresponding to the polymerization at 37°C decreased with respect to the same parameter but corresponding to the two-stage scheme. In the case of spheroid to invaded area, the negative sign indicates that the invaded area was smaller than that of the spheroid. Indeterminate values were set to zero and were subsequently identified by a "*" symbol.

Cell line	Time (h)	Concentration (mg/mL)	Percentage difference of spheroid area at time t (%)	Percentage difference of invaded area at time t (%)	Spheroid to invaded area percentage difference at time t (%). Polymerization: 37°C	Spheroid to invaded area percentage difference at time t (%). Polymerization: Two-stage
HCT-116	0	0.8	-30.2	0*	-200.0	-200.0
	24		-46.0	-100.4	-105.5	-68.4
	48		-41.7	-127.8	-124.0	-57.4
	72		-35.9	-149.2	-136.1	-60.3
	0	1.5	3.6	0*	-200.0	-200.0
	24		0.7	-15.5	-106.5	-94.4
	48		-12.8	14.0	-91.5	-111.4
	72		-17.4	12.2	-103.5	-123.5
	0	3.0	1.4	0*	-200.0	-200.0
	24		7.0	0*	-200.0	-200.0
	48		11.1	0*	-200.0	-200.0
	72		7.8	0*	-200.0	-200.0
HT-29	0	3.0	-28.3	0*	-200.0	-200.0
	24		-20.6	47.2	-176.0	-187.4
	48		-13.1	47.9	-160.4	-178.9
	72		-7.7	53.7	-159.7	-176.6

When analyzing the effects of the polymerization scheme on the HT-29 spheroids with a fixed collagen concentration of 3.0 mg/mL (blue lines in Figure **3-13**), we noticed that the spheroids seeded between two layers of hydrogels polymerized at 37°C were smaller than their counterparts polymerized following the two-stage scheme, with a percent difference of approximately 7.7% by the end of the experiment (Table **3-3**), albeit with no statistical relevance (Appendix Table **A-5**).

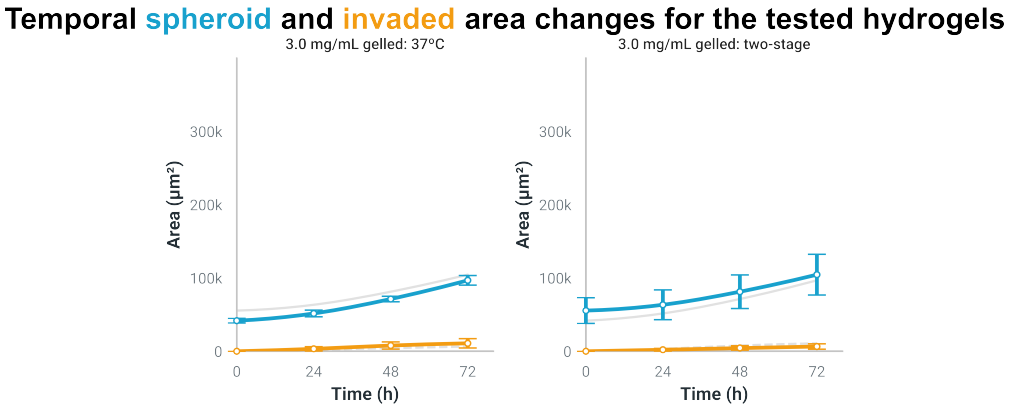

Figure 3-13: Time evolution of HT-29 spheroid and invaded area growth for the constrained 2D experiment. Time scale: hours. Area scale: μm^2. Continuous lines: Spheroid areas. Dashed lines: Invaded areas. The gray color (in both solid and continuous lines) represents either the spheroid or invaded area evolution for the rest of the non-highlighted experiments.

With respect to the invaded area of HCT-116 cells (orange lines in Figure **3-12**), we found that, under a fixed polymerization scheme, the invaded area decreased as the collagen content in the hydrogels increased (Appendix Table **A-4**). When the collagen concentration was fixed, the biggest differences were found in the low concentration (0.8 mg/mL) hydrogels (Table **3-3** and Appendix Table **A-6**). In fact, at every time point (starting at 24 hours), the percent differences revealed that the spheroids "sandwiched" in hydrogels polymerized following the two-stage scheme invaded an area at least 100% larger than their counterparts in the hydrogels polymerized directly at 37°C (Table **3-3**). This phenomenon was also present, albeit on a smaller scale, in the intermediate concentration (1.5 mg/mL) hydrogels (Appendix Table **3-3**). In contrast, for the spheroids "sandwiched" between hydrogels of high collagen concentration (3.0 mg/mL), there were no differences in the invaded area since, as we described above, cells did not migrate from the spheroids in either of the polymerization schemes. For the HT-29 spheroids (orange lines in Figure **3-13**), the invaded area was larger in the cases where the hydrogels were polymerized at 37°C (Table **3-3**). Furthermore, this result was also significant, as seen in Appendix Table **A-6**.

3.2.4.3. Fully suspended single spheroids inside a hydrogel (fully embedded experiment)

Figure **3-5**a (right panel) shows representative examples of the temporal evolution of the spheroids fully suspended inside the tested hydrogels. In all cases, there were no cells migrating from the main mass at the end of the experiment. This trend was maintained throughout the duration of the experiment (Figure **3-14**).

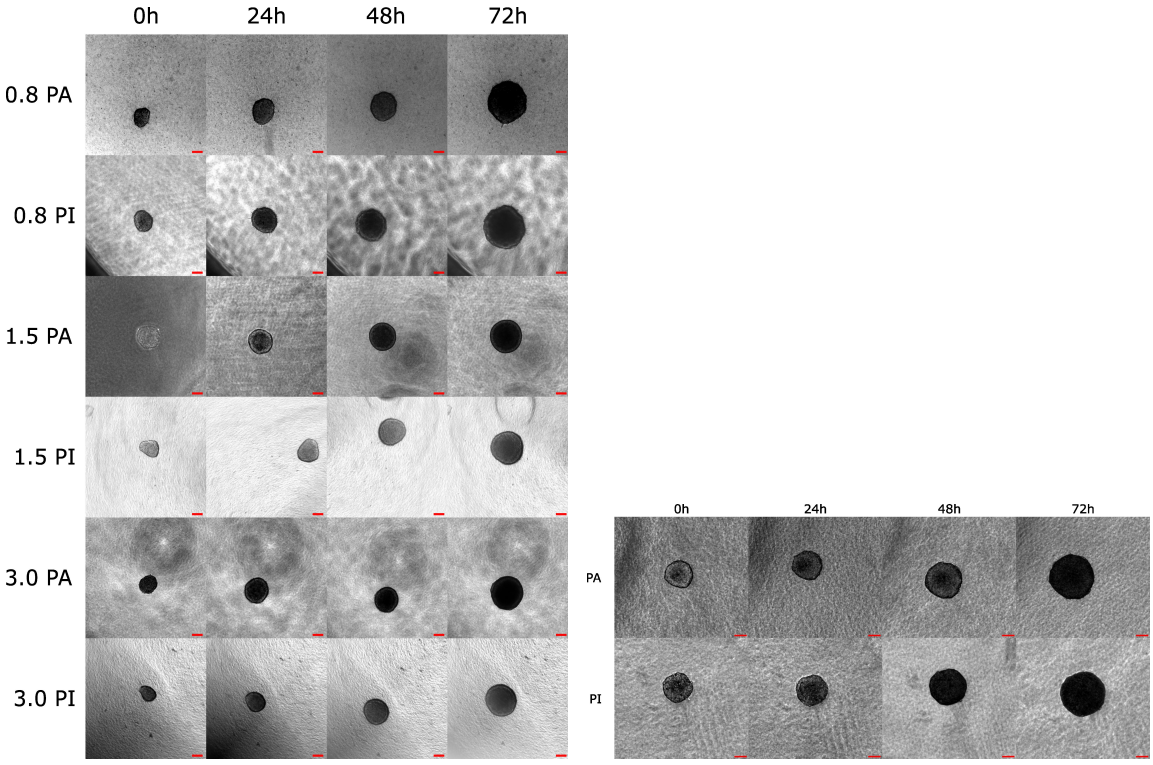

(a) HCT-116 **(b)** HT-29

Figure 3-14: Time evolution of the migration patterns for the HCT-116 and HT-29 spheroids in the fully embedded experiments. Scale bar: 100 µm. PA: polymerization following the two-stage scheme. PI: polymerization at 37°C.

With respect to the HCT-116 spheroid area (blue lines in Figure **3-15**), we observed that, under a fixed polymerization scheme, spheroids tended to decrease in area as the collagen concentration in the hydrogels increased (Appendix Table **A-7**). However, for the cases of spheroids embedded in hydrogels polymerized following the two-stage scheme, the results were not statistically significant (Appendix Table **A-7**). In turn, when the collagen concentration was fixed, the spheroids embedded inside hydrogels polymerized at 37°C were bigger than their counterparts embedded in hydrogels polymerized following the two-stage scheme (see Table **3-4** and **A-8**).

By the end of the experiment, the largest percent differences (21.9%) were again present in the hydrogels with low collagen concentration (0.8 mg/mL), followed by those with a concentration of 3.0 mg/mL (10.9%), and, finally, those with a concentration of 1.5 mg/mL (9.8%).

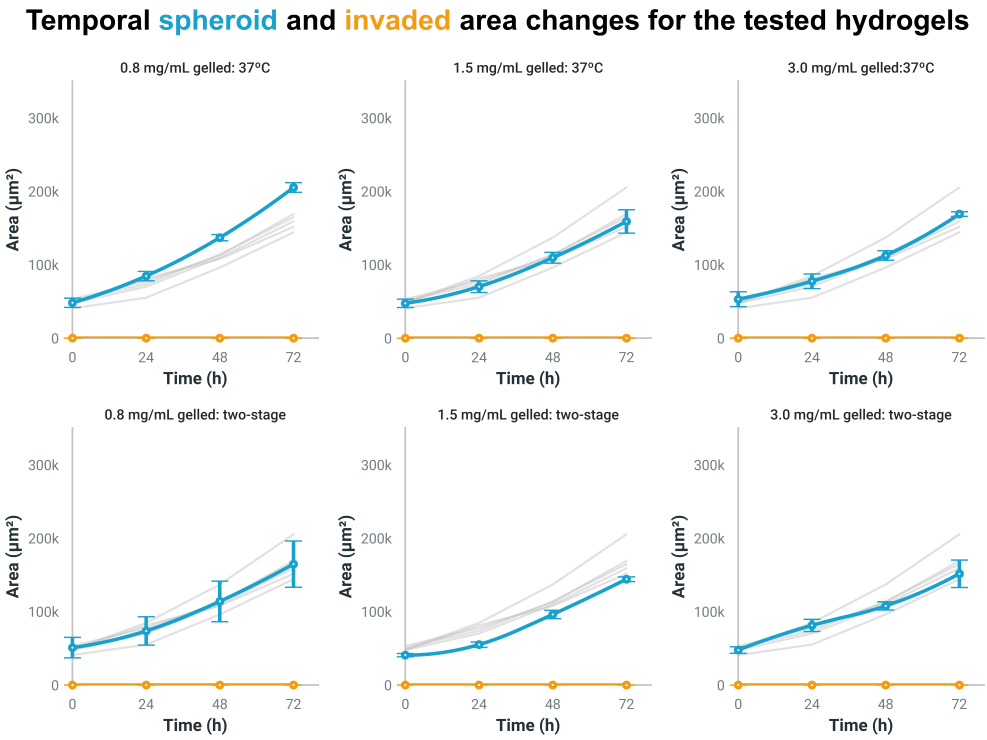

Figure 3-15: Time evolution of HCT-116 spheroid and invaded area growth for the fully embedded experiment. Time scale: hours. Area scale: μm^2. Continuous lines: Spheroid areas. Dashed lines: Invaded areas. The gray color (in both solid and continuous lines) represents either the spheroid or invaded area evolution for the rest of the 5 non highlighted experiments.

In contrast, for the HT-29 spheroids (Figure **3-16** and Table **3-4**), the spheroids embedded inside hydrogels polymerized at 37°C were smaller than their counterparts embedded in hydrogels polymerized following the two-stage scheme by approximately 11.4% at the end of the experiment. Nevertheless, the differences in area were not statistically relevant (Appendix Table **A-8**).

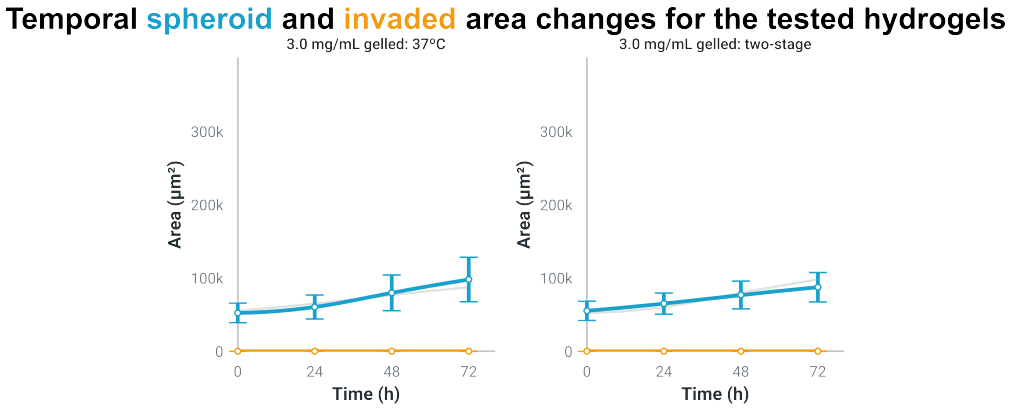

Figure 3-16: Time evolution of HCT-116 spheroid and invaded area growth for the fully embedded experiment. Time scale: hours. Area scale: μm^2. Continuous lines: Spheroid areas. Dashed lines: Invaded areas. The gray color (in both solid and continuous lines) represents either the spheroid or invaded area evolution for the rest of the 5 non highlighted experiments.

Finally, the lack of invading cells in either HCT-116 or HT-29 spheroids (orange lines in Figures **3-15** and **3-16**) in any of the tested scenarios suggests that the increased pore size and porosity of the inner zones of the hydrogels, compared to the surface of the hydrogels, prevents cell migration of the HCT cells.

Table 3-4.: Percentage differences of HCT-116 and HT-29 spheroid size and invaded area between the two polymerization schemes, calculated as explained in Chapter 2. Data for the fully embedded experiment. The negative sign indicates that the parameter corresponding to the polymerization at 37°C decreased with respect to the same parameter but corresponding to the two-stage scheme. In the case of spheroid to invaded area, the negative sign indicates that the invaded area was smaller than that of the spheroid.

Cell line	Time (h)	Concentration (mg/mL)	Percentage difference of spheroid area at time t (%)	Percentage difference of invaded area at time t (%)	Spheroid to invaded area percentage difference at time t (%). Polymerization: 37°C	Spheroid to invaded area percentage difference at time t (%). Polymerization: Two-stage
HCT-116	0	0.8	-5.4	0*	-200.0	-200.0
	24		13.8	0*	-200.0	-200.0
	48		18.3	0*	-200.0	-200.0
	72		21.9	0*	-200.0	-200.0
	0	1.5	15.3	0*	-200.0	-200.0
	24		24.2	0*	-200.0	-200.0
	48		13.1	0*	-200.0	-200.0
	72		9.8	0*	-200.0	-200.0
	0	3.0	10.7	0*	-200.0	-200.0
	24		-4.6	0*	-200.0	-200.0
	48		4.4	0*	-200.0	-200.0
	72		10.9	0*	-200.0	-200.0
HT-29	0	3.0	-5.4	0*	-200.0	-200.0
	24		-7.4	0*	-200.0	-200.0
	48		3.7	0*	-200.0	-200.0
	72		11.4	0*	-200.0	-200.0

3.3. Discussion

In the last decade, in vitro studies have demonstrated the importance of mechanical interactions between cells and their surrounding microenvironment in understanding cancer progression. However, most of these studies undermine the importance of the effect of the fabrication parameters of the scaffolds (usually made of type I collagen hydrogels) on the mechanobiological response of cells. In this study, we used pure type I collagen hydrogels fabricated with different concentrations and polymerization procedures as a model to understand the influence of their mechanical properties (measured by rheometry and AFM) and ultrastructural organization (measured by SEM) on the migration patterns of HCT-116 cells organized in multicellular spheroids.

In vitro studies have also demonstrated that the mechanical properties and the ultrastructure of different scaffolds, such as those made of type I collagen, can be modified by altering the final collagen content and the gelation temperature [195]. For example, Yang et al. reported that the mechanical properties of hydrogels polymerized following a two-stage procedure (first left at 22°C for a given amount of time and then transferred to 37°C) were between those obtained for samples polymerized at constant temperatures of 22°C and 37°C [196]. Similar results were obtained by Holder et al. despite using different polymerization temperatures and times [195].

Finally, Seo et al. [162] demonstrate that collagen fiber thickness and pore size can be controlled by adjusting the gelation temperature and that these parameters can lead to profound changes in the contractility and differentiation of adipose stromal cells (ASCs) into myofibroblasts. We have observed that both storage and loss moduli increased and stabilized once the gelation period finished, similar to previous studies [194, 196–198]. In addition, the value of the storage modulus of the polymerized hydrogels, regardless of the polymerization procedure, increased at higher collagen concentrations. This behavior has been reported before and has been attributed to the content of the protein [131, 189, 198, 199], since the increasing collagen concentration in the hydrogels results in a rise of available fibers that form a denser and, therefore, stiffer network. Furthermore, the values of the storage and loss moduli (Table **3-1**) after polymerization at 37°C were of the same order of magnitude as those of other hydrogels with analogous collagen contents [189–191, 200].

For instance, Yang et al. [189] reported that the storage modulus of a 1.5 mg/mL hydrogel polymerized at 37°C was approximately 13.14 Pa, whereas the reported value herein (for the same collagen concentration and polymerization temperature) was approximately 28 Pa. Piechocka et al. [191] using type I collagen with telopeptides reported a G' value for hydrogels with a collagen concentration of 3.0 mg/mL (polymerized at 37°C) of nearly 100 Pa, whereas the G' value reported in this document for this hydrogel and polymerization temperature was approximately 103 Pa. Last, Yang et al. [196] show the rheological behavior of a 4.0 mg/mL hydrogel polymerized following a two-stage temperature scheme similar to the one used in this manuscript, with a stable G' value lower than the obtained value for a collagen of 3.0 mg/mL here but in the same order of magnitude.

In turn, the effect of the polymerization temperature on the moduli values, with a fixed collagen concentration, indicates that the temperature at which the hydrogels initiate their polymerization is critical for their final stiffness, as described [195]. Indeed, high polymerization temperatures accelerate the formation of the collagen fiber network, yielding less organized structures with small pore sizes that ultimately alter the mechanical properties of the samples [131, 196]. In our case, samples subjected to an initial annealing at 20°C for 1 hour followed by a second annealing at 37°C (total annealing time was 24 hours) reached higher storage and loss moduli values than those directly annealed at 37°C.

With respect to the surface Young's modulus (Table **3-1**), our results may also be explained in a similar manner to the rheological behavior. Indeed, the number of fibers present at the surface is also expected to increase with the collagen concentration, thus raising the surface stiffness of hydrogels. In addition, as discussed in the above paragraph, the effect of the polymerization scheme on the surface stiffness of the hydrogels is related to the fiber network formation kinetics [196]. Thus, we anticipated that the stiffness of the surface of the hydrogels polymerized following the two-stage scheme would be higher than its counterpart in samples polymerized directly at 37°C. Lastly, results of the surface stiffness are within the range of experimental measurements

performed by Brauchle et al. [163] on collagen-rich zones of both healthy colon and carcinoma tissues. The authors report a mean Young's modulus ranging from 0.9 to 4.4 kPa for colon carcinomas and a range of 0.5 to 1.0 kPa for healthy tissue. Data for our hydrogels are within an approximate range of 0.2 to 2.0 kPa (Table **3-1**), which, according to results from the authors, are closer to healthy tissue. Our results also agree with those obtained by Pamplona et al. regarding the stiffness of healthy colon tissue [201]. However, contrary to those authors, we did not require to prepare a GelMA hydrogel to obtain stiffness similar to those of healthy tissue.

Comparison of the SEM data at the surface and inner zones of the hydrogels (Figure **3-4**) showed that collagen fibers were thicker at the inner zones of all hydrogels than at their surface. This phenomenon suggests that inner fibers act as weight-bearing columns that support the collagenous surface while maintaining the three-dimensional architecture of the hydrogels. Changes in collagen fiber thickness depending on the location within the tissue have been previously reported in vivo by Ushiki et al [202]. In their research, the authors found that collagen fibers were thicker in the outer zones of peripheral nerves (epineurium) than in their inner zones (endoneurium). These findings highlight the relationship between the function of the fiber within the tissue and its location. Indeed, in the case of the nerves, the thicker collagen fibers serve as a protective agent against tensile forces, whereas in the hydrogels, they serve as a support column, as explained above. Furthermore, the thickness of the fibers at the inner zones of the hydrogels (Figure **3-4**) had similar values to those reported in previous reports [194, 198, 199, 203]. Regarding the observed fiber orientation at the inner zones of the hydrogels, we believe this is likely an artifact generated by the cut performed to visualize the interior of the hydrogels. Lastly, the differences in the fiber distribution at the surface of the hydrogels (as a function of collagen concentration) agree with previous findings in literature, which state that collagen ultrastructure can be modulated with the polymerization temperature [194, 196]. Therefore, the results for this section corroborate that the polymerization temperature has a direct impact on the fiber distribution at the surface of the hydrogels [131], which, in turn, would explain the variability in the stiffness of the surface.

Concerning cell-related experiments, the heterogeneity of the results suggests that the contribution of the stiffness and ultrastructure of the hydrogels to the migration patterns varies depending on the location of the spheroid in the hydrogel. Thus, for the unconstrained 2D experiment, (Figures **3-6**, **3-7**, **3-8**, and **3-9**) the local stiffness of the surface of the hydrogels may be the predominant factor in determining the invaded area. Indeed, an increasingly stiff surface, as in the case for HCT-116 and HT-29 spheroids, stimulates the detachment of cells from the tumor mass and their subsequent invasion of the surrounding tissue (Figures **3-1** and **3-5**), possibly by stimulating the focal adhesion-clusters and cytoskeletal contractility of cells [60, 204]. This observation agrees with previous findings [205].

On the contrary, for the experiments where the spheroid was mixed with an unpolymerized hydrogel solution and then seeded on top of a previously polymerized layer of hydrogel (Figures **3-1**, **3-5**, **3-10** and **3-11**), the predominant factor seems to be the overall stiffness of the layer surrounding the spheroid. In fact, despite the previously polymerized layer of hydrogel, which, as we stated above, provides an attractive surface for cell migration, the presence of an additional surrounding layer of hydrogel (that polymerizes with the spheroid inside) generates a new constraint that hinders cell movement, a result that agrees with the trends observed by Liu et al. [168]. This constraint is directly related to the stiffness of the hydrogel as well as the fiber bundling when the collagen concentration is increased. As a case in point, for samples with a collagen concentration of 3.0 mg/mL, the constraint generated by the layer of hydrogel surrounding the hydrogel is powerful enough to prevent cell migration in the HCT-116 spheroids and reduce the invaded area in the HT-29 spheroids (Figure **3-5**). Conversely, in the hydrogels with a collagen concentration of 3.0 mg/mL, although the constraint of the layer surrounding the spheroids also reduce the invaded area (compared to the unconstrained 2D experiment), it does not completely avoid it (Figure **3-5**). Finally, the similarities between the values of the local and bulk mechanical properties of the hydrogels may explain the observed differences in the invaded area between the two polymerization schemes. For instance, in the hydrogels with a collagen concentration of 0.8 mg/mL, the greatest invaded area was achieved in the scaffolds polymerized following the two-stage scheme, where the values for the Young's and storage moduli were the closest (Table **3-1**). These results highlight the importance of measuring the local and mechanical properties of the samples, especially in experiments involving constrained migration along an interface. Recently, Mao et al. developed an experimental model to study the role of the mechanics of interfacial microenvironments in the migration of cancer cells [206]. Although the authors perform their study on functionalized polydimethylsiloxane (PDMS) surfaces, a key difference from our study, they do highlight the importance of the stiffness of the interface in cell migration. This agrees with our observations, especially for the constrained 2D experiment. Nevertheless, the observed in-plane migration for the unconstrained and constrained 2D experiments may be explained by the orientation of the fibers at the surface of the hydrogels. Indeed, at the surface of the hydrogels, fiber network collapses forming a planar surface that ultimately favors cell migration along the plane [207]. Finally, the complete absence of cell migration seen in the fully embedded experiments (Figures **3-5** and **3-14**), which agrees with the results shown by Dolznig et al. [169] and Ilina et al. [161], may be mainly explained by the fact that, in the absence of planar surfaces inside the hydrogels, the forces exerted by the cells on the surrounding matrix may not be strong enough to promote cell detachment from the aggregates, either as a single entity or a multicellular body [61, 187]. This may be related to the thickness of the fibers, as has been demonstrated by Mukherjee et al. [208]. Indeed, thin fibers do not provide an adequate surface area to promote cell spreading and the creation of adhesion points, resulting in impeded cell movement [208]. Furthermore, pore size may also influence the lack of cell migration in the fully embedded experiments, since it has been shown that this parameter also influences cell migration within a given matrix [209].

On the other hand, the migration patterns shown in Figure **3-1** seem to be primarily regulated by the boundary restrictions imposed on the spheroids. Therefore, in the unconstrained 2D experiment, where a single collagen surface is in contact with the spheroid, HCT-116 cells migrate preferentially in a collective manner (left panel of Figure **3-5**a and Figure **3-6**), which is a crucial characteristic of epithelial cells [60, 187]. In the case of the HT-29 spheroids, cells tended to migrate preferentially as small clusters that primarily remained close to the tumor mass (left panel of Figure **3-5**b and Figure **3-7**). However, the conjoint proliferation of these clusters and their proximity to the main mass results in the seemingly hybrid migratory patterns (cell sheets and clusters) observed in Figure **3-5**b. By contrast, in the constrained 2D experiment, HCT-116 cells (central panel in Figure **3-5**a) are forced to change their migration patterns (from collective to individual), likely because they have to overcome the physical barrier imposed by the surrounding hydrogel [60]. This observation also holds true for the HT-29 cells (central panel in Figure **3-5**b), since cells also shifted their migrating mode (from individual to collective).

On the contrary, in the hydrogels with a final collagen concentration of 3.0 mg/mL (the last two rows of the middle column in Figure 4), HT-29 cells were able to invade their immediate vicinity (in a collective manner) despite the mechanical barrier imposed by such a matrix, suggesting that HT-29 cells have weaker intercellular unions compared to the HCT-116 ones, thus facilitating the detachment from the main masses. However, the invaded area was very small compared to the size of the spheroid (Table **3-3**). Recently, Ilina et al. [161] observed uniform migration patterns for MCF-7 breast cancer spheroids at the interface between a plastic surface and the collagen matrix, with cells migrating on the plastic surface. In our results, migration occurred at the interface of the collagen matrices and was not uniform, and the invaded area was not as large as that of MCF-7 spheroids. These dissimilarities in the invaded area may be explained by the fact that a plastic surface has a higher stiffness and a more organized structure than a collagen surface.

In terms of the directionality of migrating cells, the observed anisotropy in the direction of migrating cells, especially for the HCT-116 spheroids in the unconstrained 2D experiment, may be explained by a combination of the variability in the local fiber thickness and orientation. Indeed, these two parameters may explain the presence of the sharp planar invasion fronts seen in Figure **3-5** despite the radially distributed cell sheets surrounding the spheroids, since it has been demonstrated that fiber thickness may alter the directionality and persistence of single cells [204]. Altogether, these findings highlight the importance of fiber morphology and distribution in the hydrogels for the migrating potential of colorectal cancer cells and are in accordance with previous studies [48, 210]. Thus, the uninvaded biophysical microenvironment surrounding the tumor, expressed in terms of the stiffness and ultrastructure of the surrounding collagen fibers, may become a potential target for new therapeutic strategies.

Despite the evidence presented in this document regarding the modulating role of hydrogel mechanics on cell migration, there are several limitations that must be considered. First, during rheological measurements, we did not completely reproduce the environmental conditions of the hydrogels, especially those involved in cell experiments. For instance, we measured the rheological properties of the hydrogels in the absence of CO_2. However, cell-related experiments had the gas present. The presence of CO_2 may impact the overall mechanical stiffness since it is employed to maintain a physiological pH of 7.4 for appropriate cell culture. This is an important issue because pH is a known regulating factor of the mechanical properties of a hydrogel [131]. Nevertheless, we have explored this issue by adding HEPES buffer to the hydrogel solution. This substance is commonly used in cell culture since it maintains a stable physiological pH in environments devoid of CO_2. After adding this compound to the hydrogel solution and performing the rheology, we found that there were not significant differences between the moduli values (results not shown). In second place, the model only contemplates a single protein as the component of the hydrogels. This also needs to be taken into consideration, since *in vivo* matrices are not only comprised of type I collagen, and the presence of other molecules may also impact the migration pattern of cells. In third place, we have performed our studies in a relatively small spectrum of collagen concentrations (0.8, 1.5, and 3.0 mg/mL).

Although the stiffness of our hydrogels was comparable to that of collagen-rich zones of healthy colon tissue [163], future studies in hydrogels with higher concentrations should be conducted to evaluate spheroid cell migration in cancer-associated microenvironments. Another important factor that was not taken into consideration in this work is related to the effect of matrix remodeling. As has been stated by Brauchle et al., colon cancer cells actively remodel their surrounding matrix in order to generate stiffer and more attractive pathways to facilitate the invasion of healthy tissue [163]. Finally, in this model, we did not apply external signals, such as chemoattractant gradients, to stimulate cell migration. The presence of external signaling is also important for cell migration, since it has been demonstrated that in both physiological and pathological scenarios, such as cancer, cells can be forced to migrate from their original location towards new zones due to these external signals.

4. Mechanobiological behavior of CRC spheroids under nutrient preconditioning

4.1. Introduction

Colorrectal cancer (CRC) is a leading cause of cancer-related mortality worldwide [7]. It is further aggravated because it primarily metastasizes in the liver [211], and also because recurrence of the malignancy is common even after surgery and neoadjuvant chemotherapy [212]. In order to support their elevated proliferation rates and metabolism, colorectal cancer cells require a constant supply of nutrients [213].

Glucose is a key nutrient that can significantly impact tumor growth [213]. When glucose is broken down through glycolysis, it generates ATP and a smaller byproduct called pyruvate [87]. Under aerobic conditions, pyruvate is transported into the mitochondria where it is further metabolized via the Tricarboxylic Acid (TCA) cycle and oxidative phosphorylation (OXPHOS) to produce more ATP [87]. Figure **4-1** shows a graphic depiction of the TCA cycle and OXPHOS.

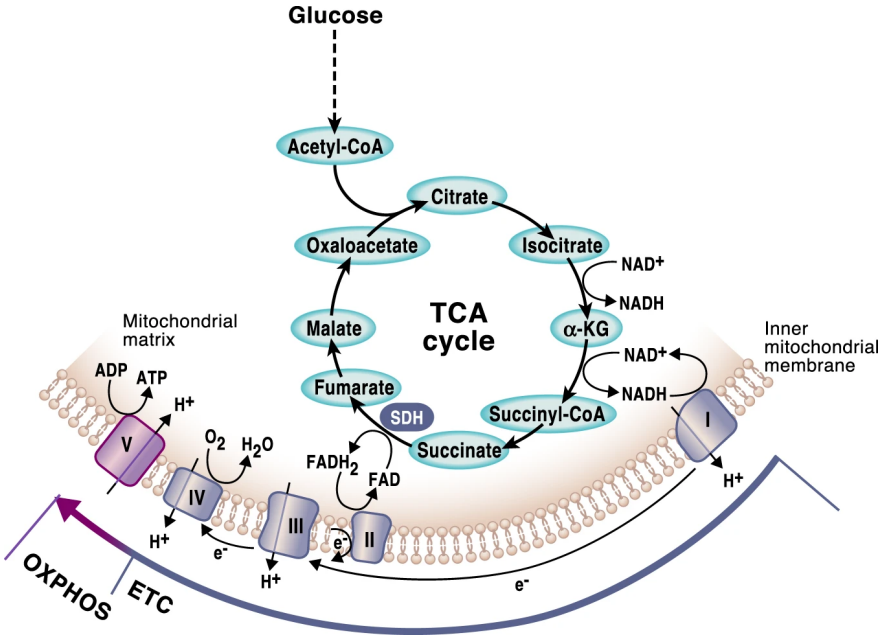

Figure 4-1: The TCA cycle and its relation with oxydative phosphorylation (OXPHOS). ETC: electron transport chain. Taken from [87].

By contrast, in hypoxic environments, pyruvate is converted into lactate to produce additional ATP. Lactate is then transported back into the cell and the mitochondria, where it is reconverted into pyruvate. Once reconverted, pyruvate is further metabolized via the TCA cycle to produce ATP through OXPHOS. Cancer cells can carry out the conversion of pyruvate to lactate and generate ATP even in the presence of oxygen, which is known as the Warburg effect [214]. However, since the amount of ATP produced is low in comparison to OXPHOS, cancer cells need high amounts of glucose to generate the necessary energy to survive [214]. Figure **4-2** shows a graphic comparison between the TCA cycle and the Warburg effect.

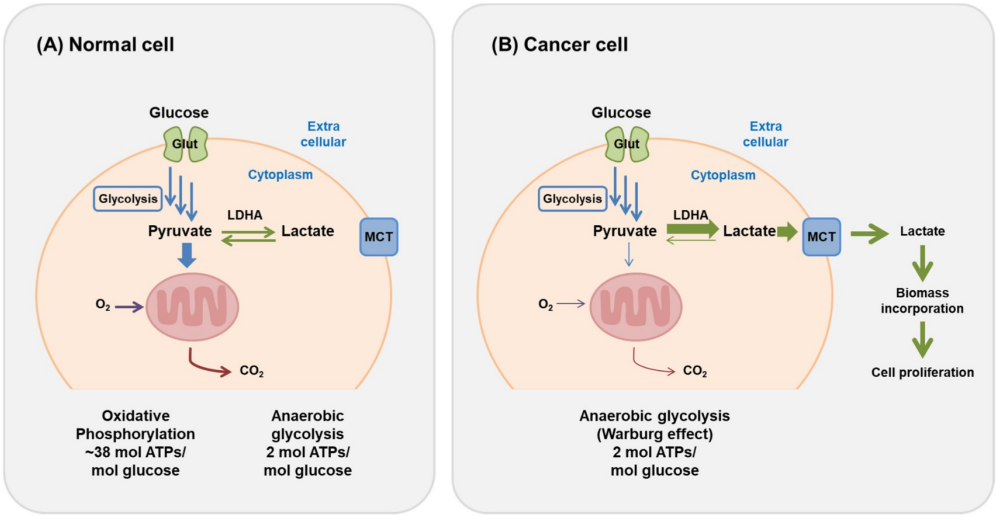

Figure 4-2: Comparison between the TCA cycle and the Warburg effect. In normal cells (left panel), pyruvate predominantly enters the TCA cycle. In cancer cells (right panel) pyruvate does not enter the TCA cycle and is instead converted into lactate even in the presence of oxygen.. Taken from [214].

Other important nutrients to the promotion of tumor growth can be found in the blood serum of patients. However, since there are important limitations regarding the accessibility and availability of human blood serum, *in vitro* cultures use Fetal Bovine Serum (FBS) instead. FBS is a complex mixture of nutrients and growth factors that can influence cancer cell behavior in various ways. For example, FBS can provide the necessary amino acids to support protein synthesis and other essential biosynthetic processes to cancer cells [215]. In addition, FBS has vitamins, minerals, growth factors, and hormones, such as insulin-like growth factor 1 (IGF-1), epidermal growth factor (EGF), and platelet-derived growth factor (PDGF), that are also required for cell growth and survival [216].

During solid tumor progression, the availability of nutrients in the tumor microenvironment changes mainly due to increased consumption of rapidly proliferating cells and poor blood supply, which impacts the metabolism of cancer cells [217].

In the case of poor blood supply, the hypoxic environment forces cells to upregulate glucose uptake and lactate production to generate energy. It also stimulates them to induce angiogenesis to promote new routes for both nutrients and oxygen delivery. Once the supply is restored, the tumor grows again, generating cycles of nutrient abundance and starvation.

Several studies have attempted to study *in vitro* the effect of nutrient starvation or deprivation by modeling their short term (less or equal than 48 hours) effects. For instance, Huang et al. analyzed the effect of different concentrations of glucose and associated metabolites (pyruvate and ATP) in the response of different CRC cell lines (HT-29, HCT-116, SW480, and Caco-2) against the chemotherapeutic agent 5-fluorouracil (5FU) [218]. For this, the authors first exposed cells in 2D cultures to various doses of 5FU in media containing different concentrations of glucose (1.0 or 4.5 g/L). The exposure was performed over a period of 48 hours. In a parallel experiment, the authors generated spheroids from these cell lines in glucose-enriched media (4.5 g/L). Following formation, the authors reduced the concentration of glucose in the medium to 5mM (1.0 g/L) and, 24 hours later, they switched again culture media to those used in the 2D experiments; that is, various doses of the drug in media containing the different concentrations of glucose. As in the 2D experiments, the exposure time to the drug was 48 hours. With their results, the authors concluded that reduction of glucose also decreased the viability of all cultures when exposed to increasing doses of 5FU, suggesting that glucose, especially at high concentrations (4.5 g/L), acts as a protective agent against the drug.

In a different experiment, Lee et al. studied the role of high glucose concentration (4.5 g/L) on the survival of HCT-116 cells against stress in the endoplasmic reticulum (ER) [219]. This organelle is responsible for protein maturation. However, when it is stressed, protein maturation does not function correctly, which increases the amount of unfolded proteins inside the organelle [220]. Thus, in order to maintain homeostasis, cells can trigger a control mechanism, called Unfolding Protein Response (UPR) that tries to lower the number of unfolded proteins in the cell [220]. If the cell successfully controls this number, UPR is deactivated. However, if it cannot balance the number of unfolded proteins, the cell can die [220]. Taking into account the UPR as a potential mechanism leading to cell death, the authors hypothesized that high concentrations of glucose could have a legacy effect on cancer cells that could protect them against ER stress even in glucose-restricted environments, through the dysregulation of UPR. To prove this hypothesis, they analyzed gene expression of HCT-116 cells cultivated in high glucose (4.5 g/L) media and compared it to the case where cells were in low glucose (1.0 g/L) media. First, cells were grown in high glucose media (with 10% FBS) and then transiently fasted in low glucose media (with 10% FBS) and low glucose media (without FBS) for 24 hours/fasting media. Then, they were exposed again to high glucose media (with 10% FBS) for another 24 hours. Subsequently, the authors performed the effect of an anti-cancer drug, called thapsigargin, in HCT-116 cells that were first exposed to high glucose and then switched to low glucose media. With their results, the authors corroborated that high glucose concentrations had lasting effects in the behavior of HCT-116 cells, helping them to attenuate the

events induced by the UPR and, consequently, resist the apoptotic effects of thapsigargin [219].

Other studies have assessed the inhibition of autophagy of different cell lines in glucose-deprived environments. Indeed, Lauzier et al. studied autophagic capacities of different CRC cell lines and their sensitivity to autophagy inhibition [98]. To do this, the authors first cultured HCT-116, Caco-2/15, SW480, HT-29, and LoVo cells in normal growth media and then switched to fully deprived media (without glucose or FBS). The duration in this condition was 4 hours. After analysis, the authors observed that, in glucose-deprived media, HCT-116 and Caco-2/15 cell lines exhibited the highest autophagic activity in comparison to the other cell lines. They also had the highest sensitivity to autophagy inhibition, as they reduced their proliferation. These results highlight that, upon nutrient-starvation, CRC cell lines have different responses to this stress by regulating autophagy. Lastly, Schroll et al. combined glucose restriction with autophagy inhibition and chemotherapy strategies to assess the effectivity of the drug in HCT-116 spheroids [221]. For this, the authors grew the spheroids in RPMI 1640 medium with glucose and 10% FBS for 10 days. Then, they changed the media of the spheroids to RPMI 1640 with no glucose and added 25 μM of cloroquine (CQ), an autophagy inhibitor [222]. 48 hours after the addition of CQ, the authors added 47.8 μM irinotecan (IR), a classic anti-cancer drug [223], to the glucose-deprived media containing CQ and maintained the experiment for another 48 hours. With their results, the authors also concluded that glucose has a protective effect against chemotherapy agents by activating autophagy.

The aforementioned studies share a common experimental approach, wherein cells are cultured in presence of glucose before being subjected to deprivation. The cyclic switch from abundance to starvation is known as preconditioning, a term that originated from experimental studies in cardiac ischaemia [224]. In this field, preconditioning refers to a defined number of repeated cycles of ischaemia and reperfusion. This scheme has been shown to help myocardial cells adapt to the ischaemia, thus reducing the size of the infarct area [224]. This adaptation occurs through transient epigenetic changes that enable myocardial cells to express genes and different molecules in adverse environmental conditions, such as hypoxia, that would be typically only expressed under physiological normoxic conditions.

In this Chapter, we perform nutrient and growth factors preconditioning experiments in combination with different initial starvation periods, and analyze their long-term response (approximately 30 days) in the mechanobiological behavior of HCT-116 and HT-29 spheroids, a scenario that has not been considered previously in literature. To do this, we first generated spheroids in media with abundance of both glucose and FBS. Then, we suspended the spheroids in glucose or FBS deprived media for intervals of time that spanned from 24 to 120 hours (initial starvation period).

Following this period, we performed alternating cyclic changes of glucose or FBS abundance and starvation with a total duration of 144 hours per cycle. In total, we carried out 2 cycles of nutrient abundance and 2 of nutrient starvation, apart from the starvation period.

This design allowed us to answer five main questions directly related to our main goal of determining whether the CRC spheroids could adapt to the time-dependent nutrient availability described *in vivo*:

1. Does the initial starvation period affect spheroid growth?
2. Does the starvation period enhance the growth behavior of the preconditioned spheroids during the period in nutrient abundance?
3. Does the first cycle in nutrient starved media generate the same response in the spheroids as in the starvation period?
4. Do the spheroids in the second cycle of nutrient abundance behave the same as in the first cycle of abundance?
5. Do the number of cycles affect the response of the spheroids in the last cycle of the experiment?

Details of the preconditioning experiments, as well as the combinations of nutrient-enriched and nutrient-deprived media, can be found in Chapter 2 of this dissertation.

4.2. Results

As explained in section 2.6 of Chapter 2, we defined four major experiments wherein we varied the concentration of either glucose or FBS to perform the preconditioning experiments. In the following sections, the nutrient-enriched medium, named DG10, contained 4.5 g/L of glucose and was supplemented with 10% FBS. In turn, the deprived medium depended on the preconditioning experiment. For the "best-to-worst" experiment, this medium, denominated D0, contained 1.0 g/L glucose and had no FBS. In the experiment where glucose was varied (glucose preconditioning experiment), the starved medium (D10) contained 1.0 g/L glucose and 10% FBS. Finally, in the case where FBS was varied (FBS preconditioning experiment), the deprived medium, called DG0, contained 4.5 g/L glucose and no FBS. We took pictures daily for the entire duration of each experiment. From the obtained data, we measured the projected area of the spheroids and assumed that the samples were completely round.

Figure **4-3** shows an overview of the preconditioning experiment. Every experiment started with an initial starvation period, in which newly formed spheroids were left in deprived media for a period of 24 to 120 hours. We chose this time span to analyze the effects of short- (less or equal than 48 hours, defined according to [106, 218, 219]) and long- (more than 48 hours) term starvation on the adaptative response of the spheroids. Afterwards, the spheroids experienced a first cycle in abundant media that lasted 144 hours. Then, they experienced a first cycle in deprived media for another 144 hours. At the end of this cycle, the spheroids experienced a second cycle in abundant media with the same duration of the previous cycles. Finally, at the end of the experiment, the spheroids experienced one final cycle of deprived media for another 144 hours.

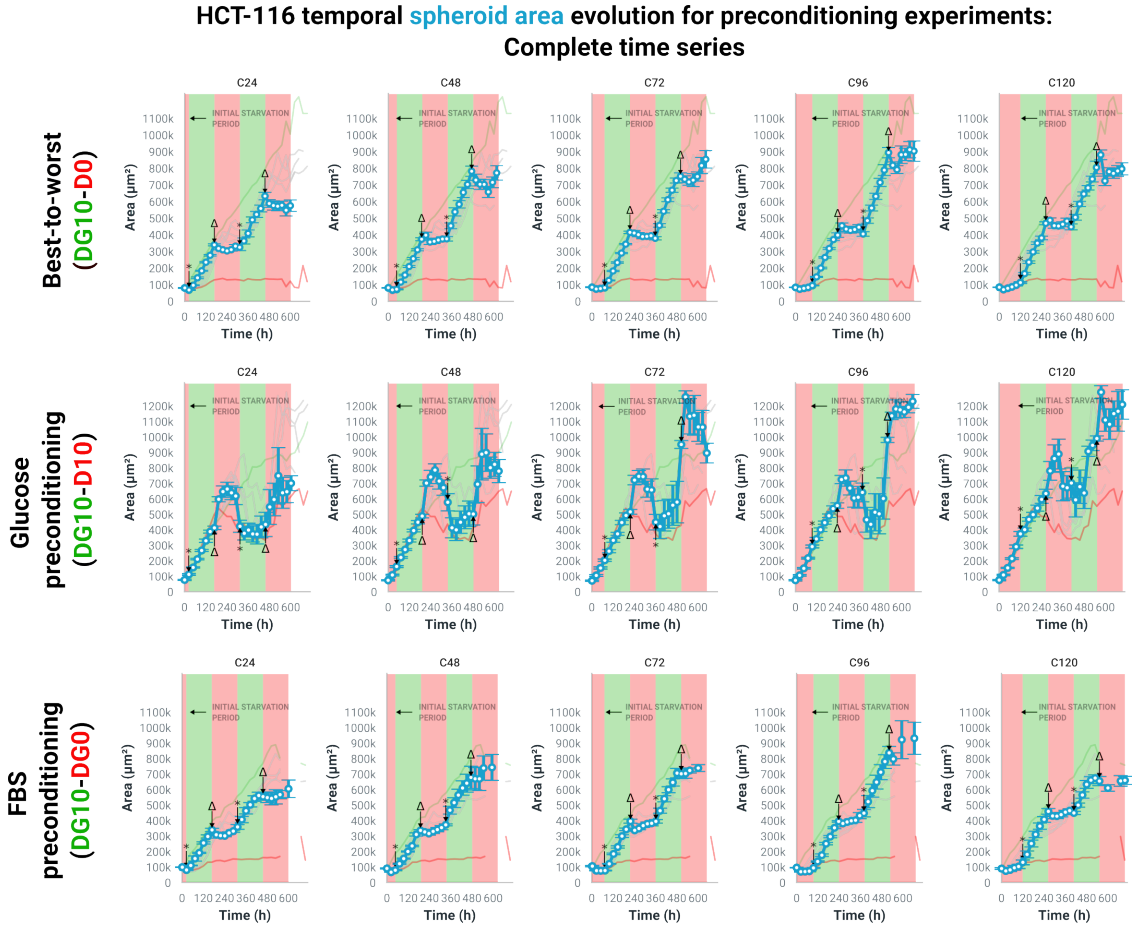

Figure 4-3: Complete time series of the preconditioning experiments for the HCT-116 cell line. In all experiments, the "*" symbols indicates the transition from deprived to abundant media, whereas the "Δ" symbol signals the transition from abundant to deprived media. Green lines: positive controls. Red lines: negative controls. Green shaded bars correspond to the periods in abundant media. Red shaded bars indicate periods in deprived media.

4.2.1. The initial starvation period enhances the growth of HCT-116 spheroids

In order to determine whether newly formed spheroids, grown in enriched medium (DG10), adapted to an initial nutrient starvation, we suspended them in a nutrient deprived medium (either D0, D10, or DG0) for a minimum of 24 hours to a maximum of 120 hours, and checked their area evolution. We defined this period as the initial starvation period. Figure **4-4** shows the time evolution of the mean spheroid area during the initial starvation period for all the proposed experiments.

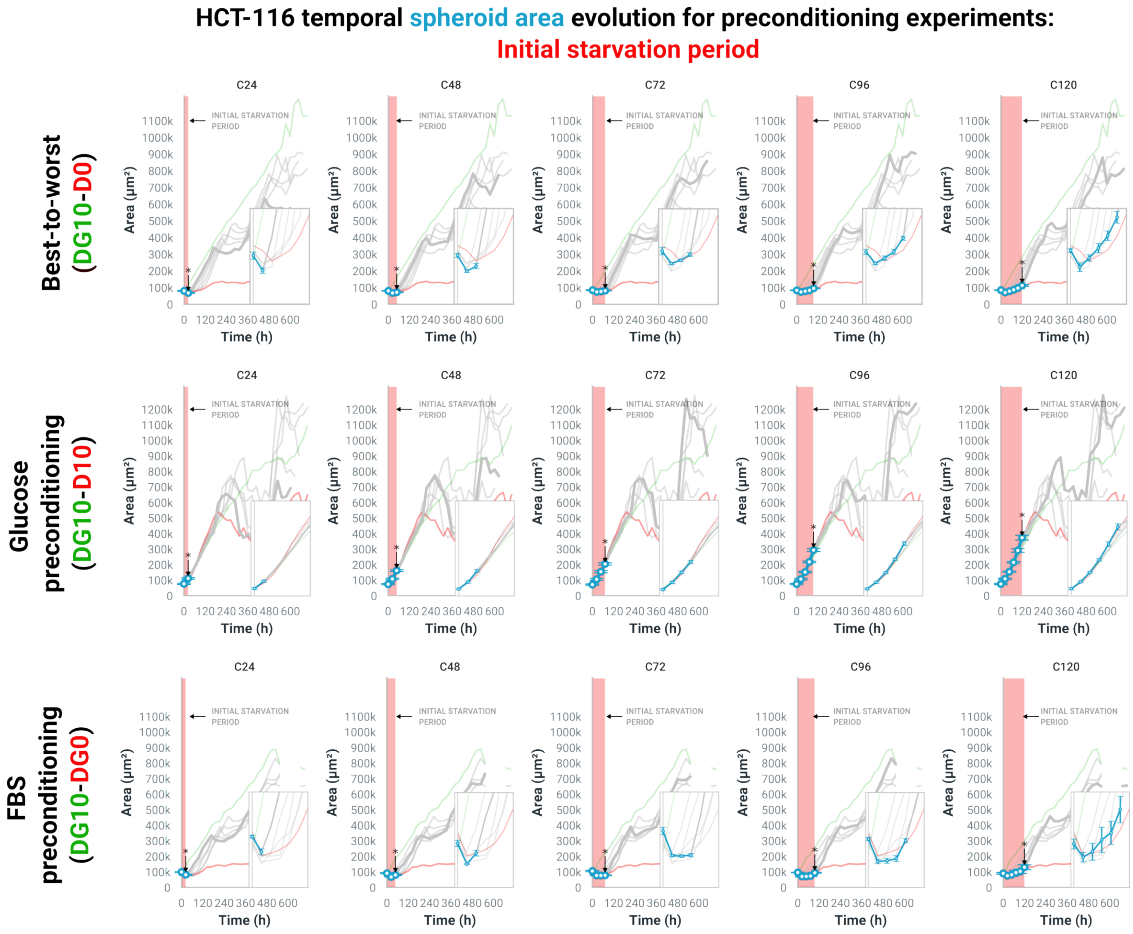

Figure 4-4: Time evolution of the mean area of each preconditioned group during the initial starvation period for the different experiments. Shaded red area highlights the area of each preconditioned groups during this period. Green lines: positive controls. Red lines: negative controls. The insets in the graphs represent a magnification of the analyzed period (highlighted by the shaded bar) in every preconditioned group.

During the first 24 hours of this period, the area of all preconditioned groups in the "best-to-worst" (DG10-D0) and FBS (DG10-DG0) preconditioning experiments decreased (respectively, first and third rows in Figure **4-4**). However, as the time inside D0 or DG0 increased, spheroids gradually adapted to the deprived environment, resulting in an increased size at the end of this phase. This was especially true in the groups that were kept for more than 72 hours in D0 or DG0 (respectively, first and third rows in Figure **4-4**).

Analysis of the growth rates of the preconditioned groups (Table **4-1**) confirmed the adapting trend of the spheroids as the initial time inside nutrient-deprived media increased. In the "best-to-worst" experiment, with respect to the negative control, the rates of the preconditioned groups were significantly lower during the first 72 hours and significantly higher afterwards. In the glucose preconditioning experiment, the growth rates of the preconditioned groups did not present statistical differences with respect to the negative control except in the C48 group, although in all groups they were higher. Finally, analysis of the mean growth rates for the FBS preconditioning experiment revealed that the preconditioned spheroids and the negative controls increased their growth rates only in the case where the spheroids were left in DG0 for 120 hours, but the differences were not statistically relevant.

Table 4-1.: Mean growth rates during the initial starvation period for all the tested experiments. $C0_{(C24)}$-$C0_{(C120)}$: Growth rate of the negative control group measured in the starvation period of the given preconditioned group. Data for the HCT-116 cell line.

Condition	**Mean growth rate during the initial starvation period (μm²/h)**		
	Best-to-worst	**Glucose prec.**	**FBS prec.**
C24	-520.41	1453.73	-730.27
C0$_{(C24)}$	-182.52	1096.53	-1072.8
C24 - C0$_{(C24)}$ **p-value**	0.015	0.12	0.25
C48	-186.23	1833.4	-235.67
C0$_{(C48)}$	-274.22	1383.33	-475.27
C48 - C0$_{(C48)}$ **p-value**	0.0044	0.0084	0.24
C72	-39.46	1848.25	-387.16
C0$_{(C72)}$	-119.19	1829.71	-261.51
C72 - C0$_{(C72)}$ **p-value**	5.2e-5	0.82	0.39
C96	121.17	2280	-19.27
C0$_{(C96)}$	-39.6	2255.35	-121.43
C96 - C0$_{(C96)}$ **p-value**	2.4e-5	0.82	0.43
C120	232.1	2486.62	331.95
C0$_{(C120)}$	66.64	2347.77	33.25
C120 - C0$_{(C120)}$ **p-value**	0.0058	0.77	0.1

We also repeated the “best-to-worst” experiment with the HT-29 cell line. Results for the overall growth trend during this cycle is shown in Figure **4-5**. Similar to the HCT-116 case, the area of the preconditioned spheroids decreased in the first 24 hours of the experiment. However, as the time inside D0 increased, the area of the spheroids gradually started to grow.

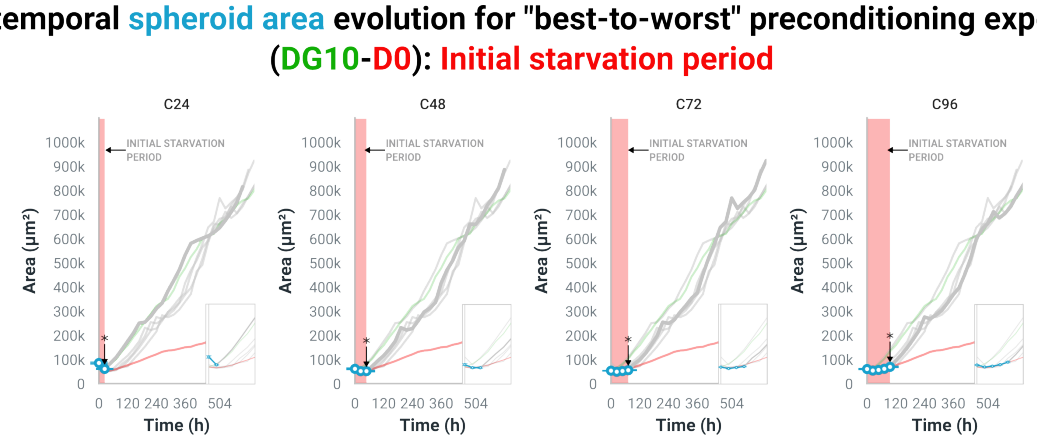

Figure 4-5: Growth trend evolution of HT-29 preconditioned spheroids during the starvation period (D0). Shaded red area highlights the area of each preconditioned groups during this period. Green line: positive control. Red line: negative control. The insets in the graphs represent a magnification of the analyzed period (highlighted by the shaded bar) in every preconditioned group.

Study of growth dynamics also confirmed the adapting trend of the spheroids with the increasing time in nutrient-deprived medium (Table **4-2**). In turn, the growth of the negative controls gradually increased during the first 96 hours of the experiment (Table **4-2**). Furthermore, comparison against the rates of the negative controls indicated that the increasing starvation period tended to reduce the differences in the growth rates. Nevertheless, all preconditioned groups grew significantly slower than the negative controls during this period.

Table 4-2.: HT-29 mean growth rates during the initial starvation period for all the tested experiments. $C0_{(C24)}$-$C0_{(C120)}$: Growth rate of the negative control group measured in the starvation period of the given preconditioned group.

Condition	Mean growth rate during the initial starvation period (µm²/h)
	Best-to-worst
C24	-414.1741
C0$_{(C24)}$	-120.4209
C24 - C0$_{(C24)}$ **p-value**	9.394e-05
C48	-200.4528
C0$_{(C48)}$	7.863521
C48 - C0$_{(C48)}$ **p-value**	0.0004588
C72	36.7653
C0$_{(C72)}$	84.23724
C72 - C0$_{(C72)}$ **p-value**	0.04253
C96	104.6702
C0$_{(C96)}$	157.5191
C96 - C0$_{(C96)}$ **p-value**	0.01326

4.2.2. The initial starvation period enhances the growth behavior of the preconditioned spheroids during the first cycle in abundant media

In all experiments, following the end of the starvation period, spheroids belonging to the preconditioned groups experienced a proportional growth that lasted for the duration of the first cycle inside DG10 (line segments between the star and triangle symbols in Figure **4-6**).

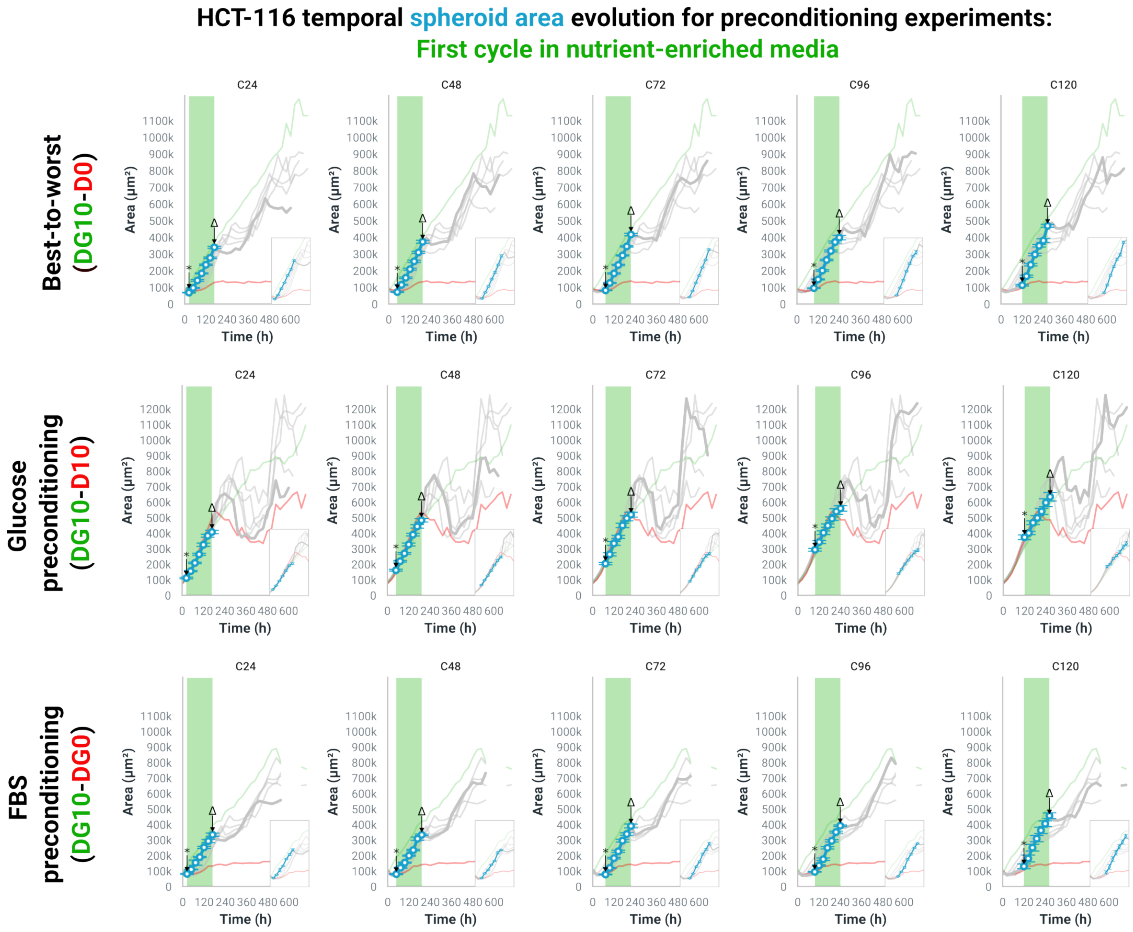

Figure 4-6: Mean area evolution of the preconditioned groups during the first cycle in abundant media (DG10). Shaded green area highlights the area of each preconditioned groups during this period. Green lines: positive controls. Red lines: negative controls. The insets in the graphs represent a magnification of the analyzed period (highlighted by the shaded bar) in every preconditioned group.

Analysis of the growth rates during this cycle (Table **4-3**) revealed that, when the preconditioned spheroids were exposed to abundant media after the initial deprivation period, the rates experienced a positive outburst that increased with the starvation period. This outburst was significant when we compared the rates of the preconditioned groups with those of the positive controls, especially in the "best-to-worst" scenario. In the experiment where glucose was restricted (glucose preconditoning) the differences in the growth rates were not statistically significant, whereas in the case where FBS was completely removed (DG10-DG0), the differences became relevant when the starvation period exceeded 72 hours.

Table 4-3.: Mean growth rates during the first cycle in nutrient-enriched media for all the tested experiments. $C10_{(C24)}$-$C10_{(C120)}$: Growth rate of the positive control group measured in the starvation period of the given preconditioned group. Data for the HCT-116 cell line.

Condition	Mean growth rate during the 1st cycle in nutrient abundance (μm²/h)		
	Best-to-worst	**Glucose prec.**	**FBS prec.**
C24	1888.24	2056.79	1754.44
C10$_{(C24)}$	1771.18	2108.07	1795.96
C24 - C10$_{(C24)}$ **p-value**	0.076	0.44	0.49
C48	2093.98	2229.39	1760.67
C10$_{(C48)}$	1770.45	2150.49	1606.4
C48 - C10$_{(C48)}$ **p-value**	5.2e-5	0.54	0.23
C72	2325.37	2189.49	2171.33
C10$_{(C72)}$	1648.14	2092.88	1440.96
C72 - C10$_{(C72)}$ **p-value**	2.0e-7	0.34	0.00056
C96	2104.82	1847.9	2066.38
C10$_{(C96)}$	1723.14	2030.09	1581.16
C96 - C10$_{(C96)}$ **p-value**	0.0065	0.27	4.6e-6
C120	2471.16	1811.18	2264.96
C10$_{(C120)}$	1593.7	1949.78	1412.58
C120 - C10$_{(C120)}$ **p-value**	8.3e-8	0.19	0.00039

When the preconditioned HT-29 spheroids were passed to the first cycle in nutrient and growth factors abundant media, they also experienced a linear growth that persisted throughout the entire duration of the cycle (line segments between the "$*$" and "Δ" symbols in Figure **4-7**). The growth rates associated to this cycle are given in Table **4-4**. From the results, we observed that the spheroids tended to grow faster as the initial starvation period increased. The achieved values, however, were similar to those obtained for the positive controls. Indeed, as seen in Table **4-4**, the differences between the growth rates of the preconditioned groups and the positive controls were not statistically significant.

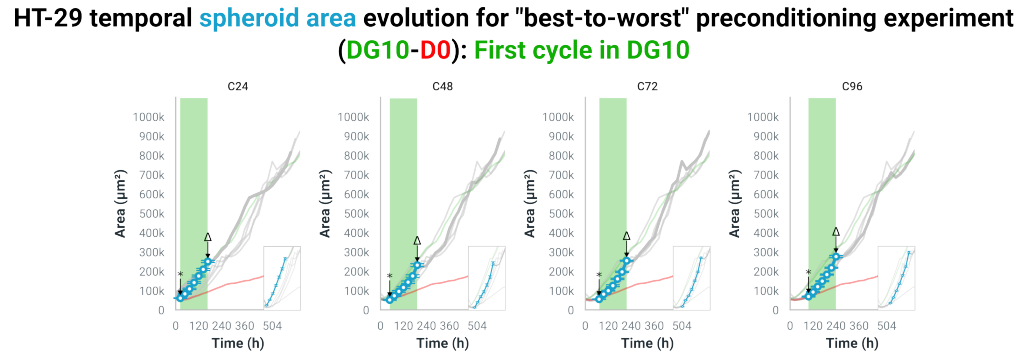

Figure 4-7: Mean area evolution of HT-29 spheroids during the first cycle in nutrient abundance of the "best-to-worst" preconditioning experiment. Shaded green area highlights the area of each preconditioned groups during this period. Green line: positive control. Red line: negative control. The insets in the graphs represent a magnification of the analyzed period (highlighted by the shaded bar) in every preconditioned group.

Table 4-4.: Mean growth rates during the first cycle in nutrient-enriched media for the "best-to-worst" preconditioning experiment. $C10_{(C24)}$-$C10_{(C120)}$: Growth rate of the positive control group measured in the starvation period of the given preconditioned group. Data for the HT-29 cell line.

Condition	Mean growth rate during the 1st cycle in nutrient abundance (µm²/h)
	DG10-D0
C24	1136.623
C10$_{(C24)}$	1125.233
C24 - C10$_{(C24)}$ **p-value**	0.6952
C48	1179.074
C10$_{(C48)}$	1234.268
C48 - C10$_{(C48)}$ **p-value**	0.1739
C72	1324.139
C10$_{(C72)}$	1291.164
C72 - C10$_{(C72)}$ **p-value**	0.3373
C96	1389.602
C10$_{(C96)}$	1318.541
C96 - C10$_{(C96)}$ **p-value**	0.2701

4.2.3. The first cycle in deprived media alters the growth of the preconditioned spheroids with respect to the initial starvation period

When the spheroids returned to the deprived media, the linear growth observed during the previous cycle was disrupted (Figure **4-8**). For the "best-to-worst" and FBS preconditioning experiments, the spheroids had an overall growth plateau, whereas in the glucose preconditioning scenario, the spheroids exhibited a non-linear behavior resembling an inverted parabola.

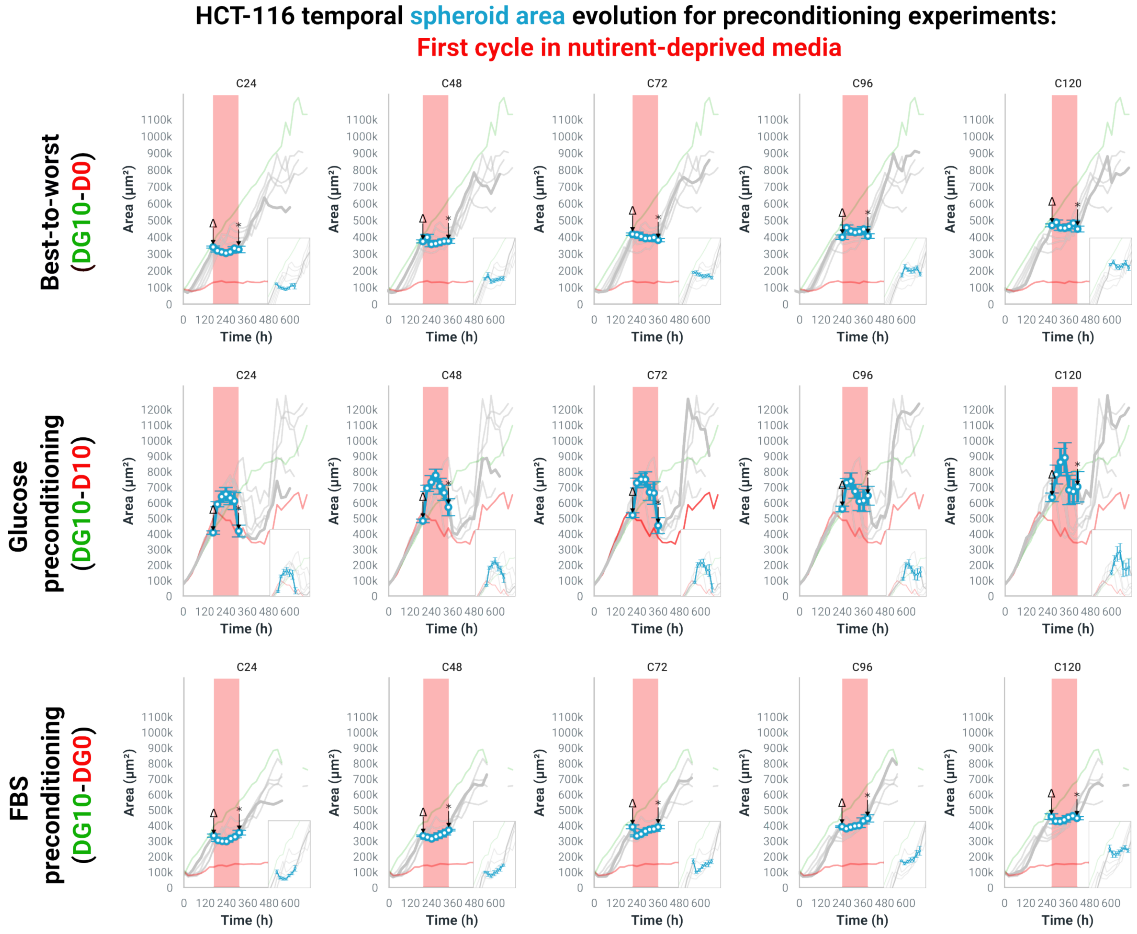

Figure 4-8: Mean area evolution of the preconditioned groups during the first cycle of starvation for all the experiments. Shaded red area highlights the area of each preconditioned groups during this cycle. Green lines: positive controls. Red lines: negative controls. The insets in the graphs represent a magnification of the analyzed period (highlighted by the shaded bar) in every preconditioned group.

Table **4-5** shows the values of the mean growth rates of each preconditioned group in all experiments, calculated for the current cycle. With respect to the negative controls, the differences in the values were, in general, not significant.

Table 4-5.: Mean growth rates during the first cycle of starvation for all the tested experiments. $C0_{(C24)}$-$C0_{(C120)}$: Growth rate of the negative control group measured in the starvation period of the given preconditioned group. Data for the HCT-116 cell line.

Condition	**Mean growth rate during the 1st cycle in nutrient starvation (µm^2/h)**		
	Best-to-worst	**Glucose prec.**	**FBS prec.**
C24	-102.68	70.09	131.87
C0$_{(C24)}$	-1.58	-798.9	134.36
C24 - C0$_{(C24)}$ **p-value**	0.0099	0.069	0.52
C48	15.95	609.76	249.72
C0$_{(C48)}$	-63.49	-710.2	48.62
C48 - C0$_{(C48)}$ **p-value**	1.0	0.038	0.00047
C72	-248.09	-466.35	-8.31
C0$_{(C72)}$	-15.47	-956.37	55.29
C72 - C0$_{(C72)}$ **p-value**	0.86	0.56	0.37
C96	47.12	594.03	366.64
C0$_{(C96)}$	10.9	-987.06	106.98
C96 - C0$_{(C96)}$ **p-value**	0.47	0.075	0.15
C120	-149.24	470.05	-70.56
C0$_{(C120)}$	-7.34	-1004.83	43.89
C120 - C0$_{(C120)}$ **p-value**	0.097	0.27	0.6

We then compared the growth rates of this cycle with the ones from the initial starvation period, as we wanted to check whether the adapting trends seen in the starvation phase were maintained in the current cycle even after experiencing an intermediate period of linear growth in nutrient and growth factors abundance. The results, shown in Table **4-6**, indicated that the rates had different behavior across the experiments.

Indeed, in the "best-to-worst" scenario, the rates of all preconditioned groups did not have statistically significant differences with respect to the ones during the initial starvation phase. Conversely, in the glucose preconditoning experiment, all rates were significantly lower than those in the initial starvation period. Finally, in the FBS preconditoning experiment, the behavior of the rates was variable. Thus, for the C24 to C72 groups, the rates were significantly higher than in the starvation period, while in the C96 and C120 groups, the rates did not have statistically relevant differences.

Table 4-6.: Percentage changes in the growth rates between the cycle of starvation and the initial starvation period. The "C1M" subindex represents the rates of the preconditioned groups during the first cycle in deprived media. The "pre" subindex represents the corresponding rates during the initial starvation period.

Condition	Best-to-worst		Glucose prec.		FBS prec.	
	Growth rate Percent change (SD)	p-value	Growth rate Percent change (SD)	p-value	Growth rate Percent change (SD)	p-value
$\mathbf{C24}_{(C1M)}$-$\mathbf{C24}_{pre}$	38.0 (38.7)	0.2145	-93.5 (1159.2)	0.00401	124.3 (138.3)	0.006698
$\mathbf{C48}_{(C1M)}$-$\mathbf{C48}_{pre}$	19.8 (161.8)	0.9393	-85.4 (382.8)	0.0002927	218.5 (213.7)	0.01061
$\mathbf{C72}_{(C1M)}$-$\mathbf{C72}_{pre}$	-42.8 (114.7)	0.2672	-133.2 (277.5)	0.00005231	148.9 (181.2)	0.01468
$\mathbf{C96}_{(C1M)}$-$\mathbf{C96}_{pre}$	-40.2 (121.5)	0.6031	-106.7 (686.0)	1.077e-06	176.4 (188.2)	0.1189
$\mathbf{C120}_{(C1M)}$-$\mathbf{C120}_{pre}$	8.7 (13.1)	0.8438	-111.5 (513.6)	0.00006104	-73.2 (203.5)	0.625

For the HT-29 cell line, the spheroids in all preconditioned groups experienced a small plateau during the first 24 hours in D0. Afterwards, contrary to the HCT-116 case, they continued to grow linearly until the end of the cycle (Figure **4-9**).

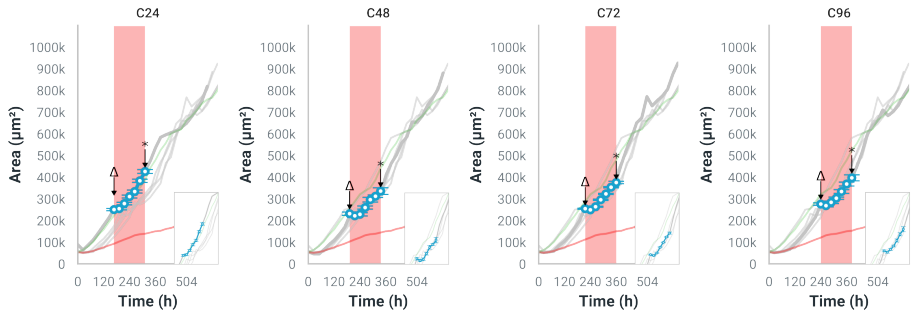

Figure 4-9: Mean area evolution of HT-29 preconditioned spheroids during the first cycle of starvation. Shaded red area highlights the area of each preconditioned groups during this cycle. Green line: positive control. Red line: negative control. The insets in the graphs represent a magnification of the analyzed period (highlighted by the shaded bar) in every preconditioned group.

Supporting this observation, results of the mean growth rates revealed that the values were all positive, including those of the negative controls (Table **4-7**). Interestingly, among themselves, all preconditioned groups grew at similar growth rates. Furthermore, these rates were significantly higher than those of the negative controls.

Table 4-7.: Mean growth rates during the first cycle of starvation in the "best-to-worst" experiment. $C0_{(C24)}$-$C0_{(C120)}$: Growth rate of the negative control group measured in the starvation period of the given preconditioned group. Data for the HT-29 cell line.

Condition	**Mean growth rate during the 1st cycle in nutrient starvation (µm²/h)**
	Best-to-worst
C24	948.3678
C0$_{(C24)}$	333.7637
C24 - C0$_{(C24)}$ **p-value**	0.0001139
C48	833.9131
C0$_{(C48)}$	286.9023
C48 - C0$_{(C48)}$ **p-value**	0.0005624
C72	936.352
C0$_{(C72)}$	249.0538
C72 - C0$_{(C72)}$ **p-value**	2.783E-07
C96	911.3622
C0$_{(C96)}$	207.0795
C96 - C0$_{(C96)}$ **p-value**	9.232e-05

We then compared the rate values of the preconditioned groups during this cycle and the starvation period (Table **4-8**). Results evidenced that all preconditioned groups grew significantly faster during this cycle compared to the initial preconditioning phase.

Table 4-8.: Percentage changes in the growth rates of HT-29 spheroids between the first cycle of starvation and the initial starvation period. The "C1M" subindex represents the rates of the preconditioned groups during the first cycle in nutrient-deprived media. The "pre" subindex represents the corresponding rates during the starvation period.

Condition	Best-to-worst	
	Growth rate Percent change (SD)	**p-value**
$\mathbf{C24}_{(C1M)}$-$\mathbf{C24}_{pre}$	329.0 (49.1)	0.0001558
$\mathbf{C48}_{(C1M)}$-$\mathbf{C48}_{pre}$	516.0 (168.5)	4.327E-05
$\mathbf{C72}_{(C1M)}$-$\mathbf{C72}_{pre}$	2446.8 (2455.8)	2.775E-05
$\mathbf{C96}_{(C1M)}$-$\mathbf{C96}_{pre}$	770.7 (235.6)	0.0002056

4.2.4. The second cycle of nutrient abundance potentiates the growth of the spheroids seen in the first cycle of nutrient abundance

During the second period inside nutrient-enriched media, preconditioned spheroids resumed their growth (Figure **4-10**). This growth, however, was not linear in all experiments. In the "best-to-worst" and FBS preconditoning experiments, all preconditioned groups had a proportional growth throughout the entire cycle. Conversely, in the glucose preconditoning experiment, the growth of the groups decayed before experiencing an outburst. This was especially true in the C72 to C120 groups.

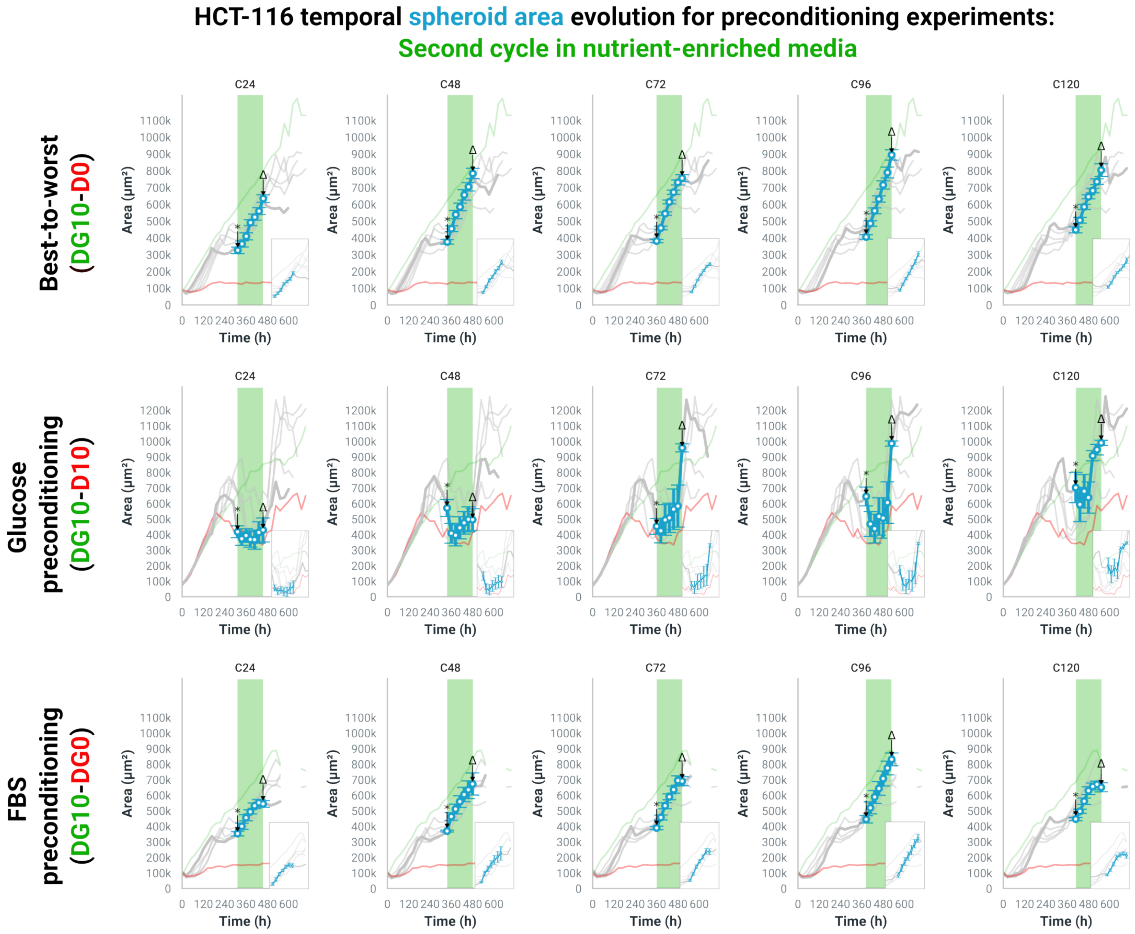

Figure 4-10: Mean area evolution of the preconditioned groups during the second cycle in abundant media for all the experiments. Shaded green area highlights the area of each preconditioned groups during this cycle. Green lines: positive controls. Red lines: negative controls. The insets in the graphs represent a magnification of the analyzed period (highlighted by the shaded bar) in every preconditioned group.

Quantitative analysis of the growth rates for the different experiments (Table **4-9**) revealed that in the "best-to-worst" and glucose preconditoning experiments, the growth rates of all preconditioned groups were significantly higher than the positive controls. By contrast, in the FBS preconditoning scenario, the corresponding rates were similar, yielding no statistically relevant differences.

Table 4-9.: Mean growth rates of HCT-116 preconditioned spheroids during the second cycle in abundant media for all the tested experiments.

Condition	Mean growth rate during the 2nd cycle in nutrient abundance (μm^2/h)		
	Best-to-worst	**Glucose prec.**	**FBS prec.**
C24	2142.22	81.74	1327.58
C10$_{(C24)}$	1470.39	1322.99	1463.08
C24 - C10$_{(C24)}$ **p-value**	0.00049	0.0061	0.76
C48	2830.21	-519.6	2101.25
C10$_{(C48)}$	1562.45	1055.27	1746.67
C48 - C10$_{(C48)}$ **p-value**	1.5E-6	0.012	0.45
C72	2602.47	3509.93	2091.93
C10$_{(C72)}$	1588.68	959.98	1799.76
C72 - C10$_{(C72)}$ **p-value**	0.00025	3.1E-7	0.31
C96	3394.34	2365.66	2678.09
C10$_{(C96)}$	1492.9	584.13	1571.69
C96 - C10$_{(C96)}$ **p-value**	9.0E-7	2.9E-5	0.068
C120	2473.47	1998.73	1418.31
C10$_{(C120)}$	1564.79	493.13	849.93
C120 - C10$_{(C120)}$ **p-value**	0.00082	0.00079	0.15

We then compared the rates of the preconditioned groups for this cycle with the ones from the first cycle in nutrient abundance. Results, which are shown in Table **4-10**, revealed varying behavior across the experiments. In the "best-to-worst" case, all preconditioned spheroids grew significantly faster than in the first cycle in nutrient abundance. By contrast, in the glucose preconditoning scenario, spheroids belonging to the C24 and C48 groups grew significantly slower than in the first cycle, whereas in the rest of the preconditioned groups, the rates were similar. Finally, in the FBS preconditoning experiment, although there was not a visible trend in the rates, they were similar to those in the first cycle in nutrient-enriched medium.

Table 4-10.: Percentage changes in the growth rates of HCT-116 preconditioned spheroids between the first and second cycles in abundant media. The "C2B" subindex represents the rates of the preconditioned groups during the second cycle in nutrient-enriched media. The "C1B" subindex represents the corresponding rates during the first cycle in nutrient-enriched media.

Condition	Best-to-worst		Glucose prec.		FBS prec.	
	Percent change (SD)	p-value	Percent change (SD)	p-value	Percent change (SD)	p-value
$\mathbf{C24}_{(C2B)}$-$\mathbf{C24}_{(C1B)}$	42.3 (11.0)	0.0118	-93.9 (899.5)	0.0001831	-21.9 (3.9)	0.05122
$\mathbf{C48}_{(C2B)}$-$\mathbf{C48}_{(C1B)}$	33.6 (4.6)	0.0002133	-97.6 (2105.8)	6.10E-05	10.8 (4.0)	0.5647
$\mathbf{C72}_{(C2B)}$-$\mathbf{C72}_{(C1B)}$	23.1 (3.9)	0.04409	24.7 (6.9)	0.06032	-0.3 (0.1)	0.9499
$\mathbf{C96}_{(C2B)}$-$\mathbf{C96}_{(C1B)}$	69.6 (9.1)	9.77E-05	6.5 (2.8)	0.6788	24.0 (3.6)	0.06182
$\mathbf{C120}_{(C2B)}$-$\mathbf{C120}_{(C1B)}$	25.2 (6.1)	0.04364	44.3 (36.1)	0.2524	-31.5 (5.1)	0.0001874

When the HT-29 preconditioned spheroids returned to nutrient-enriched medium, their growth was not interrupted (Figure **4-11**).

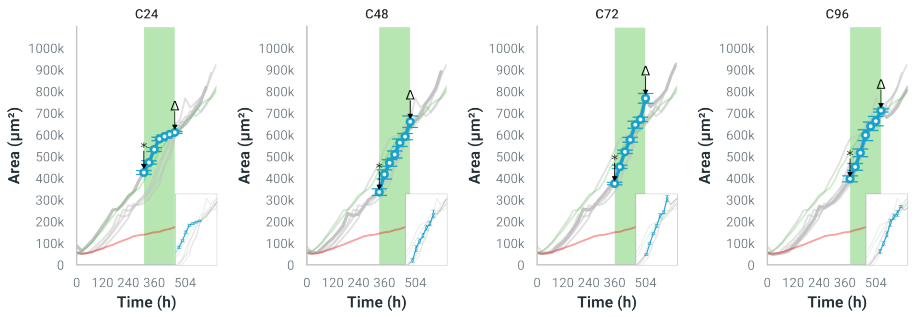

Figure 4-11: Mean area evolution of HT-29 preconditioned spheroids during the second cycle in abundant medium. Shaded green area highlights the area of each preconditioned groups during this cycle. Green line: positive control. Red line: negative control. The insets in the graphs represent a magnification of the analyzed period (highlighted by the shaded bar) in every preconditioned group.

In fact, they grew significantly faster than the positive controls, as seen in Table **4-11**. In addition, with the exception of the C48 group, the C72 and C96 groups grew significantly faster than the C24 group.

Table 4-11.: Mean growth rates during the first cycle in nutrient-enriched media for the HT-29 spheroids in the "best-to-worst" experiment.

Condition	Mean growth rate during the 2nd cycle in nutrient abundance (μm^2/h)
	Best-to-worst
C24	1877.142
C10$_{(C24)}$	1539.671
C24 - C10$_{(C24)}$ **p-value**	0.009019
C48	2106.682
C10$_{(C48)}$	1188.981
C48 - C10$_{(C48)}$ **p-value**	0.001682
C72	2590.71
C10$_{(C72)}$	1032.136
C72 - C10$_{(C72)}$ **p-value**	2.02E-09
C96	2217.358
C10$_{(C96)}$	869.6396
C96 - C10$_{(C96)}$ **p-value**	8.973E-10

When we compared the rates with those of the first cycle in DG10 (Table **4-12**), results evidenced the notorious differences between the two cycles. Indeed, as seen in Table **4-12**, the growth rate of all preconditioned groups was significantly enhanced during this cycle with respect to the first one in nutrient-enriched medium (DG10).

Table 4-12.: Percentage changes in the growth rates between the second and first cycles in abundant media. The "C2B" subindex represents the rates of the preconditioned groups during the second cycle in abundant media. The "C1B" subindex represents the corresponding rates during the first cycle in abundant media. Data for the HT-29 cell line.

Condition	Best-to-worst	
	Growth rate Percent change (SD)	**p-value**
C24$_{(C2B)}$**-C24**$_{(C1B)}$	65.2 (5.4)	0.001384
C48$_{(C2B)}$**-C48**$_{(C1B)}$	78.7 (12.1)	0.003657
C72$_{(C2B)}$**-C72**$_{(C1B)}$	95.7 (4.8)	2.268E-05
C96$_{(C2B)}$**-C96**$_{(C1B)}$	59.6 (4.3)	0.0003369

4.2.5. The previous cycles influence the response of the spheroids in the last cycle of starvation

As in the first cycle in nutrient-deprived media, the growth pattern of the HCT-116 spheroids in every preconditioned group was not linear (Figure **4-12**). Despite this intricate behavior, the spheroids tended to increase their size during the cycle.

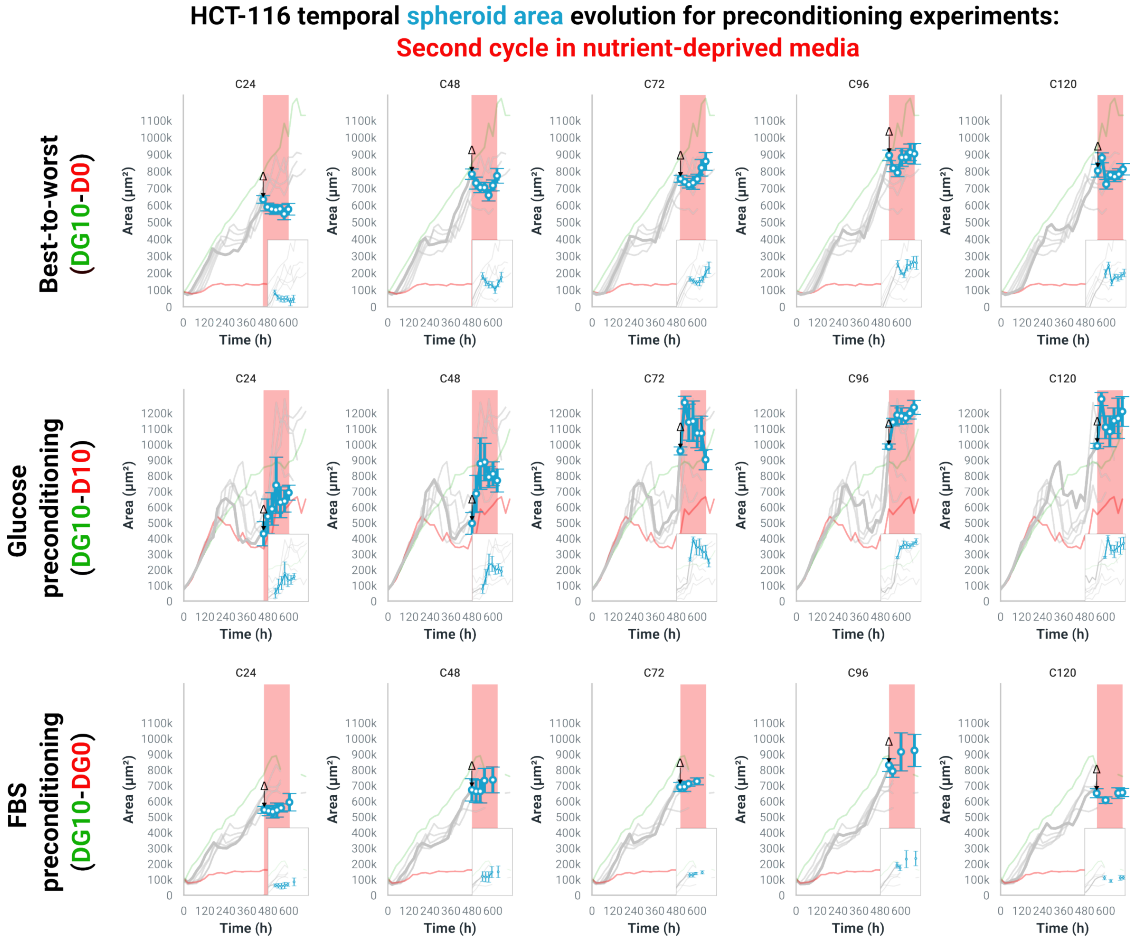

Figure 4-12: Mean area evolution of HCT-116 preconditioned groups during the second cycle of starvation for all the experiments. Shaded red area highlights the area of each preconditioned groups during this cycle. Green lines: positive controls. Red lines: negative controls. The insets in the graphs represent a magnification of the analyzed period (highlighted by the shaded bar) in every preconditioned group.

In order to quantify the previous observations, we first compared the rates of the preconditioned groups with the values of the negative controls. In the "best-to-worst" experiment, the spheroids belonging to the C24 group grew significantly slower than the negative control, whereas the samples of the C120 group grew significantly faster (Table **4-13**). For the other conditions, the differences were not statistically significant. In the glucose preconditoning case, only the C96 and C120 groups showed a significant faster rate than the negative controls. Last, in the FBS preconditoning scenario, none of the preconditioned groups exhibited significant differences with respect to the negative controls.

Table 4-13.: Mean growth rates during the second cycle in nutrient-deprived media for all the tested experiments.

Condition	**Mean growth rate during the 2nd cycle in nutrient starvation (µm^2/h)**		
	Best-to-worst	**Glucose prec.**	**FBS prec.**
C24	-401.99	1820.01	341.94
C0$_{(C24)}$	-103.73	1938.25	-80.64
C24 - C0$_{(C24)}$ **p-value**	0.02245	0.6482	0.2549
C48	-69.25	1897.55	N/A
C0$_{(C48)}$	-344.33	1630.14	N/A
C48 - C0$_{(C48)}$ **p-value**	0.1397	0.5507	N/A
C72	713.67	-387.5	N/A
C0$_{(C72)}$	-361.88	1643.24	N/A
C72 - C0$_{(C72)}$ **p-value**	0.6611	8.566e-06	N/A
C96	63.94	1739.22	647.84
C0$_{(C96)}$	578.72	-180.44	965.36
C96 - C0$_{(C96)}$ **p-value**	0.8124	0.0004277	0.2222
C120	56.05	1525.48	30.72
C0$_{(C120)}$	-110.68	676.58	-161.64
C120 - C0$_{(C120)}$ **p-value**	0.01543	0.03952	0.4206

We then compared the growth rates between both cycles in nutrient-depleted media (Table **4-14**). In the "best-to-worst" experiment, the differences for the C24 to C96 groups were not significant. For the C120 group, the spheroids grew at a significant slower rate at the second cycle in comparison to the first one. In the glucose preconditoning case, with the exception of the C72 group, spheroids grew at a significantly faster rate during the second cycle. Finally, for the FBS preconditoning scenario, the available data revealed that there were not statistically significant differences in the rate between the two cycles.

Table 4-14.: Mean growth rate differences between the cycles of starvation for all experiments. The "C2M" subindex represents the rates of the preconditioned groups during the second cycle of starvation. The "C1M" subindex represents the rates of the preconditioned groups during the first cycle of starvation. N/A: No data available.

Condition	Best-to-worst		Glucose prec.		FBS prec.	
	Percent change (SD)	p-value	Percent change (SD)	p-value	Percent change (SD)	p-value
$\mathbf{C24}_{(C2M)}$-$\mathbf{C24}_{(C1M)}$	-135.8 (166.1)	0.0806	1504.2 (18737.7)	0.0048	105.8 (226.1)	0.6449
$\mathbf{C48}_{(C2M)}$-$\mathbf{C48}_{(C1M)}$	-489.2 (3915.5)	0.3191	449.8 (2052.7)	0.013	N/A	N/A
$\mathbf{C72}_{(C2M)}$-$\mathbf{C72}_{(C1M)}$	477.9 (1575.3)	0.2482	-52.4 (113.8)	0.4548	N/A	N/A
$\mathbf{C96}_{(C2M)}$-$\mathbf{C96}_{(C1M)}$	233.0 (1048.8)	0.6663	914.3 (5874.7)	0.0004272	668.3 (957.0)	0.3528
$\mathbf{C120}_{(C2M)}$-$\mathbf{C120}_{(C1M)}$	-3.5 (6.4)	0.03845	3.3 (15.5)	0.01025	0.4 (1.2)	0.8382

We subsequently compared the rates of this cycle against the ones from the initial starvation period (table **4-15**). For the "best-to-worst" experiment, only the rate of the C120 group exhibited a significant difference with respect to the starvation period. In this case, the spheroids decreased their growth with respect to the starvation period. In turn, for the glucose preconditioning scenario, the rates of the C48 to C120 groups significantly decreased their rates with respect to their starvation period. Last, for the FBS preconditioning experiment, the available data showed variable behavior among the groups, with the rate of C24 group significantly higher than the corresponding value during the starvation period.

Table 4-15.: Percentage changes in the growth rates of HCT-116 spheroids between the second cycle of starvation and the initial starvation period. The "C2M" subindex represents the rates of the preconditioned groups during the second cycle of starvation. The "pre" subindex represents the corresponding rates during the initial starvation period.

Condition	Best-to-worst		Glucose prec.		FBS prec.	
	Percent change (SD)	p-value	Percent change (SD)	p-value	Percent change (SD)	p-value
$\mathbf{C24}_{(C2M)}$-$\mathbf{C24}_{pre}$	-46.2 (51.3)	0.321	4.8 (6.1)	0.4543	150.0 (294.0)	0.02648
$\mathbf{C48}_{(C2M)}$-$\mathbf{C48}_{pre}$	-372.7 (1252.0)	0.3498	-19.9 (17.8)	2.76E-01	N/A	N/A
$\mathbf{C72}_{(C2M)}$-$\mathbf{C72}_{pre}$	230.5 (468.0)	0.4122	-150.6 (100.9)	2.44E-04	N/A	N/A
$\mathbf{C96}_{(C2M)}$-$\mathbf{C96}_{pre}$	99.0 (335.0)	7.02E-01	-45.1 (8.1)	6.10E-05	2023.9 (3221.2)	0.1758
$\mathbf{C120}_{(C2M)}$-$\mathbf{C120}_{pre}$	-368.1 (483.2)	0.03906	-73.0 (48.7)	6.10E-05	-62.4 (91.6)	0.1132

Finally, when the preconditioned HT-29 spheroids returned once more to nutrient-deprived medium (D0), they exhibited a pronounced sustained growth pattern, in contrast to the observed behavior for HCT-116 spheroids. In the case of the C24 group, the pattern did not present growth plateaus or decays in the first 24 hours of the cycle. In the case of the C48 group, a small plateau was present during this time, whereas for the C72 and C96 cases, there was a transient growth decline 24 hours after the start of the cycle. This decline was rapidly restored in the following 48 hours (Figure **4-13**).

Figure 4-13: Area evolution of HT-29 preconditioned groups during the second cycle of starvation. Shaded red area highlights the area of each preconditioned groups during this cycle. Green line: positive control. Red line: negative control. The insets in the graphs represent a magnification of the analyzed period (highlighted by the shaded bar) in every preconditioned group.

In agreement with the above, analysis of the growth rates for this cycle (Table **4-16**) revealed that the C24 group had the highest growth rate of all the preconditioned group, while the C96 had the lowest. When we compared the rates of the preconditioned groups with those of the negative controls, we observed that the former grew significantly faster than the latter.

Table 4-16.: Mean growth rates during the second cycle of starvation for the "best-to-worst" experiment. Data for the HT-29 cell line.

Condition	Mean growth rate during the 2nd cycle in nutrient starvation ($\mu m^2/h$)
	Best-to-worst
C24	2345.224
C0$_{(C24)}$	243.2334
C24 - C0$_{(C24)}$ **p-value**	2.556E-05
C48	1581.235
C0$_{(C48)}$	295.3749
C48 - C0$_{(C48)}$ **p-value**	6.053E-07
C72	1202.093
C0$_{(C72)}$	320.2935
C72 - C0$_{(C72)}$ **p-value**	6.649E-05
C96	1142.773
C0$_{(C96)}$	351.7391
C96 - C0$_{(C96)}$ **p-value**	0.000774

Similar to the case of HCT-116, we performed comparisons of growth rate differences among the present cycle, the first cycle in nutrient-deprived medium, and the starvation period. This was done to assess whether the spheroids adapted to the harsh environment characterized by the simultaneous absence of FBS and limited glucose availability.

For the first comparison (present cycle and first cycle in nutrient-deprived medium), results show that, although the spheroids in this cycle grew faster in comparison to the first cycle in nutrient-deprived medium (Table **4-17**), the differences gradually reduced as the initial starvation period increased. Thus, the highest and lowest differences were found, respectively, in the C24 and C96 groups.

Table 4-17.: Percentage changes in the growth rates of HT-29 spheroids between the starvation cycles. The "C2M' subindex represents the rates of the preconditioned groups during the second cycle of starvation. The "C1M" subindex represents the corresponding rates during the first cycle of starvation.

Condition	Best-to-worst	
	Growth rate Percent change (SD)	p-value
$\mathbf{C24}_{(C2M)}$-$\mathbf{C24}_{(C1M)}$	147.3 (17.6)	0.0007093
$\mathbf{C48}_{(C2M)}$-$\mathbf{C48}_{(C1M)}$	89.6 (15.5)	0.0004614
$\mathbf{C72}_{(C2M)}$-$\mathbf{C72}_{(C1M)}$	28.4 (3.7)	0.02627
$\mathbf{C96}_{(C2M)}$-$\mathbf{C96}_{(C1M)}$	25.4 (4.4)	0.03771

In the final analysis, when we compared the rates of the ongoing cycle with those of the starvation period (table **4-18**), the results followed a similar trend to the calculations made for the first cycle in nutrient-deprived medium and the starvation period (Table **4-8**). Furthermore, they also corroborated that the rates were significantly higher than those observed during the starvation period.

Table 4-18.: Percentage changes in the growth rates of HT-29 spheroids between the second cycle of starvation and the initial starvation period. The "C2M" subindex represents the rates of the preconditioned groups during the second cycle in nutrient-deprived media. The "C2M" subindex represents the rates of the preconditioned groups during the second cycle in nutrient-enriched media. The "pre" subindex represents the corresponding rates during the first cycle in nutrient-enriched media.

Condition	Best-to-worst	
	Growth rate Percent change (SD)	p-value
$\mathbf{C24}_{(C2M)}$-$\mathbf{C24}_{pre}$	666.2 (96.5)	0.000171
$\mathbf{C48}_{(C2M)}$-$\mathbf{C48}_{pre}$	888.8 (260.4)	2.049E-06
$\mathbf{C72}_{(C2M)}$-$\mathbf{C72}_{pre}$	3169.6 (3201.8)	2.775E-05
$\mathbf{C96}_{(C2M)}$-$\mathbf{C96}_{pre}$	991.8 (303.8)	8.716E-05

4.2.6. The restriction of FBS combined with low glucose availability does not generate an adaptive response in HCT-116 spheroids

After performing the preconditioning experiments with DG10 and D10, we varied again the concentration of glucose but in the absence of FBS. Overall, the size of the spheroids was small and their area remained stable, as seen in Figure **4-14**. In addition, all preconditioned groups behaved very similar among themselves and also with respect to both controls. Indeed, all spheroids gradually reached a stable value that remained, in general, constant throughout the entire experiment despite the nutrient cycling.

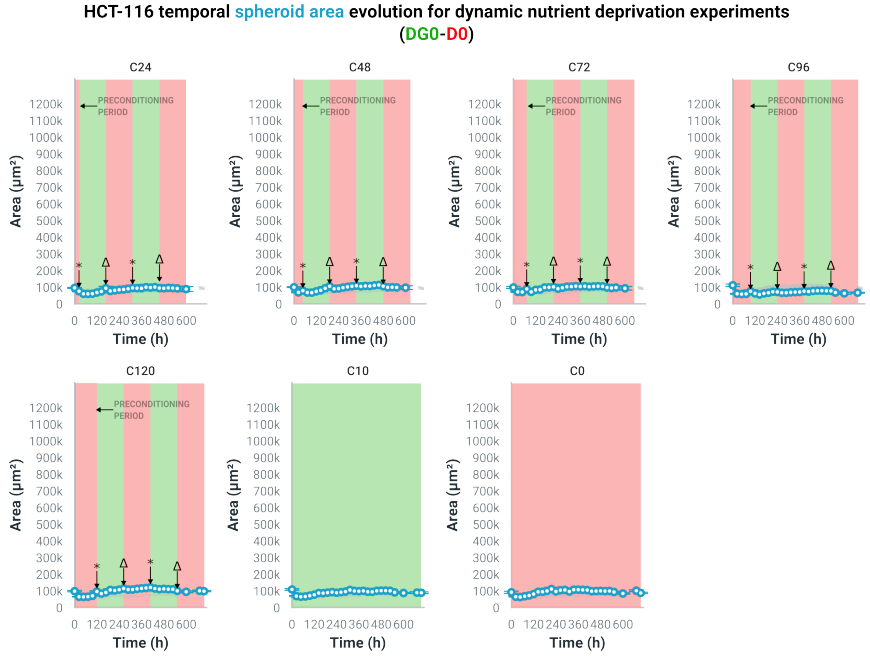

Figure 4-14: Time evolution of the area in every preconditioned group for the DG0-D0 experiment. The horizontal axis of each graph corresponds to the time (in hours) whereas the vertical one coincides with the values of the mean area (in μm^2) of every spheroid group. As explained in the Figure, the shaded area comprises the starvation period of each group. The "$*$" symbol marks the beginning of the phase from D00 to DG0 and the "Δ" one indicates the corresponding beginning of the phase from DG0 to D0. C0: Control group in D0. C10: Control group in DG0.

4.3. The necrotic core of the HCT-116 spheroids is expelled during the deprivation cycles in the "best-to-worst" experiment

In the previous sections, we focused on describing the overall behavior of the spheroid area throughout the different cycles of the tested experiments. In this section, we present the qualitative description of the spheroids emphasizing the obtained results for the HCT-116 cell line in the "best-to-worst" experiment.

During the first cycle in nutrient and growth factors abundance (DG10), all HCT-116 preconditioned spheroids grew and maintained their initial round shape, as seen in Figure **4-15**. Furthermore, approximately 72 hours after the start of each preconditioned group cycle in DG10, a necrotic core started to develop inside the samples. By the end of the cycle, the necrotic core grew along with the spheroids.

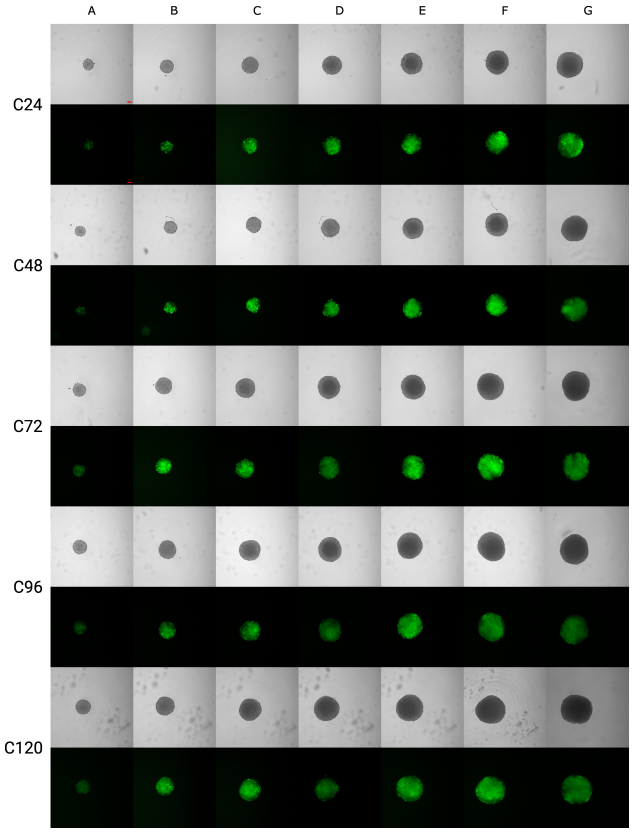

Figure 4-15: HCT-116 spheroid morphology during the first cycle in nutrient abundance. Columns A-G: Time points during the cycle. A: 0 hours. B. 24 hours. C. 48 hours. D. 72 hours. E. 96 hours. F. 120 hours. G. 144 hours. Odd rows: brightfield (BF) pictures of the spheroids. Even rows: fluorescent pictures of the spheroids. Scale bar: 100 µm.

When the preconditioned spheroids started their cycle inside nutrient-deprived medium (D0), they expelled their necrotic core approximately 48 hours after the start of the cycle. This striking phenomenon occurred in all preconditioned groups but never in either the negative or positive controls. Results are shown in Figure **4-16**. Concomitantly with the ejection, the size and shape of the spheroids were greatly altered. Indeed, the spheroids "shrinked" after the event and also deformed, acquiring an ellipsoidal shape that lasted for the remaining days inside the cycle.

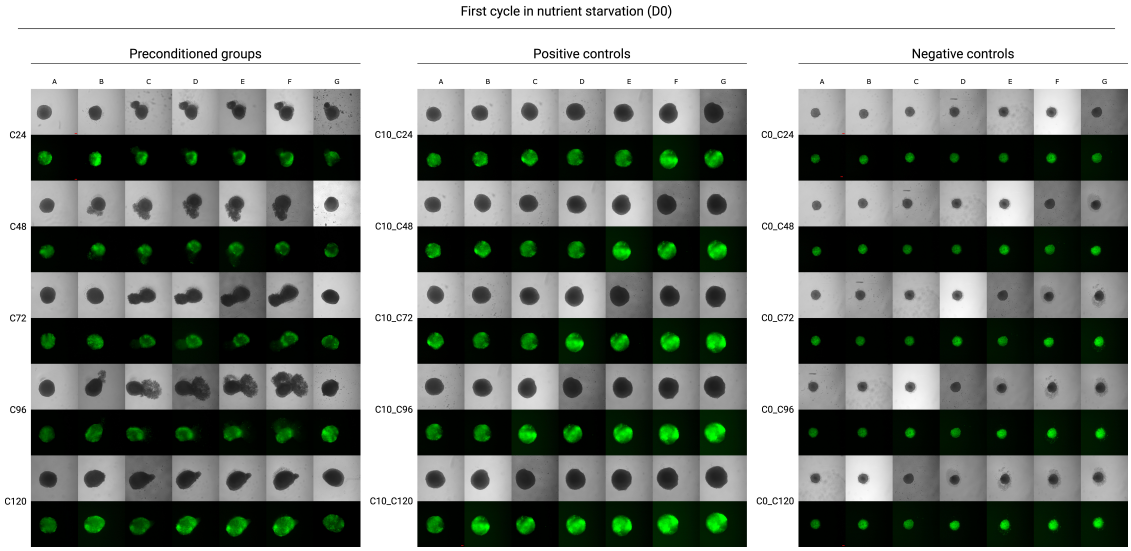

Figure 4-16: HCT-116 Spheroid behavior during the first cycle of starvation. In the case of the preconditioned groups, the necrotic core is identified by the irregular masses coming out the round spheroids. Odd rows: brightfield ((BF) pictures of the spheroids. Even rows: fluorescent pictures of the spheroids. Scale bar: 100 µm.

We then performed conventional Calcein AM/Propidium Iodide (CAM/PI) viability staining on samples of the C24 group before and after the ejection to confirm that the expelled material was indeed dead material. In our case, we only used PI, since cells were transfected with GFP, a protein that can only be expressed by living cells. Figure **4-17** shows the viability staining of preconditioned (C24, top rows in each subfigure) and positive control (bottom rows in each subfigure) spheroids at the beginning of the first cycle in deprived media and 48 hours later. Results (obtained by confocal microscopy) are separated by the fluorescence channel and then presented as an overlay. Specifically, in each subgraph the first column indicates the living cells (GFP, green channel), whereas the second one signals the dead cells (PI, red channel). With the information displayed in Figure **4-17**, we corroborated the ejected mass was mainly comprised of dead cells.

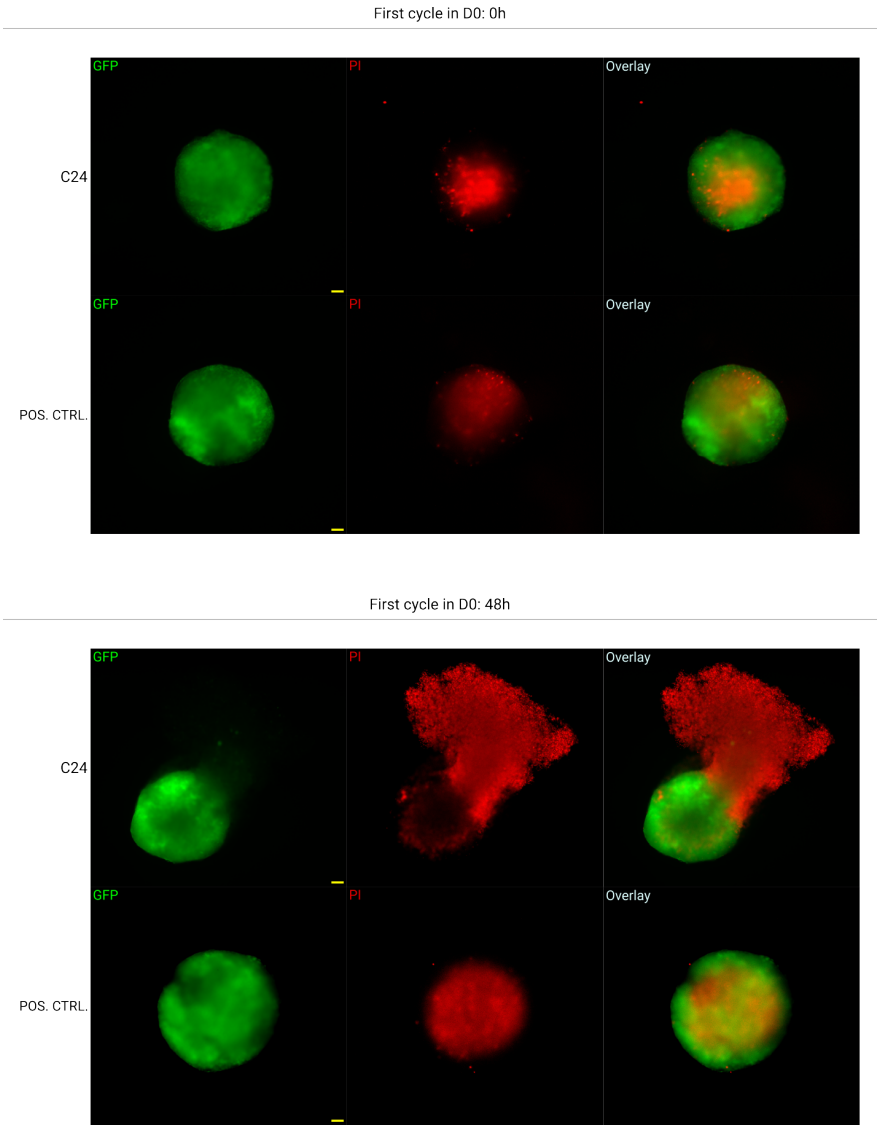

Figure 4-17: Viability assays of preconditioned (C24) spheroids and positive controls in the first cycle of starvation at: 0h (top group of images); and 48 hours (bottom group of images). GFP: Green fluorescent protein (living cells). PI: Propidium iodide (dead cells). Scale bar: 100 µm.

Following this confirmation, we asked whether the ejection also occurred during the second cycle in nutrient starvation. However, as the deprived cycles are separated by one in nutrient abundance, we first analyzed their behavior when the samples returned (for the second time) to nutrient-enriched medium. Interestingly, as seen in Figure **4-18**, spheroids were able to grow again and reacquired their round shape. Furthermore, remnants of the previous core were expelled while a new core was simultaneously formed, as evidenced by the presence of a darkened area at the center of the spheroids.

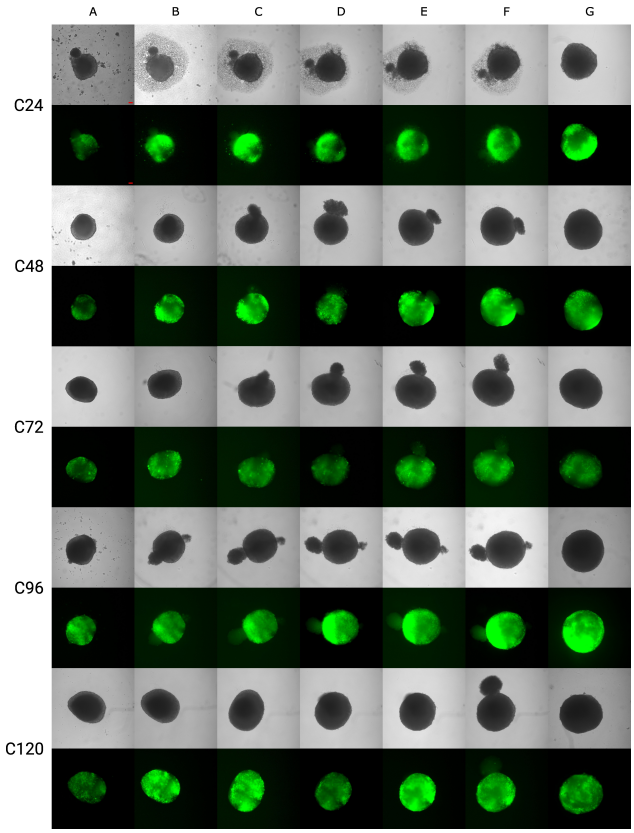

Figure 4-18: HCT-116 spheroid morphology during the second cycle in abundant media. Columns A-G: Time points during the cycle. A: 0 hours. B. 24 hours. C. 48 hours. D. 72 hours. E. 96 hours. F. 120 hours. G. 144 hours. Odd rows: brightfield ((BF)) pictures of the spheroids. Even rows: fluorescent pictures of the spheroids. Scale bar: 100 µm.

Ultimately, upon returning for the second time to nutrient-starved medium, the spheroids lost again their round morphology while also expelling their core. This second ejection was more pronounced than the previous one and was also exclusively circumscribed to the preconditioned groups. Figure **4-19** illustrates the observations.

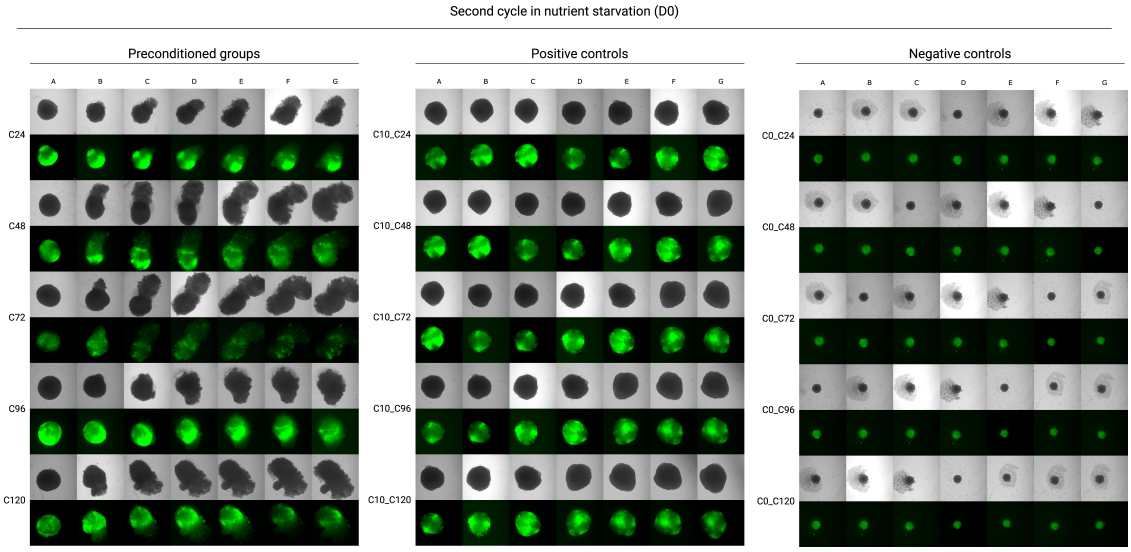

Figure 4-19: HCT-116 Spheroid behavior during the second cycle of starvation. In the case of the preconditioned groups, the necrotic core is identified by the irregular masses coming out the round spheroids. Odd rows: brightfield ((BF)) pictures of the spheroids. Even rows: fluorescent pictures of the spheroids. Scale bar: 100 µm.

4.4. Discussion

Nutrient availability changes due to the increasing demand of malignant cells during the natural progression of colorectal cancer tumors. Under sustained nutrient deprivation, cancer cells are forced to adapt to the harsh conditions by activating or upregulating alternative molecular mechanisms to the canonical pathways to generate the necessary energy to proliferate and survive. Among the numerous nutrients, glucose is a key metabolite for the survival of colorectal cancer cells, as they rely on it to produce energy through the Warburg effect. Therefore, it has been suggested that restricting the availability of glucose can be a standalone treatment option to combat cancer [225–227]. Based on this, *in vitro* studies have studied the effect of glucose restriction, combined with several drugs, on the viability of HCT-116 spheroids under steady conditions. Here, we performed long-term nutrient preconditioning by changing glucose and FBS concentration in four major experiments in two CRC cell lines: HCT-116 and HT-29. In the first experiment, named "best-to-worst", glucose concentration was reduced from 4.5 g/L to 1.0 g/L and FBS concentration was shifted from 10% v/v to 0% v/v. In the second assay, named glucose preconditioning, under a constant concentration of FBS (10% v/v), glucose was reduced from 4.5 g/L to 1.0 g/L. In the

third one, named FBS preconditioning, under constant concentration of glucose (4.5 g/L), FBS was reduced from 10% v/v to 0% v/v. Finally, in the fourth experiment, in absence of FBS (0% v/v), glucose concentration was reduced from 4.5 g/L to 1.0 g/L. This set of experiments allowed us to study the conjoint and individual effects of glucose and FBS in the response of CRC spheroids.

During the initial starvation period, our results for the "best-to-worst" experiment for either HCT-116 or HT-29 spheroids indicated that when the aggregates were left in starved-medium for less or equal than 48 hours, they decreased their size with respect to their original size at the start of the starvation period. This suggests that preconditioning spheroids for short periods of time (less than 48 hours) does not induce an adaptive response in the aggregates probably because this small time-frame is not enough to force the samples to completely change their metabolic pathways to adapt to the new nutrient-deprived environment. This hypothesis seems to be supported by previous works in literature. For instance, Lee et al. [106] demonstrated the sensitizing effects of short-term fasting in combination with chemotherapy treatments in traditional 2D cultures and mice xenografts. To do this, they reduced the concentrations of both glucose and FBS from physiological levels (1.0 g/L glucose and 10% FBS) to starved levels (0.5 g/L glucose and 1% FBS). Immediately following the starvation period (48 hours), the authors added either doxorubicin (DXR), cyclophosphamide (CP), or cisplatin and assessed their effects in the proliferation and gene expression of different cell lines. In the case of the xenografts, the authors reported growth retardation of the tumors during the fasting period. In our case, we reported growth decay of the aggregates during the same time period. However, whether the inability of our preconditioned spheroids to readily adapt to short-termed extreme conditions is caused by the same genetic and molecular mechanisms explained by the authors remains unknown. Thus, further research should be conducted to elucidate the underlying mechanisms controlling the observed growth reduction in our experiments. When the starvation period surpassed 72 hours, the spheroids resumed their growth, significantly increasing the rates with respect to the controls and also to the groups starved for less than 72 hours. This suggests that long periods of starvation induce an adaptive response in the spheroid cells, agreeing with previous findings in 2D cultures of different malignant cancer cell lines starved under similar conditions to those reported herein [105, 107]. In the FBS preconditioning experiment, we observed an even more pronounced decay compared to the "best-to-worst" experiment. This suggests that, in this phase, the lack of FBS plays a major role in the retardation of growth, an idea that is further supported by the accelerated growth observed in the glucose preconditioning experiment, in which FBS was always at a concentration of 10% v/v. This is expected, since FBS includes multiple growth factors in its composition [94, 95, 228].

Upon reintroduction to nutrient-enriched media, the generally enhanced growth rates of the HCT-116 or HT-29 spheroids seen in all preconditioned groups, compared to those of the positive controls in the "best-to-worst" experiment, might be attributed to a synergistic effect of glucose and FBS on cell proliferation. Indeed, apart from the previously mentioned positive effects of FBS on cell growth, previous reports in endometrial cancer cell lines have shown that high glucose

concentration has a stimulating effect in cell proliferation [229, 230]. This synergy appears to be further potentiated by the adaptive response observed in the initial starvation phase. Notably, the growth rates of the groups subjected to starvation periods exceeding 72 hours (C96 and C120) were notoriously higher than those of their counterparts starved for less than 72 hours (C24 and C48). The hypothesis that glucose and FBS exert a synergistic influence on cell proliferation gains additional support from the outcomes of the FBS and glucose preconditioning experiments. These experiments revealed that the individual effects of FBS and glucose also enhanced spheroid growth rates, albeit to a lesser extent compared to the "best-to-worst" scenario. This effect was particularly pronounced in the long-term preconditioned groups (C96 and C120).

During the time in which the preconditioned spheroids were exposed to nutrient-deprived media, their behavior depended on the cell line. For the HCT-116 cell line, during the first cycle in nutrient deprivation, the enhanced growth pattern acquired during the previous cycle in nutrient-enriched media was, in general, lost in all experiments. This was confirmed by the comparison of the growth rates between the preconditioned groups and the controls. Indeed, the growth rates were similar to the controls, indicating that the preconditioned spheroids did not enhance their growth during starved conditions. In turn, during the second cycle in starvation, with the exception of a few cases (C120 group in the "best-to-worst" experiment, and C96 and C120 groups in the glucose preconditioning experiment), the preconditioned groups did not enhance their growth rates compared to the controls. This suggests that, in the vast majority of cases, the adaptation mechanism acquired during the initial preconditioning phase gradually disappeared during the nutrient-abundance cycle, which partly agrees with the findings made by Tsai et al. [108]. In their research, the authors generated pancreatic ductal adenocarcinoma (PDA) cell clones that survived nutrient (both glucose and FBS) starvation. These cells were able to adapt to these extreme conditions while simultaneously improving their oncogenic potential. However, when these cells were reintroduced in nutrient-enriched medium, they gradually reversed to their original non-adapted parental state, losing their resistant abilities. In addition to the above, although the authors did not explicitly compared the growth rates during the different starvation cycles, their results show that, during the first two cycles in this condition, the rates were almost equal. We also observed this phenomenon in our experiments. Therefore, as the authors conclude in their research, it is likely that epigenetic modifications caused by the extreme environmental conditions generated in our experiments also play a major role in the biological response of the preconditioned HCT-116 spheroids. Nevertheless, this should be confirmed in future studies.

Conversely, for the HT-29 cell line, the growth rates of the preconditioned spheroids were consistently higher during the cycles in nutrient starvation with respect to the controls. Furthermore, in the last cycle, the spheroids grew significantly faster than in both the initial starvation phase and the first cycle in nutrient-deprived media. This suggests that the adaptation mechanisms acquired during the preconditioning cycle were not transitory, contrasting with the observed behavior for the HCT-116 cell line. Such mechanisms may include the activation or upregulation of alternative

metabolic pathways, such as the glutaminolysis pathway, to sustain cell function [99, 109, 229].

Finally, we observed that preconditioned HCT-116 spheroids expelled their necrotic core when passed from a rich medium (high glucose and FBS) to a deprived one (low glucose and no FBS). Due to its notoriety, an in-depth analysis of the phenomenon was necessary to unravel the possible mechanisms involved and whether it could occur in other cell lines. However, the results of this analysis will be presented in Chapter 5.

In conclusion, long-term nutrient preconditioning elicited an adaptive response in CRC spheroids that depended on the cell line and the type of preconditioning experiment. In the case of the HCT-116 cell line, only the spheroids preconditioned for more than 96 hours were able to retain the adaptive characteristics throughout the "best-to-worst" or glucose preconditioning experiments. For the HT-29 cell line, results showed that all preconditioned groups retained the adaptive mechanisms during the starvation period, resulting in increased growth even under simultaneous glucose and FBS depletion ("best-to-worst" experiment).

5. The ejection of the necrotic core as a consequence of nutrient imbalance in HCT-116 spheroids

5.1. Introduction

Spheroids and organoids are multicellular aggregates that, during their lifetime, experience multiple morphological events that alter their shape and characteristics. These events include, in the case of organoids, the formation of structures resembling the tissue or organ of origin [231], anomalous structures, such as cysts, that recapitulate pathological scenarios [232], or even swelling as an equivalent of certain pathological scenarios, such as diarrhea [233, 234]. In the case of spheroids, disaggregation [235], swelling [236] or the onset of the necrotic core are also events that modulate the morphology and functionality of these aggregates [237]. Although these changes are highly dependent on the interactions between cells and the extracellular matrix and the presence (or absence) of nutrients and different growth and differentiation factors, the cytoskeleton (CSK) of the cells also plays a major role in determining the overall behavior of the organoids or the spheroids.

The CSK is a complex network of proteins that are suspended inside the cytoplasm of cells with the capacity to self-assemble (and disassemble) in order to support multiple vital process to the cells [238]. These process include cell division [239], intra-cellular transport of organelles [240], force sensing, transmission, and generation [241, 242], adhesion [243–245], cell movement [246, 247], and adaptation and maintenance of cell shape [248]. These functions are carried out by the three main proteins composing the CSK: actin filaments, intermediate filaments, and microtubules [247] (Figure **5-1**).

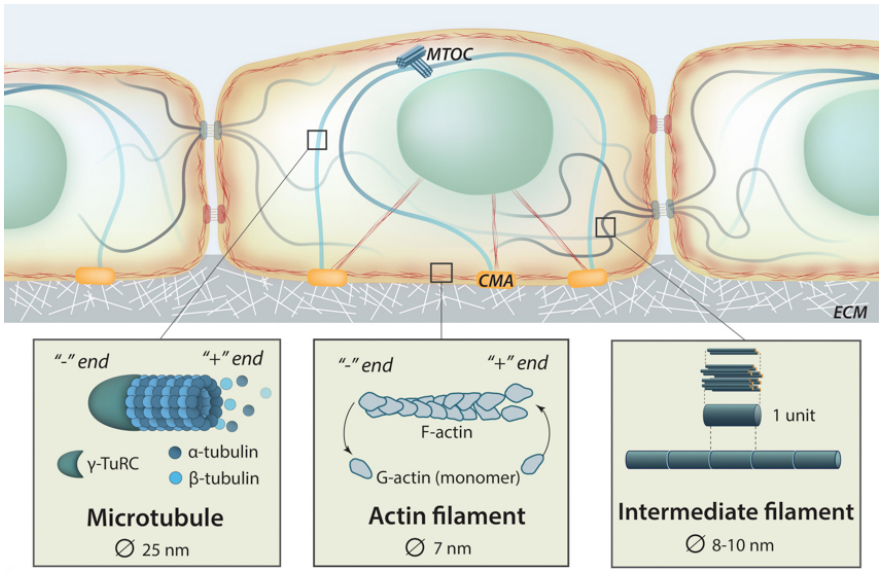

Figure 5-1: Graphic depiction of the major components of the CSK. MTOC: Microtubule organizing center. CMA: Cell-matrix adhesion. Taken from [249].

These three proteins have different chemical compositions and mechanical behavior, and are involved in the different cell processes mentioned above [238]. Thus, intermediate filaments (IF) are the softest of the three proteins [238], and help anchor organelles within the cytoplasm to facilitate their movement inside it [250]. IF also contribute in the adhesion of cells to the ECM [250]. Microtubules are the stiffest of the three proteins [238], and play a central role in cell division, as they form the mitotic spindle [251]. Finally, actin filaments are approximately an order of magnitude stiffer than the intermediate filaments, but they are softer than the microtubules [238]. These filaments are involved in a plethora of processes, which include cell movement, contraction, force transmission, and the maintenance of cell shape and mechanical support [252–254].

Actin is an abundant protein in all types of eukaryotic cells, accounting for 5 to 10% of total protein content in the cell [252]. Each molecule, or monomer, has a globular form (called G-actin) that, when assembled, forms the filamentous form of the protein (F-actin) [252]. During assembly, all the monomers are oriented in the same direction, conferring the filaments a unique polarity that plays a crucial role in the sliding of myosin along the actin filament during cell contraction [252]. The assembly and disassembly of actin filaments are dynamic reversible processes that occur in presence of ATP [252]. Indeed, G-actin monomers first bind to ATP and, with the aid of a regulatory protein called profilin, are assembled at one of the ends of the filament (the "+" end). Once assembled, ATP is converted to ADP. After this conversion, G-actin monomers, which are now bound to ADP, can be detached from the filament by another regulatory protein, called cofilin. ADP-bound G-actin monomers constitute the "-" end of the actin filament.

Actin filaments and myosin are both required to produce the contraction cells (Figure **5-2**) [255–258]. Myosin is a large protein that consists of two identical chains coiled around each other in a helical fashion [258, 259]. These are called the heavy chains. The ends of each heavy chain are conformed by two globular regions, called the globular head regions. The protein is completed by two small chains, called the light chains, surrounding the region between the globular head regions and the rest of the heavy chain [258]. Before contraction, the heads of the heavy chains are bound to a molecule of ADP and one of phosphate [253, 258, 260].

When the signal to contract is given, the globular heads release the phosphate and bind to the actin filament at specific sites. Then, they release the ADP molecule and, with the energy stored from the previous contraction, both the heads and the filament glide a small distance in the direction of the + end of the filament. During the gliding, the ADP molecule is released. The gliding continues until a new molecule of ATP binds to the head of myosin. Once this happens, the gliding stops, the heads are detached from the actin filament, and the ATP is converted into a molecule of ADP and one of phosphate. The energy created by this conversion is stored and used in the next contraction. Due to the importance of ATP in this process, its supply must be continuous [253, 258, 260].

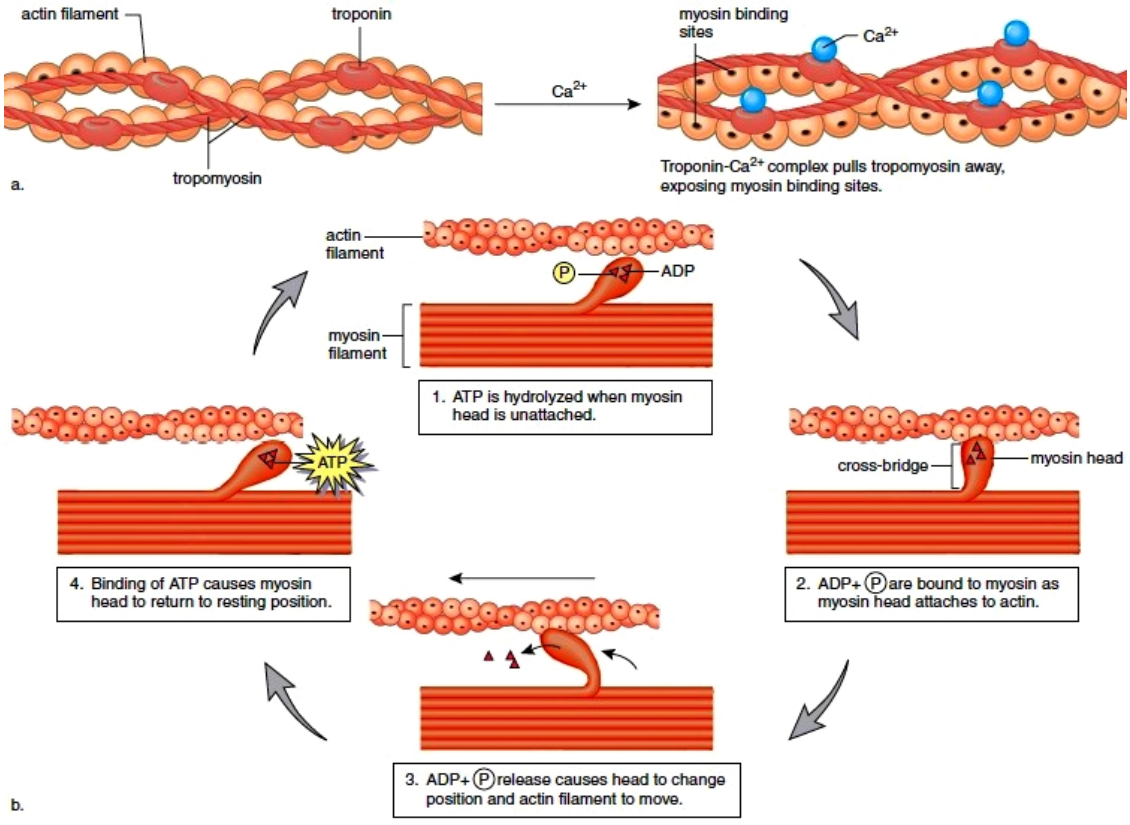

Figure 5-2: Graphic depiction of the acto-myosin contraction. Taken from [261].

Actin filaments can also assemble to form two general structures, called actin bundles (structures with parallel actin filaments) and actin networks (flexible meshworks with perpendicular filaments) [252]. The actin networks are connected to the cell membrane through a series of proteins that allow the communication of cells with the extracellular matrix and also with other neighboring cells. This is crucial in epithelial cells, such as those of the colon, since mechanical forces are transmitted from the actin network of one cell to another via the adherens junctions (Figure **5-3**) [262, 263]. Adherens junctions are a type of cell-cell junctions that are formed when a group of transmembrane proteins of one cell, called cadherins, form a bond with the cadherins of another adjacent cell [252, 256, 262, 264].

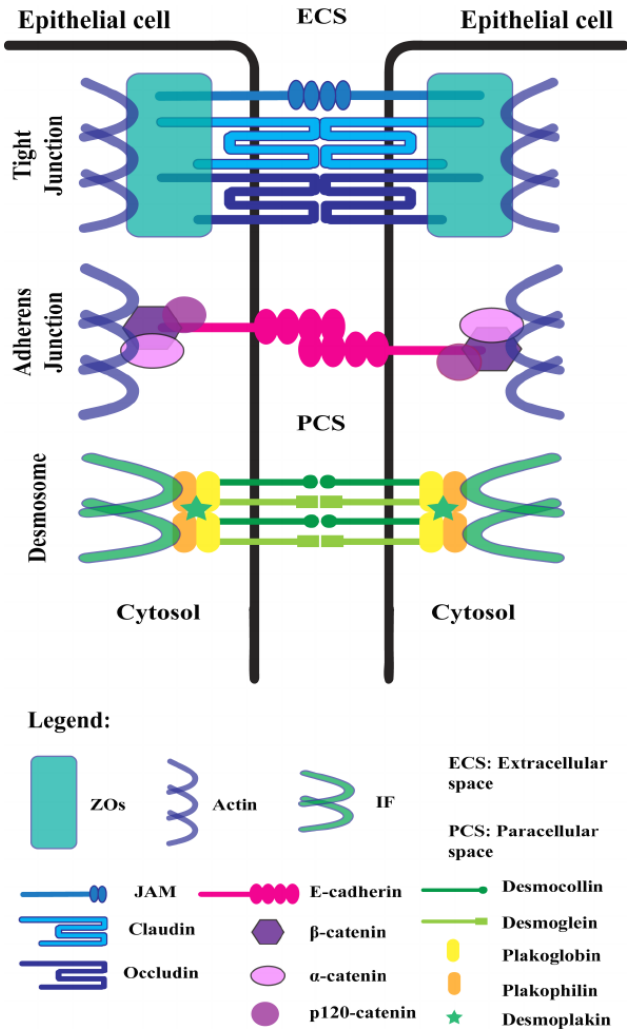

Figure 5-3: Adherens junctions and the major types of intercellular unions. Taken from [265].

When this bond forms, which only occurs in the presence of Ca^{2+}, inside the cytoplasm of both cells a series of proteins called catenins are recruited to stabilize the junction [262]. Catenins bind to both the cytoplasmic end of the cadherins and the actin filaments that are also recruited to the union site [68]. Once stabilized, the junctions form a continuous structure resembling a belt (called adhesion belt) around each cell of the epithelium [266, 267]. This belt (Figure **5-4**) is in charge of transmitting mechanical forces from one cell to another and is required to maintain the structural integrity of the epithelium [268].

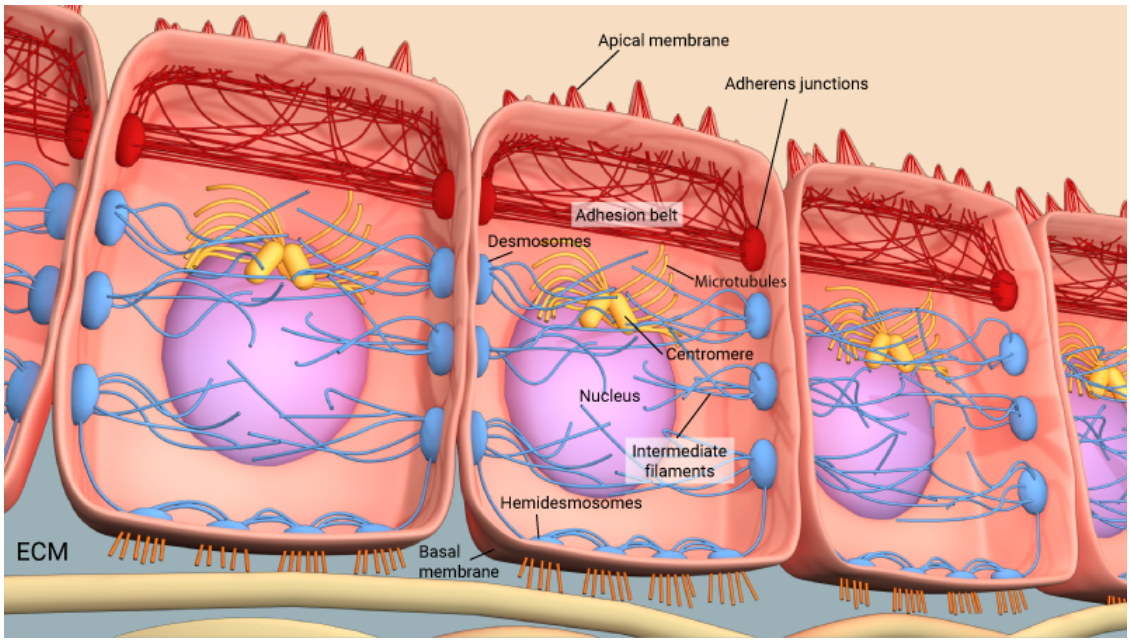

Figure 5-4: Graphic depiction of the adhesion belt and its relationship with the adherens junctions. Taken from [269].

In addition to the multiple responses at the cell level, mechanical forces are also directly involved in the final shapes that several tissues acquire during their morphogenesis. For instance, Pérez-González et al. [270] demonstrated that the resulting shape of the intestinal epithelium is the result of the coordination of the forces present in the different morphological zones in the epithelium (stem cell niche, transient amplifying zone, and villus). For this, based on organoid-derived crypts extended over functionalized PAA surfaces, the authors identified zones comparable to these morphological compartments and measured the forces exerted by the cells (in each compartment) over the substrate. They identified that the stem cell niche tended to push downwards the substrate, whereas the transit-amplifying zone tended to push it upwards but also dragged it inwards.

Finally, the villus-like domain dragged the substrate outwards. Furthermore, they were also able to discern, based on the actin and myosin distribution among the cultures, that the crypt folding is generated by the apical constriction of this compartment, which agreed with the force patterns described above.

In cancer, cell mechanics has also been studied mainly in order to understand its relation with cell invasion and metastasis [59, 271–273]. For instance, Nyberg et al. evaluated the stiffness, fluidity, and four additional parameters of single cells from different cancer cell lines (pancreatic, breast, and ovarian) [274]. By using a microfluidic device in which cells passed from a chamber to another through a constrained channel, the authors were able to predict the invading potential of the different cell types. In turn, Kim et al. studied the morphological and migrating response of breast cancer cells in collagen matrices with different degrees of fiber alignment [275]. For this, they created a vortex flow inside an unpolymerized hydrogel solution by rotating an iron particle inside a magnetic field during the gelation process of the solution. Once polymerized, in a radius of approximately 1mm around the iron bead, collagen fibers were circumferentially aligned. The alignment was lost as the radius from the bead increased. Then, with these hydrogels, the authors quantitatively analyzed the morphology of breast cancer cells and found that, in aligned fibers, cells exhibited an elongated morphology and moved preferentially in the direction of the fibers. Other studies have also studied the change of the mechanical properties of single cells due to the effect of various therapeutic drugs [273].

In the previous chapter, we discovered that, in some experiments, HCT-116 spheroids expelled their necrotic cores during the cycles in deprived media. Due to its striking notoriety, and its possible clinical implications, we decided to further study the underlying mechanisms that enable the spheroids of this particular cell line to eject their inner content to the exterior. For this, we formulated two main hypotheses. We first proposed the ejection was caused by a massive swelling of the samples stemming from an osmotic gradient. We also formulated a second hypothesis in which the ejection of the necrotic core was due to the simultaneous weakening in the contractile activity of the CSK and the expansion of the necrotic zone. In this hypothesis, cells inside the spheroids form contractile ring-shaped layers that not only confine but also compress the continuously growing necrotic core. In normal conditions, the contractile activity of the cells is supported by the abundance of nutrients, especially in the form of ATP, that allow cells to form and maintain stable cell-cell interactions and exert their contractile forces among them. This is especially true for cells such as those of the HCT-116 cell line, which require high amounts of ATP to sustain their basic functions in comparison to the HT-29 cell line [276]. However, once this nutrient supply is removed by the passing of the spheroids to nutrient-deprived media, the imbalance in nutrients forces the cells to enter in a survival-like state, ultimately disrupting their normal contractile activity and weakening the pressure on the necrotic core.

The weakening would cause the decompression of the necrotic core. Concomitantly, the core would expand, generating an isotropic deformation of the spheroid (global swelling) until it encounters a weakened zone in the rings of cells. Afterwards, the deformation would continue locally, promoting a localized swelling around this weakened zone and, consequently, its rupture and the expulsion of the material from the inside of the spheroids.

We first evaluated the validity of the first hypothesis. Then, we asked whether the ejection of the necrotic core could also occur with other cell lines. Following this, we checked whether this phenomenon could also occur inside collagen matrices. Then, we revisited the experiments described in the last chapter in order to identify the (most likely) biochemical factor responsible for the ejection of the necrotic core. Afterwards, we checked the distribution and shape of the cells inside spheroids to answer whether the contractile rings were indeed present and whether cell distribution remained constant throughout the experiments. Finally, we asked whether we could prevent the phenomenon by blocking the contractile activity of the cells with two different molecules: Y-27632 and Blebbistatin. Y-27632 is an inhibitor of the Rho-associated, coiled-coil containing protein kinase (ROCK). This pathway is involved in the formation of the actin filaments. It selectively binds to two isoforms of ROCK (ROCK1 and ROCK2 [277]) and has been widely used for enhancing the survival of human embryonic stem cells (ES) by preventing dissociation-induced apoptosis (anoikis) [278]. In turn, Blebbistatin is a specific inhibitor of myosin II. This molecule binds in the myosin II chain to the anchoring site of the actin, thus keeping myosin in an actin-detached state [279–281]. Blebbistatin has been widely used in cardiac optical mapping, a fluorescent imaging method to study the electrical behavior and calcium handling in the heart [282]. However, it has also been increasingly studied in cancer [283, 284].

In order to prove the effects of Y-27632 or Blebbistatin on the HCT-116 spheroids, we repeated the "best-to-worst" (DG10-D0) preconditioning experiment with the C24 preconditioned group. In addition, we performed the experiments until the end of the first cycle in D0. The addition schemes and concentrations used for both molecules are found in chapter 2 of this dissertation.

5.2. Results

5.2.1. The ejection of the necrotic core is not a universal event

After observing the ejection of the necrotic core in the HCT-116 spheroids, we asked whether this phenomenon could also happen in other cell lines. Therefore, in order to do this, we repeated the "best-to-worst" (DG10-D0) preconditioning experiment with two glioblastoma cell lines (U-87 MG and U-251 MG), one neuroblastoma (SH-SY5Y), and one more colorectal cell line (HT-29). With respect to the initial number of cells seeded to generate the HCT-116 spheroids, we performed preliminary tests (results not shown) to determine an adequate number of cells that would facilitate the manipulation of the samples, resulting in a number of 1000 cells. We then used this number to generate spheroids for the other tested cell lines (HT-29, U-87 MG, U-251 MG, and SH-SY5Y). However, after observing the behavior of the spheroids of these cell lines, we decided to modify the number of cells for the U-87 MG and the SH-SY5Y aggregates. In the case of the former, we increased the number to 5000 to ensure a proper formation of the necrotic core. For the SH-SY5Y line, we increased the number to 20000 initial cells to ensure the formation of the spheroids.

At the beginning of the first cycle in D0, the spheroids of U-87 MG and HT-29 cell lines were the only ones that had a necrotic core, since the spheroids of the other two cell lines were too small to develop one. In the following days, the evolution of the necrotic core did not exhibit visible changes in any of the cell lines or preconditioned groups. In fact, none of the preconditioned spheroids of the aforementioned cell lines expelled their necrotic core (Figure **5-5**).

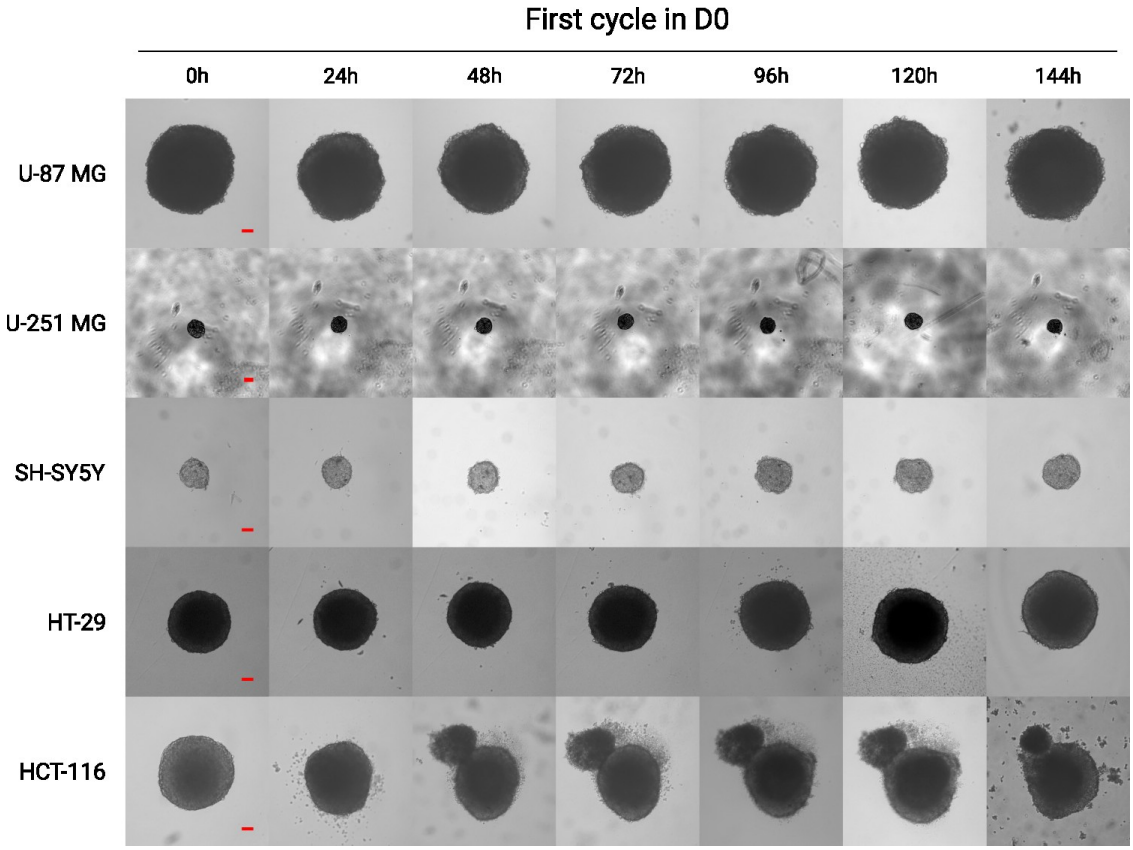

Figure 5-5: Time evolution of the spheroids of the mentioned cell lines during the first cycle in D0. All samples belong to the C24 preconditioned group. Scale bars: 100 µm.

We then continued the preconditioning experiment to see whether the spheroids were able to eject their core in the second cycle in D0, since in the HCT-116 case, the spheroids also expelled it in this cycle. We interrupted the experiment for the U-251 MG cell line because the spheroids did not grow and, consequently, did not form a necrotic core.

Results of the spheroid evolution are shown in Figure **5-6**. During this cycle, the spheroids of the SH-SY5Y cell line developed a small necrotic core at their center, while the samples of the U-87 MG and HT-29 cell lines maintained their core. However, the spheroids did not eject their core in any of the preconditioned groups.

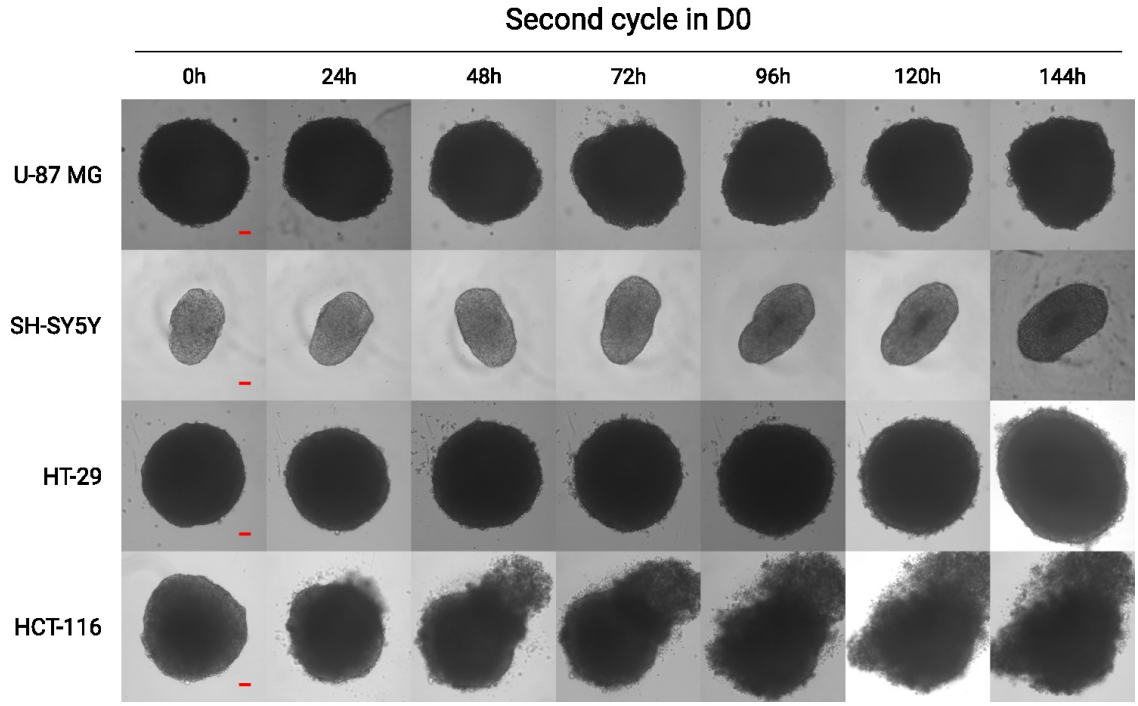

Figure 5-6: Time evolution of the spheroids of the mentioned cell lines during the second cycle in D0. All samples belong to the C24 preconditioned group. Scale bars: 100 µm.

Based on these findings, we concluded that, at least for this kind of preconditioning, the ejection of the necrotic core was not a universal event.

5.2.2. The ejection of the core is not caused by swelling of the spheroids

As we stated at the end of the introduction, we first hypothesized that the ejection was caused by a difference in osmotic pressure inside the spheroids. This gradient would favor the influx of media inside the spheroids, causing their swelling and, ultimately, their rupture and ejection of the content. Indeed, as seen in Figure **5-7**, during the moments prior to the ejection, the spheroids seemed to swell.

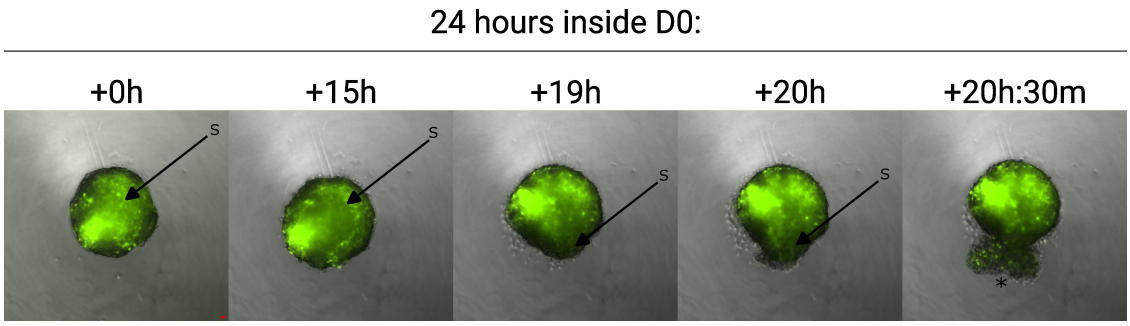

Figure 5-7: Time series of the formation of the localized swelling (identified by the "S" letter) inside the HCT-116 spheroids that led to the rupture and ejection of the necrotic core. The "*" symbol indicates the ejected necrotic core. Scale bar: 100 μm.

However, the swelling that started as a uniform event inside the spheroid, ended as a focalized event. In addition, if an osmotic gradient were present, the ejection would also be present in spheroids from other cell lines (such as those made of HT-29 cells) or even in the positive controls. Yet, that did not happen either. Thus, we decided to abandon this first hypothesis and focus on the second one.

5.2.3. The ejection of the necrotic core has variable behavior inside collagen matrices

Since the necrotic core ejection occurred during the first 48 hours of the first cycle in D0 in the spheroids suspended in nutrient-deprived media, we asked whether the same phenomenon happened during the same time points when the spheroids were "sandwiched" inside two layers of collagen hydrogel (equivalent to the constrained 2D experiment in Chapter 3) and subjected under the preconditioning experiments. The obtained results revealed that, despite developing a large necrotic core, none of the samples within any preconditioning groups expelled it during this cycle (Figure **5-8**).

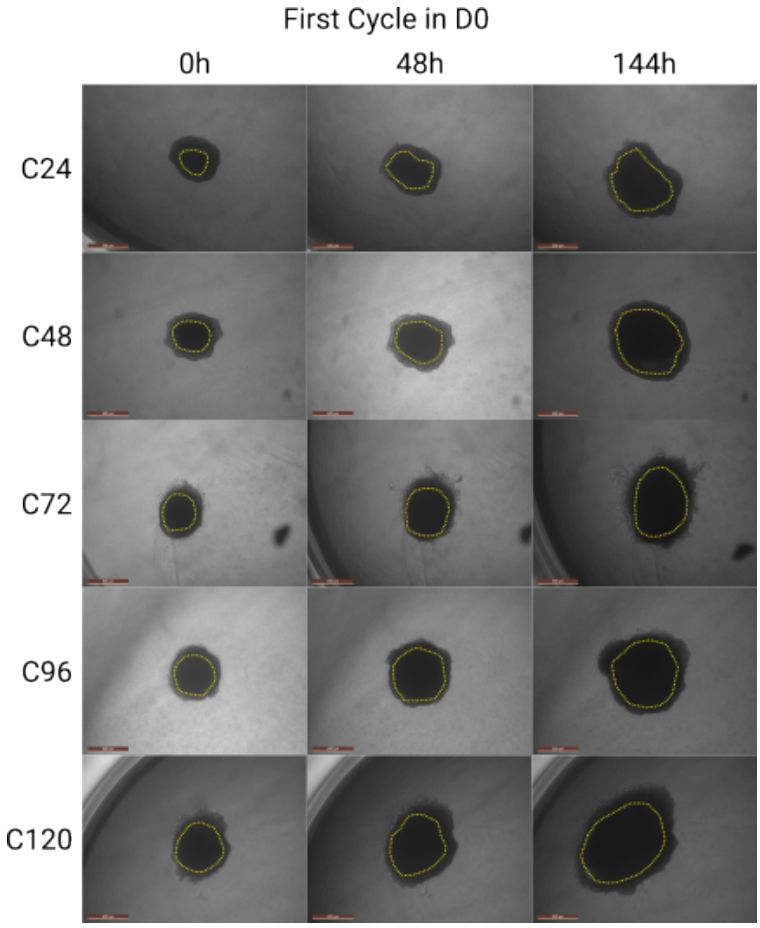

Figure 5-8: Spheroid behavior during the first cycle in D0. Dotted yellow lines indicate the necrotic core of the spheroids. Scale bar: 500 µm.

Based on the above, we asked whether the core was expelled during the remaining the cycles. Therefore, we continued the preconditioning experiments and found that a proportion of the samples within the C24, C72, C96, and C120 preconditioned groups, ranging from one-third to half, ejected their core. The ejection was confirmed by the onset of necrotic material on top of previously clean zones as well as by the lack of fluorescent signal. An example of the ejection is shown in Figure **5-9**. As seen in the Figure, the necrotic material (identified by the pink "$*$" symbol) started emerging from the main mass, in a similar manner as in the suspension cases, until it spread all over the captured field.

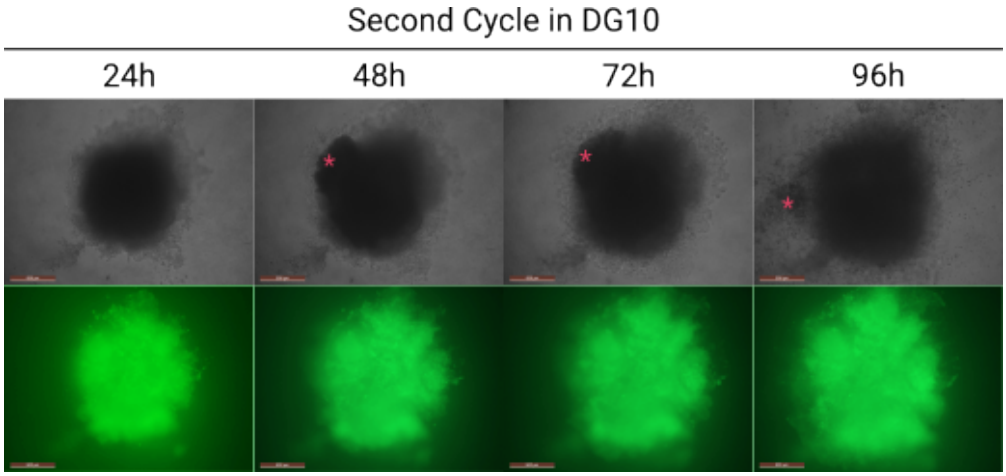

Figure 5-9: Spheroid behavior during the second cycle in DG10. Scale bar: 500 µm.

5.2.4. Glucose is a major factor for the ejection of the necrotic core

As stated at the introduction of this chapter, we asked which of the two main components of our preconditioning experiments (glucose or FBS) was a major contributor to the ejection of the necrotic core. To investigate this, we revisited the experiments where the concentration of either glucose or FBS varied while maintaining constant the concentration of the other factor.

5.2.4.1. Changes in the concentration of FBS under constant levels of glucose

Constant concentration of glucose (4.5 g/L): FBS preconditioning experiment (DG10-DG0)

In the previous chapter, we demonstrated that, during the first cycle in DG0, the samples in every preconditioned group in the FBS experiment had a similar growth behavior to that of the preconditioned groups during the first cycle in D0 in the "best-to-worst" preconditioning experiment. However, in stark contrast to the latter, the preconditioned groups in the first cycle of DG0 did not eject their necrotic core in any time point during the cycle (left panel in Figure **5-10**).

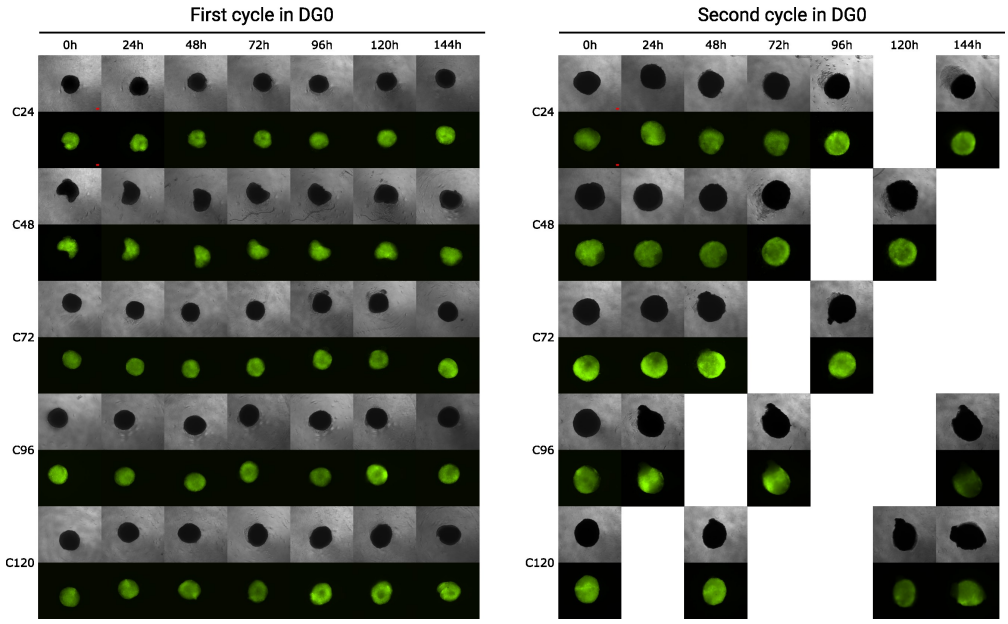

Figure 5-10: Representative example of the HCT preconditioned groups in the DG10-DG0 experiment. Scale bar: 100 µm.

During the second time in DG10, the spheroids did not eject their necrotic core, which was expected. Finally, we also checked whether the spheroids in the preconditioned groups ejected their necrotic core during the second cycle in DG0, since the preconditioned groups in the DG10-D0 experiment also ejected their core during the second cycle in D0. As seen in the right panel in Figure **5-10**, the C72, C96, and C120 preconditioned groups did eject their necrotic core in the second cycle in DG0; however, in comparison to the DG10-D0, the ejected fraction was visibly smaller. This prompted us to discard the FBS as a decisive factor for the ejection of the necrotic core.

5.2.4.2. Changes in the concentration of glucose under constant levels of FBS

Constant concentration of FBS (10% v/v): glucose preconditioning experiment (DG10-D10)

When we conducted the preconditioning experiments by varying the glucose concentration in presence of FBS, we noted that the mean area of the preconditioned spheroids had non-linear behavior, especially during the cycles in D10. In addition to this, we also observed that the negative controls also experienced drastic changes in their mean area. In both cases, the changes in area were inevitably related to the ejection of the necrotic content.

During the first cycle in D10, all preconditioning groups expelled their necrotic core during the first 48 hours of the start of the cycle in D10, as those in the DG10-D0 experiment during the first cycle in D0. However, the ejections in the DG10-D10 experiments were, in general, more pronounced than in the DG10-D0 experiments, as seen in Figure **5-11**.

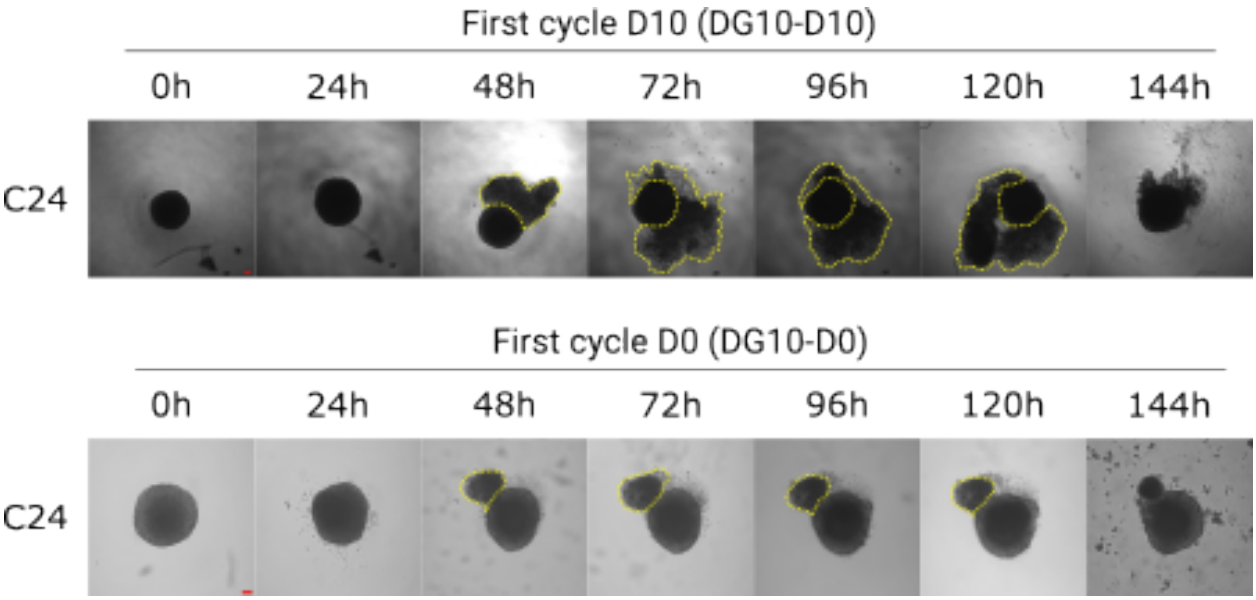

Figure 5-11: HCT-116 C24 preconditioned spheroids behavior under the first cycle in D10 (top row) and D0 (bottom row). Scale bars: 100 µm. The yellow dotted lines denote the area of the necrotic core ejected from the spheroid.

When analyzing the shape of the necrotic core in the BF images prior the ejection, we observed that, during the first cycle in D10, all samples in every preconditioned group had a well-defined round necrotic core that was concentric to the spheroid. This particular morphology was evident 24 hours after the beginning of the cycle and occupied 67.0±2.9% of the total area of the spheroid and had an average roundness of 96.2±3.6%. By contrast, during the same time point in the DG10-D0 experiments, the samples had a blurred necrotic zone with an average occupied area of 48.5±9.3%. The left panel in Figure **5-12** shows a representative example of a spheroid in the C24 preconditioned group 24 hours after the beginning of the cycle in D10, while the right panel shows an example of the same group 24 after the start of the first cycle in D0.

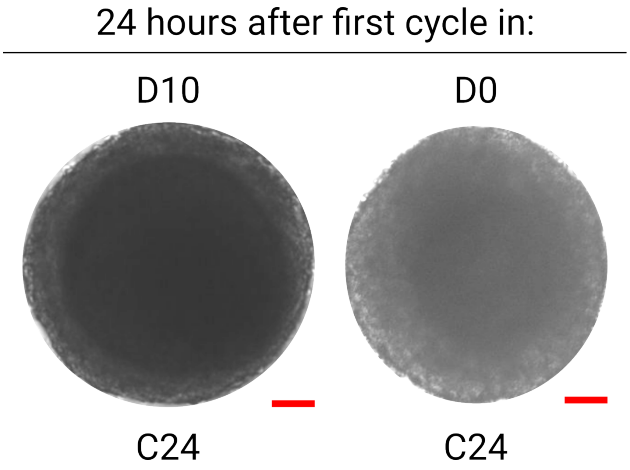

Figure 5-12: Comparison of the shape of the necrotic core for the glucose (DG10-D10, left panel) and "best-to-worst" (DG10-D0, right panel) preconditioning experiments. Scale bars: 100 µm.

During the second cycle in D10, all samples of the preconditioned groups ejected again their necrotic core in a similar fashion as in the first cycle. Interestingly, the occupied area of the necrotic core diminished (38.2±13.5%) and its shape became less round (85.8±12.8%).

Regarding the negative controls (spheroids in D10), we noticed that they also formed a well-defined necrotic core, with similar values of occupied area and shape to the preconditioned groups in the first cycle in D10. Nevertheless, the negative controls expelled their necrotic core as early as 120 hours after the start of the experiment. After these early ejections, the negative controls experienced repeated cycles of reformation and expulsion of the core that ultimately led to the creation of new small spheroids around the main mass (Figure **5-13**) that resembled the tumor buddings typically seen in histological sections of CRC patients [285–287].

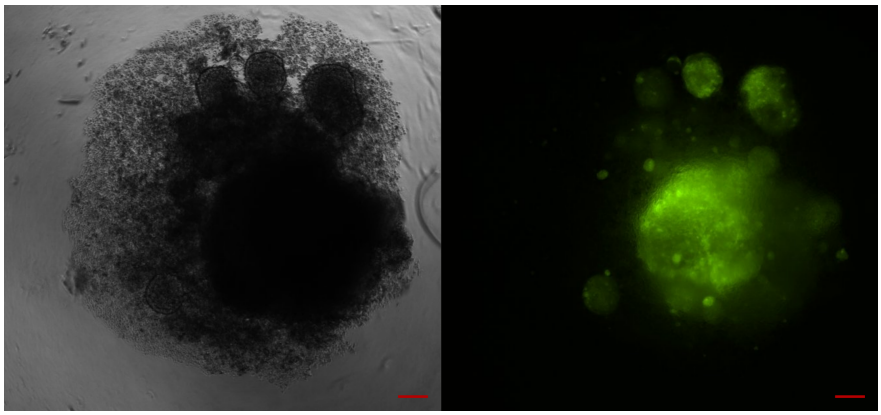

Figure 5-13: Representative example of the HCT negative controls in the glucose preconditioning experiment (DG10-D10). Picture was taken at the end of the experiment (696 hours). Scale bar: 100 µm.

5.2.5. The ejection of the necrotic core is a mechanical effect regulated by the contractile activity of the cells

5.2.5.1. Cells inside HCT-116 spheroids have elongated shapes and form concentric rings round the core

Since the CSK plays a major role in the second hypothesis that we formulated at the end of the introduction, we wanted to analyze the distribution and shape of the cells inside the spheroid and the arrangement of the CSK in these cells. To do this, we first performed TEM microscopy on sections of the spheroids. Figure **5-14** shows representative examples of semi-thin (stained with toluidine blue, left panel) and TEM micrographs of ultra-thin cuts (right panel) of two distinct zones in the semi-thin cuts.

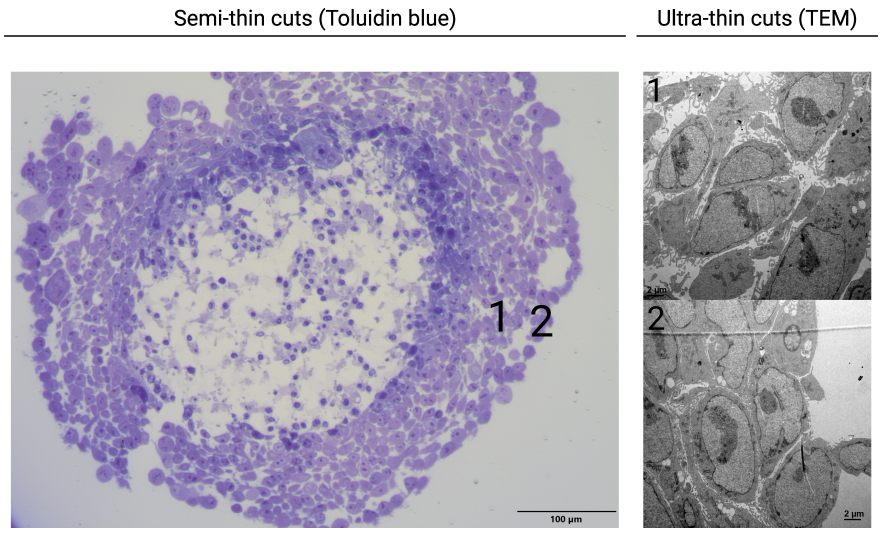

Figure 5-14: Representative images of semi-thin and ultra-thin cuts of positive control of HCT-116 spheroids in the glucose preconditioning experiment. Scale bar for the semi-thin cuts: 100 µm. Scale bar for the ultra-thin cuts: 2 µm.

Based on Figure **5-14**, we identified two distinct cell morphologies. In the first one, cells were elongated and stacked on top of each other in a circumferential pattern, with a mean roundness of 0.4 ± 0.2. These cells (identified by the label 1 in the left panel in Figure **5-14**) were always located in the inner layers of the spheroid, between the periphery of the spheroid and the center. The second morphology (identified by the label 2 in the left panel in Figure **5-14**) corresponded to cells at the periphery and surrounding the center of the spheroid. In those layers, cells were more round, with a mean roundness of 0.7 ± 0.2. In addition to this, we also observed that the nucleus of these cells tended to follow the same overall shape of the cells, regardless of their location.

Following this initial exploration of the cell distribution inside the spheroids, we asked whether cells remained in the same configuration or, by contrast, they rearranged their morphology throughout the "best-to-worst" experiment. Specifically, we asked whether the passing from DG10 to D0 could induce morphological changes in the cells comprising the spheroids. For this, we analyzed the histological sections of the positive controls and preconditioned groups of HCT-116 and HT-29 spheroids at five time points, corresponding with key moments in the preconditioning experiment: 24 hours before the passing from the cycle in DG10 to D0 (144 hours in the general timeline of the experiment), the day of passing (168 hours), approximately 12 hours after passing (180 or 183 hours), 48 hours after passing (216 hours), which corresponds to the ejection in the case of the HCT-116 cell line, and the following 24 hours (240 hours). Figure **5-15** shows the evolution of cell distribution inside HCT-116 spheroids.

Initial qualitative morphological analysis of the sections of Figure **5-15** revealed that the organization and morphology of cells, as well as the necrotic core evolution, exhibited time-dependent behavior. At 144 hours, both positive control and preconditioned spheroids had high cell density towards their inner zones. At the center of the sections, cells tended to arrange themselves in a swirling spiral pattern, while at the outer zones, they tended to arrange circumferentially around the spiral. At 168 hours, cell density at the center was not as high as in the previous hour (144), suggesting that cells were dying. Interestingly, the orientation of cells experienced a major shift, as cells in both controls and preconditioned groups seemingly orientated in a vertical direction. Towards the periphery of the samples, however, cells remained orientated in a circumferential manner. At 183 hours, the center of the preconditioned sample was almost devoid of cells, indicating the presence of a large necrotic core. Additionally, distinct rings of circumferentially oriented cells were easily observed. In the positive controls, the necrotic zone was also visible at the center of the section, but it was not as delimited as in the preconditioned group. Furthermore, the rings of circumferential cells was not as defined, although they could still be appreciated. At 216 hours, almost the entire area of the section of the preconditioned spheroid was empty, whereas in the positive control, only the center was emptier than the periphery. Last, at 240 hours, the available sections showed that cell density towards the periphery in the preconditioned group was seemingly higher than the corresponding zone in the positive control.

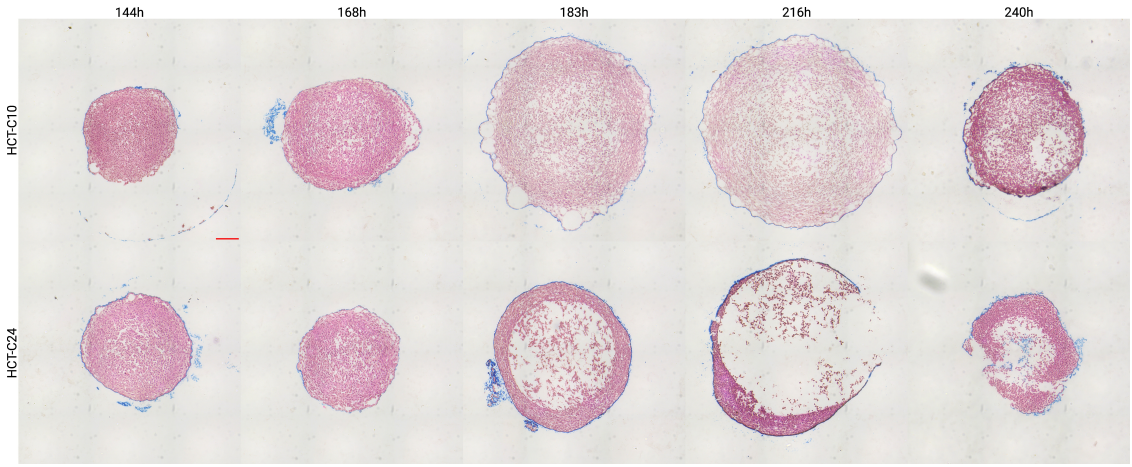

Figure 5-15: Representative Hematoxylin-Eosin (H&E) images of parafin-embedded sections of HCT-116 spheroids in the "best-to-worst" experiment. Scale bar: 100 µm.

We then performed morphometric analysis on the roundness of selected cells in each section of Figure **5-15**. For this, prior to merging the tiles to reconstruct the entire histological section, we randomly selected 5 to 6 cells per tile. Repeated selections were discarded, leaving one unique selection per tile. For the 144^{th} and 168^{th} hours, we selected samples in all the tiles; however, from the 183th hour onwards, we did not perform any selection in the tiles corresponding to the center of the spheroids, as the cells inside it were remnants of the necrotic core. A representative example of the selection on the merged tiles is shown in Figure **5-16** (the selection in all sections is shown in Appendix Figure **B-7**). Results show that, at 144 hours, cells in both positive and C24 preconditioned groups had two predominant shapes. At the periphery of the sections, cells had round morphologies, with mean roundness factor of 0.82±0.08 for the positive controls and 0.82±0.09 for the C24 preconditioned group (p-value: 0.464574). In turn, at the inner layers, cells had elongated shapes, with roundness factor of 0.36±0.09 for the positive controls and 0.31±0.11 for the C24 group (p-value: 0.0068). At 168 hours, cells in both sections also had the same distinct morphologies as in the previous case. At the periphery, roundness for the positive control and C24 group was slightly lower, with respective values of 0.77±0.12 and 0.81±0.10 (p-value: 0.1433). At the inner layers, the elongated cells had roundness values of 0.37±0.12 for the positive control, and 0.29±0.07 for the C24 group (p-value: 0.0008). At 183 hours, cells in both groups lost their round morphology and became elongated in all zones of the spheroids, with mean roundness values of 0.33±0.11 for the positive controls, and 0.31±0.08 for the preconditioned group (p-value: 0.3805). At the day of the ejection (216 hours), we observed that cells in the ring of concentric cells in the C24 preconditioned group became drastically thinner towards the rupture zone (right part of the section) whereas in the positive control, cell distribution did not experience this change. Interestingly, cells in the preconditioned group were less elongated (0.39±0.09) than the ones in the positive control (0.30±0.09), a statistical relevant result (p-value: 0.0001).

Finally, in the last time point (240 hours), cells in the preconditioned group became rounder, with a roundness value of 0.79±0.10, while in the positive controls, cells remained elongated (0.41±0.10). This, again, was a statistically relevant finding (p-value less than 0.0001).

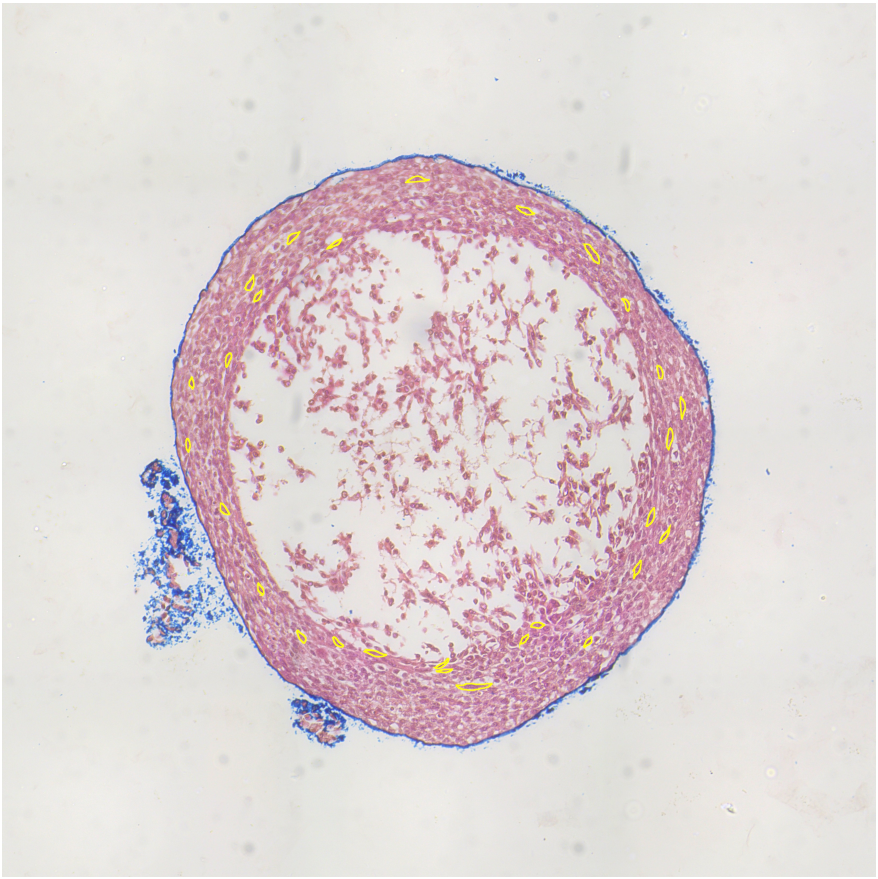

Figure 5-16: Example of cell selection for measuring roundness in the H&E sections of HCT-116 and HT-29 spheroids. Scale bar: 100 µm.

With respect to the HT-29 spheroids, results showed that, overall, cells inside the spheroids in both the positive control and C24 preconditioned groups (**5-17**) remained essentially round throughout the experiment. At 144 hours, the roundness values for the positive control and C24 group were, respectively, 0.82±0.08 and 0.81±0.08 (p-value: 0.5925).

At 168 hours, the values were 0.79±0.09 for the positive control, and 0.79±0.10 for the preconditioned group (p-value: 0.9744). At 180 hours, the roundness values increased to 0.83±0.08 (positive control) and 0.80±0.11 (preconditioned group), with a p-value of 0.2042. At 216 hours, the respective values for the positive control and C24 preconditioned group were 0.81±0.09 and 0.80±0.09 (p-value: 0.5686). Finally, in the last day of the experiment, we could not obtain a section for the C24 preconditioned group, although we did obtained one for the positive control. In this sample, cells slightly decreased their roundness, with a mean value of 0.75±0.07.

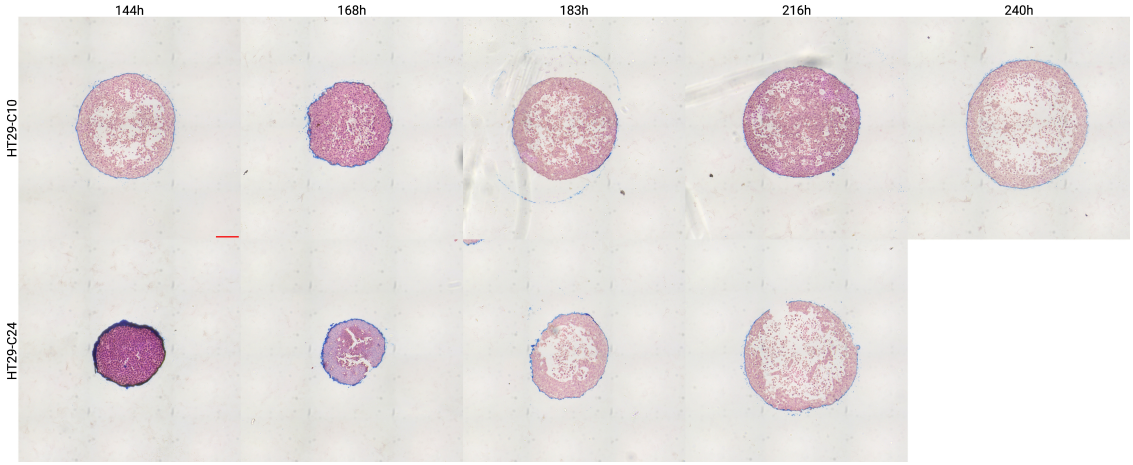

Figure 5-17: Representative Hematoxylin-Eosin (H&E) images of parafin-embedded sections of HT-29 spheroids in the "best-to-worst" experiment. Scale bar: 100 µm.

Despite the information obtained from the TEM and H&E images, we could not observe the actin filaments inside the cells. Therefore, we stained the actin filaments of the CSK with phalloidin. Afterwards, we clarified the samples and imaged the samples in a confocal microscope.

We performed the clearing protocol in order to improve the penetration distance of the light and reduce the light scattering resulting from the density of cells inside the spheroids. Figure **5-18** shows the maximum projection of confocal images of a sample preconditioned spheroid (C24 group) maintained for 168 hours. As seen in the Figure, although the clearing technique did allow us to better visualize the spheroid, the high density of cells did not permit to obtain clear images of the actin filaments inside the spheroid. Nevertheless, we did observe that the actin filaments were highly concentrated at the periphery of the cells. This was expected, since the cells were largely occupied by the nucleus (Figure **5-14**).

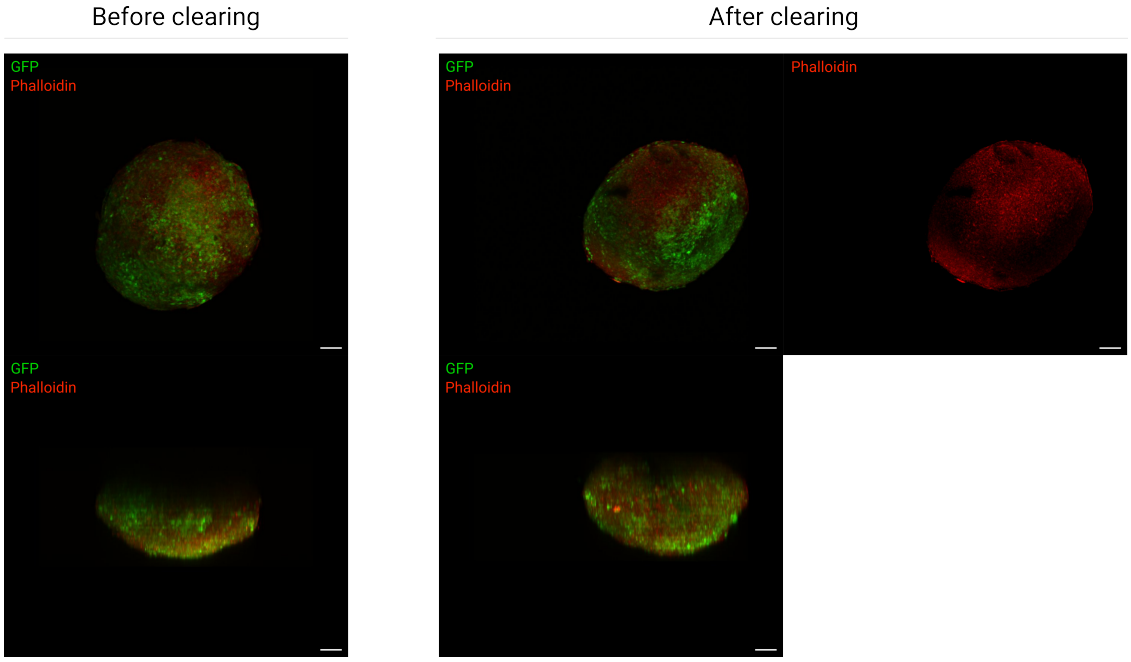

Figure 5-18: Actin filament location inside a cleared sample of a C24 preconditioned spheroid maintained for 168 hours before and after clearing. Scale bar: 100 µm.

Although we could not observe the CSK arrangement inside the cells, we corroborated that cells form concentric rings around the necrotic core. Since this distribution could favor the compression of the core, we continued our experiments and blocked cytoskeletal activity with Y-27632 or Blebbistatin. Results are shown in the following sections.

5.2.5.2. Treatment with Y-27632 inhibits cytoskeletal contraction but it also affects spheroid growth

In order to determine whether Y-27632 could prevent the ejection of the necrotic core, we designed a battery of experiments where we varied the concentration of the drug and the timing of its addition. We used the "best-to-worst" experiment as our baseline. With this design, we aimed to answer whether the ejection was dependent on the dose and the addition time. For the first part, we used increasing concentrations of the molecule, ranging from 25 to 100 μM (specific doses were 25, 50, and 100 μM). For the second part, we defined two specific moments of addition, which simulated an acute treatment scheme with the drug and a chronic one. Both schemes corresponded to the following events in the timeline of the preconditioning experiment:

1. **Chronic treatment (24^{th} hour of the experiment)**: corresponded to the beginning of the cycle in DG10. The signal was maintained throughout the rest of the experiment.

2. **Acute treatment (168^{th} hour of the experiment)**: corresponded to the transition between the cycles in DG10 and D0. The signal was kept for the duration of the cycle in D0.

The chronic effect of high doses of Y-27632 prevents the ejection of the necrotic core but it also affects cell proliferation

When we added Y-27632 at the beginning of the cycle in DG10, we observed that the ejection of the necrotic core was dose-dependent. As seen in the left panel of Figure **5-19**, the increasing doses of the molecule led to changes in the spheroid size and the capability of expelling the necrotic core. Indeed, the only concentration capable of preventing the ejection was 100 µM.

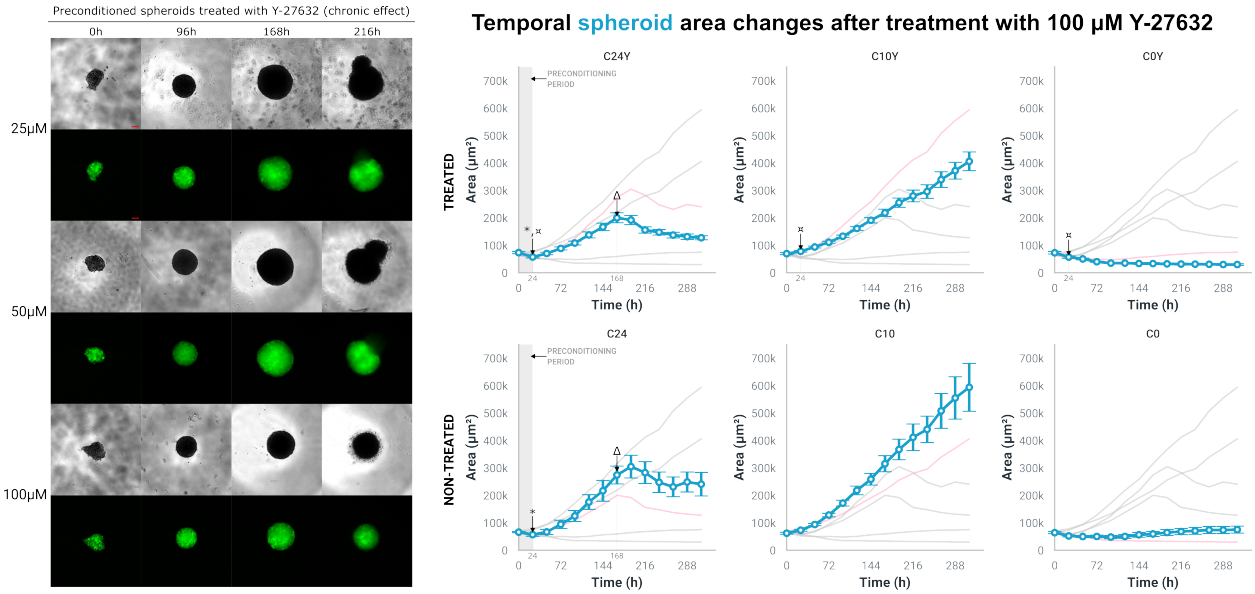

Figure 5-19: Time spheroid behavior of treated spheroids with Y-27632 in the chronic scheme. Left panel: morphological changes of the spheroids. Right panel: time evolution of the mean spheroid area after adding 100 µM Y-27632. ∗: transition from D0 to DG10. △: transition from DG10 to D0. ¤: addition of Y-27632. Scale bar: 100 µm.

For this concentration, we calculated the mean area evolution of groups not exposed to the molecule (non-treated) and those exposed to 100 µM of Y-27632 (treated groups). Results, which are shown in the right panel in Figure **5-19**, revealed that, overall, treated spheroids were smaller than the non-treated ones. Thus, we asked whether these changes in size were restricted to the phase in D0 or, by contrast, were the result of the prolonged exposure to Y-27632. To do this, we calculated the percent differences in size at every cycle (including the preconditioning period) between the treated and non-treated groups. As a guiding visualization tool, inside each subgraph in the right panel of Figure **5-19**, we compared the sizes of the blue and pale pink lines in every time point of the experiment. Based on these results we observed that, during the first 24 hours of the experiment, treated groups (first row in Figure **5-19**), were bigger than the non-treated groups. Nevertheless, the differences in size were not statistically significant. At the outset of the experiment (0 hours), in the negative controls, the treated spheroids exhibited a larger size compared to the non-treated samples, showing a percent difference of $12.8 \pm 1.2\%$ (p-value: 0.108).

Similarly, in the positive controls, the treated spheroids demonstrated a percent difference of 11.4±0.9% in size (p-value: 0.1225), while the preconditioned samples exhibited a percent difference 10.8±0.7% (p-value: 0.2237). At 24 hours, the sizes of the treated and non-treated samples were also similar. In the negative and positive controls, the respective percent differences reduced to 9.4±1.0% (p-value: 0.2162) and 6.7±0.4% (p-value: 0.9085). In the preconditioned group, the corresponding percent difference was 1.0±0.1% (p-value: 0.2673).

However, when the drug was added, which coincided with the start of the cycle in DG10, a noteworthy shift in the trends occurred. Spheroids treated with the drug, which were initially larger during the initial starvation period, began to decrease in size compared to the non-treated ones. In the case of the negative controls, the size of the treated spheroids decreased by a percent difference of 55.7±10.4% at the end of the cycle (p-value: 0.0007067). In the positive controls and preconditioned group, the treated samples reduced their size with respective percent differences of 36.2±4.0% (p-value: 0.002995) and 31.2±4.7% (p-value: 0.001191) compared to their non-treated counterparts.

Finally, in the last phase of the experiment, coinciding with the cycle in D0, the differences seen in the previous cycle became more evident; that is, treated spheroids reduced their size even more with respect to the non-treated ones. In fact, in the negative controls, the differences in size passed from 55.7±10.4% (at the start of the last phase) to 86.1±16.8% at the end of the experiment (p-value: 1.522e-05). Similarly, in the positive controls the differences in size increased from 36.2±4.0% to 37.6±6.4% (p-value at the end of the phase: 0.01352). Lastly, in the preconditioned group, the differences in size ranged from 31.2±4.7%, at the beginning of the phase, to 61.4±11.5% at the end of the experiment (p-value: 0.0001293). Based on these results, we hypothesized that the reduction in size, which is directly related to the proliferative activity of cells, was due to the prolonged exposure to the high dose of the drug.

The acute effect of Y-27632 alters the size of the spheroids and does not prevent the ejection of the necrotic core regardless of the dose

Figure **5-20** shows, in the left panel, the spheroid behavior when the different concentrations of the molecule were added in the acute effect scenario. When we added the drug, the spheroids had already formed a large necrotic core and, correspondingly, had a pretensile stress due to it that was countered by the intercellular forces exerted by the rings of cells. Strikingly, after the addition, the molecule did not prevent the ejection of the necrotic core in any of the tested concentrations, as seen in Figure **5-20**.

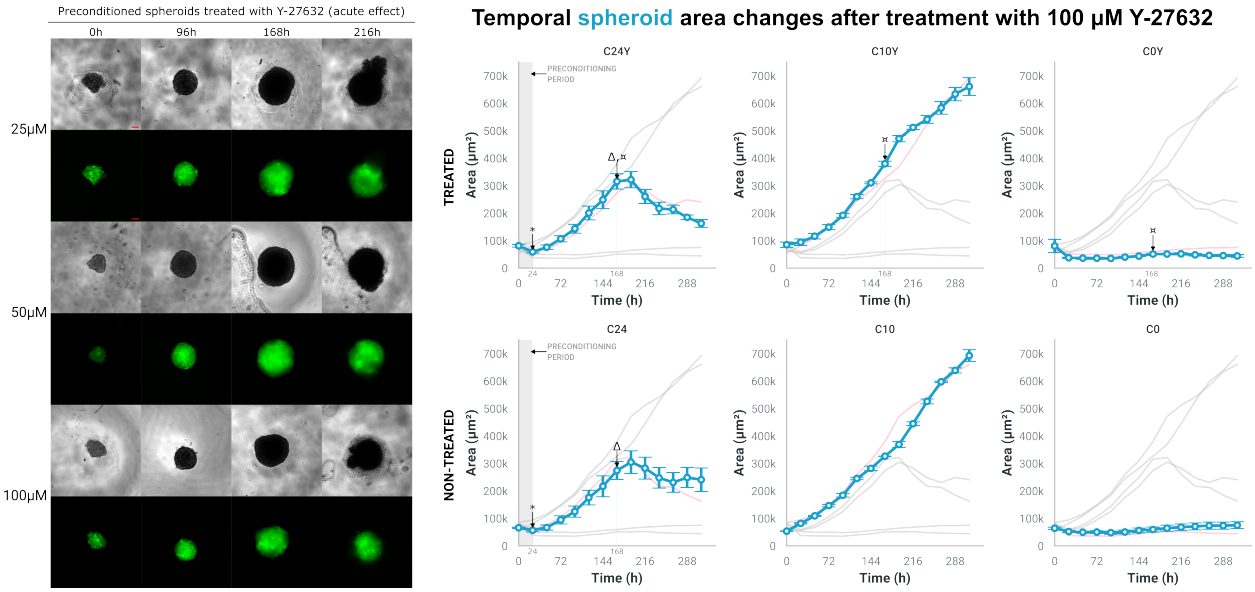

Figure 5-20: Time spheroid behavior of treated spheroids with Y-27632 in the acute scheme. Left panel: morphological changes of the spheroids. Right panel: time evolution of the mean spheroid area after adding 100 µM Y-27632. $*$: transition from D0 to DG10. Δ: transition from DG10 to D0. ¤: addition of Y-27632. Scale bar: 100 µm.

We analyzed the mean area evolution of the spheroids treated with 100 µM Y-27632 in order to compare the effect of the acute treatment with the chronic one. The results are shown in the right panel of Figure **5-20**. As in the previous section, inside each subgraph in the right panel of Figure **5-20**, we compared the sizes of the blue and pale pink lines in every time point of the experiment.

During the first 168 hours of the experiment, which included the preconditioning period (0 to 24 hours) and the cycle in DG10 (24 to 168 hours), the treated groups behaved similarly the non-treated samples and had similar sizes, with the latter being larger in size than the former. For instance, at the end of the cycle in DG10 (168 hours), in the negative controls, the difference in size between the non-treated and treated samples was 15.1±2.4% (p-value: 0.8846). In the positive controls, the corresponding value between the non-treated and treated samples was 15.1±0.4% (p-value: 0.7341) whereas for the preconditioned group, it was 14.0±2.1% (p-value: 0.8396).

Following the addition of the drug, the treated spheroids continued to reduce their size, although this reduction was not significant. Thus, at the end of the experiment, the differences in size between the non-treated and treated samples in the negative controls, the positive controls, and preconditioned group were, respectively, 52.0±10.6% (p-value: 0.7692), 4.7±0.3% (p-value: 0.8396), and 38.7±7.7% (p-value: 0.07033).

5.2.6. The biological response of HCT-116 spheroids to Blebbistatin is dose-dependent

In the previous section, we observed that treating spheroids with 100 μM Y-27632 in a chronic scheme prevented the ejection of the necrotic core in the C24 preconditioned group, with the caveat that it also altered its formation. This was a major issue, since our aim was to inhibit the necrotic core ejection in spheroids and not prevent its formation. Therefore, we decided to use Blebbistatin, another small molecule capable of blocking cytoskeletal contractile activity. However, contrary to Y-27632, which acts upstream in the ROCK/RHO signaling pathway, Blebbistatin inhibits the gliding motility of myosin II without interfering in the binding of myosin to the actin filament.

Similar to Y-27632, we also evaluated the effects of increasing concentrations of Blebbistatin (0.1, 1, 10, 25, 50, and 100 μM) in the behavior of the spheroids. Figure **5-21** shows the temporal area evolution of spheroids treated with Blebbistatin at the mentioned concentrations and time point within the experiment.

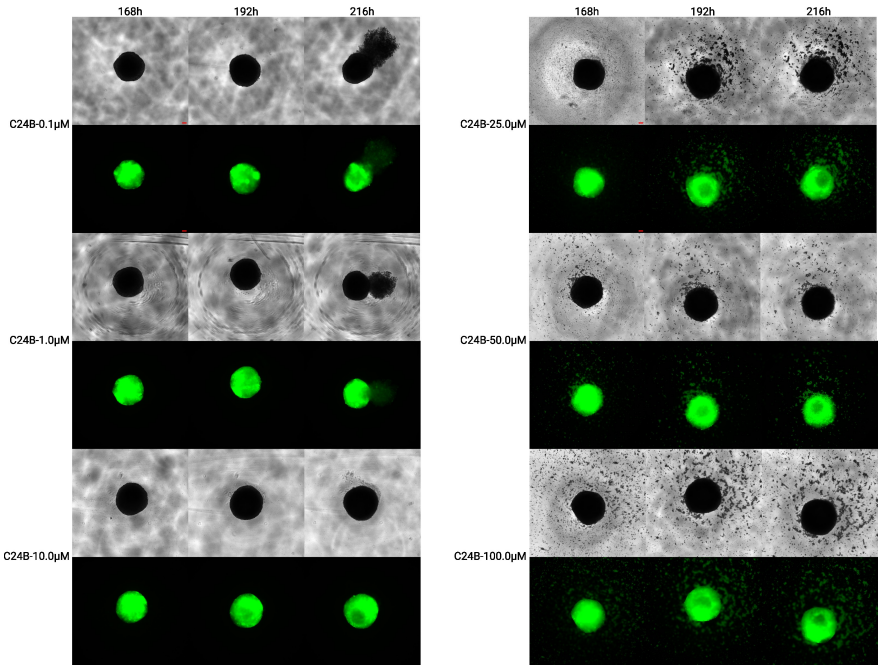

Figure 5-21: Time evolution of representative examples of treated (C24B) and non-treated samples (C24) for the C24 preconditioned group during the first cycle in D0. Scale bar: 100 μm.

As seen in the Figure, the lowest concentrations (0.1, 1, and 5 μM) of Blebbistatin did not prevent the ejection of the necrotic core, whereas those at the highest (25, 50, and 100 μM) did prevent it but they also promoted massive cell detachment from the spheroids, especially at a concentration of 100 μM. These detached cells were viable and maintained this state for the rest of the test. In contrast, when we treated the spheroids with 10 μM Blebbistatin, the samples did not eject the core and did not present cell detachment. Therefore, we used this concentration for the following analyses.

The acute treatment with 10 μM Blebbistatin prevents the ejection of the necrotic core and preserves cell proliferation

Figure **5-22** shows the evolution of the treated (identified by the letter "B") vs non-treated preconditioned spheroids in the acute treatment with 10 μM Blebbistatin, which corresponds to the first cycle in D0. Qualitative analysis of the spheroids during this cycle revealed that preconditioned spheroids treated with Blebbistatin did not eject their necrotic core in any time point during the cycle, despite having seemingly similar sizes to their non-treated counterparts before the ejection.

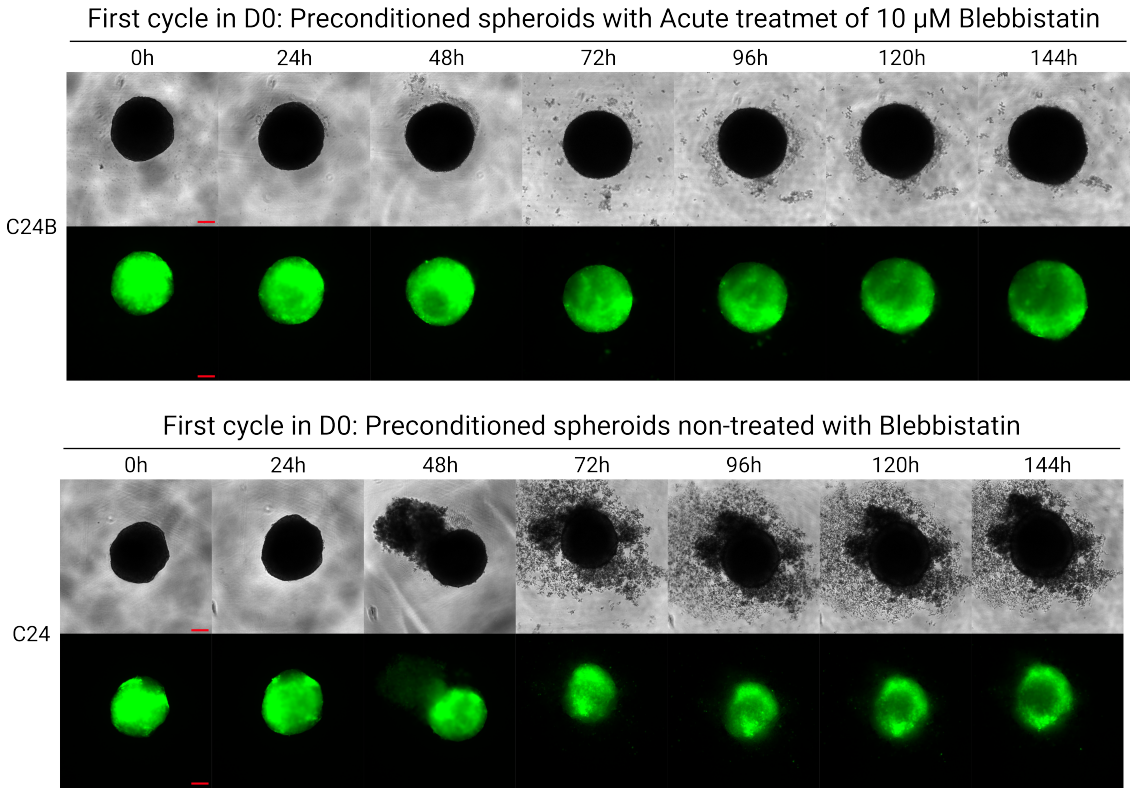

Figure 5-22: Time evolution of representative examples of treated and non-treated samples for the C24 preconditioned group during the first cycle in D0. Scale bar: 100 µm.

In order to corroborate that the treated and non-treated spheroids were similar before the addition of Blebbistatin, we quantified the area of the spheroids in the entire experiment (Figure **5-23**) and then compared the growth rates of the treated and non-treated samples within the same group (positive control, negative control, or preconditioned spheroids). We also compared the differences in size between the treated and non-treated samples.

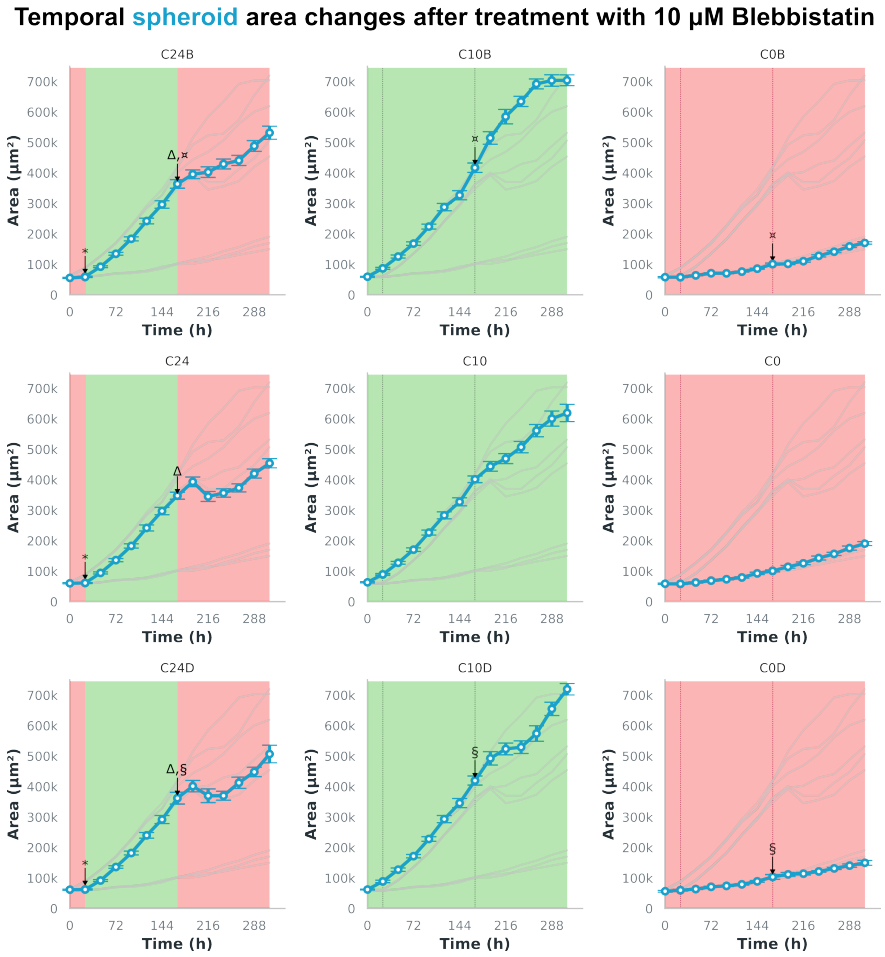

Figure 5-23: Time evolution of the spheroid area behavior of treated spheroids with Blebbistatin in the acute treatment. $*$: transition from D0 to DG10. Δ: transition from DG10 to D0. ¤: addition of Blebbistatin. §: addition of DMSO. Dashed lines indicate the preconditioning period, the cycle in DG10, and the cycle in D0 of the preconditioned group. Green hue: period in DG10. Red hue: period in D0.

During the initial 24 hours of the experiment, referred to as the initial starvation period, both treated and non-treated groups exhibited comparable behavior. For instance, in the positive control groups, the treated spheroids grew at a rate of 1140.9 µm^2/h, while the non-treated ones showed a growth rate of 1093.2 µm^2/h. Likewise, in the negative controls, the treated and non-treated samples exhibited respective growths rates of -17.1 and -0.7 µm^2/h. In the preconditioned group, treated spheroids revealed a growth rate of 114.9 µm^2/h, while the non-treated counterparts displayed a rate of 45.7 µm^2/h.

Throughout the subsequent 144 hours of the experiment, corresponding to the cycle in DG10, both treated and non-treated groups continued to exhibit similar behaviors, as demonstrated by the p-values shown in parentheses. In the negative controls, the treated samples grew at a rate of 264.6 μm^2/h, followed by the non-treated samples, which showed a rate of 294.5 μm^2/h (p-value: 0.2675). In the positive controls, the respective values for the treated and non-treated groups were 2251.5 and 2158.4 μm^2/h (p-value: 0.1261). Similarly, in the preconditioned group, the rate for the treated samples was 2124.7 μm^2/h whereas for the non-treated spheroids, it was 2039.9 μm^2/h (p-value: 0.0675).

With respect to the average percent differences between the treated and non-treated groups at the start and end of the mentioned time frame, the results also confirmed the similarity in their behavior. However, it was noteworthy that, across all experimental groups, the non-treated samples were consistently larger in size than the treated spheroids. At the beginning of the cycle in DG10, the difference in size between the treated and non-treated samples in the negative controls was 0.9$\pm$0.03% (p-value: 0.83181). In the positive controls, the difference amounted to 2.5$\pm$0.12% (p-value: 0.5949), and in the preconditioned group, it was 2.3$\pm$0.09% (p-value: 0.4124). At the end of the cycle, these differences further accentuated, with respective values for the negative controls, the positive ones, and the preconditioned groups of 0.2$\pm$0.01% (p-value: 0.713), 3.8$\pm$0.18% (p-value: 0.2017), and 4.6$\pm$0.23% (p-value: 0.0675).

During the last phase of the experiment, when the signal of Blebbistatin was activated and the preconditioned spheroids were again in D0, notable differences emerged between the treated and non-treated samples compared to the previous cycle. In particular, with the exception of the negative controls, the treated samples were always larger than the non-treated counterparts.

In the positive controls, the differences between the treated and non-treated spheroids passed from -3.8$\pm$0.18%, at the start of the phase (the negative sign indicates that the treated spheroids were smaller than the non-treated ones), to +12.8$\pm$0.67% (p-value: 0.01834) at the end of the experiment (the positive sign highlights that the treated samples were bigger than their non-treated counterparts). Correspondingly, in the preconditioned group, the difference in size increased from -4.6$\pm$0.23% at the start of the cycle to +15.8$\pm$0.83% (p-value: 0.006477) at the end of the experiment.

Conversely, in the negative controls, the differences further accentuated from -0.2±0.01%, at the beginning of the cycle, to -11.4±0.47% (p-value: 0.01368) at its conclusion. As in the positive controls, the negative sign in the percent difference values of the preconditioned and negative control groups indicates that the size of the treated spheroids was smaller than that of the non-treated counterparts.

In addition to the differences in size, the growth rates of the treated and non-treated samples also showed differences after the addition of Blebbistatin. With the exception of the negative controls, the rates of the treated spheroids were bigger than the rates of the non-treated counterparts. In the positive controls, the treated spheroids grew at a rate of 2002.0 μm^2/h, followed by the non-treated samples, which exhibited a rate of 1574.5 μm^2/h (p-value: 0.01855). In the preconditioned group, the treated samples displayed a growth rate of 1083.6 μm^2/h, surpassing the non-treated counterparts, which demonstrated a rate of 597.4 μm^2/h (p-value: 8.979e-05). Conversely, in the negative controls, the growth rate of the treated samples was 525.7 μm^2/h, while the corresponding rate for the non-treated spheroids was 628.8 μm^2/h (p-value: 0.0295).

5.3. Discussion

5.3.1. The ejection of the necrotic core is not a universal event

During the DG10-D0 preconditioning experiments, we observed that spheroids made of the HCT-116 cell line were able to expel their necrotic core during the phases in which they were deprived of nutrients, an event that, to the best of our konwledge, has not been reported in literature. This prompted us to ask several questions. In the first place, we inquired whether this phenomenon was universal or, by contrast, it was related only to the HCT-116 cell line. For this, we repeated this experiment using spheroids made of U-87 MG, U-251 MG, SH-SY5Y, and HT-29. Based on our results (Figures **5-5** and **5-6**), we concluded that it was not universal and was only circumscribed to the HCT-116 cell line. This may be explained, at least in part, by two key mechanisms: proliferation and the capability and maintenance of cytoskeletal contraction. The first mechanism is straightforward, since the necrotic core can only exist when there is sufficient cell proliferation (or a sufficient number of cells) to create gradients of nutrients and oxygen potent enough to kill the cells inside the spheroids [288, 289]. Thus, the complete absence of a necrotic core in the first cycle in D0 for the U-251 MG and SH-SY5Y explains the lack of ejection in these two cell lines, and is also in agreement with previous findings. For instance, the lack of necrotic core formation in U-251 MG spheroids has been observed previously by Rodrigues Alves et al. [290]. In their study, the authors demonstrated that U-251 MG cells showed relatively stable proliferation rates (inferred by the number of viable cells) that were low enough to promote the growth of the spheroids and the onset of a necrotic core over the course of 12 days.

This time frame is comparable to the one during the first cycle in D0 our experiments. Furthermore, the authors reported an overall spheroid size reduction for this cell line that was attributed to the intercellular interactions inside the spheroid. The size reduction for spheroids of this cell line was also observed by Waldherr et al. [291] although the authors do not comment on the possible mechanisms responsible for this reduction. For the SH-SY5Y spheroids, Jung et al. [292] also characterized the proliferation rates of spheroids of this cell line over the course of 4 days (also inferred by the number of viable cells) and found that the samples also had low proliferation rates. Furthermore, the authors showed that, despite the initial cell density used for producing the spheroids ($1x10^5$ cells/well) the spheroids did not have a necrotic core even after 96 hours of culture in growth medium.

The proliferation mechanism may also explain the behavior of the SH-SY5Y in the second cycle in D0. Indeed, although the spheroids managed to develop a necrotic core, it became evident within the last 48 hours of the experiment. With respect to the U-251 MG spheroids, our decision to interrupt the experiment at the end of the first cycle in D0 is supported by the fact that this cell line has been reported to have very low proliferation rates when cultured as multicellular spheroids, partly because of the high contractile forces exerted by the cells. By contrast, the U-87 MG and HT-29 spheroids did have large enough cores, indicating the high proliferative capacities of these cell lines [293–295]. These large cores could be, in theory, expelled from the inside of the masses. Yet, this did not happen in any of our experiments. As stated above, we hypothesized that the ejection of the core occurs because of two simultaneous effects: the expansion of the necrotic core and the weakening of the intercellular forces exerted by the rings of cells surrounding the necrotic core. This hypothesis is only true if, apart from fulfilling the proliferation requirements, the cells exert high intercellular contractile forces, when cultured as multicellular spheroids, that can be altered by external signals, such as nutrient deprivation. In the case of U-87 MG cells, previous reports show that spheroids made of this cell line downregulate the expression of E-cadherin while up-regulating N-cadherin expression, a typical feature of the epithelial-to-mesenchymal transition (EMT) [296], suggesting that the intercellular contractile forces in these spheroids are weak [297–301]. In addition, as seen from our results, the spheroids from this cell line were seemingly not affected by the changes in glucose and FBS to maintain cell functions. Conversely, the HT-29 cell line has high contractile forces, as evidenced by the upregulation of E-cadherin [119, 302–305]. However, contrary to the HCT-116 cells, the contractile activity and proliferation rates of the HT-29 line spheroids were seemingly not affected by the deprivation of glucose or FBS, as the internal architecture of both controls and preconditioned HT-29 spheroids, and their growth behavior (analyzed in the previous Chapter), was essentially the same throughout the time frame discussed herein.

This can be explained by the fact that these cells, as well as other CRC cell lines, can obtain the energy necessary to sustain their functioning through alternative metabolic routes, such as the glutaminolysis pathway [99, 109, 306–309]. Figure **5-24** shows a schematic representation of this pathway and its relation with the TCA cycle.

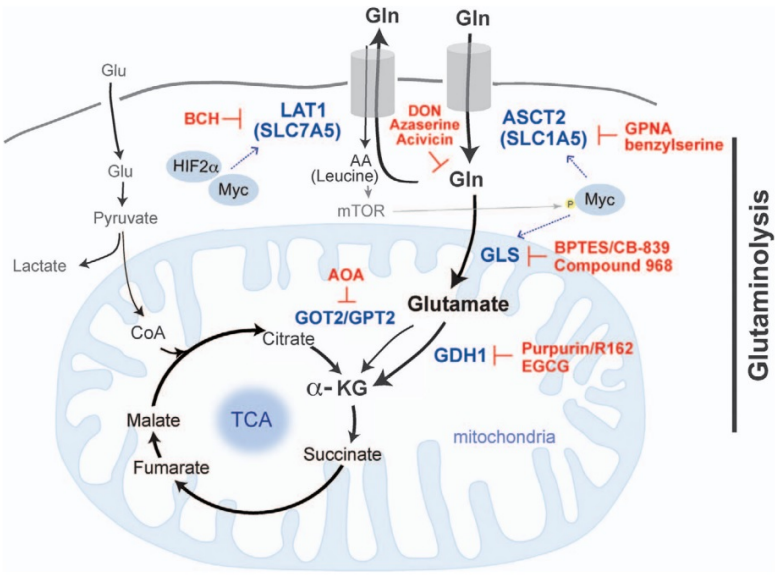

Figure 5-24: Comparison between the TCA cycle and the glutaminolysis pathway. Taken from [310].

5.3.2. Glucose is a major factor for the ejection of the necrotic core in HCT-116 cell spheroids

In close relation with the above, we then asked which of the two varied nutrients (glucose or FBS) was the major responsible for the ejection of the core in the HCT-116 spheroids. This was our second main question. Based on our findings, we conclude that glucose seems to be the major factor involved in the phenomenon. This may be explained by the fact that this cell line heavily relies on glucose availability to obtain the necessary energy to sustain the functions via the massive production of lactate (even in the presence of oxygen) in the process known as the Warburg effect [89, 218, 311]. In normal glucose conditions, this effect can prevent anoikis, a type of cell death generated by the loss of cell contact of cells with the extracellular matrix [312, 313], by reprogramming cell metabolism to promote lactate production over oxidative phosphorylation [314]. It can also confer cancer cells resistance to stress in the endoplasmic reticulum of cells, the organelle responsible for protein maturation [219].

Under stress conditions, such as those produced by the absence of glucose, this organelle fails to perform protein maturation, causing a phenomenon called unfolded protein response (UPR) that can ultimately lead to apoptosis [315]. Under glucose-deprived scenarios, several studies report that cancer cells can enable autophagy [97, 316, 317] or other alternative metabolic routes [318] to sustain their survival. Autophagy is a multistep conserved catabolic process by which cells self-digest their organelles [319]. Although this mechanism can have different roles depending on the biological context, in cancer it seems to have a protective effect against the stress generated by multiple mechanisms including nutrient deprivation or oxidative, genotoxic, and proteotoxic stresses [98] by preventing apoptosis [113, 181, 320]. In addition to the above, glucose availability and, in particular, ATP (a product of glucose metabolism) is also involved in the regulation of CSK dynamics and the maintenance and enhancement of intercellular interactions in response to external forces (reviewed in [321]). In yeasts and HeLa cells, glucose depletion leads to the immobilization of myosin on the actin filaments, thus stabilizing them and preventing their disassembly [322]. In line with this, cell-cell adhesion can also be modified by glucose availability. Indeed, Suzuki et al. demonstrated that in HepG2 cells (derived from a hepatocellular carcinoma), cell detachment was induced during glucose deprivation through the human homologue of SNARK, a member of the AMPK enzyme family, mainly by the reconversion of F-actin to G-actin [323]. Regarding cell contraction, glucose restriction can also lead to relaxation of the contractile forces, as demonstrated in endothelial cells [324]. Lastly, complete glucose removal or exhaustion lead to rapid cell death [325], especially in heavily glucose-dependent cells, such as the HCT-116 cell line [221, 326–329].

Based on the information presented above, we hypothesized that, in our experiments, where glucose was restricted either in presence or absence of FBS, cells forming the inner layers of HCT-116 spheroids might rapidly transition from a functional state to a dead state due to a rapid depletion of glucose. This transition would be mainly accompanied by a sudden weakening of cell contractions in the surviving cells, also caused by the lack of glucose and, ultimately, ATP. Concomitantly, the necrotic core, which would be compressed in normal conditions, would start to expand (as seen in Figure **5-7**), stretching the cells and their junctions. Some examples of the effects of weakening (or disrupting) the intercellular forces across spheroids has been shown by other authors [330, 331]. Noteworthy, the work by Guillaume et al. demonstrated that HCT-116 spheroids have a pre-existing mechanical stress, accumulated during their growth, by making an incision in the tumor mass and observing the subsequent deformation process [332]. After the procedure, the authors reported that the spheroids first expanded isotropically. This process was followed by a retraction at the edges of the cut area of the spheroids that depended on the initial cell seeding used to form the aggregates. In our experiments, the isotropic deformation of the spheroids caused by the expansion of the necrotic core continues deforming the spheroid (as also seen by Guillaume et al. [332]) until it encounters a weakened zone analogous to the incision zone of the same authors.

Then, the global deformation process would immediately become a local one, generating mechanical forces in the weakened zone that, in our case, would exceed the maximum resistance of the intercellular junctions and, in the case of Guillaume et al. [332], would separate the cut edges of the spheroids. Loss of the junctions would then have a tearing effect in the spheroids that, in combination with the weakening of the contraction and the expansion of the core, would allow its expulsion to the exterior through this tear.

Concerning the relative differences in the amount of expelled material between the DG10-D10 and DG10-D0 preconditioning experiments, we believe that this is related to the effect of FBS. Indeed, the presence of FBS seems to be predominantly involved in cell proliferation, due to the amount of growth factors found in this complex mixture [215]. Thus, in the case of the DG10-D10 experiments, when the spheroids are in D10, the presence of FBS stimulates cell proliferation at the outer layer of the spheroids, allowing them to grow. However, due to the mechanisms explained above, we believe that the rapid depletion of glucose inside the spheroids may lead to massive cell death. This, in conjunction to our hypothesis regarding the weakening of the cell-cell junctions (also explained above) may explain the pronounced ejections observed for this experiment (Figure **5-11**).

5.3.3. The ejection of the necrotic core is a mechanical effect regulated by the contractile activity of the cells

In order to prove that the ejection of the core was a mechanical event in which the contraction of the CSK played a central role, as we hypothesized in the paragraphs above, we first checked cell distribution inside the spheroid. The results obtained (Figure **5-14**) imply that the cells are indeed capable of forming the contractile rings around the center of the spheroid, especially at its inner layers. Daster et al. performed characterization of HCT-116 and HT-29 spheroids in different time points [333]. For this, the authors used histological, immunological, and gene expression techniques to understand how the physical characteristics of the spheroids, expressed mainly in terms of the presence or absence of hypoxic and necrotic zones, affected their resistance to 5-Fluorouracil (5FU). Although the authors did not provide quantitative measurements of the cell shape in the histological sections of the spheroids, qualitative comparison of our histological micrographs with their corresponding micrographs confirmed our findings for both cell lines, especially in the positive controls. Furthermore, our histological sections of the HT-29 spheroids are also qualitative similar to those obtained by Hardelauf et al. for this same cell line [334]. The resulting cell and nucleus shapes seen in our experiments may be due to the inner tractions that cells exert among each other [335–340]. Indeed, it has been demonstrated that, during embryo development, actomyosin contraction and membrane tension can guide cell fate and tissue patterning [337, 338, 341, 342].

The conjoint effect of these two phenomena leads to deformations in the cell that ultimately dictate the final shape of a tissue [337]. At the cellular level, control of the deformation and the associated mechanical stress is carried out by tensegrity, a mechanism related to network structures that enables them to self-stabilize through the use of pretensile stress [339]. Based on the above, the morphological aspect of cells in the histological sections of the spheroids may be the result of the reorganization of the CSK of cells in response to the mechanical force exerted by the continuously growing necrotic core. This seems particularly important in the case of the HCT-116 spheroids, as cells were largely deformed following the passing of the aggregates to D0.

When we inhibited the contractile activity of the cytoskeleton with either Y-27632 or Blebbistatin, we observed that their effect on the spheroids were dose and time dependent. For the case of Y-27632, the addition of the molecule (at a concentration of 100 μM) to the preconditioned spheroids at the beginning of the cycle in D0 (acute treatment), did not prevent the ejection of the necrotic core, as shown in Figure **5-20**. This suggests that, in this treatment scheme, this molecule does not affect the pre-existing intercellular forces in the spheroids. The effect of Y-27632 on cell contraction has also been studied in previous studies. For instance, Kim et al. evaluated the effect of the contractile forces of human dermal fibroblasts (HDFBs), cultured as cell sheets on top of temperature-sensitive hydrogels, on their self-assembly into spheroids [343]. For this, they applied two concentrations of the molecule (10 and 100 μM) for 2 hours to the sheets and analyzed their behavior. The authors found that, under the effect of the highest concentration of Y-27632, HDFBs did not self-assemble into spheroids, but maintained the existing forces of the sheets. Similar results were obtained by Lee et al. [183]. In their research, the authors formed spheroids from mesenchymal stem cells isolated from human nasal turbinate tissue following a similar protocol to the one used by Kim et al. [343]. Indeed, the authors generated cell sheets on top of temperature-sensitive hydrogels and treated them with 10 and 100 μM Y-27632 for 2 hours. As with the previous authors, exposure with 100 μM Y-27632 prevented spheroid formation. Together, these findings seem to support our hypothesis that high concentrations of the molecule do not affect preexisting intercellular forces despite the inherent differences in the experimental approaches. In turn, when 100 μM Y-27632 was added at the beginning of the cycle in DG10 (chronic treatment), the spheroids did not eject their core but their growth was also heavily restricted, as seen in Figure **5-19**. This is probably due to the fact that, at that concentration, Y-27632 restricts not only the cytoskeletal contractile activity but also cell proliferation, as these two processes are deeply interconnected through the Rho/ROCK signaling pathway [344].

The restrictive effects of Y-27632 on the proliferation of cancer cells has been previously studied by Jiang et al. [345]. In their research, the authors analyzed the proliferation of 2D cultures of two different bladder cancer cell lines (T24 and 5637), exposed to a wide range of concentrations of the molecule (0-150 μM), for independent periods of time of 24, 48, or 72 hours. After exposure, the authors observed that, in all three periods of exposure, the proliferation of both cell lines decayed in a dose-dependent manner, with the lowest values corresponding to the 150 μM. Furthermore, they also noted that, as the exposure time increased, the proliferation further decreased. For instance, in the 150 μM, the viability of T24 cells decreased from $40.38 \pm 1.38\%$ at 24 hours to $35.22 \pm 1.04\%$ at 72 hours. Although our study significantly differed from the authors in the type of cell culture (3D in our case vs 2D in theirs) as well as in the exposure time (144 hours vs 72 hours), we also observed that the proliferation of the cells in spheroids also decreased when the samples were exposed to high concentrations of the molecule.

With respect to Blebbistatin, the addition of the molecule (final concentration of 10 μM) at the start of the cycle in D0 (acute treatment) did prevent the ejection of the necrotic core. Based on this observation, and the fact that the treated spheroids had notable larger areas than their non-treated counterparts (Figure **5-23**), especially for the C24 preconditioned group and the positive control, we believe that, although the molecule does block the contractile activity of the cytoskeleton (allowing the expansion of the spheroids), it does it in a controlled manner, allowing the ring of cells to balance the forces exerted by the gradually decompressing necrotic core. Changes in the size of spheroids and in their compaction during formation after treatment with Blebbistatin have been reported previously for different cancer cell lines with concentrations equal or close to ours [283, 346, 347].

Despite the notorious event described herein, there are three major limitations that should be considered. In the first place, we only considered two nutrients as our biochemical factors: glucose and FBS. However, these two are not the only source of nutrients for cells, as aminoacids, vitamins, minerals, and lipids also intervene in the generation of energy and the correct functioning of cells. For instance, Wang et al. demonstrated that deficiencies in selenium, an essential micronutrient for animals, leads to increased apoptosis, ER stress, and alterations in the tight junctions of cells in mice intestine, as well as severe disruption in the cell organization and macro-morphology of vili [348]. Furthermore, selenium deficiency has been correlated with increased risk in developing CRC [349]. In turn, as we have discussed earlier, glutamine is a key aminoacid that should be considered, since it provides alternative metabolic routes for obtaining energy in absence of glucose [99, 109, 306–309]. In addition to the limited nutrients considered, we did not explore the effects of oxygen on our experiments. Although oxygen is not considered a nutrient [350], it does have a profound impact in the regulation of metabolism and energy obtention. Indeed, this molecule is in charge of accepting the free electrons at the end of the electron transport chain, a part of the oxidative phosphorilation process [351].

In cancer, oxygen deficiency leads to the metabolic reprogramming of cells, mainly by activating the hypoxia inducible factors (HIFs), HIF-1α and HIF-2α [352]. These factors have profound connections with glucose in cancer cells, as they increase glucose uptake through the upregulation of glucose transporters GLUT1 and GLUT3 [353]. Lastly, the third limiation corresponds to the use of monocultures of immortalized cell lines. Indeed, although these lines have provided key insights in understanding cancer, they do not take into account the heterogeneity of *in vivo* tumors. Thus, it may be relevant to include other cell populations and even patient-derived tumoroids.

In conclusion, in this chapter we demonstrate for the first time, to the best of our knowledge, that the necrotic core inside multicellular spheroids can be expelled from their interior by changing the concentration of glucose in the medium. This is a mechanical event mediated by the contractile activity of the cytoskeleton. Furthermore, it is dependent on cell proliferation inside the spheroids, the contractile capacity of the cells themselves, and external signaling, such as the nutrient deprivation, capable of disrupting the normal functioning of this contractile activity.

6. Conclusions and future work

6.1. Conclusions

During the course of this thesis, we aimed to develop 3D *in vitro* models to explore how the deregularization of CRC cell metabolism and the capacity to adapt to extreme environmental conditions could alter their invasive potential. To do this, we analyzed the effects of two major factors: the mechanical properties of the ECM, modeled herein as pure type I collagen hydrogels, and the heterogeneity in nutrient availability, modeled as alternating cycles of nutrient abundance and starvation, on the migratory patterns of CRC cells. In Chapter 3, we explored the first major factor under nutrient abundance. In Chapter 4, we studied the second major factor in absence of the mechanical component given by the ECM. Finally, in Chapter 5, we performed a detailed analysis, from a mechanical point of view, of a result discovered in Chapter 4 and combined the two factors in an initial experiment. This chapter summarizes the most important conclusions derived from the results obtained in this dissertation.

6.1.1. General conclusions for Chapter 3

- The modulation of the mechanical and ultrastructural properties of the hydrogels can be easily modulated by varying the collagen concentration and polymerization temperature of the scaffolds.

- The surface of the hydrogels is stiffer than their inner zones regardless of their concentration or poylmerization temperature.

- Changes in the polymerization protocol of hydrogels with a fixed collagen concentration can lead to differences in their mechanical properties of several orders of magnitude.

- Different migratory patterns can be obtained for a single cell line by changing their location in the hydrogels.

- The influence of local and bulk mechanical properties of the hydrogels on cell migration depends on the spatial configuration of the experiment. Thus, in the unconstrained 2D experiment, local stiffness play a predominant role (the greater the stiffness, the greater the invaded area). In the constrained 2D experiment, bulk mechanical properties dominate over the local ones (the softer the bulk stiffness, the greater the invaded area). In the fully embedded experiment, there was no cell migration. However, bulk stiffness affects the spheroid size (the greater the bulk stiffness, the lower the size).

- The directionality of the migration depends on the ultrastructure of the fibers at the surface of the hydrogels.

6.1.2. General conclusions for Chapter 4

- The initial starvation period can elicit an adaptive response of HCT-116 and HT-29 CRC spheroids. The adaptation correlates positively with the duration of the initial starvation period.
- HCT-116 cells can modify their growth pattern after two cycles of nutrient and growth factors preconditioning.
- HT-29 cells adapt more easily to changes in nutrient availability than HCT-116 cells, promoting almost constant growth.

6.1.3. General conclusions for Chapter 5

- The ejection of the necrotic core is not an universal event.
- Glucose is a major factor for the ejection of the necrotic core in HCT-116 spheroids.
- The ejection of the necrotic core is a mechanical event that involves the disregulation of the contractile activity of the CSK.

6.2. Conclusiones generales

Durante el transcurso de esta tesis, se desarrollaron modelos *in vitro* tridimensionales para explorar la forma en la que la desregularización del metabolismo celular en el CRC y la capacidad de las células para adaptarse a condiciones ambientales extremas podrían alterar su potencial invasivo. Para esto, se analizaron los efectos de dos factores principales en los patrones migratorios de células de CRC: las propiedades mecánicas de la matriz extracelular (ECM por sus siglas en inglés), modelada aquí como hidrogeles puros de colágeno tipo I; y la heterogeneidad en la disponibilidad de nutrientes, modeladas como ciclos continuos de abundancia e inanición de nutrientes. En el capítulo 3, se exploró el primer factor bajo abundancia de nutrientes. En el capítulo 4, se estudió el segundo factor en ausencia de la componente mecánica dada por la ECM. Finalmente, en el capítulo 5, se desarrolló un análisis detallado, desde el punto de vista mecánico, de un resultado descubierto en el capítulo 4 y, de manera adicional, se combinaron los dos factores en un experimento preliminar. A continuación, se presentan las conclusiones más importantes derivadas de los resultados obtenidos en esta tesis.

6.2.1. Conclusiones generales para el capítulo 3

- Las propiedades mecánicas y la ultraestructura de los hidrogeles se pueden modular fácilmente variando la concentración de colágeno y la temperatura de polimerización de las muestras.

- La superficie de los hidrogeles es más rígida que en su interior, independientemente de la concentración o la temperatura de polimerización.

- Los cambios en el esquema de polimerización de los hidrogeles, para una misma concentración de colágeno, puede llevar a diferencias en las propiedades mecánicas de varios órdenes de magnitud.

- Para una misma línea celular, se pueden obtener patrones migratorios distintos dependiendo de la posición en los hidrogeles.

- La influencia de las propiedades locales y globales de los hidrogeles en la migración celular depende de la configuración espacial del experimento. En este sentido, en el experimento donde el esferoide se encuentra sobre una cama de hidrogel (identificado como el *unconstrained 2D experiment* en la tesis), la rigidez local juega un papel predominante (a mayor rigidez local, mayor el área invadida). En el experimento en el que el esferoide se encuentra entre dos capas de colágeno (identificado como el *constrained 2D experiment* en la tesis) las propiedades globales dominan sobre las locales (a menor rigidez global, mayor área invadida). En el experimento en el que el esferoide se encontraba completamente inmerso en el hidrogel (identificado como el *fully embedded experiment* en la tesis), no hubo migración.

Sin embargo, la rigidez global afecta el tamaño del esferoide (a mayor rigidez global, menor área esferoide).

- La direccionalidad de los patrones migratorios depende de la ultraestructura de las fibras en la superficie de los hidrogeles.

6.2.2. Conclusiones generales para el capítulo 4

- El período de deprivación inicial puede elicitar una respuesta adaptativa en esferoides de las líneas celulares HCT-116 y HT-29. La adaptación está correlacionada positivamente con la duración de dicho período.
- Las células HCT-116 pueden modificar su patrón de crecimiento después de dos ciclos de precondicionamiento de nutrientes y factores de crecimiento.
- Las células HT-29 pueden adaptarse más fácilmente a los cambios en nutrientes que las HCT-116, lo que promueve un crecimiento casi constante a lo largo de los experimentos.

6.2.3. Conclusiones generales para el capítulo 5

- La eyección del núcleo necrótico no es un evento universal.
- La glucosa es el factor principal para la eyección del núcleo en esferoides de HCT-116.
- La eyección del núcleo necrótico es un evento mecánico que involucra la desregulación de la actividad contráctil del citoesqueleto.

6.3. Future work

This dissertation has laid the basis for future studies regarding the mechanobiological behavior of CRC in vitro models.

- In-depth analysis of the mechanical properties of preconditioned spheroids at key time points during the preconditioning experiments in order to determine whether there are time-dependent changes in the stiffness of the samples associated to variation in nutrient-availability.
- Measure intercellular forces inside the different preconditioned spheroids to analyze whether the initial preconditioning period also affects cell-cell interactions.
- Contrast the results of the preconditiong obtained herein with patient-derived tumoroids.
- Incorporate preconditioned spheroids at different time points inside collagen matrices to study their invasive capacity. This would include the analysis of the potential expression of genes involved in invasion and enhanced proliferation.
- Regarding the ejection of the necrotic core, a major study that may be conducted would consist on its confrontation against immune cells to analyze their response.

7. Contributions

7.1. Journal publications

1. **Castro-Abril H**, Héras J, del Barrio J, Paz L, Alcaine C, Pérez-Aliácar M, Garzón-Alvarado D, Doblaré M, Ochoa I. The Role of Mechanical Properties and Structure of Type I Collagen Hydrogels on Colorectal Cancer Cell Migration. Macromol. Biosci. 2023, 2300108. https://doi.org/10.1002/mabi.202300108.

2. Carrasco-Mantis A, Randelovic T, **Castro-Abril H**, Ochoa I, Doblaré M, Sanz-Herrera JA. A mechanobiological model for tumor spheroid evolution with application to glioblastoma: A continuum multiphysics approach. Comput Biol Med. 2023 Jun; 159:106897. https://doi.org/10.1016/j.compbiomed.2023.106897..

3. Mameli A, Hylke A, González-Lana S, **Castro-Abril H**, Le Cann K, Lampert A, Gelinck G, Kronemeijer AJ, van Breemen AJJM. Beyond mobile phone displays: Flat panel display technology for biomedical applications. Microelectronic Engineering. 2023 May; 277:112016. https://doi.org/10.1016/j.mee.2023.112016.

4. Lacalle D, **Castro-Abril H**, Randelovic T, Domínguez C, Héras J, Mata E, Mata G, Méndez Y, Pascual V, Ochoa I. SpheroidJ: An Open-Source Set of Tools for Spheroid Segmentation. Comput Methods Program Biomed. 2020, 105837, https://doi.org/10.1016/j.cmpb.2020.105837.

7.2. Conference proceedings

1. **Castro-Abril H**, Héras J, del Barrio J, Paz L, Alcaine C, Pérez-Aliácar M, Garzón-Alvarado D, Doblaré M, Ochoa I. The role of mechanical properties and structure of type I collagen hydrogels on colorectal cancer migration, EACR, Seville, Spain, June 20-23, 2022. Poster presentation.

Appendices

A. Statistical analysis results for Chapter 3

Table A-1.: Statistical results for the spheroid area evolution of HCT-116 and HT-29 spheroids in the Unconstrained 2D experiment. The coefficients were calculated with a Linear Mixed Model analysis taking into account that the collagen concentration was fixed. The reference group for performing the analysis was the spheroids polymerized following the two-stage scheme.

Spheroid area analyzed under a fixed collagen concentration in the unconstrained 2D experiment										
Cell line	**Coefficient**	**[0.8 mg/mL]**			**[1.5 mg/mL]**			**[3.0 mg/mL]**		
		Value	**Std. Error**	**p-value**	**Value**	**Std. Error**	**p-value**	**Value**	**Std. Error**	**p-value**
HCT-116	**Intercept (ref)**	11513.533	3046.470	0.0003	17887.526	2941.006	4.13E-08	17887.526	3046.417	1.00E-07
	Linear term (ref)	2116.848	72.453	9.21E-44	1835.951	63.209	1.40E-43	1835.951	70.801	4.29E-40
	Intercept (PI)	6395.813	4308.360	0.146	-5563.646	4159.211	0.189	5788.361	4308.284	0.187
	Linear term (PI)	-591.023	102.464	1.54E-07	-4.207	89.391	0.963	-127.501	100.128	0.207
HT-29	**Intercept (ref)**							77186.7	4534.2	8.42E-24
	Linear term (ref)							188693.1	10979.7	5.38E-24
	Quadratic term (ref)							35398.0	3357.8	6.52E-15
	Intercept (PI)							-16518.3	6412.3	0.019
	Linear term (PI)							-352934.0	15527.6	0.027
	Quadratic term (PI)							-3352.0	4748.6	0.48

Table A-2.: Statistical results for the spheroid and invaded area evolution of HCT-116 spheroids in the Unconstrained 2D experiment. The coefficients were calculated with a Linear Mixed Model analysis taking into account that the polymerization scheme was fixed.

Spheroid and invaded areas analyzed under a fixed polymerization scheme in the unconstrained 2D experiment							
Parameter	**Coefficient**	**Two-stage**			**37°C**		
		Value	**Std. Error**	**p-value**	**Value**	**Std. Error**	**p-value**
Spheroid area	**Intercept (ref)**	11677.629	3456.365	0.0010	11719.537	3957.252	0.004
	Linear term (ref)	2119.442	75.717	6.20E-54	1588.225	102.311	2.77E-30
	Intercept (coll.)	2354.079	1736.158	0.180	3407.811	1987.757	0.092
	Linear term (coll.)	-107.467	38.033	0.006	56.857	51.391	0.271
Invaded area	**Intercept (ref)**	-20206.977	4746.945	4.18E-05	-53010.756	9958.616	4.93E-07
	Linear term (ref)	3180.150	155.731	1.53E-40	3875.955	268.307	7.38E-28
	Intercept (coll.)	-2325.571	2384.426	0.333	3932.665	5002.288	0.435
	Linear term (coll.)	145.402	78.225	0.066	142.861	134.773	0.291

Table A-3.: Statistical results for the invaded area evolution of HCT-116 and HT-29 spheroids in the unconstrained 2D experiment. The coefficients were calculated with a Linear Mixed Model analysis taking into account that the collagen concentration was fixed. The reference group for performing the analysis was the spheroids polymerized following the two-stage scheme.

Invaded area analyzed under a fixed collagen concentration in the unconstrained 2D experiment										
Cell line	**Coefficient**	**[0.8 mg/mL]**			**[1.5 mg/mL]**			**[3.0 mg/mL]**		
		Value	**Std. Error**	**p-value**	**Value**	**Std. Error**	**p-value**	**Value**	**Std. Error**	**p-value**
HCT-116	**Intercept (ref)**	-19630.408	7515.230	0.0108	-25406.079	5743.602	3.11E-05	-25406.079	6331.209	0.0001
	Linear term (ref)	3183.659	203.330	8.65E-26	3563.710	169.803	8.06E-34	3563.710	153.911	1.08E-36
	Intercept (PI)	-35688.342	10628.140	0.0018	-13268.913	8122.680	0.111	-18313.784	8953.682	0.048
	Linear term (PI)	936.585	287.552	0.0017	335.868	240.137	0.166	801.495	217.662	0.0004
HT-29	**Intercept (ref)**							-1170.3	871.6	0.18
	Linear term (ref)							341.3	36.6	3.82E-13
	Intercept (PI)							1488.5	1232.6	0.24
	Linear term (PI)							-70.6	51.75	0.18

Table A-4.: Statistical results for the spheroid area evolution of HCT-116 spheroids in the Constrained 2D experiment. The coefficients were calculated with a Linear Mixed Model analysis taking into account that the polymerization scheme was fixed.

Spheroid and invaded areas analyzed under a fixed polymerization scheme in the constrained 2D experiment							
Parameter	**Coefficient**	**Two-stage**			**37°C**		
		Value	**Std. Error**	**p-value**	**Value**	**Std. Error**	**p-value**
Spheroid area	**Intercept (ref)**	180426.844	6626.735	1.28E-89	116425.381	6105.488	7.42E-51
	Linear term (ref)	1778566.690	93182.183	1.08E-56	835779.442	57984.356	8.63E-35
	Quadratic term (ref)	20265.243	29225.807	0.4885	38148.586	19681.524	0.054
	Intercept (coll.)	-14108.189	3530.048	0.0001	11918.795	2818.642	5.90E-05
	Linear term (coll.)	-176129.913	49505.321	0.0004	89981.402	26759.572	0.0009
	Quadratic term (coll.)	78466.460	15518.141	6.80E-07	32195.847	9068.263	0.0005
Invaded area	**Intercept (ref)**	199024.410	12538.032	2.95E-40	9718.579	11230.468	0.388
	Linear term (ref)	2902496.163	178943.720	1.76E-41	-215785.275	119276.816	0.073
	Quadratic term (ref)	302432.393	99528.953	0.003	27420.431	62248.617	0.660
	Intercept (coll.)	-106103.575	10148.377	3.69E-17	21493.217	8743.521	0.018
	Linear term (coll.)	-1649480.041	144865.791	1.10E-24	388566.746	92885.277	4.95E-05
	Quadratic term (coll.)	-288828.665	80585.422	0.0004	-76605.187	48503.107	0.116

Table A-5.: Statistical results for the spheroid area evolution of HCT-116 and HT-29 spheroids in the constrained 2D experiment. The coefficients were calculated with a Linear Mixed Model analysis taking into account that the collagen concentration was fixed. The reference group for performing the analysis was the spheroids polymerized following the two-stage scheme.

Spheroid area analyzed under a fixed collagen concentration in the constrained 2D experiment										
Cell line	**Coefficient**	**[0.8 mg/mL]**			**[1.5 mg/mL]**			**[3.0 mg/mL]**		
		Value	**Std. Error**	**p-value**	**Value**	**Std. Error**	**p-value**	**Value**	**Std. Error**	**p-value**
HCT-116	**Intercept (ref)**	167469.991	3558.380	1.55E-100	162319.589	4779.171	1.27E-92	137629.623	5280.744	1.09E-66
	Linear term (ref)	1032547.394	26659.399	3.65E-87	1371496.521	54328.332	7.18E-69	869885.711	45859.268	7.82E-47
	Quadratic term (ref)	-5878.193	14306.389	0.682	197353.835	9666.537	5.65E-54	154191.667	14285.415	9.33E-22
	Intercept (PI)	-53399.673	6337.876	1.05E-11	-18605.392	7604.128	0.017	11072.635	7310.860	0.135
	Linear term (PI)	-318242.863	47130.284	2.12E-10	-388607.103	86465.853	1.10E-05	111427.040	63489.282	0.081
	Quadratic term (PI)	80205.723	25211.634	0.002	-135530.209	15466.457	3.86E-16	-27866.892	19777.262	0.16
HT-29	**Intercept (ref)**							76026.2	4550.2	1.38E-25
	Linear term (ref)							184398.6	9550.8	4.44E-29
	Quadratic term (ref)							33711.8	5259.1	1.70E-8
	Intercept (PI)							-10421.0	6182.3	0.11
	Linear term (PI)							16737.9	12953.7	0.2
	Quadratic term (PI)							4458.5	7121.6	0.533

Table A-6.: Statistical results for the invaded area evolution of HCT-116 and HT-29 spheroids in the Constrained 2D experiment. The coefficients were calculated with a Linear Mixed Model analysis taking into account that the collagen concentration was fixed. The reference group for performing the analysis was the spheroids polymerized following the two-stage scheme. ND: No Data.

Invaded area analyzed under a fixed collagen concentration in the constrained 2D experiment										
Cell line	**Coefficient**	**[0.8 mg/mL]**			**[1.5 mg/mL]**			**[3.0 mg/mL]**		
		Value	**Std. Error**	**p-value**	**Value**	**Std. Error**	**p-value**	**Value**	**Std. Error**	**p-value**
HCT-116	**Intercept (ref)**	113794.886	5685.497	6.77E-47	162319.589	4779.171	1.27E-92	ND	ND	ND
	Linear term (ref)	1327171.909	67218.367	3.50E-46	1371496.521	54328.332	7.18E-69	ND	ND	ND
	Quadratic term (ref)	58546.030	41218.095	0.157	197353.835	9666.537	5.65E-54	ND	ND	ND
	Intercept (PI)	-87214.301	10021.364	3.58E-12	-18605.392	7604.128	0.017	ND	ND	ND
	Linear term (PI)	-1215805.335	118613.017	1.45E-19	-388607.103	86465.853	1.10E-05	ND	ND	ND
	Quadratic term (PI)	-95504.864	72761.736	0.191	-135530.209	15466.457	3.86E-16	ND	ND	ND
HT-29	**Intercept (ref)**							-21.7	433.7	0.96
	Linear term (ref)							91.4	23.4	2.1E-4
	Intercept (PI)							-48.4	580.6	0.93
	Linear term (PI)							63.1	31.8	0.051

Table A-7.: Statistical results for the spheroid area evolution of HCT-116 spheroids in the Fully Embedded experiment. The coefficients were calculated with a Linear Mixed Model analysis taking into account that the polymerization scheme was fixed.

Spheroid area analyzed under a fixed polymerization scheme in the fully embedded experiment						
Coefficient	**Two-stage**			**37°C**		
	Value	**Std. Error**	**p-value**	**Value**	**Std. Error**	**p-value**
Intercept (ref)	91840.510	9335.285	1.77E-11	114778.127	6815.841	1.64E-16
Linear term (ref)	310528.029	23565.141	6.46E-15	377270.067	27826.443	4.42E-14
Quadratic term (ref)	69319.918	9778.603	3.45E-08	40702.204	6502.786	7.84E-07
Intercept (coll.)	478.249	4474.158	0.917	-5369.394	3640.385	0.174
Linear term (coll.)	-17419.880	11257.112	0.131	-37285.902	14862.283	0.018
Quadratic term (coll.)	-16227.683	4613.410	0.001	3803.601	3473.180	0.282

Table A-8.: Statistical results for the invaded area evolution of HCT-116 and HT-29 spheroids in the Fully Embedded experiment. The coefficients were calculated with a Linear Mixed Model analysis taking into account that the collagen concentration was fixed. The reference group for performing the analysis was the spheroids polymerized following the two-stage scheme.

Spheroid area analyzed under a fixed collagen concentration in the fully embedded experiment										
Cell line	**Coefficient**	**[0.8 mg/mL]**			**[1.5 mg/mL]**			**[3.0 mg/mL]**		
		Value	**Std. Error**	**p-value**	**Value**	**Std. Error**	**p-value**	**Value**	**Std. Error**	**p-value**
HCT-116	**Intercept (ref)**	81618.269	3027.146	1.32E-16	81618.269	3027.146	1.32E-16	96996.833	3265.396	5.09E-18
	Linear term (ref)	210847.714	11231.684	1.00E-13	210847.714	11231.684	1.00E-13	213874.954	13510.052	8.87E-13
	Quadratic term (ref)	44739.697	6548.484	1.61E-06	44739.697	6548.484	1.61E-06	14467.621	7192.951	0.058
	Intercept (PI)	12827.488	4256.435	0.024	12827.488	4256.435	0.024	6023.167	5332.369	0.302
	Linear term (PI)	16963.435	15474.507	0.287	16963.435	15474.507	0.287	28411.171	22061.823	0.213
	Quadratic term (PI)	-7607.030	8827.402	0.400	-7607.030	8827.402	0.400	30734.416	11746.039	0.017
HT-29	**Intercept (ref)**							71811.1	5315.9	5.41E-20
	Linear term (ref)							137750.6	14943.8	3.65E-13
	Quadratic term (ref)							15257.5	3957.7	2.81E-4
	Intercept (PI)							-3356.8	7371.5	0.653
	Linear term (PI)							-115.3	20706.0	0.996
	Quadratic term (PI)							98.5	5470.7	0.986

B. Full time series evolution of the experiments described in Chapter 5

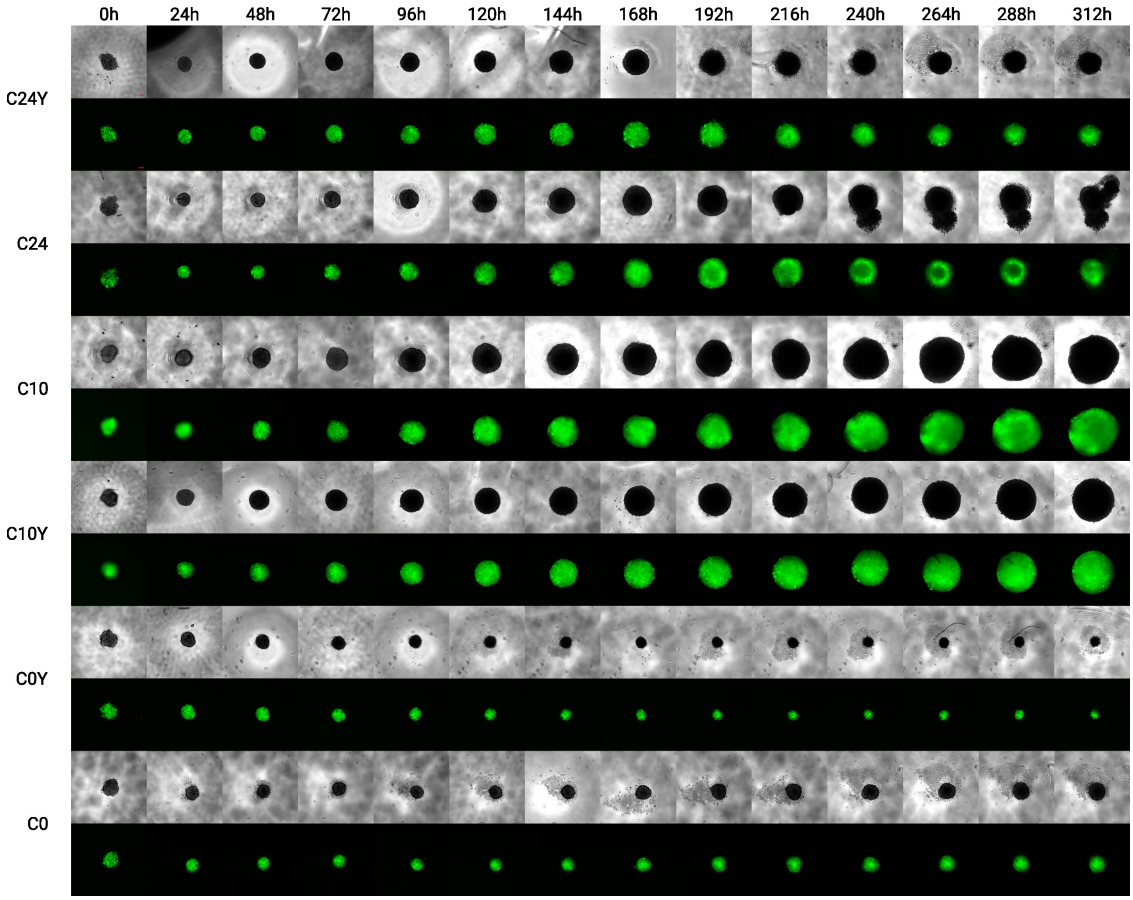

Figure B-1: Complete time series evolution of the spheroids treated with 100 μM Y-27632 (identified by the letter "Y" at the end of the label) in the chronic experiment. Scale bar: 100 μm.

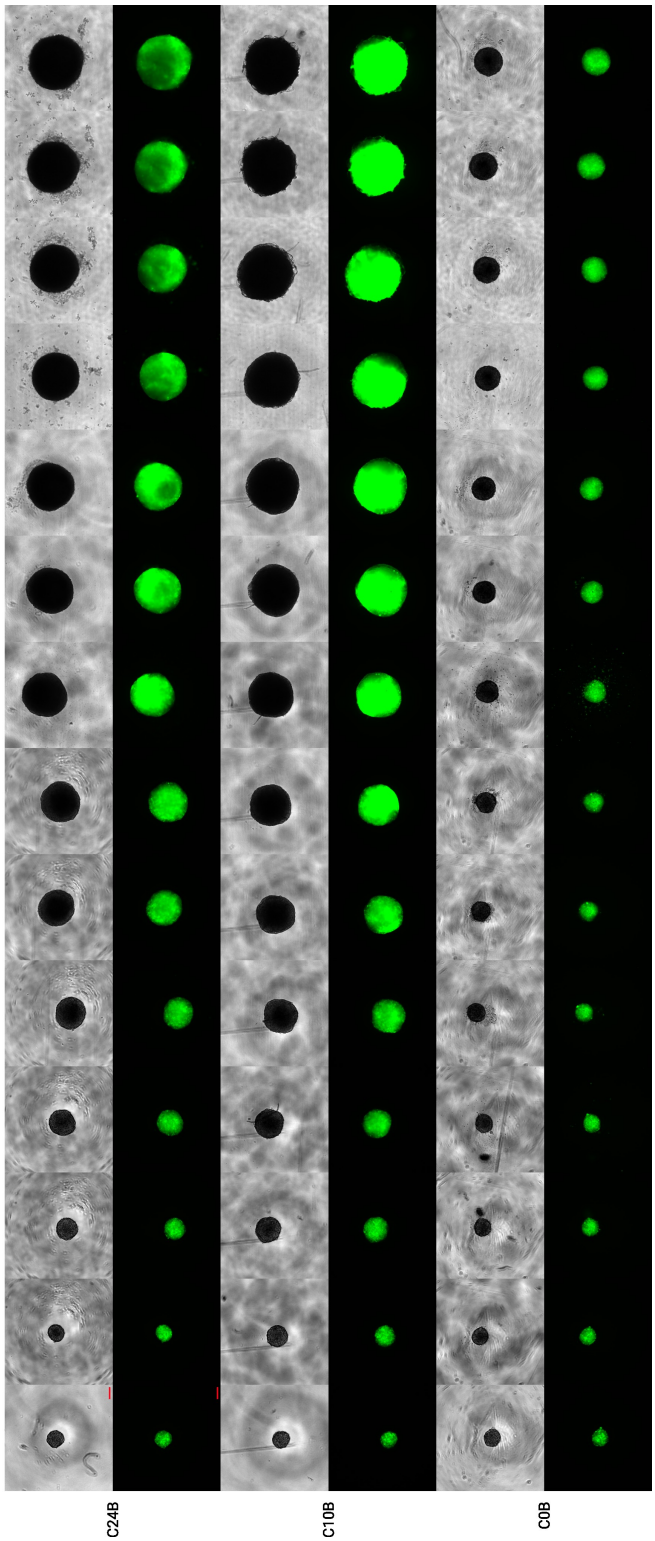

Figure B-2: Complete time series evolution of the spheroids treated with 10 μM Blebbistatin (identified by the letter "B" at the end of the label) in the chronic experiment. Scale bar: 100 μm.

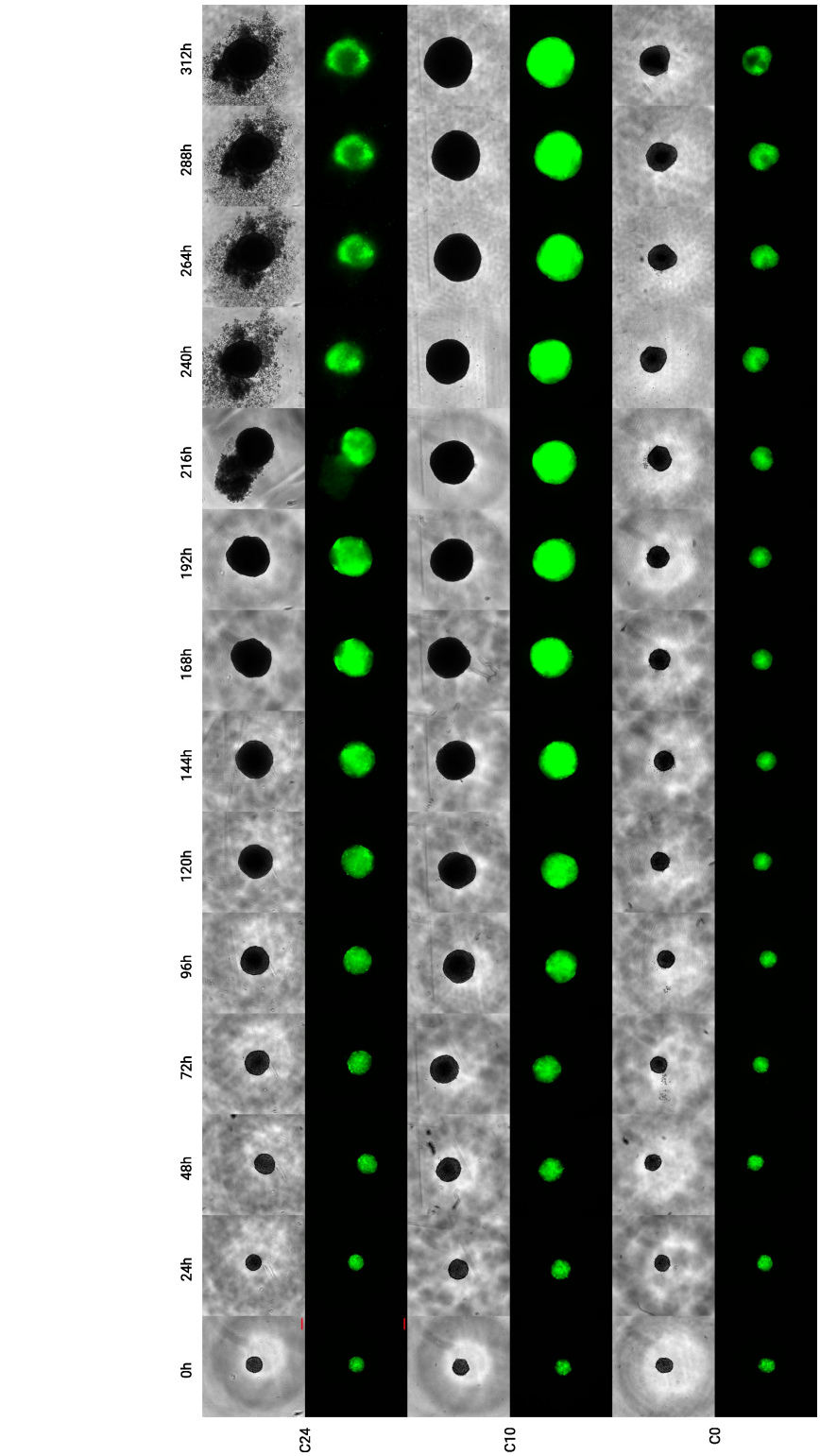

Figure B-3: Complete time series evolution of the non-treated spheroids in the Blebbistatin chronic experiment. Scale bar: 100 μm.

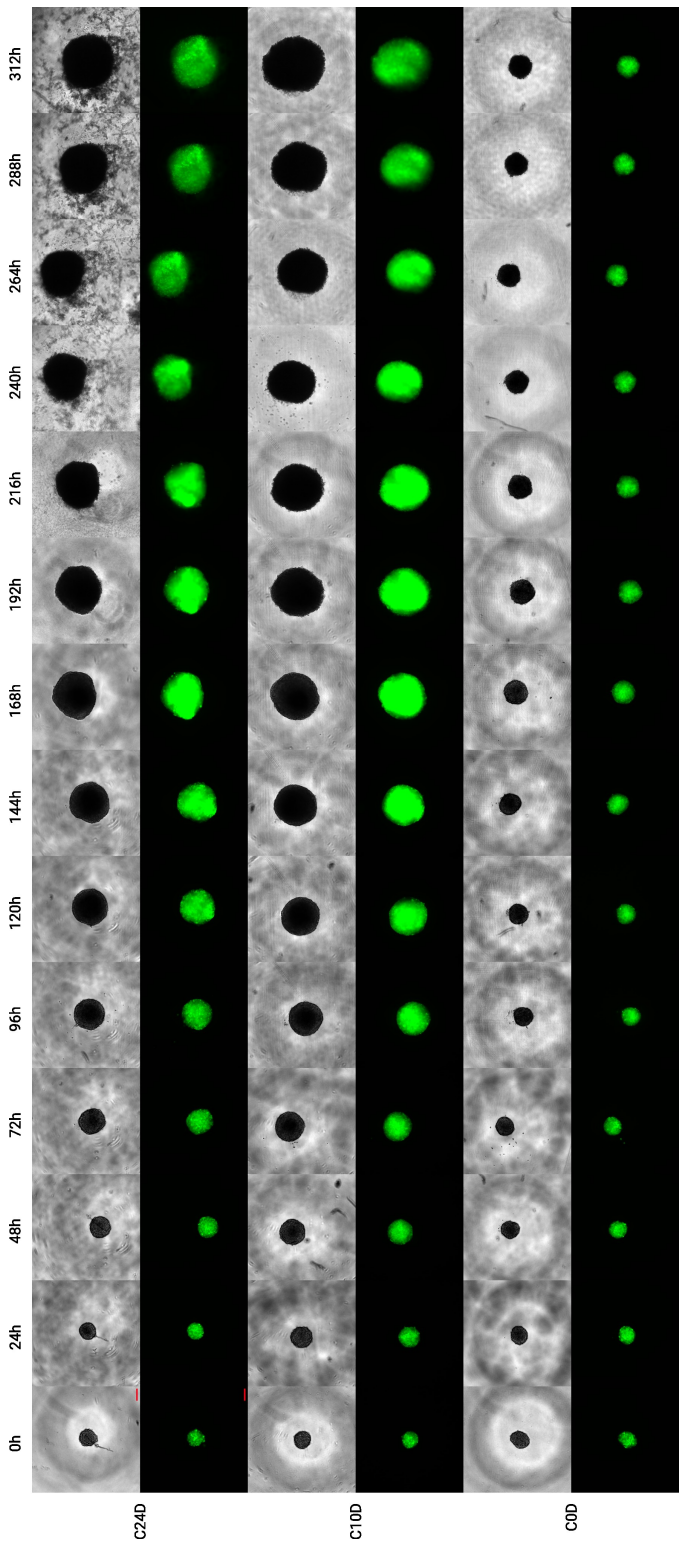

Figure B-4: Complete time series evolution of the DMSO control spheroids (identified by the letter "D" at the end of the label) in the Blebbistatin chronic experiment. Scale bar: 100 μm.

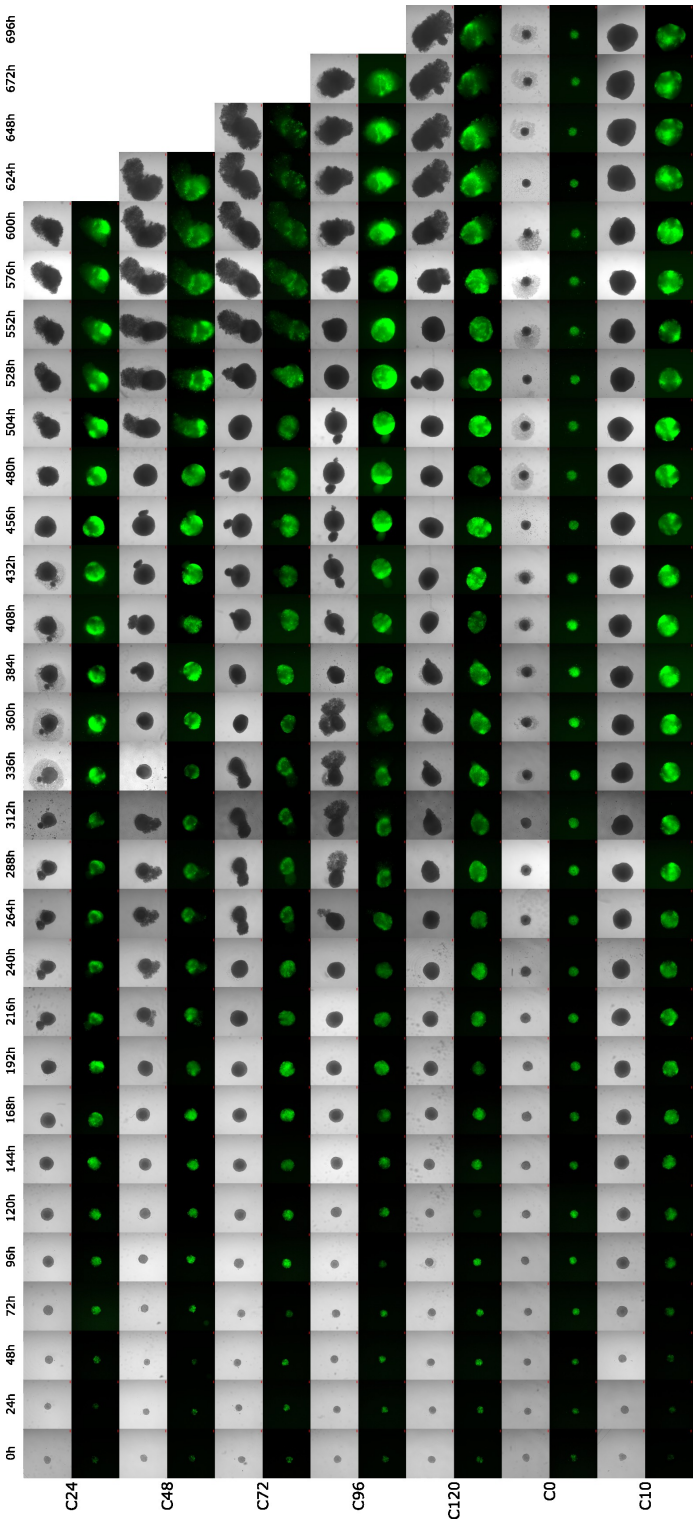

Figure B-5: Complete time series evolution of the DG10-D0 preconditioning experiment. Scale bar: 100 µm.

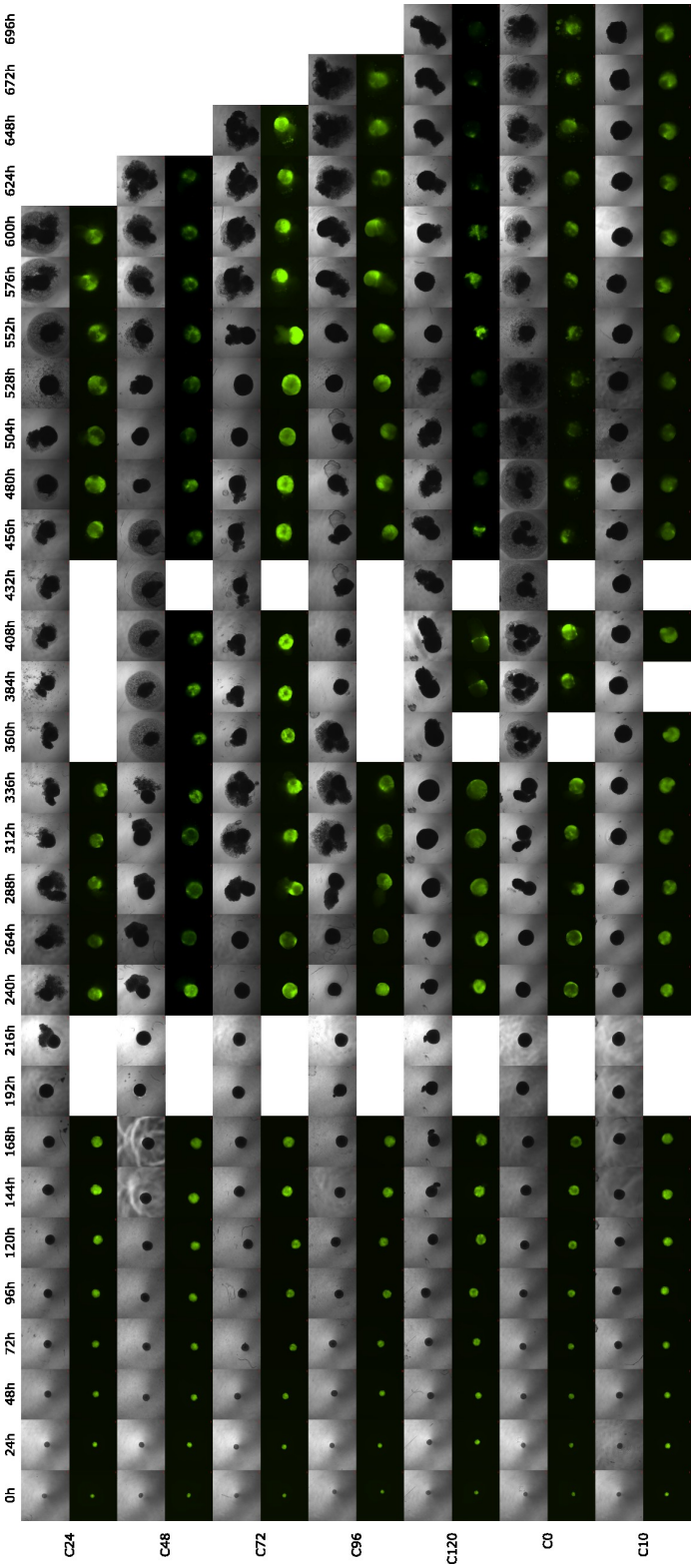

Figure B-6: Complete time series evolution of the DG10-D10 preconditioning experiment. Scale bar: 100 µm.

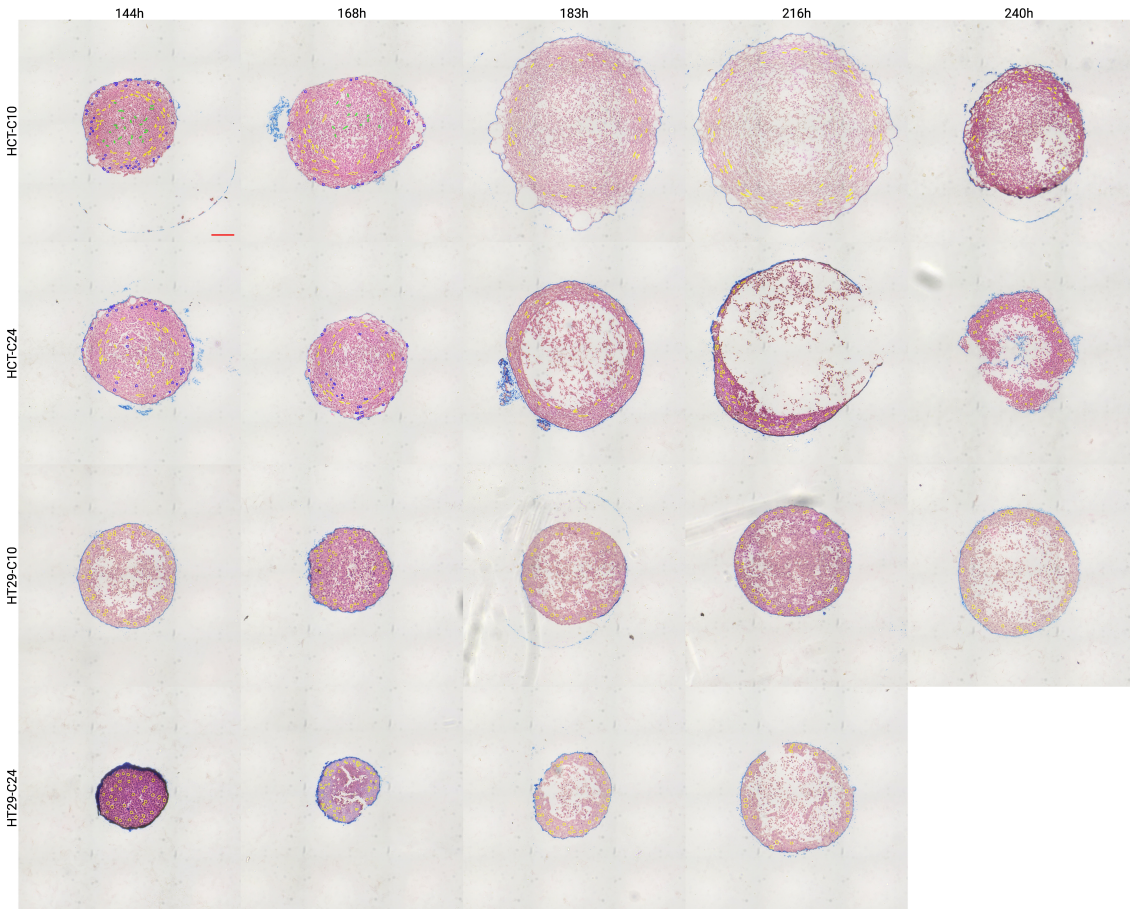

Figure B-7: Selection of cells for measuring roundness in H&E sections of HCT-116 and HT-29 spheroids. Scale bar: 100 µm.

References

[1] "Cancer keyfacts," http://www.who.int/en/news-room/fact-sheets/detail/cancer, last access: 25-10-2018.

[2] R. A. Weinberg, *The Biology of Cancer*. Garland Science, 2014.

[3] J. Luo, N. L. Solimini, and S. J. Elledge, "Review Principles of Cancer Therapy : Oncogene and Non-oncogene Addiction," *Cell*, pp. 823–837, 2009.

[4] D. Hanahan and R. A. Weinberg, "Hallmarks of cancer: the next generation," *Cell*, no. 144, pp. 646–674, 2011.

[5] D. Hanahan and L. M. Coussens, "Accessories to the Crime: Functions of Cells Recruited to the Tumor Microenvironment," *Cancer Cell*, vol. 21, no. 3, pp. 309–322, 2012. [Online]. Available: http://dx.doi.org/10.1016/j.ccr.2012.02.022

[6] D. Hanahan, "Hallmarks of Cancer: New Dimensions," *Cancer Discovery*, vol. 12, no. 1, pp. 31–46, 01 2022. [Online]. Available: https://doi.org/10.1158/2159-8290.CD-21-1059

[7] I. A. for Research on Cancer-World Health Organization, "Estimated number of new cases in 2020, worldwide, both sexes, all ages," https://gco.iarc.fr/today/online-analysis-pie?v=2020&mode=cancer&mode_population=continents&population=900&populations=900&key=total&sex=0&cancer=39&type=1&statistic=5&prevalence=0&population_group=0&ages_group%5B%5D=0&ages_group%5B%5D=17&nb_items=7&group_cancer=1&include_nmsc=1&include_nmsc_other=1&half_pie=0&donut=0, accesed: 18-07-2023.

[8] C. E. Bailey, C.-Y. Hu, Y. N. You, B. K. Bednarski, M. A. Rodriguez-Bigas, J. M. Skibber, S. B. Cantor, and G. J. Chang, "Increasing disparities in the age-related incidences of colon and rectal cancers in the united states, 1975-2010," *JAMA surgery*, vol. 150, no. 1, pp. 17–22, 2015.

[9] H. Sung, J. Ferlay, R. L. Siegel, M. Laversanne, I. Soerjomataram, A. Jemal, and F. Bray, "Global cancer statistics 2020: Globocan estimates of incidence and mortality worldwide for 36 cancers in 185 countries," *CA: a cancer journal for clinicians*, vol. 71, no. 3, pp. 209–249, 2021.

[10] E. E. Low, J. Demb, L. Liu, A. Earles, R. Bustamante, C. D. Williams, D. Provenzale, T. Kaltenbach, A. J. Gawron, M. E. Martinez *et al.*, "Risk factors for early-onset colorectal cancer," *Gastroenterology*, vol. 159, no. 2, pp. 492–501, 2020.

[11] D. V. Tauriello, A. Calon, E. Lonardo, and E. Batlle, "Determinants of metastatic competency in colorectal cancer," *Molecular Oncology*, vol. 11, no. 1, pp. 97–119, 2017.

[12] H. Clevers, "Review The Intestinal Crypt , A Prototype Stem Cell Compartment," *Cell*, vol. 154, no. 2, pp. 274–284, 2013. [Online]. Available: http://dx.doi.org/10.1016/j.cell.2013.07.004

[13] S. M. Powell, N. Zilz, Y. Beazer-Barclay, T. M. Bryan, S. R. Hamilton, S. N. Thiboudeau, B. Volgestein, and K. W. Kinzler, "APC mutations occur early during colorectal tumorigenesis," *Nature*, vol. 359, pp. 235–237, 1992.

[14] E. Botteri, S. Iodice, V. Bagnardi, S. Raimondi, A. B. Lowenfels, and P. Maisonneuve, "Smoking and colorectal cancer: a meta-analysis," *Jama*, vol. 300, no. 23, pp. 2765–2778, 2008.

[15] E. H. Jin, K. Han, C. M. Shin, D. H. Lee, S. J. Kang, J. H. Lim, and Y. J. Choi, "Sex and tumor-site differences in the association of alcohol intake with the risk of early-onset colorectal cancer," *Journal of Clinical Oncology*, vol. 0, no. 0, p. JCO.22.01895, 0, pMID: 37315287. [Online]. Available: https://doi.org/10.1200/JCO.22.01895

[16] P. J. Peeters, M. T. Bazelier, H. G. Leufkens, F. de Vries, and M. L. De Bruin, "The risk of colorectal cancer in patients with type 2 diabetes: associations with treatment stage and obesity," *Diabetes Care*, vol. 38, no. 3, pp. 495–502, 2015.

[17] F. Islami, A. Goding Sauer, K. D. Miller, R. L. Siegel, S. A. Fedewa, E. J. Jacobs, M. L. McCullough, A. V. Patel, J. Ma, I. Soerjomataram *et al.*, "Proportion and number of cancer cases and deaths attributable to potentially modifiable risk factors in the united states," *CA: a cancer journal for clinicians*, vol. 68, no. 1, pp. 31–54, 2018.

[18] S. C. Larsson, N. Orsini, and A. Wolk, "Diabetes mellitus and risk of colorectal cancer: a meta-analysis," *Journal of the National Cancer Institute*, vol. 97, no. 22, pp. 1679–1687, 2005.

[19] N. G. Amado, D. Predes, M. M. Moreno, I. O. Carvalho, F. A. Mendes, and J. G. Abreu, "Flavonoids and wnt/β-catenin signaling: Potential role in colorectal cancer therapies," *International Journal of Molecular Sciences*, vol. 15, no. 7, pp. 12 094–12 106, 2014. [Online]. Available: http://www.mdpi.com/1422-0067/15/7/12094

[20] M. J. Liptay and C. Mascaux, "Tnm staging," in *Malignant Tumors of the Lung: Evidence-based Management*, J.-P. Sculier and W. A. Fry, Eds. Berlin,

Heidelberg: Springer Berlin Heidelberg, 2004, pp. 183–188. [Online]. Available: https://doi.org/10.1007/978-3-642-18698-1_16

[21] P. F. Denoix, "Enquete permanent dans les centres anticancereux," *Bull. Inst. Nat. Hyg.*, vol. 1, pp. 70+, 1946.

[22] "Colorrectal cancer: stages," https://www.cancer.net/cancer-types/colorectal-cancer/stages, accedido: 25-10-2018.

[23] J. Flam, "High tumor stroma proportion is a worse prognostic factor in colorectal cancer," *ACTA CLINICA CROATICA*, pp. 73–79, 2017.

[24] I. J. Fidler, "The pathogenesis of cancer metastasis: the "seed and soil" hypothesis revisited," pp. 453–458, 2003.

[25] K. Podsypanina, Y.-C. N. Du, M. Jechlinger, L. J. Beverly, D. Hambardzumyan, and H. Varmus, "Seeding and propagation of untransformed mouse mammary cells in the lung," *Science*, vol. 321, pp. 1841–1844, 2008.

[26] J. Masagué and A. C. Obenauf, "Metastatic colonization," *Nature*, vol. 529, pp. 298–306, 2016.

[27] M. López-lázaro, "The migration ability of stem cells can explain the existence of cancer of unknown primary site . Rethinking metastasis ." *Oncoscience*, vol. 2, no. 5, pp. 467–475, 2015.

[28] G. Poste and I. J. Fidler, "The Pathogenesis of cancer metastasis," *Nature*, vol. 283, pp. 139–146, 1983.

[29] D. Hanahan and R. A. Weinberg, "The Hallmarks of Cancer," *Cell*, vol. 100, pp. 57–70, 2000.

[30] S. Vanharanta and J. Massagué, "Origins of Metastatic Traits," *Cancer Cell*, vol. 24, no. 4, pp. 410–421, 2014.

[31] W. H. Clark, M. A. Tucker, and A. M. Goldstein, "Parenchymal-stromal interactions in neoplasia: Theoretical considerations and observations in melanocytic neoplasia," *Acta Oncologica*, vol. 34, no. 6, pp. 749–757, 1995.

[32] K. R. Levental, H. Yu, L. Kass, J. N. Lakins, M. Egeblad, J. T. Erler, S. F. Fong, K. Csiszar, A. Giaccia, W. Weninger, M. Yamauchi, D. L. Gasser, and V. M. Weaver, "Matrix Crosslinking Forces Tumor Progression by Enhancing Integrin Signaling," *Cell*, vol. 139, no. 5, pp. 891–906, 2009. [Online]. Available: http://dx.doi.org/10.1016/j.cell.2009.10.027

[33] A. Nagelkerke, J. Bussink, A. E. Rowan, and P. N. Span, "The mechanical microenvironment in cancer: How physics affects tumours," *Seminars in Cancer Biology*, vol. 35, pp. 62–70, 2015. [Online]. Available: http://dx.doi.org/10.1016/j.semcancer.2015.09.001

[34] J. M. Lee, S. Dedhar, R. Kalluri, and E. W. Thompson, "The epithelial-mesenchymal transition: New insights in signaling, development, and disease," *Journal of Cell Biology*, vol. 172, no. 7, pp. 973–981, 2006.

[35] V. Catalano, A. Turdo, S. Di Franco, F. Dieli, M. Todaro, and G. Stassi, "Tumor and its microenvironment: A synergistic interplay," *Seminars in Cancer Biology*, vol. 23, no. 6 PB, pp. 522–532, 2013. [Online]. Available: http://dx.doi.org/10.1016/j.semcancer.2013.08.007

[36] O. De Wever and M. Mareel, "Role of tissue stroma in cancer cell invasion," *Journal of Pathology*, vol. 200, no. 4, pp. 429–447, 2003.

[37] M. J. Paszek, N. Zahir, K. R. Johnson, J. N. Lakins, G. I. Rozenberg, A. Gefen, C. A. Reinhart-King, S. S. Margulies, M. Dembo, D. Boettiger, D. A. Hammer, and V. M. Weaver, "Tensional homeostasis and the malignant phenotype," *Cancer Cell*, vol. 8, no. 3, pp. 241–254, 2005.

[38] P. P. Provenzano, D. R. Inman, K. W. Eliceiri, J. G. Knittel, L. Yan, C. T. Rueden, J. G. White, and P. J. Keely, "Collagen density promotes mammary tumor initiation and progression," *BMC Medicine*, vol. 6, pp. 1–15, 2008.

[39] O. De Wever, P. Demetter, M. Mareel, and M. Bracke, "Stromal myofibroblasts are drivers of invasive cancer growth," *International Journal of Cancer*, vol. 123, no. 10, pp. 2229–2238, 2008.

[40] M. R. Ng and J. S. Brugge, "A Stiff Blow from the Stroma: Collagen Crosslinking Drives Tumor Progression," *Cancer Cell*, vol. 16, no. 6, pp. 455–457, 2009. [Online]. Available: http://dx.doi.org/10.1016/j.ccr.2009.11.013

[41] K. Pietras and A. Östman, "Hallmarks of cancer: Interactions with the tumor stroma," *Experimental Cell Research*, vol. 316, no. 8, pp. 1324–1331, 2010. [Online]. Available: http://dx.doi.org/10.1016/j.yexcr.2010.02.045

[42] J. Jose, R. Samaniego, J. G. Goetz, S. Minguet, I. Navarro-le, T. Pellinen, A. Echarri, A. Cerezo, E. Calvo, M. Tello, T. Osteso-iba, E. Cukierman, A. J. P. Klein-szanto, R. Garcia, P. J. Keely, P. Sa, and M. A. D. Pozo, "Biomechanical Remodeling of the Microenvironment by Stromal Caveolin-1 Favors Tumor Invasion and Metastasis," *Cell*, pp. 148–163, 2011.

[43] H. Yu, J. K. Mouw, and V. M. Weaver, "Forcing form and function: Biomechanical regulation of tumor evolution," *Trends in Cell Biology*, vol. 21, no. 1, pp. 47–56, 2011. [Online]. Available: http://dx.doi.org/10.1016/j.tcb.2010.08.015

[44] M. Otranto, V. Sarrazy, B. Hinz, and G. Gabbiani, "The role of the myofibroblast in tumor stroma remodeling," *Cell Adhesion & Migration*, no. 6, pp. 203–219, 2012.

[45] H. Nyström, "Stromal collagens in colorectal cancer and in colorectal liver metastases: Tumour biological implications and a source for novel tumour markers," Ph.D. dissertation, Umea University, 2013.

[46] B. Hinz, "Myofibroblasts," *Experimental Eye Research*, vol. 142, pp. 56–70, 2015.

[47] K. M. Riching, B. L. Cox, M. R. Salick, C. Pehlke, A. S. Riching, S. M. Ponik, B. R. Bass, W. C. Crone, Y. Jiang, A. M. Weaver, K. W. Eliceiri, and P. J. Keely, "3D collagen alignment limits protrusions to enhance breast cancer cell persistence," *Biophysical Journal*, vol. 107, no. 11, pp. 2546–2558, 2015. [Online]. Available: http://dx.doi.org/10.1016/j.bpj.2014.10.035

[48] W. Han, S. Chen, W. Yuan, Q. Fan, J. Tian, X. Wang, L. Chen, X. Zhang, W. Wei, R. Liu, J. Qu, Y. Jiao, R. H. Austin, and L. Liu, "Oriented collagen fibers direct tumor cell intravasation," *Proceedings of the National Academy of Sciences*, vol. 113, pp. 11 208–11 213, 2016. [Online]. Available: http://www.pnas.org/lookup/doi/10.1073/pnas.1610347113

[49] F. Spill, D. S. Reynolds, R. D. Kamm, and M. H. Zaman, "Impact of the physical microenvironment on tumor progression and metastasis," *Current Opinion in Biotechnology*, vol. 40, pp. 41–48, 2016. [Online]. Available: http://dx.doi.org/10.1016/j.copbio.2016.02.007

[50] M. Takatsuna, S. Morohashi, T. Yoshizawa, H. Hirai, T. Haga, R. Ota, K. Saito, Y. Wu, H. Seino, Y. Aoyagi, S. Terai, and H. Kijima, "Myofibroblast distribution is associated with invasive growth types of colorectal cancer," *Oncology Reports*, vol. 36, no. 6, pp. 3154–3160, 2016.

[51] P. Nam Tay, P. Tan, Y. Lan, C. H.-W. Leung, M. Laban, T. C. Tan, H. Ni, J. Manikandan, S. B. A. Rashid, B. Yan, C. T. Yap, L. H. Kim Lin, Y. C. Lim, and S. C. Hooi, "Palladin, an actin-associated protein, is required for adherens junction formation and intercellular adhesion in HCT116 colorectal cancer cells," *International Journal of Oncology*, vol. 37, pp. 909–926, 2010.

[52] T. Wu and Y. Dai, "Tumor microenvironment and therapeutic response," *Cancer Letters*, vol. 387, pp. 61–68, 2017. [Online]. Available: http://dx.doi.org/10.1016/j.canlet.2016.01.043

[53] T. F. Hansen, S. Kjaer-Frifeldt, J. Lindebjerg, S. R. Rafaelsen, L. H. Jensen, A. Jakobsen, and F. B. Sörensen, "Tumor-stroma ratio predicts recurrence in patients with colon cancer treated with neoadjuvant chemotherapy," *Acta Oncologica*, vol. 57, no. 4, pp. 528–533, 2018. [Online]. Available: https://doi.org/10.1080/0284186X.2017.1385841

[54] C. T. Lim, B. Alexander, and M. P. Sheetz, "Mechanobiology," *Journal of the Royal Society Interface*, vol. 7, pp. S291–S293, 6 2010.

[55] M. C. van der Meulen and R. Huiskes, "Why mechanobiology?: A survey article," *Journal of Biomechanics*, vol. 35, no. 4, pp. 401–414, 2002. [Online]. Available: https://www.sciencedirect.com/science/article/pii/S0021929001001841

[56] D. Wirtz, K. Konstantopoulos, and P. C. Searson, "The physics of cancer: the role of physical interactions and mechanical forces in metastasis." *Nature reviews. Cancer*, vol. 11, pp. 512–22, 6 2011.

[57] Q. Luo, D. Kuang, B. Zhang, and G. Song, "Cell stiffness determined by atomic force microscopy and its correlation with cell motility," *Biochimica et Biophysica Acta (BBA) - General Subjects*, vol. 1860, no. 9, pp. 1953–1960, 2016. [Online]. Available: https://www.sciencedirect.com/science/article/pii/S030441651630215X

[58] K. D. Nyberg, S. L. Bruce, A. V. Nguyen, C. K. Chan, N. K. Gill, T.-H. Kim, E. K. Sloan, and A. C. Rowat, "Predicting cancer cell invasion by single-cell physical phenotyping," *Integrative Biology*, vol. 10, no. 4, pp. 218–231, 03 2018. [Online]. Available: https://doi.org/10.1039/C7IB00222J

[59] W. Yu, S. Sharma, E. Rao, A. C. Rowat, J. K. Gimzewski, D. Han, and J. Rao, "Cancer cell mechanobiology: a new frontier for cancer research," *Journal of the National Cancer Center*, vol. 2, no. 1, pp. 10–17, 2022. [Online]. Available: https://www.sciencedirect.com/science/article/pii/S2667005421000727

[60] P. Friedl and K. Wolf, "Plasticity of cell migration: A multiscale tuning model," *Journal of Cell Biology*, vol. 188, pp. 11–19, 2010.

[61] P. Friedl and S. Alexander, "Cancer invasion and the microenvironment: Plasticity and reciprocity," *Cell*, vol. 147, pp. 992–1009, 2011. [Online]. Available: http://dx.doi.org/10.1016/j.cell.2011.11.016

[62] X. Trepat, Z. Chen, and K. Jacobson, "Cell migration." *Comprehensive Physiology*, vol. 2, pp. 2369–92, 10 2012.

[63] M. Lintz, A. Munoz, and C. A. Reinhart-King, "The mechanics of single cell and collective migration of tumor cells." *Journal of biomechanical engineering*, vol. 139, pp. 0 210 051–9, 2 2017.

[64] M. Tozluoğlu, A. L. Tournier, R. P. Jenkins, S. Hooper, P. A. Bates, and E. Sahai, "Matrix geometry determines optimal cancer cell migration strategy and modulates response to interventions," *Nature cell biology*, vol. 15, no. 7, pp. 751–762, 2013.

[65] M. Abedin and N. King, "Diverse evolutionary paths to cell adhesion." *Trends in cell biology*, vol. 20, pp. 734–42, 12 2010.

[66] B. Acharya and A. Yap, "Cell-cell adhesion and the cytoskeleton," in *Encyclopedia of Cell Biology*, R. A. Bradshaw and P. D. Stahl, Eds. Waltham: Academic Press, 2016, pp. 704–712. [Online]. Available: https://www.sciencedirect.com/science/article/pii/B9780123944474200680

[67] C. Zihni, C. Mills, K. Matter, and M. S. Balda, "Tight junctions: from simple barriers to multifunctional molecular gates," *Nature Reviews Molecular Cell Biology*, vol. 17, pp. 564–580, 2016. [Online]. Available: https://doi.org/10.1038/nrm.2016.80

[68] A. Hartsock and W. J. Nelson, "Adherens and tight junctions: Structure, function and connections to the actin cytoskeleton," *Biochimica et Biophysica Acta (BBA) - Biomembranes*, vol. 1778, pp. 660–669, 3 2008.

[69] E. Delva, D. K. Tucker, and A. P. Kowalczyk, "The desmosome." *Cold Spring Harbor perspectives in biology*, vol. 1, p. a002543, 8 2009.

[70] J. Brunner, S. Ragupathy, and G. Borchard, "Target specific tight junction modulators," *Advanced Drug Delivery Reviews*, vol. 171, pp. 266–288, 2021. [Online]. Available: https://www.sciencedirect.com/science/article/pii/S0169409X21000429

[71] R. B. Hazan, L. Kang, B. P. Whooley, P. I. Borgen, R. B. Hazan, L. Kang, B. P. Whooley, P. I. Borgen, R. B. Hazan, L. A. N. Kang, B. P. Whooley, and P. Borgen, "Cell Adhesion and Communication N-Cadherin Promotes Adhesion Between Invasive Breast Cancer Cells and the Stroma N-Cadherin Promotes Adhesion Between Invasive Breast Cancer Cells and the Stroma," *Cell Adhesion and Communication*, vol. 4, no. 6, pp. 399–411, 1997.

[72] J. G. Lock, B. Wehrle-Haller, and S. Stromblad, "Cell-matrix adhesion complexes: master control machinery of cell migration." *Seminars in cancer biology*, vol. 18, pp. 65–76, 2 2008.

[73] W. Zhang, Y. Liu, and H. Zhang, "Extracellular matrix: an important regulator of cell functions and skeletal muscle development," *Cell and Bioscience*, vol. 11, 12 2021.

[74] P. Murray, G. Frampton, and P. N. Nelson, "Cell adhesion molecules. sticky moments in the clinic." *BMJ (Clinical research ed.)*, vol. 319, pp. 332–4, 8 1999.

[75] B. Geiger, J. P. Spatz, and A. D. Bershadsky, "Environmental sensing through focal adhesions." *Nature reviews. Molecular cell biology*, vol. 10, pp. 21–33, 1 2009.

[76] D. E. Discher, P. Janmey, and Y.-L. Wang, "Tissue cells feel and respond to the stiffness of their substrate." *Science (New York, N.Y.)*, vol. 310, pp. 1139–43, 11 2005.

[77] P. Ekblom, D. Vestweber, and R. Kemler, "Cell-matrix interactions and cell adhesion during development," *Annual Review of Cell Biology*, vol. 2, no. 1, pp. 27–47, 1986, pMID: 3548769. [Online]. Available: https://doi.org/10.1146/annurev.cb.02.110186.000331

[78] J. R. Sims, S. Karp, and D. E. Ingber, "Altering the cellular mechanical force balance results in integrated changes in cell, cytoskeletal and nuclear shape," *Journal of Cell Science*, vol. 103, no. 4, pp. 1215–1222, 12 1992. [Online]. Available: https://doi.org/10.1242/jcs.103.4.1215

[79] "What are cell-matrix adhesions?" https://www.mechanobio.info/what-is-mechanosignaling/what-is-the-extracellular-matrix-and-the-basal-lamina/, accesed: 19-07-2023.

[80] P. P. Provenzano, K. W. Eliceiri, J. M. Campbell, D. R. Inman, J. G. White, and P. J. Keely, "Collagen reorganization at the tumor-stromal interface facilitates local invasion," *BMC Medicine*, vol. 4, no. 38, pp. 1–15, 2006.

[81] J. M. Ayuso, H. A. Basheer, R. Monge, P. Sánchez-Álvarez, M. Doblaré, S. D. Shnyder, V. Vinader, K. Afarinkia, L. J. Fernández, and I. Ochoa, "Study of the chemotactic response of multicellular spheroids in a microfluidic device," *PLoS ONE*, vol. 10, no. 10, pp. 1–16, 2015.

[82] X. Gong, J. Kulwatno, and K. Mills, "Rapid fabrication of collagen bundles mimicking tumor-associated collagen architectures," *Acta Biomaterialia*, vol. 108, pp. 128–141, 2020. [Online]. Available: https://www.sciencedirect.com/science/article/pii/S1742706120301513

[83] B. Alberts, A. Johnson, and J. Lewis, "Chapter 11, the cytoskeleton and cell movement," in *Molecular Biology of the Cell. 4th edition*. Garland science, 2002, ch. 2, available from: https://www.ncbi.nlm.nih.gov/books/NBK26882/.

[84] "Cell energy and cell functions," https://www.nature.com/scitable/topicpage/cell-energy-and-cell-functions-14024533/, accesed: 19-09-2023.

[85] M. Akram, "Mini-review on glycolysis and cancer," *Journal of Cancer Education*, vol. 28, pp. 454–457, 2013. [Online]. Available: https://doi.org/10.1007/s13187-013-0486-9

[86] T. Alabduladhem and B. Bordoni, "Physiology, krebs cycle. [updated 2022 nov 23]." 2023. [Online]. Available: https://www.ncbi.nlm.nih.gov/books/NBK556032/

[87] I. Martínez-Reyes and N. S. Chandel, "Mitochondrial tca cycle metabolites control physiology and disease," *Nature Communications*, vol. 11, p. 102, 1 2020.

[88] O. Deshpande and S. Mohiuddin, "Biochemistry, oxidative phosphorylation. [updated 2023 jul 31]." 2023. [Online]. Available: https://www.ncbi.nlm.nih.gov/books/NBK553192/

[89] X. Zhong, X. He, Y. Wang, Z. Hu, H. Huang, S. Zhao, P. Wei, and D. Li, "Warburg effect in colorectal cancer: the emerging roles in tumor microenvironment and therapeutic implications," *Journal of Hematology & Oncology*, vol. 15, p. 160, 11 2022.

[90] J. Mathew, P. Sankar, and M. Varacallo, "Physiology, blood plasma. [updated 2023 apr 24]." 2023. [Online]. Available: https://www.ncbi.nlm.nih.gov/books/NBK531504/

[91] B. A. Barton, "Chapter 2 - general biology of salmonids," in *Principles of Salmonid Culture*, ser. Developments in Aquaculture and Fisheries Science, W. Pennell and B. A. Barton, Eds. Elsevier, 1996, vol. 29, pp. 29–95. [Online]. Available: https://www.sciencedirect.com/science/article/pii/S0167930996800056

[92] S. Schenk, G. J. Schoenhals, G. de Souza, and M. Mann, "A high confidence, manually validated human blood plasma protein reference set," *BMC Medical Genomics*, vol. 1, p. 41, 12 2008.

[93] K. Tateishi, W. Ando, C. Higuchi, D. A. Hart, J. Hashimoto, K. Nakata, H. Yoshikawa, and N. Nakamura, "Comparison of human serum with fetal bovine serum for expansion and differentiation of human synovial msc: Potential feasibility for clinical applications," *Cell Transplantation*, vol. 17, no. 5, pp. 549–557, 2008, pMID: 18714674. [Online]. Available: https://doi.org/10.3727/096368908785096024

[94] S. Liu, W. Yang, Y. Li, and C. Sun, "Fetal bovine serum, an important factor affecting the reproducibility of cell experiments." *Scientific reports*, vol. 13, p. 1942, 2 2023.

[95] C.-Y. Fang, C.-C. Wu, C.-L. Fang, W.-Y. Chen, and C.-L. Chen, "Long-term growth comparison studies of fbs and fbs alternatives in six head and neck cell lines," *PLOS ONE*, vol. 12, p. e0178960, 6 2017.

[96] D. J. Brat, B. Kaur, and E. G. V. Meir, "Genetic modulation of hypoxia induced gene expression and angiogenesis: relevance to brain tumors." *Frontiers in bioscience : a journal and virtual library*, vol. 8, pp. d100–16, 1 2003.

[97] S. N. Devenport, R. Singhal, M. D. Radyk, J. G. Taranto, S. A. Kerk, B. Chen, J. W. Goyert, C. Jain, N. K. Das, K. Oravecz-Wilson, L. Zhang, J. K. Greenson, Y. E. Chen, S. A. Soleimanpour, P. Reddy, C. A. Lyssiotis, and Y. M. Shah, "Colorectal cancer cells utilize autophagy to maintain mitochondrial metabolism for cell proliferation under nutrient stress." *JCI insight*, vol. 6, 6 2021.

[98] A. Lauzier, J. Normandeau-Guimond, V. Vaillancourt-Lavigueur, V. Boivin, M. Charbonneau, N. Rivard, M. S. Scott, C. M. Dubois, and S. Jean, "Colorectal cancer cells respond differentially to autophagy inhibition in vivo," *Scientific Reports*, vol. 9, p. 11316, 8 2019.

[99] M. Spada, C. Piras, G. Diana, V. P. Leoni, D. V. Frau, G. Serreli, G. Simbula, R. Loi, A. Noto, F. Murgia, P. Caria, and L. Atzori, "Glutamine starvation affects cell cycle, oxidative homeostasis and metabolism in colorectal cancer cells," *Antioxidants*, vol. 12, p. 683, 3 2023.

[100] K. Srichaikul, R. A. Hegele, and D. J. Jenkins, "Great chinese famine and the effects on cardiometabolic health for future generations," *Hypertension*, vol. 79, no. 3, pp. 532–535, 2022. [Online]. Available: https://www.ahajournals.org/doi/abs/10.1161/HYPERTENSIONAHA.121.18546

[101] P. González-Rodríguez, J. Fullgrabe, and B. Joseph, "The hunger strikes back: an epigenetic memory for autophagy," *Cell Death & Differentiation*, vol. 30, pp. 1404–1415, 6 2023.

[102] J. C. Gomez-Verjan, O. S. Barrera-Vázquez, L. García-Velázquez, R. Samper-Ternent, and P. Arroyo, "Epigenetic variations due to nutritional status in early-life and its later impact on aging and disease," *Clinical Genetics*, vol. 98, pp. 313–321, 10 2020.

[103] C. Tiffon, "The impact of nutrition and environmental epigenetics on human health and disease." *International journal of molecular sciences*, vol. 19, 11 2018.

[104] C. Gregg, "Starvation and climate change-how to constrain cancer cell epigenetic diversity and adaptability to enhance treatment efficacy," *Frontiers in Ecology and Evolution*, vol. 9, 6 2021.

[105] K. Izuishi, K. Kato, T. Ogura, T. Kinoshita, and H. Esumi, "Remarkable Tolerance of Tumor Cells to Nutrient Deprivation: Possible New Biochemical Target for Cancer Therapy," *Cancer Research*, vol. 60, no. 21, pp. 6201–6207, 11 2000.

[106] C. Lee, L. Raffaghello, S. Brandhorst, F. M. Safdie, G. Bianchi, A. Martin-Montalvo, V. Pistoia, M. Wei, S. Hwang, A. Merlino, L. Emionite, R. de Cabo, and V. D. Longo, "Fasting cycles retard growth of tumors and sensitize a range of cancer cell types to chemotherapy," *Science Translational Medicine*, vol. 4, 3 2012.

[107] W. Palm, "Metabolic plasticity allows cancer cells to thrive under nutrient starvation," *Proceedings of the National Academy of Sciences*, vol. 118, 4 2021.

[108] P.-Y. Tsai, M.-S. Lee, U. Jadhav, I. Naqvi, S. Madha, A. Adler, M. Mistry, S. Naumenko, C. A. Lewis, D. S. Hitchcock, F. R. Roberts, P. DelNero, T. Hank, K. C. Honselmann, V. M. Oyarvide, M. Mino-Kenudson, C. B. Clish, R. A. Shivdasani, and N. Y. Kalaany, "Adaptation of pancreatic cancer cells to nutrient deprivation is reversible and requires glutamine synthetase stabilization by mtorc1," *Proceedings of the National Academy of Sciences*, vol. 118, 3 2021.

[109] V. Viallard, C. Denis, V. Trocheris, and J. Murat, "Effect of glutamine deprivation and glutamate or ammonium chloride addition on growth rate, metabolism and differentiation of human colon cancer cell-line ht29," *International Journal of Biochemistry*, vol. 18, pp. 263–269, 1 1986.

[110] M. Kapalczynska, T. Kolenda, W. Przybyla, M. Zajaczkowska, A. Teresiak, V. Filas, M. Ibbs, R. Blizniak, L. Luczewski, and K. Lamperska, "2d and 3d cell cultures â€" a comparison of different types of cancer cell cultures," *Archives of Medical Science*, 2016.

[111] S. Breslin and L. O'Driscoll, "Three-dimensional cell culture: the missing link in drug discovery," *Drug Discovery Today*, vol. 18, pp. 240–249, 3 2013.

[112] B. M. Baker and C. S. Chen, "Deconstructing the third dimension â€" how 3d culture microenvironments alter cellular cues," *Journal of Cell Science*, 1 2012.

[113] K. Sato, K. Tsuchihara, S. Fujii, M. Sugiyama, T. Goya, Y. Atomi, T. Ueno, A. Ochiai, and H. Esumi, "Autophagy is activated in colorectal cancer cells and contributes to the tolerance to nutrient deprivation," *Cancer Research*, vol. 67, pp. 9677–9684, 10 2007.

[114] K. Ohshima and E. Morii, "Metabolic reprogramming of cancer cells during tumor progression and metastasis," *Metabolites*, vol. 11, p. 28, 1 2021.

[115] D. E. Biancur and A. C. Kimmelman, "The plasticity of pancreatic cancer metabolism in tumor progression and therapeutic resistance," *Biochimica et Biophysica Acta (BBA) - Reviews on Cancer*, vol. 1870, pp. 67–75, 8 2018.

[116] R. E. Brown, S. P. Short, and C. S. Williams, "Colorectal cancer and metabolism," *Current Colorectal Cancer Reports*, vol. 14, pp. 226–241, 12 2018.

[117] M. Reina-Campos, J. Moscat, and M. Diaz-Meco, "Metabolism shapes the tumor microenvironment," *Current Opinion in Cell Biology*, vol. 48, pp. 47–53, 10 2017.

[118] T. Stankovic, T. Randelovic, M. Dragoj, S. S. Buric, L. Fernández, I. Ochoa, V. M. Pérez-García, and M. Pesic, "In vitro biomimetic models for glioblastoma-a promising tool for drug response studies," *Drug Resistance Updates*, vol. 55, p. 100753, 3 2021.

[119] E. Gheytanchi, M. Naseri, F. Karimi-Busheri, F. Atyabi, E. S. Mirsharif, M. Bozorgmehr, R. Ghods, and Z. Madjd, "Morphological and molecular characteristics of spheroid formation in ht-29 and caco-2 colorectal cancer cell lines," *Cancer Cell International*, vol. 21, p. 204, 4 2021.

[120] T. R. Tidwell, G. V. Rosland, K. J. Tronstad, K. SÃ¸reide, and H. R. Hagland, "Metabolic flux analysis of 3d spheroids reveals significant differences in glucose metabolism from matched 2d cultures of colorectal cancer and pancreatic ductal adenocarcinoma cell lines," *Cancer & Metabolism*, vol. 10, p. 9, 12 2022.

[121] A. Sargenti, F. Musmeci, F. Bacchi, C. Delprete, D. A. Cristaldi, F. Cannas, S. Bonetti, S. Pasqua, D. Gazzola, D. Costa, F. Villa, M. R. Zocchi, and A. Poggi, "Physical characterization of colorectal cancer spheroids and evaluation of nk cell infiltration through a flow-based analysis," *Frontiers in Immunology*, vol. 11, 12 2020.

[122] F. Hirschhaeuser, H. Menne, C. Dittfeld, J. West, W. Mueller-Klieser, and L. A. Kunz-Schughart, "Multicellular tumor spheroids: An underestimated tool is catching up again," *Journal of Biotechnology*, vol. 148, pp. 3–15, 7 2010.

[123] F. Robledo, L. González-Hodar, P. Tapia, A.-M. Figueroa, F. Ezquer, and V. Cortés, "Spheroids derived from the stromal vascular fraction of adipose tissue self-organize in complex adipose organoids and secrete leptin," *Stem Cell Research & Therapy*, vol. 14, p. 70, 4 2023.

[124] X. Gong, C. Lin, J. Cheng, J. Su, H. Zhao, T. Liu, X. Wen, and P. Zhao, "Generation of multicellular tumor spheroids with microwell-based agarose scaffolds for drug testing," *PLOS ONE*, vol. 10, p. e0130348, 6 2015.

[125] S. A. Langhans, "Three-dimensional in vitro cell culture models in drug discovery and drug repositioning," *Frontiers in Pharmacology*, vol. 9, 1 2018.

[126] J. Ro, J. Kim, and Y.-K. Cho, "Recent advances in spheroid-based microfluidic models to mimic the tumour microenvironment," *The Analyst*, vol. 147, pp. 2023–2034, 2022.

[127] R. Vadivelu, H. Kamble, M. Shiddiky, and N.-T. Nguyen, "Microfluidic technology for the generation of cell spheroids and their applications," *Micromachines*, vol. 8, p. 94, 3 2017.

[128] M. Marimuthu, N. Rousset, A. St-Georges-Robillard, M. A. Lateef, M. Ferland, A.-M. Mes-Masson, and T. Gervais, "Multi-size spheroid formation using microfluidic funnels," *Lab on a Chip*, vol. 18, pp. 304–314, 2018.

[129] N. Azizipour, R. Avazpour, M. Sawan, D. H. Rosenzweig, and A. Ajji, "Uniformity of spheroids-on-a-chip by surface treatment of pdms microfluidic platforms," *Sensors & Diagnostics*, vol. 1, pp. 750–764, 2022.

[130] G. R. Souza, J. R. Molina, R. M. Raphael, M. G. Ozawa, D. J. Stark, C. S. Levin, L. F. Bronk, J. S. Ananta, J. Mandelin, M.-M. Georgescu, J. A. Bankson, J. G. Gelovani, T. C. Killian, W. Arap, and R. Pasqualini, "Three-dimensional tissue culture based on magnetic cell levitation," *Nature Nanotechnology*, vol. 5, pp. 291–296, 4 2010.

[131] E. E. Antoine, P. P. Vlachos, and M. N. Rylander, "Review of collagen i hydrogels for bioengineered tissue microenvironments: Characterization of mechanics, structure, and transport," *Tissue Engineering – Part B: Reviews*, vol. 20, pp. 683–696, 2014.

[132] M. Albu, I. Titorencu, and M. Ghica, "Collagen-based drug delivery systems for tissue engineering. in: Pignatello, r.(ed.) biomaterials applications for nanomedicine," *Intech Open Acces Publisher, Rijeka*, vol. 339, 2011.

[133] K. G. Nairon, T. J. DePalma, J. M. Zent, J. L. Leight, and A. Skardal, "Tumor cell-conditioned media drives collagen remodeling via fibroblast and pericyte activation in an in vitro premetastatic niche model," *iScience*, vol. 25, p. 104645, 7 2022.

[134] M. Devarasetty, A. Skardal, K. Cowdrick, F. Marini, and S. Soker, "Bioengineered submucosal organoids for in vitro modeling of colorectal cancer," *Tissue Engineering Part A*, vol. 23, pp. 1026–1041, 10 2017.

[135] R. E. Rivero, V. Capella, A. C. Liaudat, P. Bosch, C. A. Barbero, N. RodrÃguez, and C. R. Rivarola, "Mechanical and physicochemical behavior of a 3d hydrogel scaffold during cell growth and proliferation," *RSC Advances*, vol. 10, pp. 5827–5837, 2020.

[136] M. Jeitany, C. Leroy, P. Tosti, M. Lafitte, J. L. Guet, V. Simon, D. Bonenfant, B. Robert, F. Grillet, C. Mollevi, S. E. Messaoudi, A. Otandault, L. Canterel-Thouennon, M. Busson, A. R. Thierry, P. Martineau, J. Pannequin, S. Roche, and A. Sirvent, "Inhibition of ddr 1-bcr signalling by nilotinib as a new therapeutic strategy for metastatic colorectal cancer," *EMBO Molecular Medicine*, vol. 10, 4 2018.

[137] M. Demeter, I. Calina, A. Scarisoreanu, M. Micutz, and M. A. Kaya, "Correlations on the structure and properties of collagen hydrogels produced by e-beam crosslinking," *Materials*, vol. 15, p. 7663, 10 2022.

[138] A. Avendano, J. J. Chang, M. G. Cortes-Medina, A. J. Seibel, B. R. Admasu, C. M. Boutelle, A. R. Bushman, A. A. Garg, C. M. DeShetler, S. L. Cole, and J. W. Song, "Integrated biophysical characterization of fibrillar collagen-based hydrogels," *ACS Biomaterials Science & Engineering*, vol. 6, pp. 1408–1417, 3 2020.

[139] S. I. Fraley, P. hsun Wu, L. He, Y. Feng, R. Krisnamurthy, G. D. Longmore, and D. Wirtz, "Three-dimensional matrix fiber alignment modulates cell migration and mt1-mmp utility by spatially and temporally directing protrusions," *Scientific Reports*, vol. 5, p. 14580, 10 2015.

[140] B. M. Leung, S. C. Lesher-Perez, T. Matsuoka, C. Moraes, and S. Takayama, "Media additives to promote spheroid circularity and compactness in hanging drop platform," *Biomaterials Science*, vol. 3, pp. 336–344, 2015.

[141] P. Longati, X. Jia, J. Eimer, A. Wagman, M.-R. Witt, S. Rehnmark, C. Verbeke, R. Toftgard, M. Lohr, and R. L. Heuchel, "3d pancreatic carcinoma spheroids induce a matrix-rich, chemoresistant phenotype offering a better model for drug testing," *BMC Cancer*, vol. 13, p. 95, 12 2013.

[142] J. L. Hutter and J. Bechhoefer, "Calibration of atomic–force microscope tips," *Review of Scientific Instruments*, vol. 64, pp. 1868–1873, 1993.

[143] S. Lempereur, E. Machado, F. Licata, L. Buzer, I. Robineau, J. Hémon, P. Banerjee, N. D. Crozé, M. Léonard, P. Affaticati, A. Jenett, H. Talbot, and J.-S. Joly, "Zebrainspector, a whole organism screening platform enabling volumetric analysis of zebrafish brain white matter," *bioRxiv*, 2020. [Online]. Available: https://www.biorxiv.org/content/early/2020/10/26/2020.10.26.353656

[144] D. Lacalle, H. A. Castro-Abril, T. Randelovic, C. Domínguez, J. Heras, E. Mata, G. Mata, Y. Méndez, V. Pascual, and I. Ochoa, "Spheroidj: An open–source set of tools for spheroid segmentation," *Computer Methods and Programs in Biomedicine*, vol. 200, p. 105837, 2021. [Online]. Available: https://www.sciencedirect.com/science/article/pii/S0169260720316709

[145] R. C. Team, "R: A language and environment for statistical computing," 2013. [Online]. Available: http://www.r-project.org/

[146] J. Pinheiro and D. Bates, *Mixed-Effects Models in S and S-PLUS*. Springer New York, NY, 2000.

[147] J. Pinheiro, D. Bates, and R. C. Team, "nlme: Linear and nonlinear mixed effects models," 2022, r package version 3.1-159. [Online]. Available: https://cran.r-project.org/package=nlme

[148] K. Oberauer, "The importance of random slopes in mixed models for bayesian hypothesis testing," *Psychological Science*, vol. 33, pp. 648–665, 2022, pMID: 35357978. [Online]. Available: https://doi.org/10.1177/09567976211046884

[149] E. Whitley and J. Ball, "Statistics review 6: Nonparametric methods." *Critical care (London, England)*, vol. 6, pp. 509–13, 12 2002.

[150] ——, "Statistics review 5: Comparison of means." *Critical care (London, England)*, vol. 6, pp. 424–8, 10 2002.

[151] A. Ghasemi and S. Zahediasl, "Normality tests for statistical analysis: a guide for non-statisticians." *International journal of endocrinology and metabolism*, vol. 10, pp. 486–9, 2012.

[152] K. Fradette, H. J. Keselman, J. Algina, L. Lix, and R. R. Wilcox, "Conventional and robust paired and independent-samples t tests: Type i error and power rates," *Journal of Modern Applied Statistical Methods*, vol. 2, pp. 481–496, 2003.

[153] E. Whitley and J. Ball, "Statistics review 3: Hypothesis testing and p values," *Critical Care*, vol. 6, p. 222, 2002.

[154] P. S. Steeg, "Tumor metastasis: mechanistic insights and clinical challenges," *Nature Medicine*, vol. 12, pp. 895–904, 2006. [Online]. Available: https://doi.org/10.1038/nm1469

[155] S. Cattin, L. Ramont, and C. Ruegg, "Characterization and in vivo validation of a three–dimensional multi–cellular culture model to study heterotypic interactions in colorectal cancer cell growth, invasion and metastasis," *Frontiers in Bioengineering and Biotechnology*, vol. 6, pp. 1–14, 2018.

[156] G. Ciccone, O. Dobre, G. M. Gibson, J. M. Rey, C. G. Garcia, M. Vassalli, M. S. Sanchez, and M. Tassieri, "What caging force cells feel in 3d hydrogels: A rheological perspective," *Advanced Healthcare Materials*, vol. 9, pp. 1–6, 2020.

[157] R. Weigert, M. Sramkova, L. Parente, P. Amornphimoltham, and A. Masedunskas, "Intravital microscopy: a novel tool to study cell biology in living animals." *Histochemistry and cell biology*, vol. 133, pp. 481–491, 5 2010.

[158] Y. W. Choo, J. Jeong, and K. Jung, "Recent advances in intravital microscopy for investigation of dynamic cellular behavior in vivo." *BMB reports*, vol. 53, pp. 357–366, 7 2020.

[159] N. Levy, "The use of animal as models: Ethical considerations," *International Journal of Stroke*, vol. 7, pp. 440–442, 2012, pMID: 22712743. [Online]. Available: https://doi.org/10.1111/j.1747--4949.2012.00772.x

[160] M. Mak, F. Spill, R. D. Kamm, and M. H. Zaman, "Single–cell migration in complex microenvironments: Mechanics and signaling dynamics." *Journal of biomechanical engineering*, vol. 138, p. 21004, 2 2016.

[161] O. Ilina, P. G. Gritsenko, S. Syga, J. Lippoldt, C. A. M. L. Porta, O. Chepizhko, S. Grosser, M. Vullings, G.-J. Bakker, J. Starruss, P. Bult, S. Zapperi, J. A. Kas, A. Deutsch, and P. Friedl, "Cell-cell adhesion and 3d matrix confinement determine jamming transitions in breast cancer invasion," *Nature Cell Biology*, vol. 22, pp. 1103–1115, 2020. [Online]. Available: https://doi.org/10.1038/s41556--020--0552--6

[162] B. R. Seo, X. Chen, L. Ling, Y. H. Song, A. A. Shimpi, S. Choi, J. Gonzalez, J. Sapudom, K. Wang, R. C. A. Eguiluz, D. Gourdon, V. B. Shenoy, and C. Fischbach, "Collagen microarchitecture mechanically controls myofibroblast differentiation," *Proceedings of the National Academy of Sciences of the United States of America*, vol. 117, 2020.

[163] E. Brauchle, J. Kasper, R. Daum, N. Schierbaum, C. Falch, A. Kirschniak, T. E. Schaffer, and K. Schenke-Layland, "Biomechanical and biomolecular characterization of extracellular matrix structures in human colon carcinomas," *Matrix Biology*, vol. 68–69, pp. 180–193, 2018, sI : Fibrosis - Mechanisms and Translational Aspects. [Online]. Available: https://www.sciencedirect.com/science/article/pii/S0945053X1730447X

[164] L. G. Rodriguez, X. Wu, and J.-L. Guan, "Wound–healing assay." *Methods in molecular biology (Clifton, N.J.)*, vol. 294, pp. 23–29, 2005.

[165] K. F. Lei, H.-P. Tseng, C.-Y. Lee, and N.-M. Tsang, "Quantitative study of cell invasion process under extracellular stimulation of cytokine in a microfluidic device," *Scientific Reports*, vol. 6, p. 25557, 2016. [Online]. Available: https://doi.org/10.1038/srep25557

[166] N. Kramer, A. Walzl, C. Unger, M. Rosner, G. Krupitza, M. HengstschlÃ¤ger, and H. Dolznig, "In vitro cell migration and invasion assays," *Mutation Research – Reviews in Mutation Research*, vol. 752, pp. 10–24, 2013.

[167] H.-C. Chen, "Boyden chamber assay." *Methods in molecular biology (Clifton, N.J.)*, vol. 294, pp. 15–22, 2005.

[168] H. Liu, T. Lu, G. J. Kremers, A. L. Seynhaeve, and T. L. T. Hagen, "A microcarrier–based spheroid 3d invasion assay to monitor dynamic cell movement in extracellular matrix," *Biological Procedures Online*, vol. 22, pp. 1–12, 2020.

[169] H. Dolznig, C. Rupp, C. Puri, C. Haslinger, N. Schweifer, E. Wieser, D. Kerjaschki, and P. Garin-Chesa, "Modeling colon adenocarcinomas in vitro: A 3d co-culture system induces cancer-relevant pathways upon tumor cell and stromal fibroblast interaction," *American Journal of Pathology*, vol. 179, pp. 487–501, 2011. [Online]. Available: http://dx.doi.org/10.1016/j.ajpath.2011.03.015

[170] C. J. Olsen, J. Moreira, E. M. Lukanidin, and N. S. Ambartsumian, "Human mammary fibroblasts stimulate invasion of breast cancer cells in a three–dimensional culture and increase stroma development in mouse xenografts," *BMC Cancer*, vol. 10, p. 444, 2010. [Online]. Available: https://doi.org/10.1186/1471--2407--10--444

[171] J.-I. Park, J. Lee, J.-L. Kwon, H.-B. Park, S.-Y. Lee, J.-Y. Kim, J. Sung, J. M. Kim, K. S. Song, and K.-H. Kim, "Scaffold-free coculture spheroids of human colonic adenocarcinoma cells and normal colonic fibroblasts promote tumorigenicity in nude mice." *Translational oncology*, vol. 9, pp. 79–88, 2 2016.

[172] M. Ducker, V. Millar, D. Ebner, and F. G. Szele, "A semi–automated and scalable 3d spheroid assay to study neuroblast migration," *Stem Cell Reports*, vol. 15, pp. 789–802, 2020. [Online]. Available: https://www.sciencedirect.com/science/article/pii/S2213671120302897

[173] E. T. Costa and A. A. Camargo, "Beyond the proteolytic activity: Examining the functional relevance of the ancillary domains using tri–dimensional (3d) spheroid invasion assay." *Methods in molecular biology (Clifton, N.J.)*, vol. 1731, pp. 155–168, 2018.

[174] M. Vinci, C. Box, and S. A. Eccles, "Three–dimensional (3d) tumor spheroid invasion assay," *JoVE*, p. e52686, 2015. [Online]. Available: https://www.jove.com/t/52686

[175] K. M. Charoen, B. Fallica, Y. L. Colson, M. H. Zaman, and M. W. Grinstaff, "Embedded multicellular spheroids as a biomimetic 3d cancer model for evaluating drug and drug–device combinations." *Biomaterials*, vol. 35, pp. 2264–2271, 2 2014.

[176] J. Lecomte, A. Masset, S. Blacher, L. Maertens, A. Gothot, M. Delgaudine, F. Bruyere, O. Carnet, J. Paupert, M. Illemann, J.-M. Foidart, I. K. Lund, G. Hoyer-Hansen, and A. Noel, "Bone marrow–derived myofibroblasts are the providers of pro–invasive matrix metalloproteinase 13 in primary tumor." *Neoplasia (New York, N.Y.)*, vol. 14, pp. 943–951, 10 2012.

[177] J. Ko, J. Ahn, S. Kim, Y. Lee, J. Lee, D. Park, and N. L. Jeon, "Tumor spheroid–on–a–chip: a standardized microfluidic culture platform for investigating tumor angiogenesis," *Lab Chip*, vol. 19, pp. 2822–2833, 2019. [Online]. Available: http://dx.doi.org/10.1039/C9LC00140A

[178] J. Guyon, L. Andrique, N. Pujol, G. V. RÃ¸sland, G. Recher, A. Bikfalvi, and T. Daubon, "A 3d spheroid model for glioblastoma." *Journal of visualized experiments : JoVE*, 4 2020.

[179] J.-B. Guy, S. Espenel, A. Vallard, P. Battiston-Montagne, A.-S. Wozny, D. Ardail, G. Alphonse, C. Rancoule, C. Rodriguez-Lafrasse, and N. Magne, "Evaluation of the cell invasion and migration process: A comparison of the video microscope–based scratch wound assay and the boyden chamber assay." *Journal of visualized experiments : JoVE*, 11 2017.

[180] S. D. Richbart, J. C. Merritt, E. G. Moles, K. C. Brown, A. A. Adeluola, P. T. Finch, J. A. Hess, M. T. Tirona, S. L. Miles, M. A. Valentovic, and P. Dasgupta, "Spherical invasion assay: A novel method to measure invasion of cancer cells," *Bio–protocol*, vol. 12, p. e4320, 2022. [Online]. Available: https://doi.org/10.21769/BioProtoc.4320

[181] T. Jiang, J. Munguia-Lopez, S. Flores-Torres, J. Grant, S. Vijayakumar, A. D. Leon-Rodriguez, and J. M. Kinsella, "Bioprintable alginate/gelatin hydrogel 3d in vitro model systems induce cell spheroid formation." *Journal of visualized experiments : JoVE*, 7 2018.

[182] L. D. Moor, S. Fernandez, C. Vercruysse, L. Tytgat, M. Asadian, N. D. Geyter, S. V. Vlierberghe, P. Dubruel, and H. Declercq, "Hybrid bioprinting of chondrogenically induced human mesenchymal stem cell spheroids," *Frontiers in Bioengineering and Biotechnology*, vol. 8, 2020.

[183] Y. B. Lee, E. M. Kim, H. Byun, H. kwan Chang, K. Jeong, Z. M. Aman, Y. S. Choi, J. Park, and H. Shin, "Engineering spheroids potentiating cell-cell and cell-ecm interactions by self-assembly of stem cell microlayer," *Biomaterials*, vol. 165, pp. 105–120, 5 2018.

[184] J. M. Ayuso, R. Monge, A. Martínez-González, M. V.-M. noz, G. A. Llamazares, J. Berganzo, A. Hernández-Laín, J. Santolaria, M. Doblaré, C. Hubert, J. N. Rich, P. Sánchez-Gómez, V. M. Pérez-García, I. Ochoa, and L. J. Fernández, "Glioblastoma on a microfluidic chip: Generating pseudopalisades and enhancing aggressiveness through blood vessel obstruction events," *Neuro–Oncology*, vol. 19, pp. 503–513, 2017. [Online]. Available: https://doi.org/10.1093/neuonc/now230

[185] M. Anguiano, C. Castilla, M. Maska, C. Ederra, R. Peláez, X. Morales, G. M. noz Arrieta, M. Mujika, M. Kozubek, A. M. noz Barrutia, A. Rouzaut, S. Arana, J. M. Garcia-Aznar, and C. O. de Solorzano, "Characterization of three–dimensional cancer cell migration in mixed collagen–matrigel scaffolds using microfluidics and image analysis," *PLoS ONE*, vol. 12, 2017.

[186] M. Z. I. Mollah, H. M. Zahid, Z. Mahal, M. Rashed, and I. Faruque, "The usages and potential uses of alginate for healthcare applications," *Frontiers in Molecular Biosciences*, vol. 8, pp. 1–12, 2021.

[187] P. Friedl and K. Wolf, "Tumour–cell invasion and migration: Diversity and escape mechanisms," *Nature Reviews Cancer*, vol. 3, pp. 362–374, 2003.

[188] S. V. Helvert, C. Storm, and P. Friedl, "Mechanoreciprocity in cell migration," *Nature Cell Biology*, vol. 20, 2018.

[189] Y. L. Yang and L. J. Kaufman, "Rheology and confocal reflectance microscopy as probes of mechanical properties and structure during collagen and collagen/hyaluronan self–assembly," *Biophysical Journal*, vol. 96, pp. 1566–1585, 2009. [Online]. Available: http://dx.doi.org/10.1016/j.bpj.2008.10.063

[190] R. C. Arevalo, J. S. Urbach, and D. L. Blair, "Size–dependent rheology of type–i collagen networks," *Biophysical Journal*, vol. 99, pp. L65–L67, 2010. [Online]. Available: http://dx.doi.org/10.1016/j.bpj.2010.08.008

[191] I. K. Piechocka, A. S. V. Oosten, R. G. Breuls, and G. H. Koenderink, "Rheology of heterotypic collagen networks," *Biomacromolecules*, vol. 12, pp. 2797–2805, 2011.

[192] I. Argatov, A. Iantchenko, and V. Kocherbitov, "How to define the storage and loss moduli for a rheologically nonlinear material?: A constructive review of nonlinear rheological measures," *Continuum Mechanics and Thermodynamics*, vol. 29, pp. 1375–1387, 2017.

[193] J. Iturri and J. L. Toca-Herrera, "Characterization of cell scaffolds by atomic force microscopy," *Polymers*, vol. 9, 2017. [Online]. Available: https://www.mdpi.com/2073--4360/9/8/383

[194] C. B. Raub, V. Suresh, T. Krasieva, J. Lyubovitsky, J. D. Mih, A. J. Putnam, B. J. Tromberg, and S. C. George, "Noninvasive assessment of collagen gel microstructure and mechanics using multiphoton microscopy," *Biophysical Journal*, vol. 92, pp. 2212–2222, 2007.

[195] A. J. Holder, N. Badiei, K. Hawkins, C. Wright, P. R. Williams, and D. J. Curtis, "Control of collagen gel mechanical properties through manipulation of gelation conditions near the sol–gel transition," *Soft Matter*, vol. 14, pp. 574–580, 2018.

[196] Y. L. Yang, S. Motte, and L. J. Kaufman, "Pore size variable type i collagen gels and their interaction with glioma cells," *Biomaterials*, vol. 31, pp. 5678–5688, 2010.

[197] M. Achilli and D. Mantovani, "Tailoring mechanical properties of collagen–based scaffolds for vascular tissue engineering: The effects of ph, temperature and ionic strength on gelation," *Polymers*, vol. 2, pp. 664–680, 2010.

[198] Y. L. Yang, L. M. Leone, and L. J. Kaufman, "Elastic moduli of collagen gels can be predicted from two–dimensional confocal microscopy," *Biophysical Journal*, vol. 97, pp. 2051–2060, 2009. [Online]. Available: http://dx.doi.org/10.1016/j.bpj.2009.07.035

[199] T. Ushiki, "Collagen fibers, reticular fibers and elastic fibers. a comprehensive understanding from a morphological viewpoint," *Archives of Histology and Cytology*, vol. 65, no. 2, pp. 109–126, 2002.

[200] C. B. Raub, J. Unruh, V. Suresh, T. Krasieva, T. Lindmo, E. Gratton, B. J. Tromberg, and S. C. George, "Image correlation spectroscopy of multiphoton images correlates with collagen mechanical properties," *Biophysical Journal*, vol. 94, pp. 2361–2373, 2008. [Online]. Available: http://dx.doi.org/10.1529/biophysj.107.120006

[201] R. Pamplona, S. González-Lana, P. Romero, I. Ochoa, R. Martín-Rapún, and C. Sánchez-Somolinos, "Tuning of mechanical properties in photopolymerizable gelatin-based hydrogels for in vitro cell culture systems," *ACS Applied Polymer Materials*, vol. 5, no. 2, pp. 1487–1498, 2023. [Online]. Available: https://doi.org/10.1021/acsapm.2c01980

[202] T. Ushiki and C. Ide, "Three–dimensional architecture of the endoneurium with special reference to the collagen fibril arrangement in relation to nerve fibers," *Archivum histologicum japonicum*, vol. 49, pp. 553–563, 1986.

[203] J. Xie, M. Bao, S. M. Bruekers, and W. T. Huck, "Collagen gels with different fibrillar microarchitectures elicit different cellular responses," *ACS Applied Materials and Interfaces*, vol. 9, pp. 19 630–19 637, 2017.

[204] S. Meehan and A. S. Nain, "Role of suspended fiber structural stiffness and curvature on single–cell migration, nucleus shape, and focal–adhesion–cluster length." *Biophysical journal*, vol. 107, pp. 2604–2611, 12 2014.

[205] C. Lo, H. Wang, M. Dembo, and Y. Wang, "Cell movement is guided by the rigidity of the substrate," *Biophysical Journal*, vol. 79, pp. 144–152, 2000.

[206] B.-H. Mao, M. T. K. Nguyen, M.-J. Tang, R. D. Kamm, and T.-Y. Tu, "The interface stiffness and topographic feature dictate interfacial invasiveness of cancer spheroids," *Biofabrication*, 2022. [Online]. Available: http://iopscience.iop.org/article/10.1088/1758--5090/acaa00

[207] I. Pajic-Lijakovic, M. Milivojevic, and A. G. Clark, "Collective cell migration on collagen–i networks: The impact of matrix viscoelasticity," *Frontiers in Cell and Developmental Biology*, vol. 10, pp. 1–8, 2022.

[208] A. Mukherjee, B. Behkam, and A. S. Nain, "Cancer cells sense fibers by coiling on them in a curvature–dependent manner," *iScience*, vol. 19, pp. 905–915, 2019. [Online]. Available: https://doi.org/10.1016/j.isci.2019.08.023

[209] C. M. Murphy, M. G. Haugh, and F. J. O'Brien, "The effect of mean pore size on cell attachment, proliferation and migration in collagen–glycosaminoglycan scaffolds for bone tissue engineering," *Biomaterials*, vol. 31, pp. 461–466, 2010. [Online]. Available: http://dx.doi.org/10.1016/j.biomaterials.2009.09.063

[210] H. E. Balcioglu, B. van de Water, and E. H. J. Danen, "Tumor–induced remote ecm network orientation steers angiogenesis," *Scientific Reports*, vol. 6, p. 22580, 2016. [Online]. Available: https://doi.org/10.1038/srep22580

[211] E. Pretzsch, F. Bosch, J. Neumann, P. Ganschow, A. Bazhin, M. Guba, J. Werner, and M. Angele, "Mechanisms of metastasis in colorectal cancer and metastatic organotropism: Hematogenous versus peritoneal spread," *Journal of Oncology*, vol. 2019, pp. 1–13, 9 2019.

[212] R. C. Oliveira, H. Alexandrino, M. A. Cipriano, and J. G. T. ao, "Liver metastases and histological growth patterns: Biological behavior and potential clinical implications-another path to individualized medicine?" *Journal of oncology*, vol. 2019, p. 6280347, 2019.

[213] X. Lin, Z. Xiao, T. Chen, S. H. Liang, and H. Guo, "Glucose metabolism on tumor plasticity, diagnosis, and treatment," *Frontiers in Oncology*, vol. 10, 3 2020.

[214] S.-H. Kim and K.-H. Baek, "Regulation of cancer metabolism by deubiquitinating enzymes: The warburg effect," *International Journal of Molecular Sciences*, vol. 22, p. 6173, 6 2021.

[215] N. Ahmadiankia, "In vitro and in vivo studies of cancer cell behavior under nutrient deprivation," *Cell Biology International*, vol. 44, pp. 1588–1597, 8 2020.

[216] H. E. Mohamed, M. E. Asker, N. S. Kotb, and A. M. E. Habab, "Human platelet lysate efficiency, stability, and optimal heparin concentration required in culture of mammalian cells," *BLOOD RESEARCH*, vol. 55, pp. 35–43, 3 2020.

[217] P. Altea-Manzano, A. M. Cuadros, L. A. Broadfield, and S.-M. Fendt, "Nutrient metabolism and cancer in the in vivo context: a metabolic game of give and take," *EMBO reports*, vol. 21, 10 2020.

[218] C.-Y. Huang, C.-Y. Huang, Y.-C. Pai, B.-R. Lin, T.-C. Lee, P.-H. Liang, and L. C.-H. Yu, "Glucose metabolites exert opposing roles in tumor chemoresistance," *Frontiers in Oncology*, vol. 9, 11 2019.

[219] H. M. Lee, S. C. Lee, L. He, A. P. S. Kong, D. Mao, Y. Hou, A. C. K. Chung, G. Xu, R. C. W. Ma, and J. C. N. Chan, "Legacy effect of high glucose on promoting survival of hct116 colorectal cancer cells by reducing endoplasmic reticulum stress response." *American journal of cancer research*, vol. 11, pp. 6004–6023, 2021.

[220] A. Read and M. Schroder, "The unfolded protein response: An overview," *Biology*, vol. 10, p. 384, 4 2021.

[221] M. M. Schroll, G. J. LaBonia, K. R. Ludwig, and A. B. Hummon, "Glucose restriction combined with autophagy inhibition and chemotherapy in hct 116 spheroids decreases cell clonogenicity and viability regulated by tumor suppressor genes," *Journal of Proteome Research*, vol. 16, pp. 3009–3018, 8 2017.

[222] M. Mauthe, I. Orhon, C. Rocchi, X. Zhou, M. Luhr, K.-J. Hijlkema, R. P. Coppes, N. Engedal, M. Mari, and F. Reggiori, "Chloroquine inhibits autophagic flux by decreasing autophagosome-lysosome fusion," *Autophagy*, vol. 14, pp. 1435–1455, 8 2018.

[223] M. Kciuk, B. Marciniak, and R. Kontek, "Irinotecanâ€"still an important player in cancer chemotherapy: A comprehensive overview," *International Journal of Molecular Sciences*, vol. 21, p. 4919, 7 2020.

[224] R. J. Edwards, A. T. Saurin, R. D. Rakhit, and M. S. Marber, "Therapeutic potential of ischaemic preconditioning," *British Journal of Clinical Pharmacology*, vol. 50, pp. 87–97, 8 2000.

[225] M. MATTSON and R. WAN, "Beneficial effects of intermittent fasting and caloric restriction on the cardiovascular and cerebrovascular systems," *The Journal of Nutritional Biochemistry*, vol. 16, pp. 129–137, 3 2005.

[226] V. D. Longo and M. P. Mattson, "Fasting: molecular mechanisms and clinical applications." *Cell metabolism*, vol. 19, pp. 181–92, 2 2014.

[227] L. Raffaghello, F. Safdie, G. Bianchi, T. Dorff, L. Fontana, and V. D. Longo, "Fasting and differential chemotherapy protection in patients." *Cell cycle (Georgetown, Tex.)*, vol. 9, pp. 4474–6, 11 2010.

[228] D. Y. Lee, S. Y. Lee, S. H. Yun, J. W. Jeong, J. H. Kim, H. W. Kim, J. S. Choi, G.-D. Kim, S. T. Joo, I. Choi, and S. J. Hur, "Review of the current research on fetal bovine serum and the development of cultured meat." *Food science of animal resources*, vol. 42, pp. 775–799, 9 2022.

[229] Z. Song, B. Wei, C. Lu, P. Li, and L. Chen, "Glutaminase sustains cell survival via the regulation of glycolysis and glutaminolysis in colorectal cancer." *Oncology letters*, vol. 14, pp. 3117–3123, 9 2017.

[230] J. Han, L. Zhang, H. Guo, W. Z. Wysham, D. R. Roque, A. K. Willson, X. Sheng, C. Zhou, and V. L. Bae-Jump, "Glucose promotes cell proliferation, glucose uptake and invasion in endometrial cancer cells via ampk/mtor/s6 and mapk signaling." *Gynecologic oncology*, vol. 138, pp. 668–75, 9 2015.

[231] Z. Zhao, X. Chen, A. M. Dowbaj, A. Sljukic, K. Bratlie, L. Lin, E. L. S. Fong, G. M. Balachander, Z. Chen, A. Soragni, M. Huch, Y. A. Zeng, Q. Wang, and H. Yu, "Organoids," *Nature Reviews Methods Primers*, vol. 2, p. 94, 12 2022.

[232] N. M. Cruz, X. Song, S. M. Czerniecki, R. E. Gulieva, A. J. Churchill, Y. K. Kim, K. Winston, L. M. Tran, M. A. Diaz, H. Fu, L. S. Finn, Y. Pei, J. Himmelfarb, and B. S. Freedman, "Organoid cystogenesis reveals a critical role of microenvironment in human polycystic kidney disease." *Nature materials*, vol. 16, pp. 1112–1119, 11 2017.

[233] S. F. Boj, A. M. Vonk, M. Statia, J. Su, R. R. G. Vries, J. M. Beekman, and H. Clevers, "Forskolin-induced swelling in intestinal organoids: An in vitro assay for assessing drug response in cystic fibrosis patients." *Journal of visualized experiments : JoVE*, 2 2017.

[234] D. Muilwijk, E. de Poel, P. van Mourik, S. W. F. Suen, A. M. Vonk, J. E. Brunsveld, E. Kruisselbrink, H. Oppelaar, M. C. Hagemeijer, G. Berkers, K. M. de Winter-de Groot, S. Heida-Michel, S. R. Jans, H. van Panhuis, M. M. van der Eerden, R. van der Meer, J. Roukema, E. Dompeling, E. J. M. Weersink, G. H. Koppelman, R. Vries, D. D. Z. van Ommen, M. J. C. Eijkemans, C. K. van der Ent, and J. M. Beekman, "Forskolin-induced organoid swelling is associated with long-term cystic fibrosis disease progression." *The European respiratory journal*, vol. 60, 8 2022.

[235] K. M. Burleson, L. K. Hansen, and A. P. N. Skubitz, "Ovarian carcinoma spheroids disaggregate on type i collagen and invade live human mesothelial cell monolayers." *Clinical & experimental metastasis*, vol. 21, pp. 685–97, 2004.

[236] S. M. Grist, S. S. Nasseri, L. Laplatine, J. C. Schmok, D. Yao, J. Hua, L. Chrostowski, and K. C. Cheung, "Long-term monitoring in a microfluidic system to study tumour spheroid response to chronic and cycling hypoxia," *Scientific Reports*, vol. 9, p. 17782, 11 2019.

[237] M. Barisam, M. S. Saidi, N. Kashaninejad, and N.-T. Nguyen, "Prediction of necrotic core and hypoxic zone of multicellular spheroids in a microbioreactor with a u-shaped barrier." *Micromachines*, vol. 9, 2 2018.

[238] Q. Wen and P. A. Janmey, "Polymer physics of the cytoskeleton." *Current opinion in solid state & materials science*, vol. 15, pp. 177–182, 10 2011.

[239] Y. Nakaseko and M. Yanagida, "Cytoskeleton in the cell cycle," *Nature*, vol. 412, pp. 291–292, 7 2001.

[240] S. L. Rogers and V. I. Gelfand, "Membrane trafficking, organelle transport, and the cytoskeleton," *Current Opinion in Cell Biology*, vol. 12, pp. 57–62, 2 2000.

[241] N. Wang and Z. Suo, "Long-distance propagation of forces in a cell," *Biochemical and Biophysical Research Communications*, vol. 328, pp. 1133–1138, 3 2005.

[242] S. Chanet and A. C. Martin, "Mechanical force sensing in tissues," 2014, pp. 317–352.

[243] T. Akisaka, H. Yoshida, R. Suzuki, and K. Takama, "Adhesion structures and their cytoskeleton-membrane interactions at podosomes of osteoclasts in culture," *Cell and Tissue Research*, vol. 331, pp. 625–641, 3 2008.

[244] S. Linder, "The matrix corroded: podosomes and invadopodia in extracellular matrix degradation," *Trends in Cell Biology*, vol. 17, pp. 107–117, 3 2007.

[245] A. Ratheesh and A. S. Yap, "A bigger picture: classical cadherins and the dynamic actin cytoskeleton," *Nature Reviews Molecular Cell Biology*, vol. 13, pp. 673–679, 10 2012.

[246] G. Cooper, "Chapter 11, the cytoskeleton and cell movement," in *The Cell: A Molecular Approach. 2nd edition*. Sunderland (MA): Sinauer Associates, 2000, ch. 11, available from: https://www.ncbi.nlm.nih.gov/books/NBK9893/.

[247] S. Seetharaman and S. Etienne-Manneville, "Cytoskeletal crosstalk in cell migration," *Trends in Cell Biology*, vol. 30, pp. 720–735, 9 2020.

[248] T. R. Polte, G. S. Eichler, N. Wang, and D. E. Ingber, "Extracellular matrix controls myosin light chain phosphorylation and cell contractility through modulation of cell shape and cytoskeletal prestress," *American Journal of Physiology-Cell Physiology*, vol. 286, pp. C518–C528, 3 2004.

[249] "What is the cytoskeleton?" https://www.mechanobio.info/cytoskeleton-dynamics/what-is-the-cytoskeleton/#what-is-the-cytoskeleton/, accesed: 29-09-2023.

[250] S. Etienne-Manneville, "Cytoplasmic intermediate filaments in cell biology," *Annual Review of Cell and Developmental Biology*, vol. 34, pp. 1–28, 10 2018.

[251] G. Cooper, "Microtubules," in *The Cell: A Molecular Approach. 2nd edition*. Sunderland (MA): Sinauer Associates, 2000, ch. 11, available from: https://www.ncbi.nlm.nih.gov/books/NBK9893/.

[252] ——, "Structure and organization of actin filaments," in *The Cell: A Molecular Approach. 2nd edition*. Sunderland (MA): Sinauer Associates, 2000, ch. 11, available from: https://www.ncbi.nlm.nih.gov/books/NBK9893/.

[253] Hohmann and Dehghani, "The cytoskeleton-a complex interacting meshwork," *Cells*, vol. 8, p. 362, 4 2019.

[254] T. D. Pollard and J. A. Cooper, "Actin, a central player in cell shape and movement," *Science*, vol. 326, pp. 1208–1212, 11 2009.

[255] M. Murrell, P. W. Oakes, M. Lenz, and M. L. Gardel, "Forcing cells into shape: the mechanics of actomyosin contractility," *Nature Reviews Molecular Cell Biology*, vol. 16, pp. 486–498, 8 2015.

[256] S. de Beco, F. Amblard, and S. Coscoy, "New insights into the regulation of e-cadherin distribution by endocytosis," pp. 63–108, 2012.

[257] G. H. Koenderink and E. K. Paluch, "Architecture shapes contractility in actomyosin networks," *Current Opinion in Cell Biology*, vol. 50, pp. 79–85, 2 2018.

[258] G. Cooper, "Actin, myosin, and cell movement," in *The Cell: A Molecular Approach. 2nd edition*. Sunderland (MA): Sinauer Associates, 2000, ch. 11, available from: https://www.ncbi.nlm.nih.gov/books/NBK9893/.

[259] D. Robinson, Y.-S. Kee, T. Luo, and A. Surcel, "7.5 understanding how dividing cells change shape," *Comprehensive Biophysics*, pp. 48–72, 2012.

[260] H. L. Sweeney and D. W. Hammers, "Muscle contraction," *Cold Spring Harbor Perspectives in Biology*, vol. 10, p. a023200, 2 2018.

[261] "The role of actin and myosin," http://encyclopedia.lubopitko-bg.com/The_Role_of_Actin_and_Myosin.html, accesed: 29-09-2023.

[262] L. R. Lessey, S. C. Robinson, R. Chaudhary, and J. M. Daniel, "Adherens junction proteins on the move-from the membrane to the nucleus in intestinal diseases," *Frontiers in Cell and Developmental Biology*, vol. 10, 10 2022.

[263] A. Esmaeilniakooshkghazi, E. Pham, S. P. George, A. Ahrorov, F. R. Villagomez, M. Byington, S. Mukhopadhyay, S. Patnaik, J. C. Conrad, M. Naik, S. Ravi, N. Tebbutt, J. Mooi, C. M. Reehorst, J. M. Mariadason, and S. Khurana, "In colon cancer cells fascin1 regulates adherens junction remodeling," *The FASEB Journal*, vol. 37, 3 2023.

[264] K. Manibog, K. Sankar, S.-A. Kim, Y. Zhang, R. L. Jernigan, and S. Sivasankar, "Molecular determinants of cadherin ideal bond formation: Conformation-dependent unbinding on a multidimensional landscape," *Proceedings of the National Academy of Sciences*, vol. 113, 9 2016.

[265] A. J. Knights, A. P. W. Funnell, M. Crossley, and R. C. M. Pearson, "Holding tight: Cell junctions and cancer spread." *Trends in cancer research*, vol. 8, pp. 61–69, 2012.

[266] W. Meng and M. Takeichi, "Adherens junction: molecular architecture and regulation." *Cold Spring Harbor perspectives in biology*, vol. 1, p. a002899, 12 2009.

[267] S. Yonemura, M. Itoh, A. Nagafuchi, and S. Tsukita, "Cell-to-cell adherens junction formation and actin filament organization: similarities and differences between non-polarized fibroblasts and polarized epithelial cells," *Journal of Cell Science*, vol. 108, pp. 127–142, 1 1995.

[268] H. A. Muller and E. Wieschaus, "armadillo, bazooka, and stardust are critical for early stages in formation of the zonula adherens and maintenance of the polarized blastoderm epithelium in drosophila." *The Journal of cell biology*, vol. 134, pp. 149–163, 7 1996.

[269] "What are cell-cell adhesions?" https://www.mechanobio.info/what-is-mechanosignaling/what-are-cell-cell-adhesions/, accesed: 29-09-2023.

[270] C. Pérez-González, G. Ceada, F. Greco, M. Matejcic, M. Gómez-González, N. Castro, A. Menendez, S. Kale, D. Krndija, A. G. Clark, V. R. Gannavarapu, A. álvarez Varela, P. Roca-Cusachs, E. Batlle, D. M. Vignjevic, M. Arroyo, and X. Trepat, "Mechanical compartmentalization of the intestinal organoid enables crypt folding and collective cell migration," *Nature Cell Biology*, vol. 23, pp. 745–757, 7 2021.

[271] S. C. Schwager, P. V. Taufalele, and C. A. Reinhart-King, "Cell-cell mechanical communication in cancer," *Cellular and Molecular Bioengineering*, vol. 12, pp. 1–14, 2 2019.

[272] F. Bordeleau, T. A. Alcoser, and C. A. Reinhart-King, "Physical biology in cancer. 5. the rocky road of metastasis: the role of cytoskeletal mechanics in cell migratory response to 3d matrix topography," *American Journal of Physiology-Cell Physiology*, vol. 306, pp. C110–C120, 1 2014.

[273] S. Sharma, C. Santiskulvong, J. Rao, J. K. Gimzewski, and O. Dorigo, "The role of rho gtpase in cell stiffness and cisplatin resistance in ovarian cancer cells," *Integr. Biol.*, vol. 6, pp. 611–617, 2014.

[274] K. D. Nyberg, S. L. Bruce, A. V. Nguyen, C. K. Chan, N. K. Gill, T.-H. Kim, E. K. Sloan, and A. C. Rowat, "Predicting cancer cell invasion by single-cell physical phenotyping," *Integrative Biology*, vol. 10, pp. 218–231, 4 2018.

[275] J. Kim, Y. Cao, C. Eddy, Y. Deng, H. Levine, W.-J. Rappel, and B. Sun, "The mechanics and dynamics of cancer cells sensing noisy 3d contact guidance," *Proceedings of the National Academy of Sciences*, vol. 118, 3 2021.

[276] Y. Zhou, F. Tozzi, J. Chen, F. Fan, L. Xia, J. Wang, G. Gao, A. Zhang, X. Xia, H. Brasher, W. Widger, L. M. Ellis, and Z. Weihua, "Intracellular atp levels are a pivotal determinant of chemoresistance in colon cancer cells," *Cancer Research*, vol. 72, pp. 304–314, 1 2012.

[277] O. Nakagawa, K. Fujisawa, T. Ishizaki, Y. Saito, K. Nakao, and S. Narumiya, "Rock-i and rock-ii, two isoforms of rho-associated coiled-coil forming protein serine/threonine kinase in mice," *FEBS Letters*, vol. 392, pp. 189–193, 8 1996.

[278] K. Watanabe, M. Ueno, D. Kamiya, A. Nishiyama, M. Matsumura, T. Wataya, J. B. Takahashi, S. Nishikawa, S. ichi Nishikawa, K. Muguruma, and Y. Sasai, "A rock inhibitor permits survival of dissociated human embryonic stem cells," *Nature Biotechnology*, vol. 25, pp. 681–686, 6 2007.

[279] B. Tian, B. T. Gabelt, P. Kaufman, and B. Geiger, "The cytoskeletal network of the trabecular meshwork." Elsevier, 2010, pp. 549–555.

[280] B. I. Roman, S. Verhasselt, and C. V. Stevens, "Medicinal chemistry and use of myosin ii inhibitor (s)-blebbistatin and its derivatives," *Journal of Medicinal Chemistry*, vol. 61, pp. 9410–9428, 11 2018.

[281] T. Sakamoto, J. Limouze, C. A. Combs, A. F. Straight, and J. R. Sellers, "Blebbistatin, a myosin ii inhibitor, is photoinactivated by blue light," *Biochemistry*, vol. 44, pp. 584–588, 1 2005.

[282] C. O'Shea, S. N. Kabir, A. P. Holmes, M. Lei, L. Fabritz, K. Rajpoot, and D. Pavlovic, "Cardiac optical mapping - state-of-the-art and future challenges," *The International Journal of Biochemistry & Cell Biology*, vol. 126, p. 105804, 9 2020.

[283] A. J. Devanny, M. B. Vancura, and L. J. Kaufman, "Exploiting differential effects of actomyosin contractility to control cell sorting among breast cancer cells," *Molecular Biology of the Cell*, vol. 32, 11 2021.

[284] R. Y. Nguyen, H. Xiao, X. Gong, A. Arroyo, A. T. Cabral, T. T. Fischer, K. M. Flores, X. Zhang, M. E. Robert, B. E. Ehrlich, and M. Mak, "Cytoskeletal dynamics regulates stromal invasion behavior of distinct liver cancer subtypes," *Communications Biology*, vol. 5, p. 202, 3 2022.

[285] A. Lugli, R. Kirsch, Y. Ajioka, F. Bosman, G. Cathomas, H. Dawson, H. E. Zimaity, J.-F. Fléjou, T. P. Hansen, A. Hartmann, S. Kakar, C. Langner, I. Nagtegaal, G. Puppa, R. Riddell, A. Ristimaki, K. Sheahan, T. Smyrk, K. Sugihara, B. Terris, H. Ueno, M. Vieth, I. Zlobec,

and P. Quirke, "Recommendations for reporting tumor budding in colorectal cancer based on the international tumor budding consensus conference (itbcc) 2016," *Modern Pathology*, vol. 30, pp. 1299–1311, 9 2017.

[286] V. H. Koelzer, I. Zlobec, and A. Lugli, "Tumor budding in colorectal cancer-ready for diagnostic practice?" *Human Pathology*, vol. 47, pp. 4–19, 1 2016.

[287] I. Zlobec, M. D. Berger, and A. Lugli, "Tumour budding and its clinical implications in gastrointestinal cancers," *British Journal of Cancer*, vol. 123, pp. 700–708, 9 2020.

[288] J. Friedrich, R. Ebner, and P. D. L. A. Kunz-Schughart, "Experimental anti-tumor therapy in 3-d: Spheroids-old hat or new challenge?" *International Journal of Radiation Biology*, vol. 83, no. 11-12, pp. 849–871, 2007, pMID: 18058370. [Online]. Available: https://doi.org/10.1080/09553000701727531

[289] X. Cui, Y. Hartanto, and H. Zhang, "Advances in multicellular spheroids formation," *Journal of The Royal Society Interface*, vol. 14, p. 20160877, 2 2017.

[290] S. R. Alves, I. R. Calori, H. Bi, and A. C. Tedesco, "Characterization of glioblastoma spheroid models for drug screening and phototherapy assays," *OpenNano*, vol. 9, p. 100116, 1 2023.

[291] L. Waldherr, M. Seitanidou, M. Jakesová, V. Handl, S. Honeder, M. Nowakowska, T. Tomin, M. K. Rad, T. Schmidt, J. Distl, R. Birner-Gruenberger, G. Campe, U. Schafer, M. Berggren, B. Rinner, M. Asslaber, N. Ghaffari-Tabrizi-Wizsy, S. Patz, D. T. Simon, and R. Schindl, "Targeted chemotherapy of glioblastoma spheroids with an iontronic pump," *Advanced Materials Technologies*, vol. 6, p. 2001302, 5 2021.

[292] G.-S. Jung, K.-M. Lee, J.-K. Park, S.-K. Choi, and W. B. Jeon, "Morphogenetic and neuronal characterization of human neuroblastoma multicellular spheroids cultured under undifferentiated and all-trans-retinoic acid-differentiated conditions." *BMB reports*, vol. 46, pp. 276–81, 5 2013.

[293] A. Seyfoori, E. Samiei, N. Jalili, B. Godau, M. Rahmanian, L. Farahmand, K. Majidzadeh-A, and M. Akbari, "Self-filling microwell arrays (sfmas) for tumor spheroid formation," *Lab on a Chip*, vol. 18, pp. 3516–3528, 2018.

[294] S. R. Modarai, L. M. Opdenaker, V. Viswanathan, J. Z. Fields, and B. M. Boman, "Somatostatin signaling via sstr1 contributes to the quiescence of colon cancer stem cells," *BMC Cancer*, vol. 16, p. 941, 12 2016.

[295] S. J. Han, S. Kwon, and K. S. Kim, "Challenges of applying multicellular tumor spheroids in preclinical phase," *Cancer Cell International*, vol. 21, p. 152, 3 2021.

[296] R. Kalluri and R. A. Weinberg, "The basics of epithelial-mesenchymal transition," *Journal of Clinical Investigation*, vol. 119, pp. 1420–1428, 6 2009.

[297] M.-G. Noh, S.-J. Oh, E.-J. Ahn, Y.-J. Kim, T.-Y. Jung, S. Jung, K.-K. Kim, J.-H. Lee, K.-H. Lee, and K.-S. Moon, "Prognostic significance of e-cadherin and n-cadherin expression in gliomas." *BMC cancer*, vol. 17, p. 583, 8 2017.

[298] L. J. Lewis-Tuffin, F. Rodriguez, C. Giannini, B. Scheithauer, B. M. Necela, J. N. Sarkaria, and P. Z. Anastasiadis, "Misregulated e-cadherin expression associated with an aggressive brain tumor phenotype." *PloS one*, vol. 5, p. e13665, 10 2010.

[299] K. Habra, J. R. D. Pearson, and S. E. B. McArdle, "Robust formation of optimal single spheroids towards cost-effective in vitro three-dimensional tumor models," *FEBS Open Bio*, vol. 13, pp. 1266–1277, 7 2023.

[300] B. S. Winters, S. R. Shepard, and R. A. Foty, "Biophysical measurement of brain tumor cohesion," *International Journal of Cancer*, vol. 114, pp. 371–379, 4 2005.

[301] B. Hegedus, F. Marga, K. Jakab, K. L. Sharpe-Timms, and G. Forgacs, "The interplay of cell-cell and cell-matrix interactions in the invasive properties of brain tumors," *Biophysical Journal*, vol. 91, pp. 2708–2716, 10 2006.

[302] Z. Zibaei, E. Babaei, A. R. N. Zamani, R. Rahbarghazi, and H. J. Azeez, "Curcumin-enriched gemini surfactant nanoparticles exhibited tumoricidal effects on human 3d spheroid ht-29 cells in vitro," *Cancer Nanotechnology*, vol. 12, p. 3, 12 2021.

[303] I. Druzhkova, M. Shirmanova, N. Ignatova, V. Dudenkova, M. Lukina, E. Zagaynova, D. Safina, S. Kostrov, D. Didych, A. Kuzmich, G. Sharonov, O. Rakitina, I. Alekseenko, and E. Sverdlov, "Expression of emt-related genes in hybrid e/m colorectal cancer cells determines fibroblast activation and collagen remodeling," *International Journal of Molecular Sciences*, vol. 21, p. 8119, 10 2020.

[304] S. K. Green, G. Francia, C. Isidoro, and R. S. Kerbel, "Antiadhesive antibodies targeting e-cadherin sensitize multicellular tumor spheroids to chemotherapy in vitro." *Molecular cancer therapeutics*, vol. 3, pp. 149–59, 2 2004.

[305] A. Riedl, M. Schlederer, K. Pudelko, M. Stadler, S. Walter, D. Unterleuthner, C. Unger, N. Kramer, M. Hengstschlager, L. Kenner, D. Pfeiffer, G. Krupitza, and H. Dolznig, "Comparison of cancer cells cultured in 2d vs 3d reveals differences in akt/mtor/s6-kinase signaling and drug response," *Journal of Cell Science*, 1 2016.

[306] J. H. Kim, K. J. Lee, Y. Seo, J.-H. Kwon, J. P. Yoon, J. Y. Kang, H. J. Lee, S. J. Park, S. P. Hong, J. H. Cheon, W. H. Kim, and T. I. Kim, "Effects of metformin on colorectal cancer stem cells depend on alterations in glutamine metabolism," *Scientific Reports*, vol. 8, p. 409, 1 2018.

[307] J. Li, P. Song, L. Zhu, N. Aziz, Q. Zhou, Y. Zhang, W. Xu, L. Feng, D. Chen, X. Wang, and H. Jin, "Synthetic lethality of glutaminolysis inhibition, autophagy inactivation and asparagine depletion in colon cancer," *Oncotarget*, vol. 8, pp. 42 664–42 672, 6 2017.

[308] M. Gutiérrez-Salmerón, S. R. Lucena, A. Chocarro-Calvo, J. M. García-Martínez, R. M. M. Orozco, and C. García-Jiménez, "Metabolic and hormonal remodeling of colorectal cancer cell signalling by diabetes," *Endocrine-Related Cancer*, vol. 28, pp. R191–R206, 6 2021.

[309] B. J. Altman, Z. E. Stine, and C. V. Dang, "From krebs to clinic: glutamine metabolism to cancer therapy," *Nature Reviews Cancer*, vol. 16, pp. 619–634, 10 2016.

[310] L. Jin, G. N. Alesi, and S. Kang, "Glutaminolysis as a target for cancer therapy," *Oncogene*, vol. 35, pp. 3619–3625, 7 2016.

[311] P. D. Antone, "Energy metabolism in cancer cells: How to explain the warburg and crabtree effects?" *Medical Hypotheses*, vol. 79, pp. 388–392, 9 2012.

[312] M. Taddei, E. Giannoni, T. Fiaschi, and P. Chiarugi, "Anoikis: an emerging hallmark in health and diseases," *The Journal of Pathology*, vol. 226, pp. 380–393, 1 2012.

[313] R. Palorini, G. Votta, Y. Pirola, H. D. Vitto, S. D. Palma, C. Airoldi, M. Vasso, F. Ricciardiello, P. P. Lombardi, C. Cirulli, R. Rizzi, F. Nicotra, K. Hiller, C. Gelfi, L. Alberghina, and F. Chiaradonna, "Protein kinase a activation promotes cancer cell resistance to glucose starvation and anoikis," *PLOS Genetics*, vol. 12, p. e1005931, 3 2016.

[314] S. Kamarajugadda, L. Stemboroski, Q. Cai, N. E. Simpson, S. Nayak, M. Tan, and J. Lu, "Glucose oxidation modulates anoikis and tumor metastasis," *Molecular and Cellular Biology*, vol. 32, pp. 1893–1907, 5 2012.

[315] M. Cnop, F. Foufelle, and L. A. Velloso, "Endoplasmic reticulum stress, obesity and diabetes," *Trends in Molecular Medicine*, vol. 18, pp. 59–68, 1 2012.

[316] A. Walker, A. Singh, E. Tully, J. Woo, A. Le, T. Nguyen, S. Biswal, D. Sharma, and E. Gabrielson, "Nrf2 signaling and autophagy are complementary in protecting breast cancer cells during glucose deprivation." *Free radical biology & medicine*, vol. 120, pp. 407–413, 5 2018.

[317] Q. Meng, J. Xu, C. Liang, J. Liu, J. Hua, Y. Zhang, Q. Ni, S. Shi, and X. Yu, "Gpx1 is involved in the induction of protective autophagy in pancreatic cancer cells in response to glucose deprivation," *Cell Death & Disease*, vol. 9, p. 1187, 12 2018.

[318] Z. Li, Y. Wang, H. Wu, L. Zhang, P. Yang, and Z. Li, "Grp78 enhances the glutamine metabolism to support cell survival from glucose deficiency by modulating the β-catenin signaling," *Oncotarget*, vol. 5, pp. 5369–5380, 7 2014.

[319] B. Levine and D. J. Klionsky, "Development by self-digestion: molecular mechanisms and biological functions of autophagy," *Developmental Cell*, vol. 6, pp. 463–477, 4 2004.

[320] J. Tan, H.-L. Wang, J. Yang, Q.-Q. Liu, C.-M. Li, Y.-Q. Wang, L.-N. Fu, Q.-Y. Gao, Y.-X. Chen, and J.-Y. Fang, "Jmjd2b-induced amino acid alterations enhance the survival of colorectal cancer cells under glucose-deprivation via autophagy," *Theranostics*, vol. 10, pp. 5763–5777, 2020.

[321] G. Liu, J. Li, and C. Wu, "Reciprocal regulation of actin filaments and cellular metabolism," *European Journal of Cell Biology*, vol. 101, p. 151281, 9 2022.

[322] L. Xu and A. Bretscher, "Rapid glucose depletion immobilizes active myosin v on stabilized actin cables," *Current Biology*, vol. 24, pp. 2471–2479, 10 2014.

[323] A. Suzuki, G. ichi Kusakai, A. Kishimoto, Y. Minegichi, T. Ogura, and H. Esumi, "Induction of cell-cell detachment during glucose starvation through f-actin conversion by snark, the fourth member of the amp-activated protein kinase catalytic subunit family," *Biochemical and Biophysical Research Communications*, vol. 311, pp. 156–161, 11 2003.

[324] J. Doukas, A. H. Cutler, C. A. Boswell, I. Joris, and G. Maino, "Reversible endothelial cell relaxation induced by oxygen and glucose deprivation. a model of ischemia in vitro." *The American journal of pathology*, vol. 145, pp. 211–9, 7 1994.

[325] I. Chiodi, G. Picco, C. Martino, and C. Mondello, "Cellular response to glutamine and/or glucose deprivation in in vitro transformed human fibroblasts," *Oncology Reports*, 4 2019.

[326] C. Dai, F. Sun, C. Zhu, and X. Hu, "Tumor environmental factors glucose deprivation and lactic acidosis induce mitotic chromosomal instability - an implication in aneuploid human tumors," *PLoS ONE*, vol. 8, p. e63054, 5 2013.

[327] H. Wu, Z. Ding, D. Hu, F. Sun, C. Dai, J. Xie, and X. Hu, "Central role of lactic acidosis in cancer cell resistance to glucose deprivation-induced cell death," *The Journal of Pathology*, vol. 227, pp. 189–199, 6 2012.

[328] N. A. Graham, M. Tahmasian, B. Kohli, E. Komisopoulou, M. Zhu, I. Vivanco, M. A. Teitell, H. Wu, A. Ribas, R. S. Lo, I. K. Mellinghoff, P. S. Mischel, and T. G. Graeber, "Glucose deprivation activates a metabolic and signaling amplification loop leading to cell death," *Molecular Systems Biology*, vol. 8, 1 2012.

[329] M. Fouad, A. Agha, M. A. Merzabani, and S. Shouman, "Resveratrol inhibits proliferation, angiogenesis and induces apoptosis in colon cancer cells," *Human & Experimental Toxicology*, vol. 32, pp. 1067–1080, 10 2013.

[330] C. A. Czajka, A. N. Mehesz, T. C. Trusk, M. J. Yost, and C. J. Drake, "Scaffold-free tissue engineering: Organization of the tissue cytoskeleton and its effects on tissue shape," *Annals of Biomedical Engineering*, vol. 42, pp. 1049–1061, 5 2014.

[331] N. V. Kosheleva, I. V. Ilina, I. M. Zurina, A. E. Roskova, A. A. Gorkun, A. V. Ovchinnikov, M. B. Agranat, and I. N. Saburina, "Laser-based technique for controlled damage of mesenchymal cell spheroids: a first step in studying reparation in vitro," *Biology Open*, vol. 5, pp. 993–1000, 7 2016.

[332] L. Guillaume, L. Rigal, J. Fehrenbach, C. Severac, B. Ducommun, and V. Lobjois, "Characterization of the physical properties of tumor-derived spheroids reveals critical insights for pre-clinical studies," *Scientific Reports*, vol. 9, p. 6597, 4 2019.

[333] S. Daster, N. Amatruda, D. Calabrese, R. Ivanek, E. Turrini, R. A. Droeser, P. Zajac, C. Fimognari, G. C. Spagnoli, G. Iezzi, V. Mele, and M. G. Muraro, "Induction of hypoxia and necrosis in multicellular tumor spheroids is associated with resistance to chemotherapy treatment," *Oncotarget*, vol. 8, pp. 1725–1736, 1 2017.

[334] H. Hardelauf, J.-P. Frimat, J. D. Stewart, W. Schormann, Y.-Y. Chiang, P. Lampen, J. Franzke, J. G. Hengstler, C. Cadenas, L. A. Kunz-Schughart, and J. West, "Microarrays for the scalable production of metabolically relevant tumour spheroids: a tool for modulating chemosensitivity traits," *Lab Chip*, vol. 11, pp. 419–428, 2011.

[335] J. R. Sims, S. Karp, and D. E. Ingber, "Altering the cellular mechanical force balance results in integrated changes in cell, cytoskeletal and nuclear shape," *Journal of Cell Science*, vol. 103, pp. 1215–1222, 12 1992.

[336] W. Goldmann, "Mechanical aspects of cell shape regulation and signaling," *Cell Biology International*, vol. 26, pp. 313–317, 4 2002.

[337] H. Vignes, C. Vagena-Pantoula, and J. Vermot, "Mechanical control of tissue shape: Cell-extrinsic and -intrinsic mechanisms join forces to regulate morphogenesis," *Seminars in Cell & Developmental Biology*, vol. 130, pp. 45–55, 10 2022.

[338] R. Link, K. Weibenbruch, M. Tanaka, M. Bastmeyer, and U. S. Schwarz, "Cell shape and forces in elastic and structured environments: From single cells to organoids," *Advanced Functional Materials*, 5 2023.

[339] D. E. Ingber, "Tensegrity-based mechanosensing from macro to micro," *Progress in Biophysics and Molecular Biology*, vol. 97, pp. 163–179, 6 2008.

[340] Y. Alvarez and M. Smutny, "Emerging role of mechanical forces in cell fate acquisition," *Frontiers in Cell and Developmental Biology*, vol. 10, 5 2022.

[341] M. Bergert, S. Lembo, S. Sharma, L. Russo, D. Milovanovic, K. H. Gretarsson, M. Bormel, P. A. Neveu, J. A. Hackett, E. Petsalaki, and A. D.-M. noz, "Cell surface mechanics gate embryonic stem cell differentiation," *Cell Stem Cell*, vol. 28, pp. 209–216.e4, 2 2021.

[342] H. D. Belly, A. Stubb, A. Yanagida, C. Labouesse, P. H. Jones, E. K. Paluch, and K. J. Chalut, "Membrane tension gates erk-mediated regulation of pluripotent cell fate," *Cell Stem Cell*, vol. 28, pp. 273–284.e6, 2 2021.

[343] E. M. Kim, Y. B. Lee, H. Byun, H. kwan Chang, J. Park, and H. Shin, "Fabrication of spheroids with uniform size by self-assembly of a micro-scaled cell sheet (μcs): The effect of cell contraction on spheroid formation," *ACS Applied Materials & Interfaces*, vol. 11, pp. 2802–2813, 1 2019.

[344] S. Kumper, F. K. Mardakheh, A. McCarthy, M. Yeo, G. W. Stamp, A. Paul, J. Worboys, A. Sadok, C. Jorgensen, S. Guichard, and C. J. Marshall, "Rho-associated kinase (rock) function is essential for cell cycle progression, senescence and tumorigenesis." *eLife*, vol. 5, p. e12994, 1 2016.

[345] L. JIANG, J. WEN, and W. LUO, "Rho-associated kinase inhibitor, y-27632, inhibits the invasion and proliferation of t24 and 5367 bladder cancer cells," *Molecular Medicine Reports*, vol. 12, pp. 7526–7530, 11 2015.

[346] L. Derycke, C. Stove, A.-S. Vercoutter-Edouart, O. D. Wever, L. Dollé, N. Colpaert, H. Depypere, J.-C. Michalski, and M. Bracke, "The role of non-muscle myosin iia in aggregation and invasion of human mcf-7 breast cancer cells," *The International Journal of Developmental Biology*, vol. 55, pp. 835–840, 2011.

[347] S. Gayan, A. Teli, and T. Dey, "Inherent aggressive character of invasive and non-invasive cells dictates the in vitro migration pattern of multicellular spheroid," *Scientific Reports*, vol. 7, p. 11527, 9 2017.

[348] F. Wang, N. Sun, H. Zeng, Y. Gao, N. Zhang, and W. Zhang, "Selenium deficiency leads to inflammation, autophagy, endoplasmic reticulum stress, apoptosis and contraction abnormalities via affecting intestinal flora in intestinal smooth muscle of mice," *Frontiers in Immunology*, vol. 13, 7 2022.

[349] R. L. Nelson, H. Abcarian, T. M. Nelson, A. Misumi, H. Kako, S. Rizk, and H. Sky-Peck, "The effect of dietary selenium deficiency on acute colorectal mucosal nucleotoxicity induced by several carcinogens in the rodent," *The American Journal of Surgery*, vol. 172, pp. 85–88, 7 1996.

[350] P. Trayhurn, "Oxygen-a critical, but overlooked, nutrient," *Frontiers in Nutrition*, vol. 6, 2 2019.

[351] R. Zhao, S. Jiang, L. Zhang, and Z. Yu, "Mitochondrial electron transport chain, ros generation and uncoupling (review)," *International Journal of Molecular Medicine*, 5 2019.

[352] B. Qiu and M. C. Simon, "Oncogenes strike a balance between cellular growth and homeostasis," *Seminars in Cell & Developmental Biology*, vol. 43, pp. 3–10, 7 2015.

[353] A. Nagao, M. Kobayashi, S. Koyasu, C. C. T. Chow, and H. Harada, "Hif-1-dependent reprogramming of glucose metabolic pathway of cancer cells and its therapeutic significance," *International Journal of Molecular Sciences*, vol. 20, p. 238, 1 2019.